Υ production and polarization in pp collisions at $\sqrt{s}$ = 13 TeV at the CERN LHC

Yanchun Ding

THÈSE de DOCTORAT DE
L'UNIVERSITÉ CLAUDE BERNARD LYON 1

en cotutelle avec la Central China Normal University-Chine

Ecole Doctorale : PHAST 52
Physique et Astrophysique

Discipline : Physique

Soutenue publiquement le 16/12/2022 par :

Yanchun DING

Υ production and polarization in pp collisions at $\sqrt{s} = 13$ TeV at the CERN LHC

Devant le jury composé de :

Nicole BASTID Professeure des Universités, LPC Clermont-Ferrand	**Rapporteuse**
Jinhui CHEN Professeur, Université de Fudan, Shanghai	**Rapporteur**
Brigitte CHEYNIS Chargée de Recherches CNRS, IP2I Lyon	**Directrice de thèse**
Mei HUANG Professeure, Académie Chinoise des Sciences, Pékin	**Présidente**
Imad LAKTINEH Professeur des Universités, IP2I Lyon	**Examinateur**
Laure MASSACRIER Chargée de Recherches CNRS, IJCLab Orsay	**Examinatrice**
Xiaoming ZHANG Professeur associé, CCNU Wuhan	**Co-Directeur de thèse**
Daicui ZHOU Professeur, CCNU Wuhan	**Directeur de thèse**
Antonio URAS Chargé de Recherches CNRS, IP2I Lyon	**Invité**

Abstract

Quarkonium (e.g. J/ψ or Υ and their excited states), bound states of charm and anticharm ($c\bar{c}$) or bottom and antibottom ($b\bar{b}$) quarks, represent an effective tool to test our understanding of quantum chromodynamics (QCD), concerning both their production mechanisms in vacuum or vacuum-like hadronic environments, and their interaction with the deconfined medium produced in ultra-relativistic heavy-ion collisions.

Among the available tools to characterize quarkonium production in proton-proton collisions, the correlation between quarkonium production and the charged-particle multiplicity is particularly helpful in order to investigate the interplay between soft and hard production mechanisms of quarkonium. In this context, the charged-particle multiplicity allows one to characterize the properties of the underlying event (including the role of multiparton interactions), acting as an effective scaling parameter determining the deviation of the observed effects from the vacuum reference, independently of the collision mode size. Another interesting tool to constrain our understanding of quarkonium production, is the study of quarkonium polarization, i.e. the spin alignment of a given quarkonium state with respect to a chosen axis.

ALICE is an experiment at the CERN Large Hadron Collider (LHC), dedicated to the study of hadronic collisions from pp to Pb–Pb, where a hot and dense medium can be created, named quark-gluon plasma. With the Run 2 data taking of the LHC, the highest collision energies ever delivered in the laboratory have become accessible.

In this thesis, the measurement of Υ(1S), Υ(2S), and Υ(3S) yields as a function of the charged-particle multiplicity density $\mathrm{d}N_{\mathrm{ch}}/\mathrm{d}\eta$, using the ALICE experiment at the LHC, is reported in pp collisions at $\sqrt{s} = 13$ TeV. The Υ meson yields are measured at forward rapidity ($2.5 < y < 4$) in the dimuon decay channel, whereas the charged-particle multiplicity is defined at central rapidity ($|\eta| < 1$). Both quantities are normalized to their average value in minimum bias events. The increase of the self-normalized Υ(1S), Υ(2S), and Υ(3S) yields is found to be compatible with a linear scaling with the self-normalized $\mathrm{d}N_{\mathrm{ch}}/\mathrm{d}\eta$, within the uncertainties. The measured Υ excited-to-ground state self-normalized yield ratios are found to be compatible with unity within uncertainties. Similarly, the measured double ratio of the self-normalized Υ(1S) to the self-normalized J/ψ yields, both measured at forward rapidity, is compatible with unity for self-normalized charged-particle multiplicity beyond one. The measurements are compared with theoretical predictions incorporating initial or final state effects.

The Υ(1S) polarization has been also measured in pp collisions at $\sqrt{s} = 13$ TeV; the analysis could not be

extended to the excited states Υ(2S) and Υ(3S) due to the limited size of the available data sample. The Υ(1S) polarization parameters λ_θ, λ_φ and $\lambda_{\theta\varphi}$ have been measured as a function of $p_{\rm T}$ both in the Helicity and Collins-Soper reference frames. No significant deviation from a zero-polarization scenario is observed for the Υ(1S) in pp collisions, as expected from the Next-to-Leading-Order QCD calculations. This result is consistent with the measurement performed by LHCb in pp collisions at $\sqrt{s} = 8$ TeV in a similar kinematic region ($2.2 < y < 4.5$) within large uncertainties.

Keywords: ALICE, Quarkonium, charged-particle multiplicity, Υ(1S), Υ(2S), Υ(3S), MPI, QGP, polarization, Helicity, Collins-Soper, Next-to-Leading-Order QCD

Résumé

Les états de quarkonium (e.g. J/ψ ou Υ et leurs états excités), états liés de quarks charme et anticharme ($c\bar{c}$) ou bottom et antibottom ($b\bar{b}$) fournissent un moyen efficace de tester notre compréhension de la chromodynamique quantique (QCD), à la fois en ce qui concerne leurs mécanismes de production dans le vide ou dans des environnements hadroniques de type vide et leur interaction avec le milieu déconfiné produit en collisions d'ions lourds ultra-relativistes.

Parmi les outils offerts pour caractériser la production de quarkonium en collisions proton-proton, la corrélation entre production de quarkonium et multiplicité de particules chargées est particulièrement pertinente pour mettre en évidence le rôle joué par les mécanismes durs et doux de production de quarkonium. Dans ce contexte, la multiplicité de particules chargées permet d'établir les propriétés de l'événement sous-jacent (y compris le rôle des interactions multi-partoniques), agissant comme un paramètre d'échelle effectif, déterminant l'écart des effets observés à la référence du vide, indépendamment de la taille du système. L'étude de la polarisation de quarkonium, i.e. l'alignement d'un état donné de quarkonium par rapport à un axe choisi, est un autre outil intéressant pour éclairer notre compréhension de la production de quarkonium.

ALICE est une expérience installée au LHC (Large Hadron Collider) du CERN, dédiée à l'étude de collisions hadroniques de proton-proton à Pb–Pb, où un milieu chaud et dense peut être créé, nommé le Plasma de Quarks-Gluons (QGP). Cette thèse décrit la mesure des Υ(1S), Υ(2S), et Υ(3S) en fonction de la densité de multiplicité de particules chargées $\mathrm{d}N_{\mathrm{ch}}/\mathrm{d}\eta$, effectuée par l'expérience ALICE du LHC en collisions proton-proton à $\sqrt{s} =$ 13 TeV. Les mésons Υ sont mesurés à rapidité avant ($2.5 < y < 4$) dans le canal de désintégration dimuon, tandis que la multiplicité de particules chargées est mesurée aux rapidités centrales ($|\eta| < 1$). Ces deux quantités sont normalisées à leurs valeurs moyennes obtenues dans les événements de biais minimum. L'augmentation observée des taux de production des Υ(1S), Υ(2S) et Υ(3S) en fonction de la multiplicité de particules chargées normalisée est compatible avec une évolution linéaire, compte-tenu des barres d'erreur. Les rapports états excités sur fondamentaux normalisés sont compatibles avec l'unité, compte tenu des barres d'erreur. De même, le double rapport normalisé Υ(1S) sur J/ψ, tous deux aux rapidités avant, est compatible avec l'unité pour des multiplicités de particules chargées normalisées au delà de 1. Les mesures sont confrontées à des prédictions de modèles théoriques incorporant des effets d'états initiaux ou finaux.

La polarisation du Υ(1S) a aussi été mesurée en collisions proton-proton à $\sqrt{s} = 13$ TeV. Du fait de la taille réduite du lot de données collectées, l'analyse n'a pas pu être menée pour les états Υ(2S) et Υ(3S). Les paramètres de polarisation λ_θ, λ_φ et $\lambda_{\theta\varphi}$ ont été extraits pour le Υ(1S) en fonction de l'impulsion transverse dans les référentiels de référence de l'hélicité et de Collins-Soper. Aucun écart significatif du scénario de polarisation nulle a été observé pour le Υ(1S) en collisions pp, conformément aux prédictions de calculs Next-to-Leading-Order QCD. Ce résultat est en accord avec une mesure effectuée par la collaboration LHCb en collisions pp à $\sqrt{s} = 8$ TeV dans une région cinématique similaire ($2.2 < y < 4.5$).

Mots-clefs: ALICE, Quarkonium, multiplicité de particules chargées, Υ(1S), Υ(2S), Υ(3S), MPI, QGP, polarisation, hélicité, Collins-Soper, Next-to-Leading-Order QCD

Contents

Chapter 1

Introduction

The quark–gluon plasma (QGP) is a deconfined state of hadronic matter predicted by Quantum Chromodynamics (QCD), the theory of the strong interaction, which can be produced in laboratory in ultra–relativistic heavy-ion collisions. Heavy quarks, (charm or bottom quarks), are expected to be produced in the early stages of such collisions, before the formation of the QGP, and they would go through the whole QGP evolution. In this context, quarkonium states (bound states composed of a heavy $q\bar{q}$ pair), are among the most powerful probes of the QGP, characterized by a small size ($<$1 fm) and large binding energy (of the order of few hundred MeV). For the J/ψ $c\bar{c}$ state, in particular, there are some evidences showing that in the presence of a QGP, certain mechanisms such as color screening and dynamical dissociation would lead to a sequential suppression of the corresponding population, while regeneration (due to the statistical recombination of $c\bar{c}$ pairs) may on the contrary contribute to increase the measured yield. In more general terms, a proper understanding of quarkonium production is crucial both in small collision systems like proton-proton, where the basic concepts of QCD, can be investigated, and in heavy–ion collisions where the QGP properties can be characterized. In this thesis, the multiplicity dependence of the Υ(nS) production and the Υ(1S) polarization in proton-proton collisions are studied and discussed in order to constrain the quarkonium production mechanisms.

1.1 The quark–gluon plasma

The universe was filled with an astoundingly hot and dense soup made of various elementary particles for a few millionths of a second just after the Big Bang. Quarks and gluons, carriers of the strong force that usually ”glues” quarks together into protons, neutrons, and other hadronic states, were the dominant particles in this medium. Quarks and gluons were only loosely connected under conditions of exceedingly high temperature and density, allowing them to freely travel in a state known as a quark-gluon plasma (QGP). Powerful accelerators cause collisions between heavy ions, such gold or lead nuclei, to mimic the circumstances of the very early universe. The hundreds

of protons and neutrons in two such nuclei collide with one another in these heavy–ion collisions with energy up to a few trillion electronvolts each, forming a fireball in which hadronic matter ”melts” into a QGP. The fireball expands and cools, and the individual quarks and gluons (collectively known as partons) recombine (hadronize) into hadronic states that flow away in all directions. The final-state particles are mainly pions and kaons, which are light (u, d, s) quark-antiquark pairs. Most of them can be investigated by analyzing the distribution and energy of the resulting fragments. Early research revealed that the QGP acts less like a gas and more like a perfect fluid with low viscosity. There are other experimental observations that help to further characterize the QGP state, among which one can cite: the suppression of high p_{T} particles and jets due to energy loss of the partons in the hot and dense medium; the enhancement of strange and multi–strange particles and signatures of a collective motion of the medium (see Ref. [1] and references therein). Among the various probes of the QGP, heavy quarks (charm and beauty) are of particular interest: due to their large mass, they are mainly produced in hard processes at the early stages of the heavy–ion collision, and subsequently interact with the strongly-interacting medium formed in the collision.

1.2 Introduction to quarkonium

Quarkonium states are composed of a charm (c, $\mathrm{m}_c \sim 1.3$ GeV/c^2) or bottom (b, $\mathrm{m}_b \sim 4.2$ GeV/c^2) quark and its corresponding anti-quark: these two families of bound states, named “charmonium” and “bottomonium”, respectively, are a powerful tool to understand the QCD. Both perturbative and non-perturbative aspects of QCD are involved in the mechanisms driving quarkonium production, and therefore it has to be treated with approaches that include both regimes. For this reason, quarkonium production represents a still open field in high energy physics, with some aspects related to its production that are not completely understood. Moreover, being produced in the early stages of hadronic collisions, they represent a very versatile probe to investigate the properties of the QGP produced in heavy-ion collisions.

1.2.1 Charmonium and bottomonium

A $c\bar{c}$ resonance with a mass of approximately 3.1 GeV/c^2, named J/ψ, was originally detected in 1974 by two distinct laboratories almost simultaneously [2, 3]. The first group was the one by S. Ting and collaborators, who noticed a significant peak in the electron-positron invariant mass spectrum (shown in the left of Fig. 1.1), when 30 GeV protons accelerated by the Alternating Gradient Synchrotron (AGS) at the Brookhaven National Laboratory (BNL) collided with a fixed target [2]. The second group was the one by B. Richter and collaborators, who observed the same structure in e^+e^- annihilation (shown in the right of Fig. 1.1) at the electron-positron storage ring SPEAR at the Stanford Linear Accelerator Center (SLAC) [3]. The same group at the SLAC also found the ψ(2S), the first

excited state of J/ψ. The charmonium spectrum for states under the open heavy-flavor pair production threshold is depicted in Fig. 1.2.

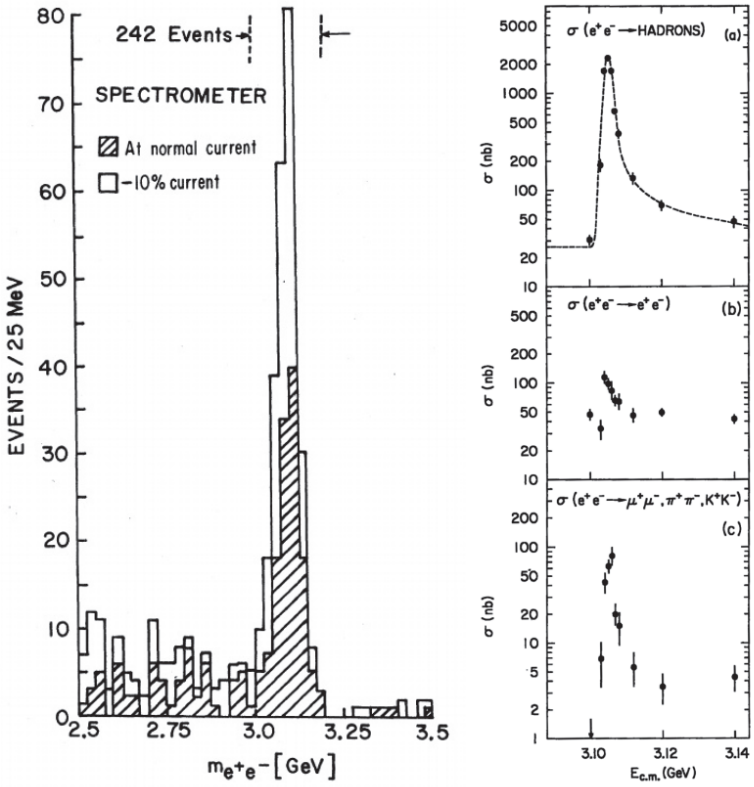

Figure 1.1: Left: Invariant mass distribution of e^+e^- pairs produced in the reaction p+Be from proton beams accelerated at the alternating gradient synchrotron of the BNL [2]. Right: Cross section as a function of energy for multi-hadron final states (top), e^+e^- (middle) and $\mu^+\mu^-$, $\pi^+\pi^-$ and K^+K^- (bottom). The curve in (a) is the expected shape of the δ-function folded with the Gaussian energy spread of the beams and including radiative processes [3].

A new resonance, named Υ, was discovered in the dimuon mass spectrum at around 9.5 GeV/c^2 in 400 GeV proton-nucleus collisions at Fermilab in 1977 [5]. It was soon determined that this particle was the lightest vector meson, and its excited states, Υ(2S) and Υ(3S), were observed in 1977 [6] and 1979 [7], respectively. The main Υ decay modes are summarized in Fig. 1.3, and Tab. 1.1. Notably, a large fraction of Υ(1S) component comes from feed-down, i.e. Υ(1S) produced in the decay of the heavier (excited) states.

The states of charmonium and bottomonium are both categorized using the quantum numbers — principal quantum number (n), orbital angular momentum (L), spin (S) and total angular momentum (J), and using the spectroscopic notation ($n^{2S+1}L_J$). Additionally, they can be described using the J^{PC} convention, where $\mathrm{P} = (-1)^{L+1}$ and $\mathrm{C} = (-1)^{L+S}$ are used to represent the parity and the charge conjugation, respectively. The two states that are most frequently formed are S-wave ($L = 0$) and P-wave ($L = 1$). When it comes to S-waves, if they are singlets of the total angular momentum ($J = 0$), they are called η_c (or η_b). If they are triplets ($J = 1$), they are named $\psi(c\bar{c})$ (or $\Upsilon(b\bar{b})$). While when it comes to P-wave triplets, they are known as χ_c (or χ_b).

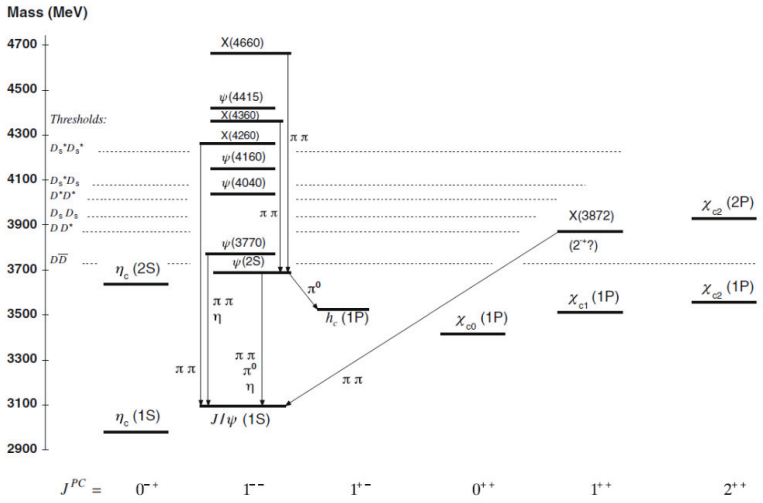

Figure 1.2: Charmonium decay modes with spectroscopy notation [4].

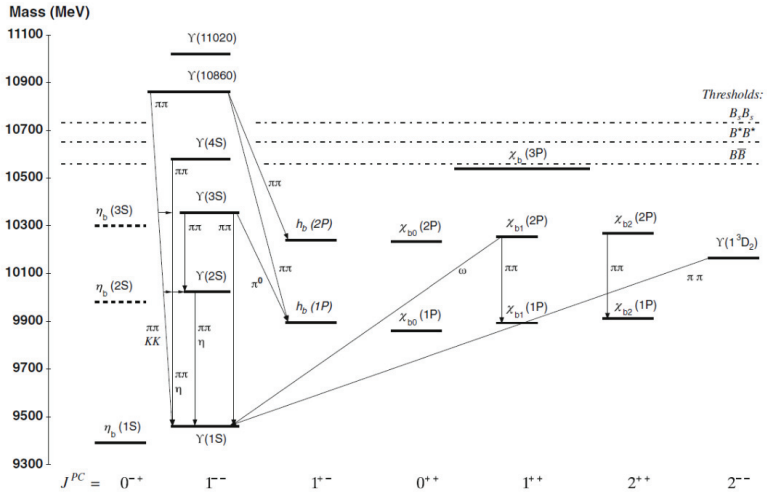

Figure 1.3: Bottomonium decay modes with spectroscopy notation [4].

State	Υ(1S)	Υ(2S)	Υ(3S)
$m(\mathrm{MeV}/c^2)$	9460.30 ± 0.26	10023.26 ± 0.31	10355.2 ± 0.5
$\Gamma(\mathrm{keV}/c^2)$	54.02 ± 1.25	31.98 ± 2.63	20.32 ± 1.85
Principal hadronic decays	ggg (81.7%) γgg (2.2%) ηX (2.9%) $D^{*\pm}X$ (2.5%)	ggg (58.8%) γgg (8.8%) $\Upsilon(1S)\pi^+\pi^-$ (17.9%) $\Upsilon(1S)\pi^0\pi^0$ (8.6%)	ggg (35.7%) $\Upsilon(2S)\pi^+\pi^-$ (2.8%) $\Upsilon(2S)\pi^0\pi^0$ (1.9%) $\Upsilon(2S)\gamma\gamma$ (5.0%) $\Upsilon(1S)\pi^+\pi^-$ (4.4%) $\Upsilon(1S)\pi^0\pi^0$ (2.2%)
Principal leptonic decays	e^+e^- (2.4%) $\mu^+\mu^-$ (2.5%) $\tau^+\tau^-$ (2.6%)	e^+e^- (1.9%) $\mu^+\mu^-$ (1.9%) $\tau^+\tau^-$ (2.0%)	$\mu^+\mu^-$ (2.2%) $\tau^+\tau^-$ (2.3%)

Table 1.1: Summary of the most significant characteristics of the Υ(nS) states. The percentages in brackets are the branching ratios [8].

1.2.2 Quarkonium production mechanism

Quarkonium production in pp collisions

Various theoretical models have been developed in the last decades, in an effort to describe the complete picture of the production mechanism, from the hard partonic interaction to heavy-quark pair ($Q\bar{Q}$) hadronization in quarkonium. A factorization hypothesis between hard and soft scales serves as the basis for most common available approaches. First phenomenological attempts (e.g. the Color Evaporation Model [9]) have been replaced by the Non-Relativistic QCD (NRQCD) [10], a rigorous effective field theory. Two models can be derived from this framework based on the sub-processes considered: the Color-Singlet Model (CSM) [11, 12] and the Color-Octet Model (COM) [10]. The CSM considers a wave function computed at zero $q\bar{q}$ separation, i.e. without any free parameter, and assumes no evolution of the quantum color-singlet state between the production of $Q\bar{Q}$ and the formation of quarkonium state. On the contrary, Long-Distance Matrix Elements (LDMEs) are introduced by the COM to account for the hadronization probability in a quarkonium state, according to its final quantum numbers. Recently, an improved version of the Color Evaporation Model (ICEM) has been developed to better describe the production of heavy quarkonia. Unlike the traditional Color Evaporation Model, ICEM incorporates a constraint that requires the invariant mass of the intermediate heavy quark-antiquark pair to be greater than the mass of the produced quarkonium. This constraint helps improve the description of heavy quarkonium production and provides a more accurate modeling of the underlying physics involved [13].

Recent measurements at the LHC have demonstrated the importance of color-octet terms in describing the J/ψ, ψ(2S), and Υ(nS) (n=1, 2 or 3) production cross sections [14, 15], illustrated in Fig. 1.4 and 1.5. In the left panel of Fig. 1.4, the ALICE measurement of inclusive J/ψ cross section at forward rapidity as a function of transverse momentum (p_{T}) in pp collisions at $\sqrt{s} = 13$ TeV [14] is compared to the results of two model calculations: (a) the first is based on NRQCD calculation [16] and provides predictions at high p_{T}. (b) the second is based on NRQCD coupled to a Color Glass Condensate (CGC) approach [17] and makes predictions for J/ψ at low p_{T}. The non-prompt contribution from B-mesons, is calculated using Fixed-Order Next-to-Leading Logarithm (FONLL) [18] and added to the prompt J/ψ cross section since the ALICE results are relative to the inclusive production. With this combination of models, it is possible to achieve a good description of the cross section over the whole range of transverse momentum covered by the measurements. Similar results are available for ψ(2S), as shown in the right panel of Fig. 1.4. For the the Υ(nS) (n = 1, 2 or 3) states, a measurement of the transverse momentum dependence of the differential production cross sections in pp collisions at $\sqrt{s} = 13$ TeV is provided by the CMS collaboration [15], even if in a range limited to $p_{\mathrm{T}} > 20$ GeV/c. In this case, the experimental measurements are in agreement with the NRQCD predictions [19], as shown in Fig. 1.5. Moreover, the ICEM model does a rather reasonable predictions for the quarkonium production cross sections [20].

Other measurements, are at odds with the NRQCD calculations, as shown in Fig. 1.6. This figure shows

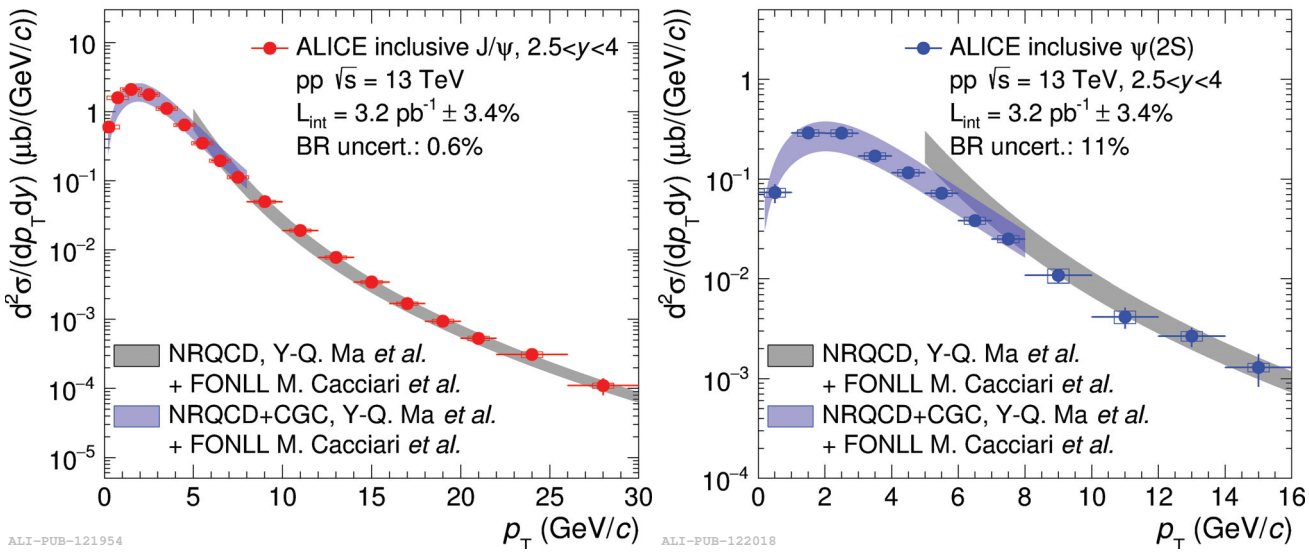

Figure 1.4: Differential cross sections of inclusive J/ψ (left) and inclusive ψ(2S) (right) in pp collisions at $\sqrt{s} = 13$ TeV with ALICE, compared to predictions from NRQCD [16] coupled to a FONLL [18] (grey), and NRQCD coupled to a CGC [17] and FONLL (blue). Figures taken from Ref. [14].

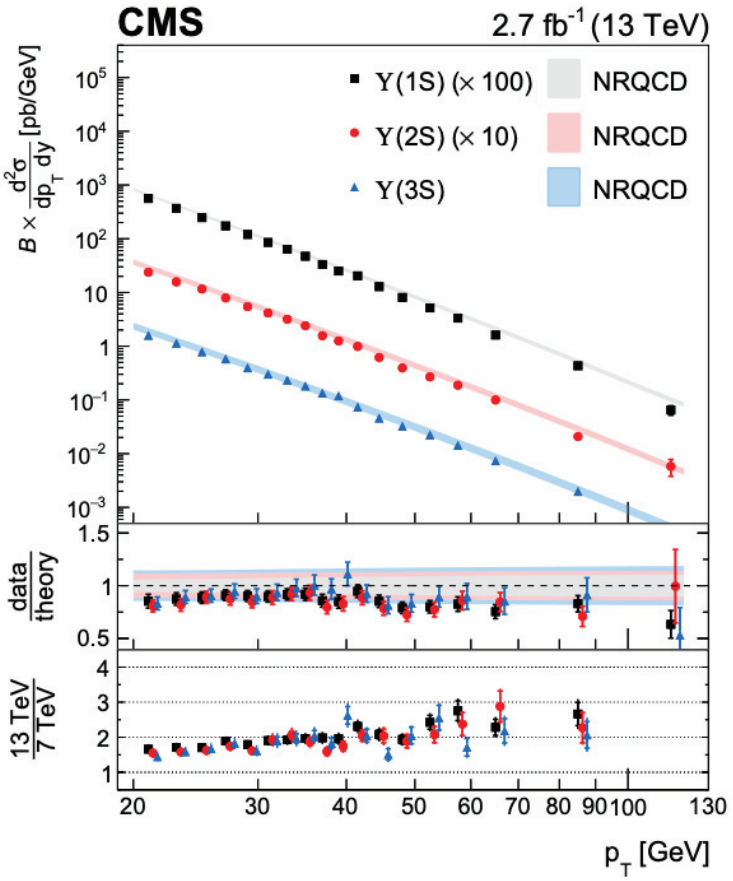

Figure 1.5: Differential production cross sections times the dimuon branching fractions of the Υ(nS) ($n = 1, 2, 3$) mesons as function of transverse momentum in pp collisions at $\sqrt{s} = 13$ TeV with CMS in $|y| < 1.2$, compared to NRQCD predictions [19]. Figure taken from [15].

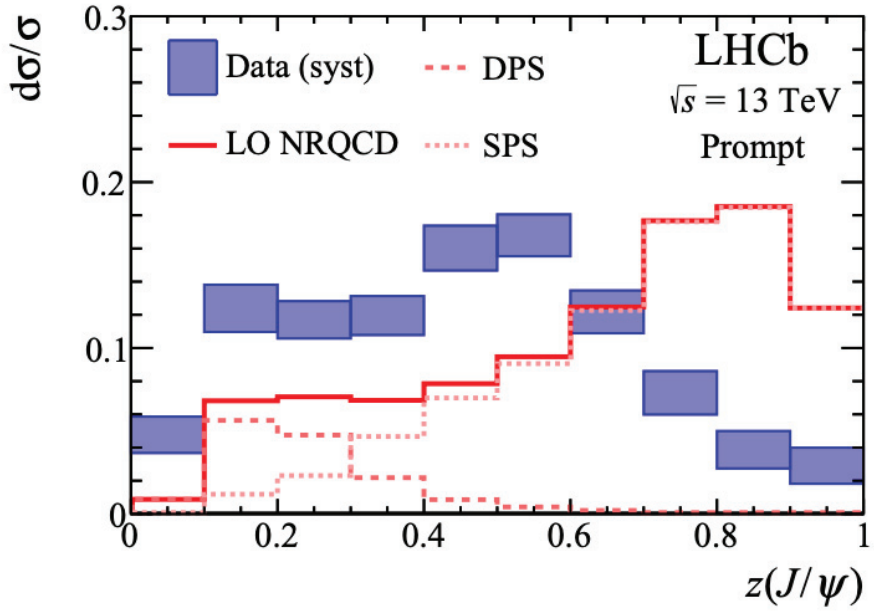

Figure 1.6: Comparison between theoretical predictions and experimental results of quarkonium production in pp collisions: J/ψ production in jets at $\sqrt{s} = 13$ TeV with LHCb [21]. Figure taken from Ref. [21].

a measurement of the J/ψ production in jets measured by LHCb collaboration [21], which shows discrepancies between Leading-Order NRQCD predictions and experimental results. The momentum fraction (z(J/ψ)) of the jet carried by prompt J/ψ does not match the NRQCD-based predictions as implemented in PYTHIA 8.

Beyond the production cross-section, the J/ψ polarization is another significant observable of interest for challenging theoretical predictions: small longitudinal polarization of J/ψ has been observed under different experimental conditions (see Ref. [26] and references therein), in contrast with the predictions of some of the available theoretical models. The CSM, for instance, predicts significant transverse polarization at leading order, but substantial longitudinal polarization at higher orders [22]. Since gluon fragmentation is the dominant production process at high p_{T} and the J/ψ is assumed to carry over the gluon polarization, the NRQCD predicts a large transverse polarization at high p_{T}. There is no polarization, in contrast, in the predictions of the CEM because any possible initial polarization is washed out by soft gluon exchanges [27]. In Fig. 1.7, a measurement of J/ψ polarization as a function of p_{T} in pp collisions at $\sqrt{s} = 7$ TeV [26] is compared to CSM and several NRQCD predictions by different groups, using different experimental data to constrain the LDMEs [22–25]. It is important to acknowledge that the LHCb results take into account the influence of feed-down, whereas the theoretical calculations by CSM and NRQCD [22] do not incorporate feed-down from excited states. Therefore, the CSM does not agree with the data, while the various NRQCD predictions vary widely, with one of them coming near to the data [24, 25]. Notably, the contribution of radiatively-decaying P-wave χ_c states to the J/ψ yield introduces additional uncertainties to the theoretical predictions for the J/ψ polarization. The CSM can only be brought into agreement with data under extreme assumptions for the polarization of the J/ψ from χ_c feed-down [28].

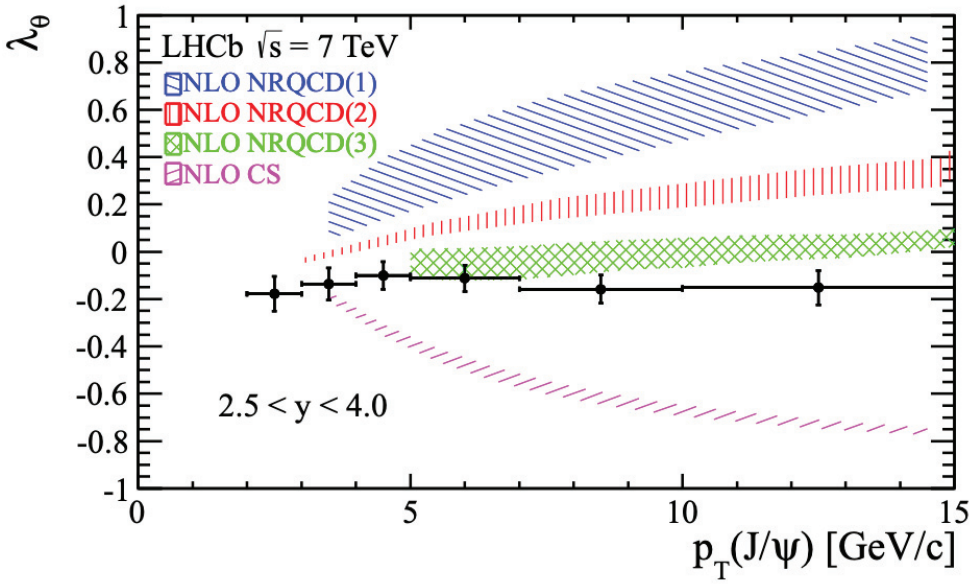

Figure 1.7: Comparison of prompt J/ψ polarization as a function of transverse momentum at $\sqrt{s} = 7$ TeV in pp collisions, compared to NRQCD [22–25] and CSM [22] predictions. Figure taken from [26].

In short, a full theoretical understanding of charmonium and bottomonium production in pp collisions is still missing, and none of the models that have been used can adequately and simultaneously account for all the features observed in experiments, the two main ones being the quarkonium production cross section and its polarization. New experimental results in the bottomonium sector will certainly provide valuable inputs to these studies.

Quarkonium production in heavy-ion collisions

The importance of quarkonia in the study and the characterization of the deconfined medium produced in heavy-ion collisions stems from two facts. On one hand, the mass of heavy quarks is too large for a significant thermal production to take place in the medium: the charm and bottom quarks are almost exclusively produced in the initial hard partonic interactions, and preserve their identity throughout the medium's evolution. On the other hand, the binding into quarkonium occurs at much lower energy scales and is therefore medium-sensitive: in particular, quarkonium production is expected to be significantly suppressed in the medium due to color screening, as proposed in 1986 by T. Matsui and H. Satz [29] and dynamical dissociation [30]. According to the dissociation scenario, quarkonium suppression should take place at different temperatures, depending on the binding energies of each state. In particular, strongly bound states, such as the J/ψ and Υ(1S), should melt at higher temperatures than less strongly bound ones, such as the ψ(2S), Υ(2S), and Υ(3S), respectively. Therefore, an estimate of the initial temperature reached in collisions [31] could be obtained by studying the in-medium dissociation probability of such states. Unfortunately, however, several factors such as feed-down contributions from higher-mass resonances into the observed quarkonium yield, and other competing mechanisms, such as cold nuclear matter effects [32] and

quarkonium production via recombination [33, 34], make it difficult to predict the exact suppression pattern.

The recombination mechanism, in particular, becomes a major competitor of dissociation for large enough charm densities. According to this mechanism, the J/ψ could be statistically formed from uncorrelated $c\bar{c}$ pairs from different initial hard collisions if the charm density in the system is high enough, as proposed in Ref. [35], a condition which is expected to take place when the center of mass energy of collisions increases. Due to the recombination of these quarks throughout the collision history [36] or during hadronization [35, 37], the abundance of c and $\bar{c}$ quarks in high colliding energy may thus provide an additional charmonium production mechanism, differing from the J/ψ produced from $c\bar{c}$ pairs from the same hard collision. The competition between the dissociation and recombination mechanisms is illustrated in Fig. 1.8, where the suppression of J/ψ production in heavy-ion collisions is shown to be weaker at higher energies compared to measurements at lower energies: at low collision energy the sequential suppression mechanism is dominant, whereas at higher energy the suppression is reduced due to the role of recombination, and possibly even overcompensated at sufficiently high energies. The interpretation of the experimental results at high energies as an evidence of regeneration of charmonium either during the deconfined stage of the evolution of the medium [36] or solely at the phase boundary [38], is one of the most convincing indications of the production of a deconfined medium in heavy-ion collisions.

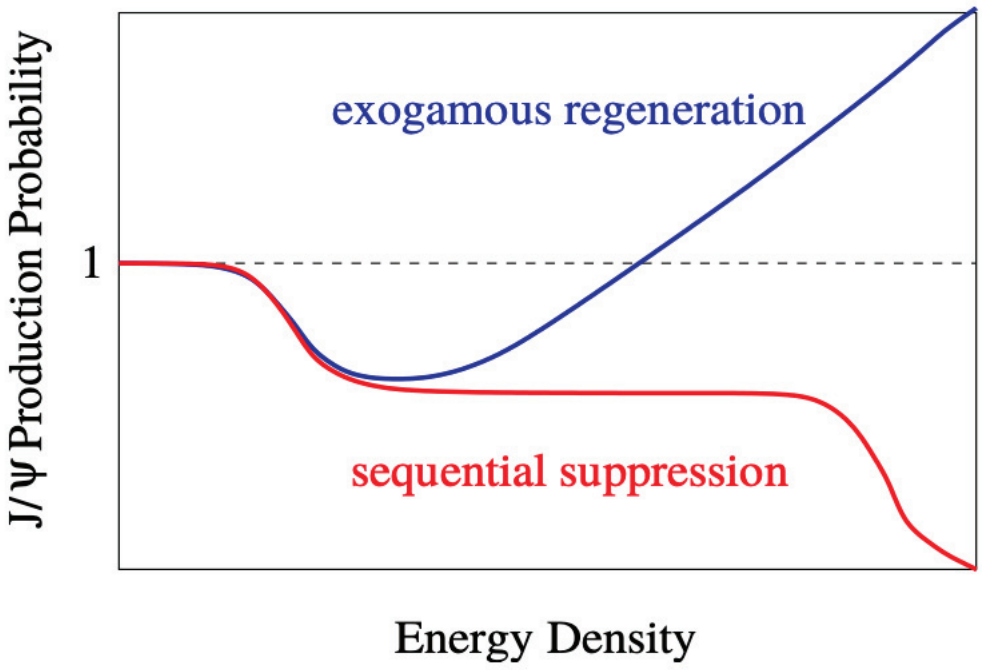

Figure 1.8: J/ψ suppression and (re)generation in a deconfined medium. Figure taken from [39].

The in-medium modification of quarkonium production is typically quantified by the nuclear modification factor R_{AA}, which is defined as the ratio of the quarkonium yield in A–A collisions and the expected value obtained scaling the pp yield by the average number of binary nucleon-nucleon collisions ($\langle N_{\mathrm{coll}} \rangle$), obtained using a Glauber model

calculation (see Ref. [40], and references therein):

$$R_{\mathrm{AA}} = \frac{\mathrm{d}^2 N_{\mathrm{AA}}/\mathrm{d}p_{\mathrm{T}}\mathrm{d}y}{\langle N_{\mathrm{coll}}\rangle \mathrm{d}^2 N_{\mathrm{pp}}/\mathrm{d}p_{\mathrm{T}}\mathrm{d}y} \tag{1.1}$$

where $N_{\mathrm{AA(pp)}}$ denotes quarkonium yield in A–A (pp) collisions, p_{T} is the transverse momentum and y is the rapidity. The difference of R_{AA} with respect to unity quantifies the global effect of the deconfined medium on quarkonium production in heavy-ion collisions (specifically, if $R_{\mathrm{AA}} < 1$, the quarkonium yield is suppressed; if $R_{\mathrm{AA}} > 1$, it is enhanced).

Over the past decades, studies on the J/ψ production in heavy-ion collisions have been performed at the CERN SPS [41, 42] and RHIC [43–46], systematically revealing a reduction in the J/ψ production yield (R_{AA} <1). The amount of suppression observed by experiments performed as the CERN SPS and RHIC is similar [47], even though the colliding energies among these experiments are very different ($\sqrt{s_{\mathrm{NN}}} \approx 20$ and 200 GeV, respectively). At the LHC J/ψ production is measured in Pb–Pb collisions at $\sqrt{s_{\mathrm{NN}}}$ = 2.76 and 5.02 TeV: at these energies, the suppression is enhanced by the higher temperature and the longer lifetime of the medium, but at the same time the regeneration mechanism starts to play a significant role due to the large number of $c\bar{c}$ pairs produced. The measurements performed by the ALICE collaboration, resulting in a smaller suppression with respect to lower energy measurement [48] at low p_{T} in the most central collisions (centrality: 0-20%), can indeed be interpreted as a strong indication of the role of recombination. At high p_{T}, where recombination is expected to be less effective, ATLAS and CMS results indicate a strong J/ψ suppression for the most central collisions [49, 50]. The available results for the J/ψ R_{AA} are generally well described by the model calculations implementing transport and statistical hadronization mechanisms (see Ref. [51] and references therein).

The study of ψ(2S) production is also of particular interest. The strength of medium effects on its production might be significantly different from that of the J//ψ because of the larger size and weaker binding of the ψ(2S) state. The smaller binding energy should make it easier for the ψ(2S) to dissociate in the medium, leading to sequential melting. Furthermore, the recombination processes might in principle exhibit different features, with the larger-size charmonium states being produced later in the evolution of the system [53]. The ψ(2S) production was measured at the LHC in Pb–Pb collisions at $\sqrt{s_{\mathrm{NN}}}$ = 5.02 TeV by CMS [50, 56], ATLAS [49], and ALICE [52]. A stronger suppression is observed for ψ(2S) with respect to J/ψ. As shown in Fig. 1.9, the ALICE measurement is compared to the calculations of transport (TAMU) [53] and statistical hadronization models (SHMc) [54, 55]. The TAMU model exhibits a good agreement with the measured R_{AA} for both J/ψ and ψ(2S); the SHMc model reproduces the J/ψ data, but underestimates ψ(2S) production in central and semicentral collisions. Fig. 1.10 shows the ratio and the double ratio (with respect to pp) of the ψ(2S) and J/ψ cross sections as a function of centrality. No significant centrality dependence is observed for the cross section ratio, in contrast to the results from the NA50 experiment at the CERN SPS [57], which measured a decrease of the ratio with increasing centrality, although at ~ 100 times smaller energy.

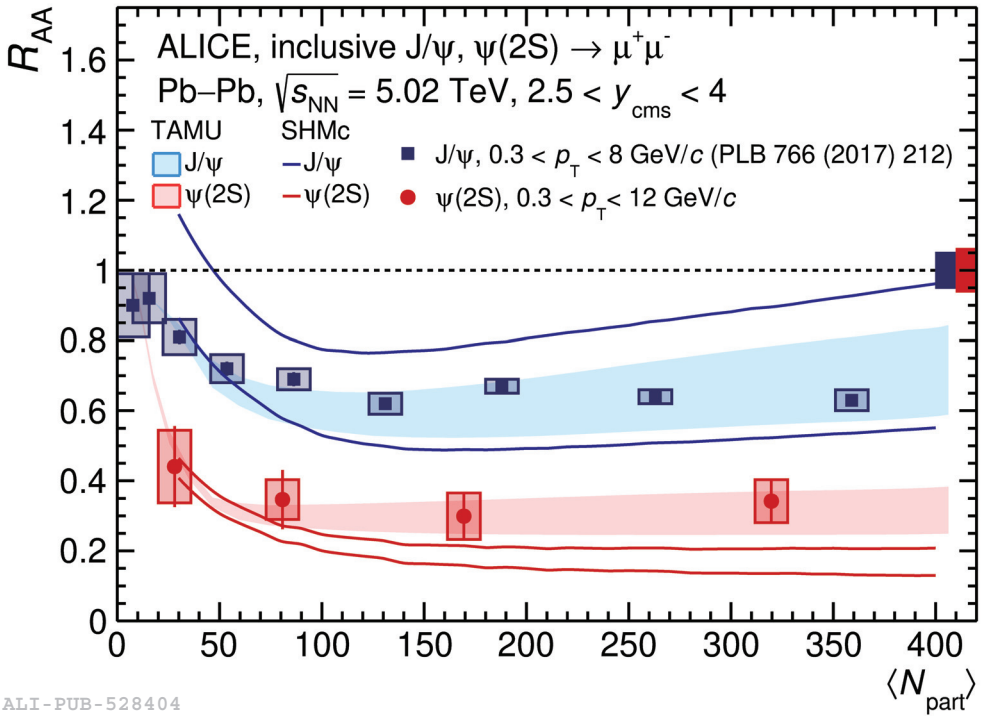

Figure 1.9: The measurement of $R_{\rm AA}$ of J/ψ [51] and ψ(2S) [52] as a function of $\langle N_{\rm part}\rangle$ in Pb–Pb collisions at $\sqrt{s_{\rm NN}}$ = 5.02 TeV with ALICE, compared to TAMU [53] and SHMc [54, 55] models. Figure taken from Ref. [52].

The cross section ratios can be reproduced by the TAMU model, while the SHMc model underestimates the data in central events. The double ratio, evaluated with respect to the pp reference, shows a ψ(2S) suppression by a factor of about 50% relative to pp, similar as the NA50 experiment [57].

At LHC energies, quarkonium study can be extended beyond charmonium measurements, which was also the case at lower energies, to include the bottomonium family. Bottomonium resonances should be able to provide additional insight on the mechanisms driving the behavior of quarkonium in hot matter. Since b and $\bar{b}$ quarks are much less abundant in the medium than c and $\bar{c}$ quarks, Υ production is expected to be less affected by the recombination mechanism. In addition, the stronger binding energy and larger size of bottomonium states contribute to their reduced susceptibility to the influence of cold nuclear matter. The stronger binding between the bottom quark and its antiquark provides more stability, making it less likely for the bottomonium states to be disrupted or dissociated by interactions with the nuclear medium. Moreover, the larger size of bottomonium states leads to a weaker overlap with the surrounding nuclear matter, resulting in a reduced probability of interactions and modifications. Consequently, bottomonium states are indeed generally expected to experience less impact from cold nuclear matter compared to charmonium states in the same nuclear environment.

The CMS collaboration pioneered the measurements in the bottomonium with the observation of a strong suppression of the Υ(1S) state in Pb–Pb collisions at $\sqrt{s_{\rm NN}}$ = 2.76 and 5.02 TeV [58–61]. The same measurement allowed to show that the production of the excited Υ(2S) state is much more strongly suppressed with respect to the

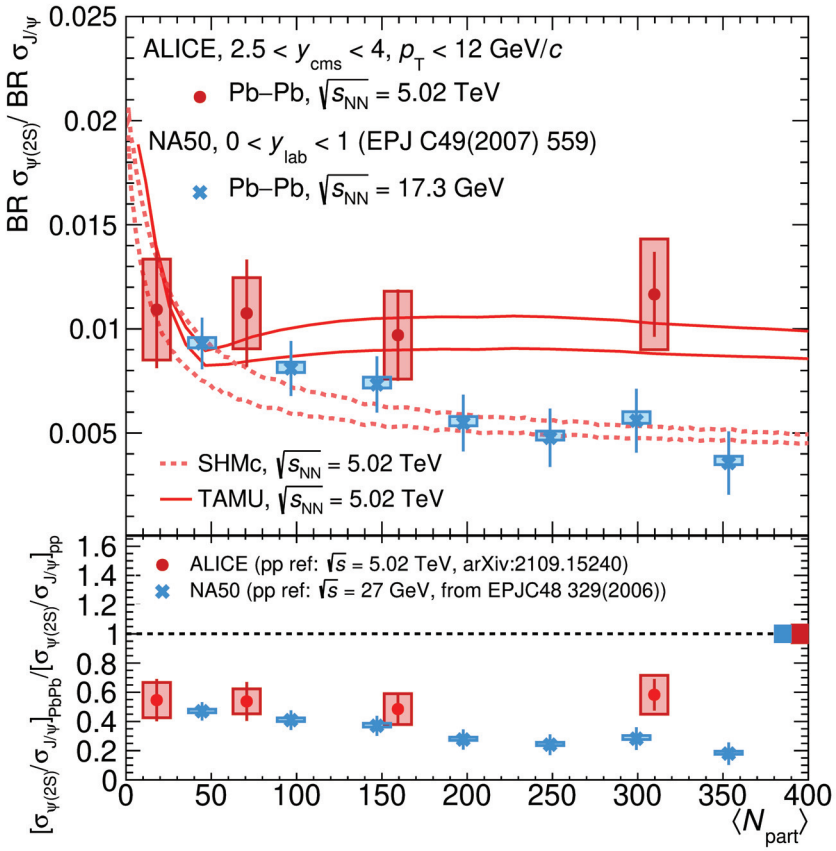

ALI-PUB-528400

Figure 1.10: Top panel: ratio of the ψ(2S) [52] and J/ψ [51] cross sections as a function of centrality; bottom panel: double ratio of the ψ(2S) and J/ψ, normalized to the corresponding pp value. The results are compared to TAMU [53] and SHMc [54, 55] models, and to the SPS NA50 experiment [57]. Figure taken from Ref. [52].

ground state, whereas the strongest suppression was observed for the Υ(3S) state, with a measured $R_{\rm AA}$ below 0.096 at 95% confidence level [61]. These results are complemented by measurements performed by the ALICE collaboration, which reported the suppression of Υ production at forward rapidity ($2.5 < y < 4.0$) in Pb–Pb collisions at the same energies as CMS [62–64]. The measurements are compared with calculations based on transport and rate equations, such as the predictions from the comover model [65], the hydrodynamic model [66] and transport approaches [67, 68] are compared with the data in Fig. 1.11. The various calculations reproduce the trend of the data within the corresponding uncertainties. For the Υ(1S), the experimental points lie on the lower limit of the prediction from the comover interaction model [65] and the one of the coupled Boltzmann equations [68]. The sharp slope expected in all cases for the $R_{\rm AA}$ of Υ(2S) towards small values of $\langle N_{\rm part} \rangle$ is hard to compare to the data because of the limited statistics.

Figure 1.12 illustrates the yield ratio of Υ(2S) to Υ(1S) in Pb–Pb collisions. The observed ratio is compared to the predictions from Statistical Hadronization Model (SHM) [55]. The SHM assumes that the final-state yields of

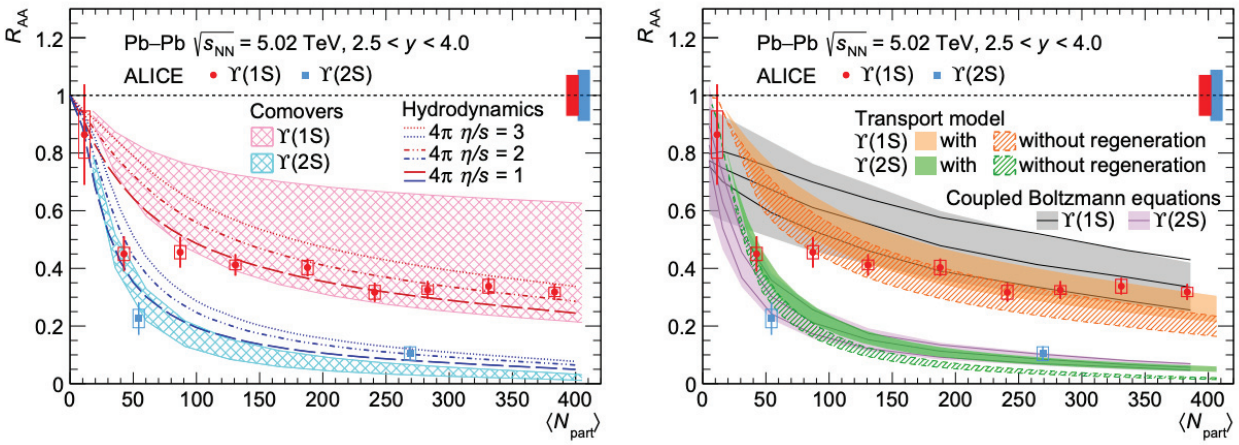

Figure 1.11: Nuclear modification factor R_{AA} of Υ(1S) and Υ(2S) as a function of centrality. The filled boxes at unity correspond to the relative uncertainties correlated with centrality. The results are compared with calculations from the comover [65] and the hydrodynamic [66] models in the left panel and with the transport descriptions [67, 68] in the right panel. Figures taken from Ref. [64].

hadrons can be calculated based on the resonance gas densities, using common values for the chemical freeze-out temperature and baryochemical potential. These values correspond to the phase boundary between the QGP and the hadronic phase. The SHM also extends its approach to the heavy-flavor production, assuming that heavy quarks reach kinetic equilibration before freeze-out and that total heavy quark conservation using the production from initial hard scatterings as an input. The model calculates the abundances of various heavy-flavor species by considering thermal weights, and for non-central collisions, it introduces a contribution from surface interactions resembling those in proton-proton (pp) collisions. However, the predictions based on the SHM underestimate the measured yield ratio of Υ(2S) to Υ(1S) in the most central collisions. To further assess the validity of the model, it is necessary to compare its predictions with other measurements in the bottom sector [64].

1.3 Quarkonium production as a function of charged-particle multiplicity in small systems

At the LHC energies, our understanding of hadronic collisions has been challenged by the observation that a large class of phenomena, traditionally associated to the presence of a deconfined medium, shows indeed a smooth evolution from small colliding systems such as pp and proton–lead (p–Pb) to large systems like lead–lead (Pb–Pb) [69, 70]. It is still actively debated whether these phenomena could be ascribed to the formation of a hot and dense medium in small systems, or to other collective effects or specific QCD processes at play in high charged-particle multiplicity events, possibly associated to a peculiar initial state of the collision. For this reason, it is important to characterize the initial phase of the hadronic collisions and especially the mechanisms respon-

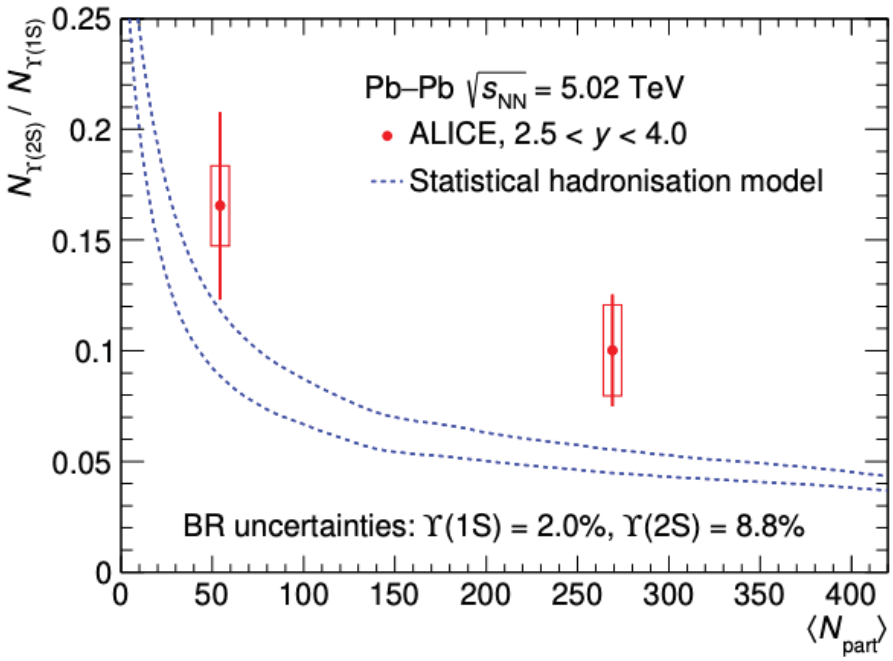

Figure 1.12: Ratio of Υ(2S) to Υ(1S) yields as a function of centrality. The results are displayed on top of the statistical hadronization model [55], The two curves represent the uncertainty of the pp-like contribution of the corona of the nuclear overlap. Figure taken from Ref. [64].

sible for high charged-particle multiplicity density events[1]. One of these mechanisms is the so-called multiparton interaction (MPI) mechanism, which allows for the simultaneous occurrence of several incoherent binary partonic interactions in a single pp collision [71]. MPIs play a significant role in describing the soft component of the hadronic interactions, as confirmed by the measured charged-particle multiplicity distributions in pp collisions at the center-of-mass energies $\sqrt{s} = 0.9$–8 TeV [72]. Based on this, event generators such as PYTHIA 8 [73, 74] and EPOS [75] currently highlight the importance of MPIs in building the charged-particle multiplicity distributions in hadronic interactions [76]. MPIs also affect the hard component in hadronic interactions. In this context, inclusive production processes are customarily described in a factorization approach, where the perturbative treatment of the early-stage hard-parton scattering processes, described by perturbative QCD (pQCD), is followed by the subsequent, soft-scale, hadronization of the scattered partons resulting in their binding into color-neutral states. Particularly for quarkonium production, where several descriptions are used for the hadronization process of the quarkonium states (e.g. the color singlet and color octet ones) [77, 78], it is interesting to study how MPIs could possibly affect the initial heavy-quark production especially at high charged-particle multiplicity densities [79].

Understanding the correlation between soft and hard components of high-multiplicity events in small collision systems like pp is, thus, fundamental to disentangle initial and final state effects affecting particle production, and to achieve a better understanding of MPIs or other possible underlying mechanisms [79]. The ALICE collaboration

[1] Here and in the rest of this thesis, "charged-particle multiplicity density" is defined as the number of charged particles produced per unit of pseudorapidity η, where the pseudorapidity is defined as $\eta = -\ln\tan(\theta/2)$, θ being the polar angle of a particle momentum with respect to the beam axis.

has already contributed to these studies by measuring quarkonium and open heavy-flavor self-normalized yields as a function of the self-normalized charged-particle multiplicity density[2], $\mathrm{d}N_{\mathrm{ch}}/\mathrm{d}\eta/\langle \mathrm{d}N_{\mathrm{ch}}/\mathrm{d}\eta \rangle$, in two different rapidity regions, with and without a rapidity gap between the hard probe and the charged particles, for center-of-mass energies of 5.02, 7, 8.16, and 13 TeV [80–84]. Measurements that consider the presence or absence of a rapidity gap between the hard probes and the associated charged particles can provide valuable insights into disentangling initial state effects from final state effects. By studying the charged particles in the vicinity of the hard probes, one can investigate the influence of the surrounding medium and its interactions with the hard-scattered particles. The presence of a rapidity gap can suggest a reduced interaction between the medium and the hard probes, providing information about the initial state conditions. On the other hand, the absence of a rapidity gap implies a significant interaction with the medium and indicates the influence of final state effects. Furthermore, analyzing the charged-particle multiplicity in relation to the presence or absence of a rapidity gap allows for a better understanding of potential biases that may arise from the hard-scattering products. This helps to discern the genuine effects originating from the interaction with the medium and disentangle them from other contributions.

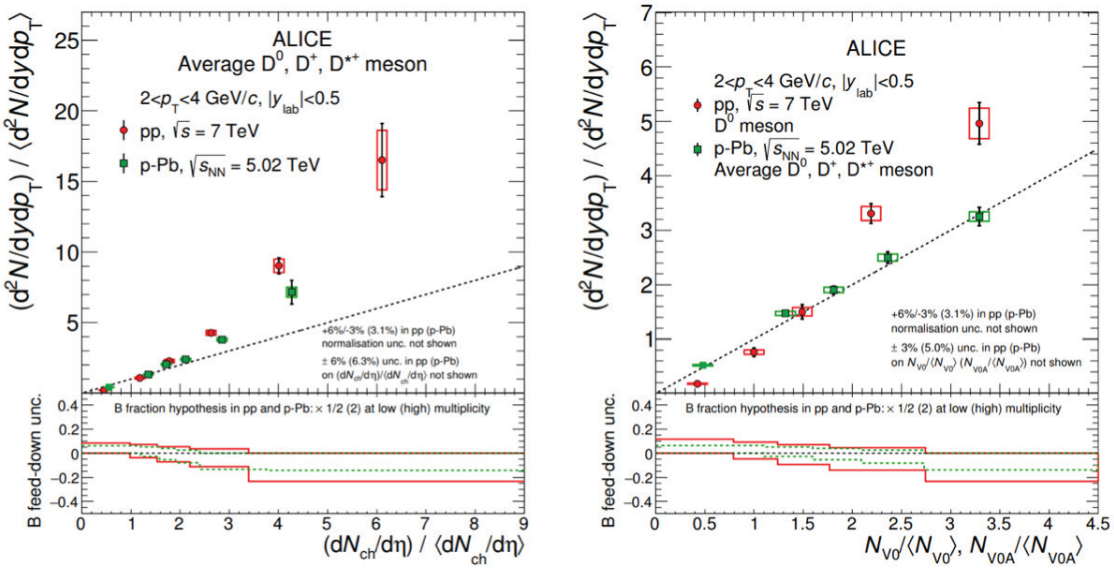

(a) Multiplicity at central rapidity

(b) Multiplicity at backward rapidity

Figure 1.13: Average self-normalized D-meson yields in $|y_{\mathrm{lab}}| < 0.5$ as a function of self-normalized charged-particle multiplicity at central rapidity $|\eta| < 1$ (left) and at backward rapidity $2.8 < \eta < 5.1$ (including $-3.7 < \eta < -1.7$ in pp data sample) for $2 < p_{\mathrm{T}} < 4$ GeV/c. The self-normalized yields are presented in the top panels with their statistical (vertical bars) and systematic (boxes) uncertainties, apart from the uncertainty on the B feed-down fraction, which is drawn separately in the bottom panels. The dashed lines are drawn to the diagonal. Figures taken from Ref. [85].

In the charm sector, in particular, two different regions, corresponding to central and forward rapidity regions, are observed in the existing ALICE measurements. When the hard process is measured in the central rapidity region, a faster than linear increase with respect to the charged-particle multiplicity density is observed for D mesons [81] (see

[2] The self-normalization is defined as the ratio of a given quantity over its average value.

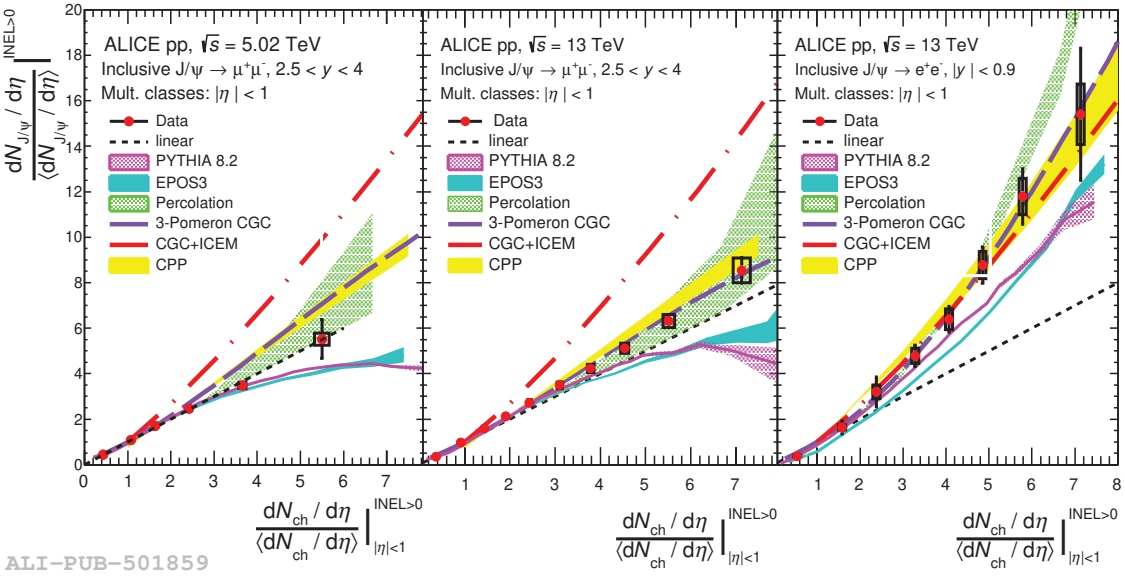

Figure 1.14: Comparison of the self-normalized J/ψ yield as a function of the self-normalized charged-particle density with model predictions: CPP [86], CGC with improved color evaporation model (ICEM) [87], 3-Pomeron CGC [88], Percolation [89], EPOS3 event generator [90], and PYTHIA 8.2 [91] at forward rapidity in pp collisions at $\sqrt{s}$ = 5.02 (left) and 13 TeV (middle). The right hand side figure shows the results from midrapidity compared to the corresponding theoretical model estimations for pp collisions at $\sqrt{s}$ = 13 TeV [84]. Figure taken from Ref. [80].

Fig. 1.13), and J/ψ [82, 84] (see Fig. 1.14), independently of the rapidity range of the multiplicity measurement. More specifically, the probability to produce a J/ψ is observed to increase by a factor ~ 15 in events reaching ~ 7 times the mean charged-particle multiplicity. A qualitatively similar, faster than linear increase is also reported by the STAR collaboration in events reaching up to ~ 4 times the mean charged-particle multiplicity, in pp collisions at a lower energy ($\sqrt{s} = 200$ GeV), in the same rapidity region [92]. This departure from linearity is qualitatively (but in most cases not quantitatively) described by models through the implementation of mechanisms able to reduce soft particle production at the highest charged-particle multiplicity densities, without affecting the hard process production. This is achieved, in terms of final-state effects, through the string percolation mechanism in the percolation model [89], and through a realistic treatment of the hydrodynamical evolution in small systems within the EPOS event generator [75]. Alternative interpretations of the observed non-linearity have also been proposed in terms of initial state effects rather than final state effects. In this case, the main proposed mechanisms are the gluon saturation and the gluon field fluctuations. The gluon saturation is implemented within the Color-Glass Condensate (CGC) framework [87, 88] or as a component of the MPI formalism in the EPOS 3 event generator [90]. The gluon field fluctuations are due either to higher Fock states increasing the number of gluons [93] or to a possible impact parameter dependence of the parton distribution functions [94, 95]. On the contrary, an almost linear correlation between the hard process yield and the charged-particle multiplicity density has been reported by ALICE in J/ψ measurements at forward rapidity in pp collisions at $\sqrt{s} = 5.02$, 7 and 13 TeV, with the multiplicity measurement at central rapidity [80, 82]. PYTHIA 8 and EPOS event generators fail to describe the behavior of J/ψ and D-meson production in high-multiplicity events,

both at central and forward rapidity, while a better description is provided by the percolation model and by models including gluon field fluctuations or saturation in the initial state. Moreover, most of the available models do not provide a simultaneous description of the different behaviors observed in the two rapidity regions [80, 84], with the exception of the aforementioned percolation model, and the approach involving gluon field fluctuations with higher Fock states.

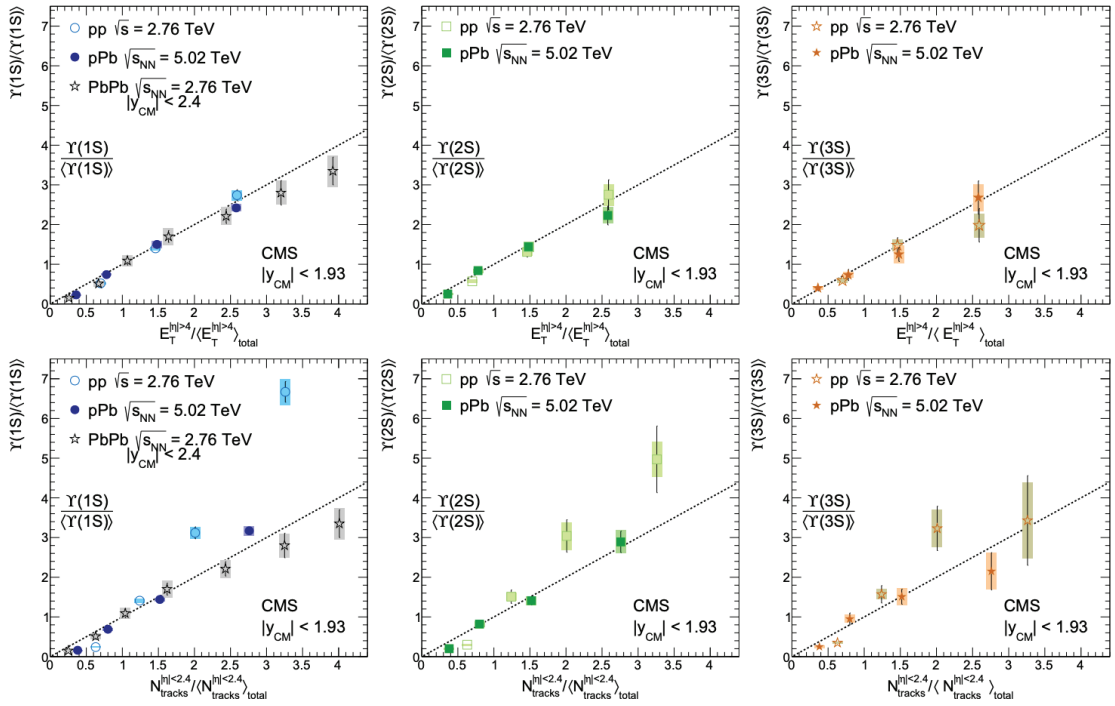

Figure 1.15: The Υ(nS) cross section versus transverse energy measured at $4 < |\eta| < 5.2$ (top row) and versus charged-track multiplicity measured in $|\eta| < 2.4$ (bottom row), measured in $|y_{\mathrm{CM}}| < 1.93$ in pp collisions at $\sqrt{s}$ = 2.76 TeV and p–Pb collisions at $\sqrt{s_{\mathrm{NN}}}$ = 5.02 TeV. For Υ(1S), the Pb–Pb data at $\sqrt{s_{\mathrm{NN}}}$ = 2.76 TeV (open stars) are overlaid. Cross sections and x-axis variables are normalized by their corresponding activity-integrated values. Figure taken from [96].

Hard probe measurements as a function of charged-particle multiplicity in pp collisions are also available in the beauty sector, in particular for the bottomonium states Υ(1S), Υ(2S), and Υ(3S). Studying the production of these states in a high charged-particle multiplicity environment, in the more general context of hadronic collisions, is of particular interest since excited states are characterized by lower binding energies than the ground state [31, 78, 97]. Hence, they are more sensitive to any possible dissociation mechanism at play in the final state, should these mechanisms be associated to the formation of a hot and dense medium (QGP) [98] or to final-state interactions such as those implemented in comover models [99, 100]. As already discussed for charmonium measurements, bottomonium studies can also help to understand the peculiar regime of high charged-particle multiplicity density in small collision systems like pp. The CMS collaboration investigated the event-activity dependence of Υ(nS) self-normalized production at central rapidity in pp, p–Pb and Pb–Pb collisions [96, 101]. In Fig. 1.15, it shows that the self-normalized cross section ratios, Υ(nS)/$\langle\Upsilon(\mathrm{nS})\rangle$, increase with event activity, independent of the colliding

system. However, a significant reduction of excited-to-ground-state ratios with increasing event activity, and no dependence on the azimuthal angle separation between the charged particles and the Υ momentum direction, are reported (see Fig. 1.16). The reduction is found to be stronger in p–Pb collisions. The ALICE collaboration observed a suppression of the Υ(1S) yields, measured at forward rapidity, in p–Pb collisions at $\sqrt{s} = 8.16$ TeV with respect to the ones measured in pp collisions at the same center-of-mass energy [102]. Models based on coherent parton energy loss or interactions with comoving particles, including nuclear shadowing, fairly describe the data at forward (p-going) rapidity, while they tend to overestimate the nuclear modification factor at backward (Pb-going) rapidity. The Υ(2S) nuclear modification factor has also been measured, showing a strong suppression, similar to the one measured for the Υ(1S), both at backward and forward rapidities. Measurements of bottomonium production at both central and forward rapidities in various collision systems is essential to better characterize the initial and final state effects affecting particle production and their potential dependence on the charged-particle multiplicity density.

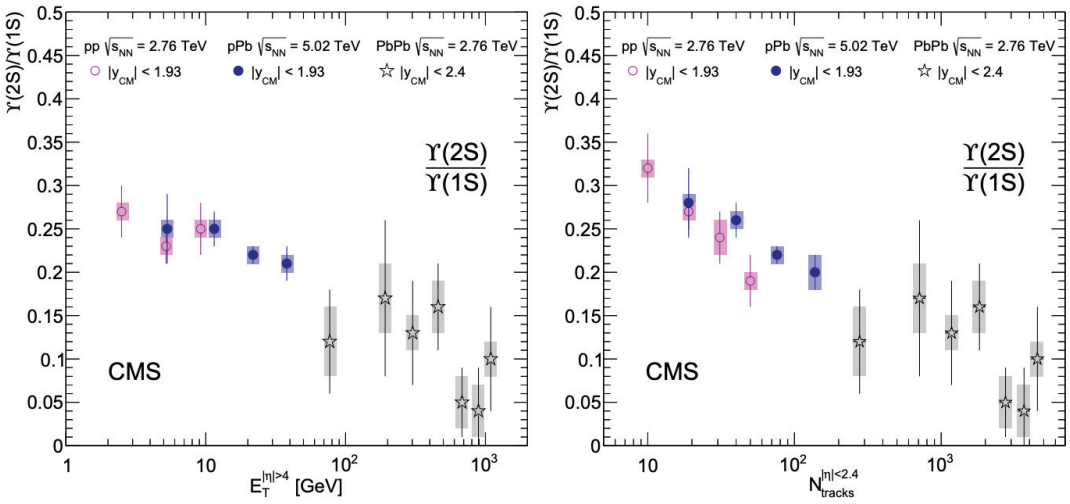

Figure 1.16: Single cross section ratios Υ(2S)/Υ(1S) for $|y_{\mathrm{CM}}| < 1.93$ versus transverse energy measured at $4 < |\eta| < 5.2$ (left) and (right) charged-particle multiplicity measured in $|\eta| < 2.4$, for pp collisions at $\sqrt{s}$ = 2.76 TeV (open circles) and p–Pb collisions at $\sqrt{s_{\mathrm{NN}}}$ = 5.02 TeV (closed circles). Both figures also include the Υ(2S)/Υ(1S) ratios for $|y_{\mathrm{CM}}| < 2.4$ measured in Pb–Pb collisions at $\sqrt{s_{\mathrm{NN}}}$ = 2.76 TeV (open stars). Figures taken from [96].

The first analysis described in this thesis (Chapters 4 and 5) concerns on the measurements performed with the ALICE detector of the Υ(1S), Υ(2S), and Υ(3S) yields, and excited-to-ground-state ratios, as a function of charged-particle multiplicity density in pp collisions at $\sqrt{s} = 13$ TeV. Υ(nS) states are reconstructed in the dimuon decay channel at forward rapidity, whereas the charged-particle multiplicity density is estimated at central rapidity. This configuration enables a rapidity gap between the measurements of Υ yield and charged-particle multiplicity density.

1.4 Quarkonium polarization

One of the most powerful tools for the characterization of quarkonium production mechanisms in hadronic collisions is the study of the polarization of the produced bound states. Additionally, since polarization is influenced by the surrounding environment during particle formation, it provides a valuable means to investigate the impact of a deconfined medium on the formation of a bound state composed of a heavy quark and antiquark. In the following sections, a general introduction is given to the most important concepts about polarization, focusing on the main theoretical aspect and on the most relevant available experimental results.

1.4.1 Vector meson polarization

Polarization quantifies the degree to which the spin of a given particle is aligned along a specified axis. The spin is an intrinsic quantum number characterizing elementary particle and systems, and it can be specified in terms of the total spin number (s); the algebra of the spin is analogous to that of the orbital angular momentum, so one can visualize the spin as a vector in the usual 3D space. The total angular momentum operator $\vec{J}$ then can be defined as:

$$\vec{J} = \vec{L} + \vec{S} \tag{1.2}$$

where $\vec{L}$ and $\vec{S}$ are the orbital angular momentum and spin operators, respectively. Given that both $\vec{L}$ and $\vec{S}$ are arbitrary vectors in 3D space, the maximum and minimum values permitted for the module are $|\vec{L}+\vec{S}|$ and $||\vec{L}|-|\vec{S}||$, respectively. If the module of the vectors is identified by the corresponding eigenvalues, l, s, and j, the $\vec{J}$ eigenvalues can range in the following interval:

$$|l - s| < j < l + s \tag{1.3}$$

The component j_z along the z-direction serves as another means of describing the total angular momentum. The angular momentum state for a given particle can be then expressed as $|j, j_z\rangle$. Vector mesons are characterized by spin–1 states. This is the case of the vector quarkonium states like J/ψ and Υ(1S), having $s = 1$ and $l = 0$, which result in $j = 1$, so that the specified component j_z can take values $+1$, 0, and -1. So, a generic vector meson, $\mathcal{V}$, can be written as:

$$|\mathcal{V}\rangle = |j,\ j_z\rangle = |1,\ j_z\rangle = b_{+1}|1,\ +1\rangle + b_0|1,\ 0\rangle + b_{-1}|1,\ -1\rangle \tag{1.4}$$

where b_{+1}, b_0, and b_{-1} are the coefficients of this linear combination and they define the particle polarization. Specifically, the given particle is transversely polarized if $b_0 = 0$ and $|b_{+1} + b_{-1}| = 1$; and longitudinally polarized if

$b_0 = 1$ and the other two coefficients are null. In practice, it is not possible to directly determine the values of b_{+1}, b_0, and b_{-1} with an experimental measurement; it is however possible, from first principles, to establish a relationship between the coefficients b_{+1}, b_0, and b_{-1} and the angular distribution of the decay products of the observed state (see Ref. [103]). This allows to define an indirect approach to extract the particle polarization, starting from the study of the anisotropies of the angular distribution of the particle decay products. In the following, the specific case of the 2-body decay of a vector quarkonium state is discussed. The discussion is taken from [103].

The vector quarkonium states ($J^{\mathrm{PC}} = 1^{--}$), can decay electromagnetically into two leptons. To further fix how to experimentally determine the "spin alignment" of a vector quarkonium state by measuring the angular distribution of its dilepton decay, the J/ψ state is used as an example for convenience, but the considerations and results are applicable to any $J^{\mathrm{PC}} = 1^{--}$ state. Fig. 1.17 shows a J/ψ state moving in the z-direction that decays into dilepton $\ell^+\ell^-$. In the J/ψ rest frame, the back-to-back emission of $\ell^+\ell^-$ defines the reference axis z', which is conventionally aligned along the direction of the positive lepton ℓ^+. As shown in Fig. 1.17, the total angular momentum of each state can be expressed as follows:

- Before decay, the J/ψ total angular momentum along z-axis is expressed as $|\mathrm{J}/\psi : 1,\ m\rangle$ with $m = 0,\ \pm 1$;
- After the 2-body decay, the total angular momentum of $\ell^+\ell^-$ state can be written as an eigenstate of J_z, i.e. $|\ell^+\ell^- : 1,\ l = m\rangle$ relative to the z-axis with $l = m$. The condition $l = m$ follows from angular momentum conservation;
- After decay, the total momentum of $\ell^+\ell^-$ state can also be written as an eigenstate of $J_{z'}$, i.e. $|\ell^+\ell^- : 1,\ l' = \pm 1\rangle$ with respect to the z'-axis. The condition $l' = \pm 1$ is due to the "helicity conservation" for massless fermions in the decay process J/$\psi \to \gamma^* \to \ell^+\ell^-$ (left panel of Fig. 1.17). Consequently, the dilepton system has the same angular momentum projection along the z'-axis as the virtual photon. The decay leptons (μ) are definitely not massless, but this assumption is approximately reasonable because their masses are negligible compared to the lightest vector quarkonium state, J/ψ ($m_\mu \approx 105\ \mathrm{MeV}/c^2 \ll m_{\mathrm{J}/\psi} \approx 3.096\ \mathrm{GeV}/c^2$).

The $J_{z'}$ state can be expressed as a superposition of eigenstates of J_z by imposing a rotation operator. $R(\alpha,\ \beta,\ \gamma)$ represents a rotation from a generic set of axis $(x,\ y,\ z)$ to the set $(x',\ y',\ z')$, where $\alpha,\ \beta,\ \gamma$ are the Euler angles characterizing the orientation of the second frame with respect to the first one. Then an eigenstate $|J, M'\rangle$ of $J_{z'}$ can be written as a superposition of eigenstates $|J, M\rangle$ of J_z via the transformation [104]:

$$|J, M'\rangle = \sum_{M=-J}^{+J} \mathcal{D}^J_{MM'}(R)|J, M\rangle \tag{1.5}$$

The complex matrix elements $\mathcal{D}^J_{MM'}$ in Eq. 1.5 are defined as:

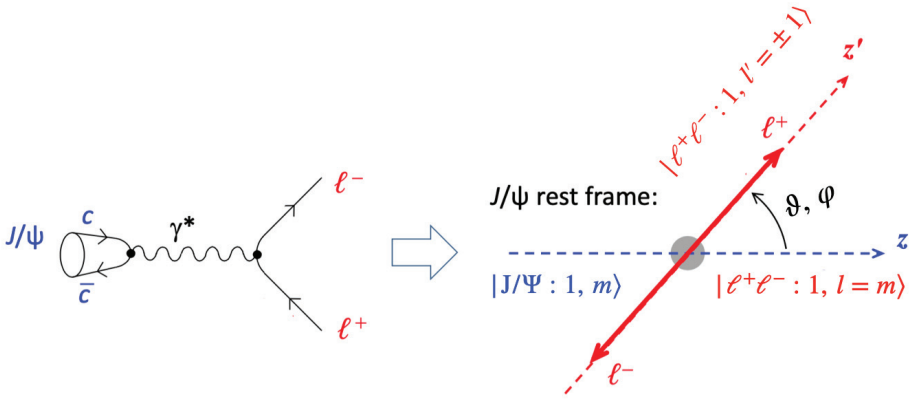

Figure 1.17: Sketch of the J/ψ decays into dilepton, J/$\psi \to \ell^+\ell^-$.

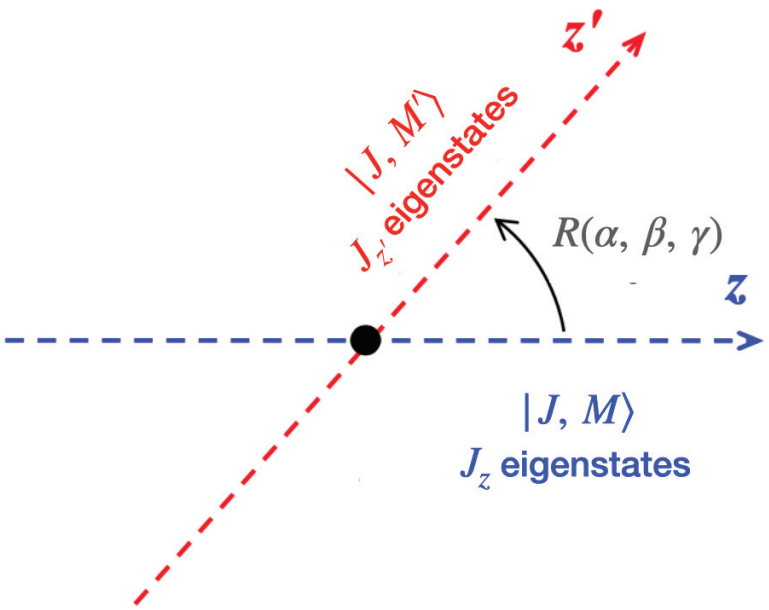

Figure 1.18: Schematic picture of rotation of angular momentum eigenstates.

$$\begin{aligned}\mathcal{D}^{J}_{MM'}(\alpha,\beta,\gamma) &= \langle J,M|e^{-i\alpha J_z}e^{-i\beta J_y}e^{-i\gamma J_z}|J,M'\rangle \\ &= e^{-iM\alpha}d^{J}_{MM'}(\beta)e^{-iM'\gamma}\end{aligned} \tag{1.6}$$

where $d^{J}_{MM'}(\beta)$ are the elements of the real reduced rotation matrices, which according to formalism described by Condon and Shortley [104] can be written as:

$$\begin{aligned}d^{J}_{MM'}(\beta) = &\sum_{t=max(0,M-M')}^{min(J=M,J-M')}(-1)^{t} \\ &\times \frac{\sqrt{(J+M)!(J-M)!(J+M')!(J-M')!}}{(J+M-t)!(J-M'-t)!t!(t-M+M')!} \\ &\times (\cos\frac{\beta}{2})^{2J+M-M'-2t}(\sin\frac{\beta}{2})^{2t-M+M'}\end{aligned} \tag{1.7}$$

The most general rotation from a reference characterized by a quantization axis (z) to a frame characterized by a quantization axis (z') can be expressed by considering the Euler angles $\beta = \theta$ and $\alpha = -\gamma = \varphi$. In this case, the angular momentum state of the dilepton can be re-written as:

$$|\ell^{+}\ell^{-}:1,\ l'\rangle = \sum_{l=0,\ l\pm1}\mathcal{D}^{1}_{ll'}(\varphi,\theta,-\varphi)|\ell^{+}\ell^{-}:1,\ l\rangle \tag{1.8}$$

One can then express the transition operator $\mathcal{B}$ allowing to compute the amplitude of the partial process J/$\psi(m) \rightarrow \ell^{+}\ell^{-}(l')$ as follows:

$$\begin{aligned}B_{ml'} &= \sum_{l=0,\ l\pm1}\mathcal{D}^{1*}_{ll'}(\varphi,\theta,-\varphi)\langle\ell^{+}\ell^{-}:1,l|\mathcal{B}|\mathrm{J}/\psi:1,m\rangle \\ &= \sum_{l=0,\ l\pm1}\mathcal{D}^{1*}_{ll'}(\varphi,\theta,-\varphi)B\delta_{ml} \\ &= B\mathcal{D}_{ml'}(\varphi,\theta,-\varphi)\end{aligned} \tag{1.9}$$

In Eq. 1.9, the form of $\langle\ell^{+}\ell^{-}:1,l|\mathcal{B}|\mathrm{J}/\psi:1,m\rangle = B\delta_{ml}$ results from the angular momentum conservation, with B independent of m (for rotational invariance). The total amplitude for J/$\psi(m) \rightarrow \ell^{+}\ell^{-}(l')$, where the J/$\psi$ is given by the superposition written in Eq. 1.4, is:

$$\begin{aligned}B_{l'} &= \sum_{m=0,\ \pm1}b_m B\mathcal{D}^{1*}_{ml'}(\varphi,\theta,-\varphi) \\ &= \sum_{m=0,\ \pm1}a_m\mathcal{D}^{1*}_{ml'}(\varphi,\theta,-\varphi).\end{aligned} \tag{1.10}$$

The transition probability is obtained by squaring Eq. 1.10 and summing over the (unobserved) spin alignments ($l' = \pm1$) in the dilepton system, with equal weights assigned to the two configurations for parity conservation:

$$W(\cos\theta,\varphi) \propto \sum_{l'\pm1} |B_{l'}|^2 \tag{1.11}$$

Using Eq. 1.6 and Eq. 1.7, the d elements are:

$$d^1_{0,\,\pm1} = \pm\frac{\sin\theta}{\sqrt{2}},\quad d^1_{\pm1,\,\pm1} = \frac{1+\cos\theta}{2},\quad d_{\pm1,\,\mp1} = \frac{1-\cos\theta}{2} \tag{1.12}$$

Hence, the angular distribution is written as:

$$\begin{aligned} W(\cos\theta,\varphi) \propto \frac{\mathcal{N}}{3+\lambda_\theta}\cdot(1 &+ \lambda_\theta\cos^2\theta \\ &+ \lambda_\varphi\sin^2\theta\cos2\varphi + \lambda_{\theta\varphi}\sin2\theta\cos\varphi \\ &+ \lambda^\perp_\varphi\sin^2\theta\sin2\varphi + \lambda^\perp_{\theta\varphi}\sin2\theta\sin\varphi) \end{aligned} \tag{1.13}$$

where $\mathcal{N} = |a_0|^2 + |a_1|^2 + |a_2|^2$ and

$$\begin{aligned} \lambda_\theta &= \frac{\mathcal{N} - 3|a_0|^2}{\mathcal{N}+|a_0|^2} \\ \lambda_\varphi &= \frac{2\mathrm{Re}[a^{(i)*}_{+1}a_{-1}]}{\mathcal{N}+|a_0|^2} \\ \lambda_{\theta\varphi} &= \frac{\sqrt{2}\mathrm{Re}[a^{(i)*}_0(a_{+1}-a_{-1})]}{\mathcal{N}+|a_0|^2} \\ \lambda^\perp_\varphi &= \frac{-2\mathrm{Im}[a^*_{+1}a_{-1}]}{\mathcal{N}+|a_0|^2} \\ \lambda^\perp_{\theta\varphi} &= \frac{-2\sqrt{2}\mathrm{Im}[a^*_0(a_{+1}+a_{-1})]}{\mathcal{N}+|a_0|^2} \end{aligned} \tag{1.14}$$

The most common angular distribution is given by Eq. 1.13, but it can be further simplified. The last two terms in Eq. 1.13 introduce an asymmetry of the distribution by reflection with respect to the production plane (x,z), an asymmetry which is not forbidden in individual (parity-conserving) events. In hadronic collisions, due to the intrinsic parton transverse momenta, for example, the "natural" polarization plane does not coincide event-by-event with the experimental production plane. However, the symmetry by reflection must be a property of the observed event distribution when only parity-conserving processes contribute. This means that the terms in $\sin^2\theta\sin2\varphi$ and $\sin2\theta\sin\varphi$ are unobservable, since they vanish on average (see Refs. [103, 105]). The observable angular distribution in Eq. 1.13 can be simplified as:

$$W(\cos\theta,\varphi) \propto \frac{1}{3+\lambda_\theta}\cdot(1+\lambda_\theta\cos^2\theta + \lambda_\varphi\sin^2\theta\cos2\varphi + \lambda_{\theta\varphi}\sin2\theta\cos\varphi) \tag{1.15}$$

As an alternative to a multi-parameter fit to the angular distribution in Eq. 1.15, the integration over either $\cos\theta$

or φ leads to several one-dimensional angular distributions:

$$W(\cos\theta) \propto \frac{1}{3+\lambda_\theta}(1+\lambda_\theta \cos^2\theta), \tag{1.16}$$

$$W(\varphi) \propto 1 + \frac{2\lambda_\varphi}{3+\lambda_\theta}\cos 2\varphi, \tag{1.17}$$

from which λ_θ and λ_φ can be determined in two separate steps, possibly improving the stability of the fit procedures in low-statistics analyses. The $\lambda_{\theta\varphi}$ term, vanishes in both integrations but can be obtained by defining a variable $\tilde{\varphi}$ as:

$$\tilde{\varphi} = \begin{cases} \varphi - \frac{3}{4}\pi, & \cos\theta < 0 \\ \varphi - \frac{1}{4}\pi, & \cos\theta > 0 \end{cases} \tag{1.18}$$

Hence, the $\lambda_{\theta\varphi}$ parameter can be extracted from:

$$W(\tilde{\varphi}) \propto 1 + \frac{\sqrt{2}\lambda_{\theta\varphi}}{3+\lambda_\theta}\cos\tilde{\varphi}. \tag{1.19}$$

According to Eq. 1.14, the polarization parameters directly show dependence on the coefficients of b_0 and $b_{\pm1}$ in Eq. 1.4 ($b_m B = a_m$, see Eq. 1.10). As a consequence, it is possible to extract the spin-alignment straightforwardly by fitting the observable angular distribution. As an example, considering two extreme scenarios of pure transverse and longitudinal polarization for the J/ψ, the polarization parameters (λ_θ, λ_φ and $\lambda_{\theta\varphi}$) can be obtained in the following, respectively.

- If the J/ψ has pure **transverse** polarization, then:

$$b_{0,\,-1} = 0, \;\; b_{+1} = 1 \;\; \text{or} \;\; b_{0,\,+1} = 0, \;\; b_{-1} = 1$$

  and the polarization parameters obtained by substituting a_m ($b_m B = a_m$, $m = -1,\ 0,\ 1$) in Eq. 1.14 are:

$$\lambda_\theta = +1, \;\; \lambda_\varphi = 0, \;\; \lambda_{\theta\varphi} = 0$$

- If the J/ψ has pure **longitudinal** polarization, then:

$$b_0 = 1, \;\; b_{\pm1} = 0$$

and the polarization parameters obtained by substituting a_m ($b_m B = a_m$, $m = -1,\ 0,\ 1$) in Eq. 1.14 are:

$$\lambda_\theta = -1, \quad \lambda_\varphi = 0, \quad \lambda_{\theta\varphi} = 0$$

With Eq. 1.14 and imposing the condition $|\lambda_\theta \leq 1|$, the relations among the polarization parameters are:

$$\begin{cases} |\lambda_\varphi| \leq \frac{1}{2}(1+\lambda_\theta) \\ |\lambda_{\theta\varphi}| \leq \frac{1}{2}(1-\lambda_\varphi) \\ (1+2\lambda_\varphi)^2 + 2\lambda_{\theta\varphi}^2 \leq 1, \quad \text{for } \lambda_\varphi < -\frac{1}{3} \end{cases} \tag{1.20}$$

1.4.2 Reference frames

The choice of a coordinate system is needed when dealing with the measurement of any angular distribution. However, the actual definition of the decay reference axis with respect to the beam direction is not unique, and different definitions of the reference axis are likely to yield different values for the polarization parameters (λ_θ, λ_φ, and $\lambda_{\theta\varphi}$). At the same time, the evaluation of polarization parameters using multiple reference systems can help in further constraining the various mechanisms involved in the production process.

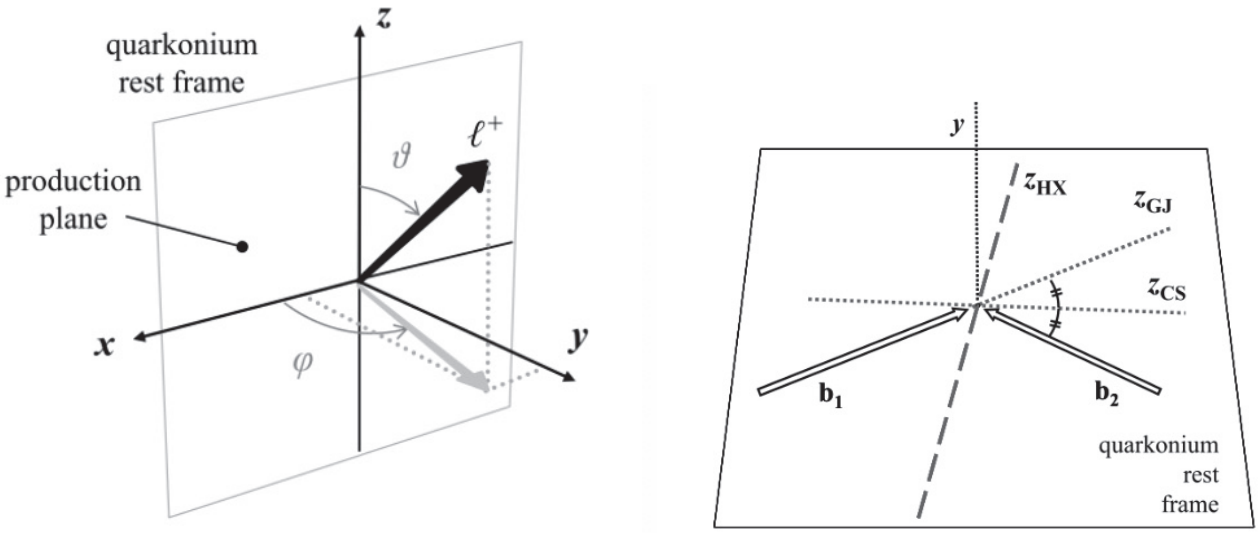

Figure 1.19: Left: coordinate system used for the measurement of a two-body decay angular distribution in the quarkonium reference frame. Right: illustration of three different definitions of the reference axis (HX = Helicity, CS = Collins-Soper, GJ = Gottfrid-Jackson) [103]. Figures taken from [103].

The reference frames considered in the study of polarization can be defined according to the orientation of the z-axis. Among the most common choices one finds:

- **Helicity (HE)**: the z-axis is defined as the flight direction of the quarkonium in the centre-of-mass of the

colliding system;

- **Collins-Soper, (CS)**: the z-axis is the bisector of the angle between one beam and the opposite of the other beam [106];

- **Gottfried–Jackson, (GJ)**: the direction of the momentum of one of the two colliding beams [107].

Helicity (HE) and Collins-Soper (CS) are the two most common reference frames utilized in quarkonium polarization. These two frames differ from one another by a rotation of 90° around the y-axis when the quarkonium is produced at high transverse momentum (p_{T}) and negligible longitudinal momentum ($|p_{\mathrm{L}}|$), i.e. $p_{\mathrm{T}} \gg |p_{\mathrm{L}}|$. In the limit of zero p_{T} of the quarkonium , the two frames tend to coincide with each other.

All the possible polarization axes are related to the production plane, so it is possible to parameterize the transformation from one reference frame to the other with an angle which describes a rotation around the y-axis. A purely geometrical transformation can be applied to the observable angular distribution instead of rotating the angular momentum state vectors. The rotation matrix is written as:

$$R_y(\delta) = \begin{pmatrix} \cos\delta & 0 & -\sin\delta \\ 0 & 1 & 0 \\ \sin\delta & 0 & \cos\delta \end{pmatrix}, \tag{1.21}$$

where δ indicates the angle between the two different reference frames. In spherical coordinate, the unit vector $\hat{r} = (\sin\theta\cos\varphi, \sin\theta\sin\varphi, \cos\theta)$ indicating the lepton direction in the old frame ($\hat{r}$) is then expressed as $\hat{r} = R_y(\delta)^{-1}\hat{r'}$ in the new frame ($\hat{r'}$). Then the angular distribution in the new frame is:

$$W'(\cos\theta', \varphi') \propto \frac{1}{3+\lambda'_\theta} \cdot (1 + \lambda'_\theta \cos^2\theta' + \lambda'_\varphi \sin^2\theta' \cos 2\varphi' + \lambda'_{\theta\varphi} \sin 2\theta' \cos\varphi'), \tag{1.22}$$

where

$$\begin{cases} \lambda'_\theta = \dfrac{\lambda_\theta - 3\Lambda}{1+\Lambda} \\ \lambda'_\varphi = \dfrac{\lambda_\varphi + \Lambda}{1+\Lambda} \\ \lambda'_{\theta\varphi} = \dfrac{\lambda_{\theta\varphi}\cos 2\delta - \frac{1}{2}(\lambda_\theta - \lambda_\varphi \sin 2\delta)}{1+\Lambda} \end{cases} \tag{1.23}$$

And the Λ is calculated as:

$$\Lambda = \frac{1}{2}(\lambda_\theta - \lambda_\varphi)\sin^2\delta - \frac{1}{2}\lambda_{\theta\varphi}\sin 2\delta \tag{1.24}$$

With the above relations, it is directly to verify the invariant quantity:

$$\mathcal{F}_{c_1,c_2,c_3} = \frac{(3+\lambda_\theta) + c_1(1-\lambda_\varphi)}{c_2(3+\lambda_\theta) + c_3(1-\lambda_\varphi)} \tag{1.25}$$

where c_1, c_2 and c_3 are real numbers. Taking into account a specific set of $(c_1, c_2, c_3) = (-3, 0, 1)$, an invariant-frame quantity $\tilde{\lambda}$ can then be found:

$$\tilde{\lambda} = \mathcal{F}_{-3,0,1} = \frac{\lambda_\theta + 3\lambda_\varphi}{1 - \lambda_\varphi} \tag{1.26}$$

The invariant-frame coefficient $\tilde{\lambda}$ is particularly useful when the polarization parameters are measured in two or more reference frames, since it can used to verify whether the results in the different reference frames are consistent or not.

1.4.3 Quarkonium polarization: experimental results and comparison to models

As quarkonium polarization is one of the most interesting aspects of quarkonium production, it has been thoroughly investigated not only in different theoretical models, but also in a variety of experiments. Calculations implementing NRQCD [10], which can reproduce the differential cross sections of J/ψ and Υ mesons produced at Tevatron [108–110] and LHC [111–113] energies, are not able, however, to properly describe the experimental results on the polarization. At the Tevatron, in particular, the model predicts for the J/ψ a stronger transverse polarization [114] than observed in the data [115]. In this context, the Υ polarization is a more conclusive test of NRQCD because it satisfies the nonrelativistic approximation much better than the J/ψ [116]. Some significant results from the Tevatron, RHIC, and LHC experiments are going to be reported and discussed in the following sections.

Results at the Tevatron

Quarkonium polarization was studied at Tevatron by both CDF and D0 collaborations with the data collected in $\mathrm{p\bar{p}}$ collisions. The prompt J/ψ and ψ(2S) polarizations at midrapidity ($|y| < 0.6$) as a function of transverse momentum at $\sqrt{s} = 1.96$ TeV have been measured by CDF collaboration [115] in the Helicity frame. In the left panel of Fig. 1.20, a small longitudinal polarization is observed for the prompt J/ψ measured in data. Besides that, one can see the discrepancy among data and theoretical calculations, especially for NRQCD, which does not follow the data trend. A similar behavior is observed for ψ(2S), as shown in the right panel of Fig. 1.20, even if the large uncertainties prevent from drawing a firm conclusion. However, when the prompt J/ψ measured at lower energy $\sqrt{s} = 1.8$ TeV with CDF collaboration [117], a different behavior is observed — at lower energy measurement, a small transverse polarization is observed for the prompt J/ψ. This outcome is still puzzling.

The D0 collaboration was also able to measure the inclusive Υ polarization [118] with the large data sample collected during Run II. Unlike what has been observed in the charmonium sector, the NRQCD factorization approach appears to describe the trend of the experimental results for the Υ(1S) in the high-p_T region, whereas no model could match the data at low p_T. This measurement contradicts the CDF measurement [109], since it does not show such a strong longitudinal polarization for Υ(1S) with CDF collaboration, as shown in the left panel of Fig. 1.21 (black points). The Υ(2S) polarization was also measured with D0 collaboration [118], as illustrated in the right panel of

Fig. 1.21, but the limited size of the data sample does not allow to draw any firm conclusion. The fact that the picture of quarkonium polarization at the Tevatron was not very clear, motivated the interest in the quarkonium polarization measurements at higher colliding energies.

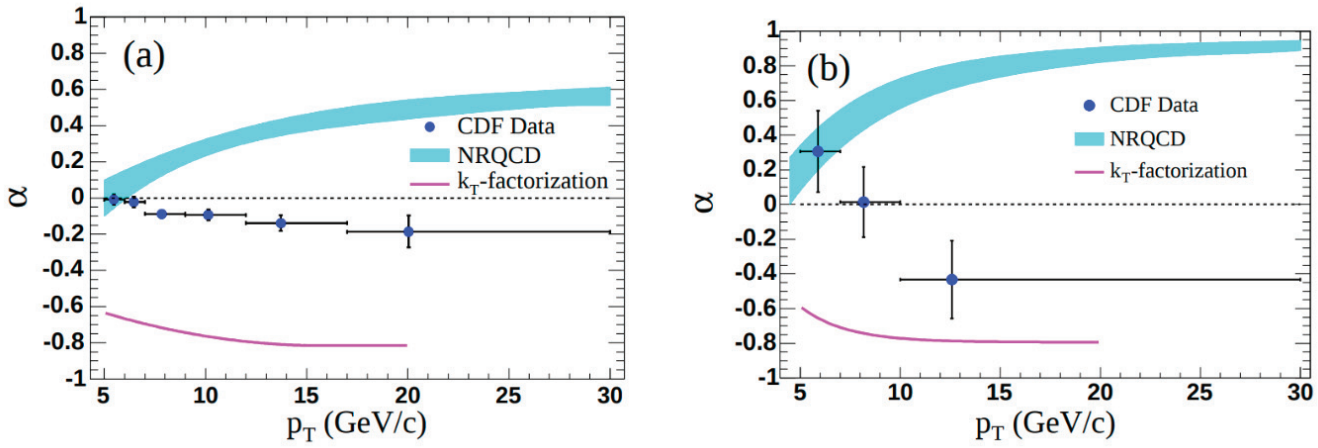

Figure 1.20: Prompt J/ψ (a) and ψ(2S) (b) polarization parameter α (same as λ_θ) as a function of transverse momentum, measured at central rapidity ($|y| < 0.6$) at $\sqrt{s} = 1.96$ TeV with CDF collaboration [115], compared with NRQCD [119] and k_{T} factorization [120] predictions. Figures taken from Ref. [115].

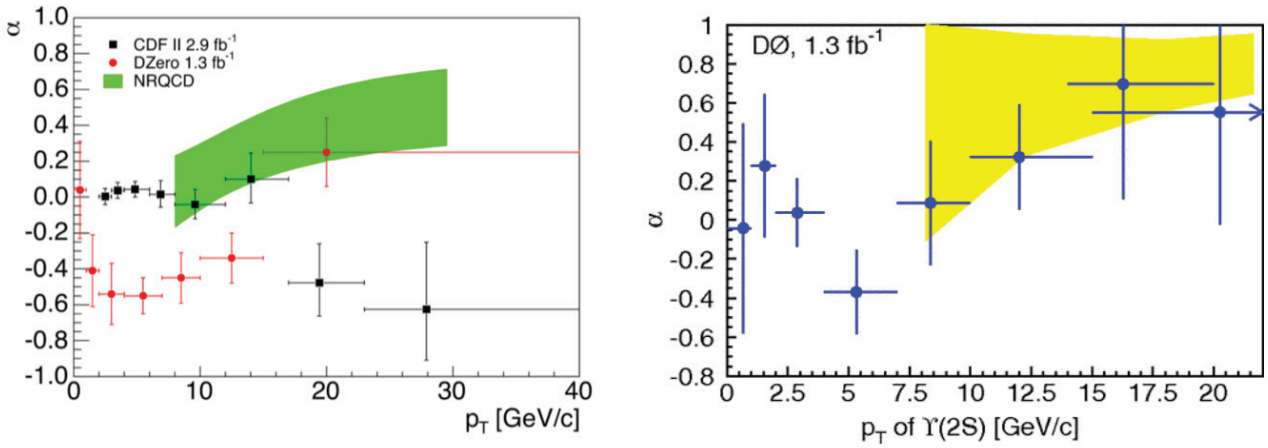

Figure 1.21: Left: Υ(1S) polarization parameter α (same as λ_θ) as a function of transverse momentum measured by D0 [118] and CDF [109] collaborations at $\sqrt{s} = 1.96$ TeV. Right: Υ(2S) polarization parameter α (same as λ_θ) as a function of transverse momentum measured by D0 collaboration at $\sqrt{s} = 1.96$ TeV [118]. Both results are compared with LO NRQCD predictions [121]. Figures taken from Refs. [109, 118].

Results at the RHIC

The J/ψ polarization has also been widely investigated at RHIC in pp collisions. For example, the STAR collaboration studied the inclusive J/ψ polarization parameters λ_θ, λ_φ, and $\lambda_{\theta\varphi}$ as a function of p_{T} both in the dielectron

($|y| < 1$) and dimuon ($|y| < 0.5$) decay channels at $\sqrt{s} = 200$ GeV in both HE and CS reference frames [122]. All three polarization parameters were found to be consistent with zero within statistical and systematic uncertainties with no significant p_{T} dependence, except for λ_θ in the CS frame in the highest p_{T} bin. A fair agreement among the two decay channels was found, despite the slightly different kinematic ranges covered. As shown in Fig. 1.22, among the various theoretical models, the one implementing NRQCD calculations and a CGC scenario (CGC+NRQCD) [123] gives the best overall description of the experimental results. Additionally, for λ_θ in the HE frame, the ICEM calculation [124] predicts a sizable transverse polarization at low p_{T}.

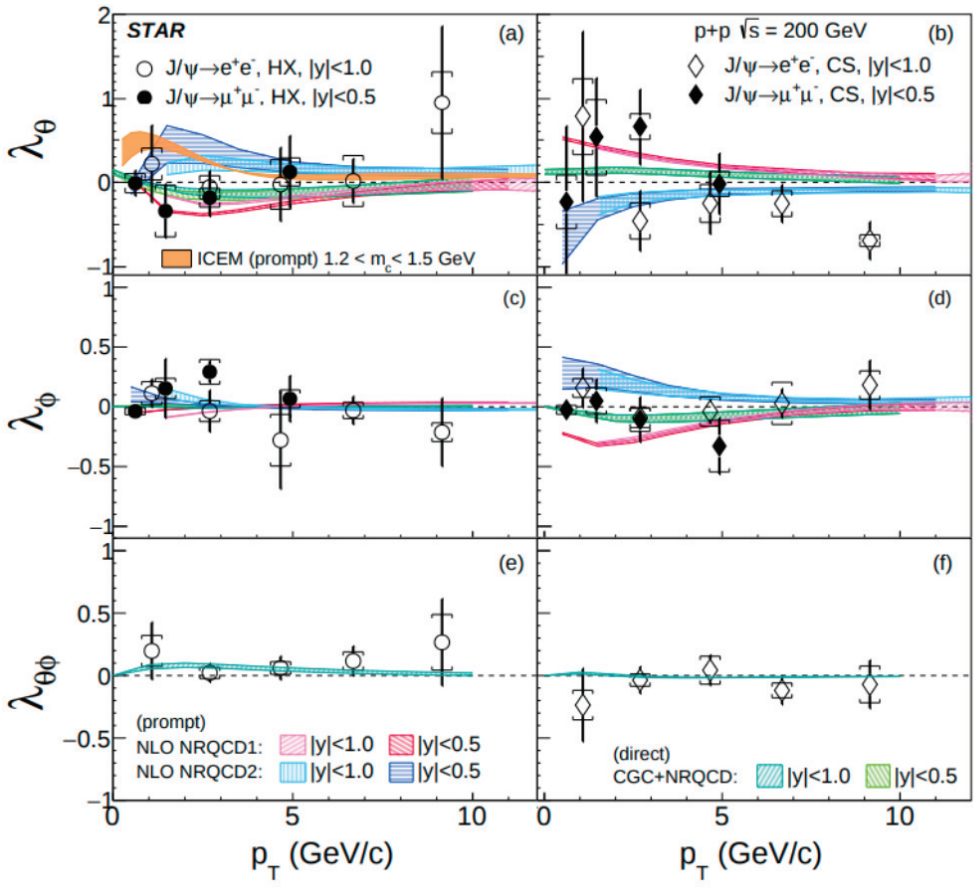

Figure 1.22: J/ψ polarization parameters λ_θ, λ_φ and $\lambda_{\theta\varphi}$ as a function of p_{T} in the Helicity (HX, left) and Collins-Soper (CS, right) reference frames with STAR collaboration [122]. The J/ψ is measured via its dieletron (open point) or dimuon (full point) decay channel. The data results are compared with model predictions [123–126]. ICEM and the two NLO NRQCD calculations are for prompt J/ψ, while the CGC+NRQCD is for direct J/ψ. Figure taken from Ref. [122].

Results at the LHC

The LHC allows for extending the study of polarization at the highest center-of-mass energies available in laboratory, resulting in larger cross-sections for both charmonium and bottomonium states. The first inclusive J/ψ

polarization measurement was performed by ALICE at $\sqrt{s}$ =7 TeV [127]. This first measurement, carried out in the kinematical region $2.5 < y < 4.0$ and $2 < p_{\mathrm{T}} < 8$ GeV/c, exhibits polarization parameters λ_θ and λ_φ consistent with zero within uncertainties, in both HE and CS reference frames. This result was confirmed by the later LHCb measurement, improving the precision of the measurement in a similar rapidity range ($2 < y < 4.5$) [26]: the polarization parameters λ_φ and $\lambda_{\theta\varphi}$ were found to be compatible with zero in both the HE and CS reference frames, while a small but significant longitudinal polarization ($\lambda_\theta^{\mathrm{HE}} = -0.145 \pm 0.027$) was observed in the HE reference frame. The ALICE measurement for the polarization of inclusive J/ψ at $\sqrt{s} = 8$ TeV [128] was also found to be in agreement with the two earlier results. The experimental data were also compared to model predictions: the CSM and NRQCD calculations [22, 24] predict an opposite p_{T} trend for all polarization parameters in both HE and CS reference frames, both predictions being in disagreement with the experimental results, as shown in Fig. 1.23. The CGC+NRQCD calculations [123], as shown in Fig. 1.24, describe the results much better than the CSM and NRQCD computations, even though the CGC+NRQCD prefers a small transverse polarization ($\lambda_\theta > 0$) and the experimental data seem on the contrary to follow a weak longitudinal polarization ($\lambda_\theta < 0$) at small p_{T}.

The CMS collaboration has measured prompt J/ψ and ψ(2S) polarization parameters as a function of p_{T} at $\sqrt{s}$ = 7 TeV in three rapidity ranges: $|y| < 0.6$, $0.6 < |y| < 1.2$, and $1.2 < |y| < 1.5$ [23]. The J/ψ and ψ(2S) results are relative to the ranges $14 < p_{\mathrm{T}} < 70$ GeV/c and $14 < p_{\mathrm{T}} < 50$ GeV/c, respectively, complementing at high p_{T} the results from the ALICE and LHCb collaborations. All the measured polarization parameters are consistent with zero within the uncertainties, in contrast with the NLO NRQCD predictions [125] of a large transverse polarization at high-p_{T}.

Bottomonium polarization can also be measured at the LHC, thanks to the large $b\bar{b}$ production cross-section corresponding to the available center-of-mass energies. The CMS collaboration measured the polarization parameters for Υ(1S), Υ(2S), and Υ(3S) in the range of $10 < p_{\mathrm{T}} < 50$ GeV/c for $|y| < 0.6$ and $0.6 < |y| < 1.2$ [116], as shown in Fig. 1.25, with no large transverse or longitudinal polarization being observed in the investigated kinematic region. LHCb performed the same measurement at the forward rapidity for $p_{\mathrm{T}} < 20$ GeV/c at $\sqrt{s} = 7$ and 8 TeV [129], measuring no significant polarization over the considered kinematic region in both HE and CS reference frames.

An additional interesting measurement has been recently reported by the CMS collaboration — the first experimental constraints on the polarization of promptly-produced χ_{c1} and χ_{c2} mesons in pp collisions at $\sqrt{s} = 8$ TeV [130], performed in the J/$\psi\,\gamma$ decay channel. The polarizations are measured in the Helicity frame, through the analysis of the χ_{c2} to χ_{c1} yield ratio as a function of the relevant angular variables, in three bins of J/ψ transverse momentum. While no differences are seen between the two states in terms of azimuthal decay angle distributions, they are observed to have significantly different polar anisotropies. The measurement favors a scenario where at least one of the two states is strongly polarized in the HE frame, in agreement with nonrelativistic quantum chromodynamics predictions. This finding marks a new milestone in the experimental study of quarkonium production, as well as the first important indication of differences in the polarization of different quarkonium states.

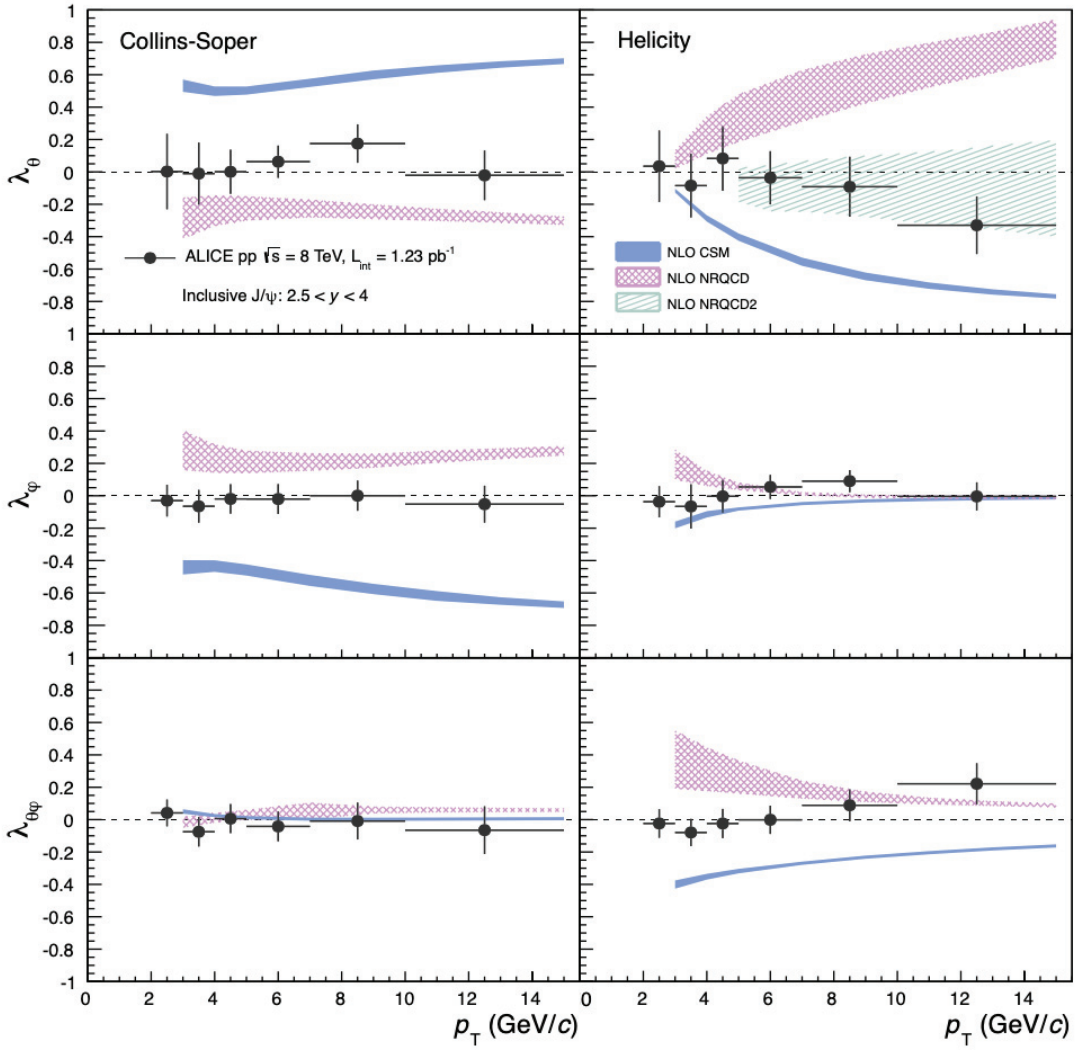

Figure 1.23: J/ψ polarization parameters λ_θ, λ_φ and $\lambda_{\theta\varphi}$ as a function of p_{T} in pp collisions at $\sqrt{s} = 8$ TeV with ALICE, compared with NLO CSM [22], NRQCD [22] and NRQCD2 [24] model predictions. Figure taken from Ref. [128].

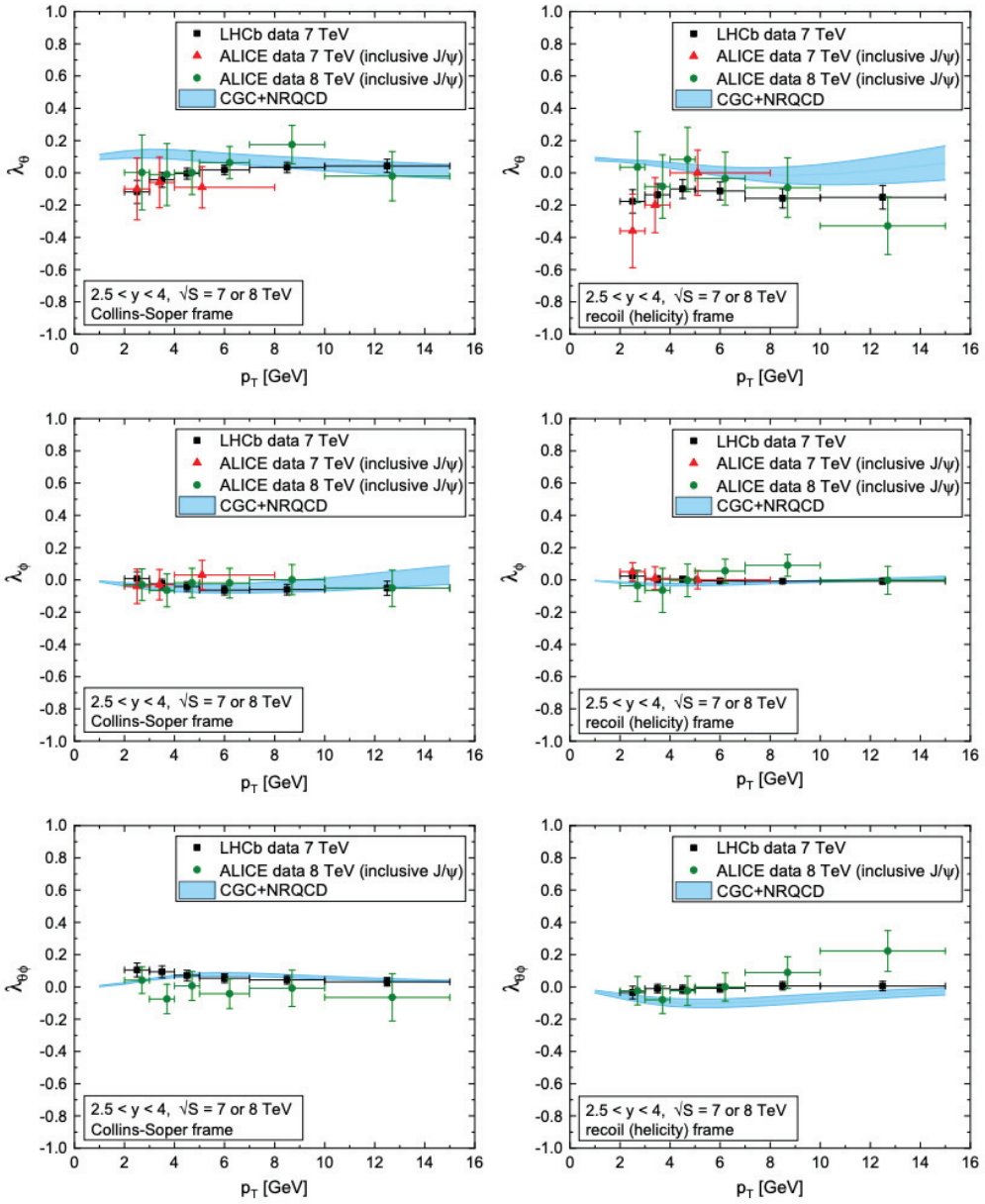

Figure 1.24: The polarization parameters as a function of transverse momentum p_{T} in the Helicity (right column) and Collins-Soper frame (left column) with LHCb [26] and ALICE [127, 128], compared with CGC+NRQCD calculations [123]. Figure taken from [123].

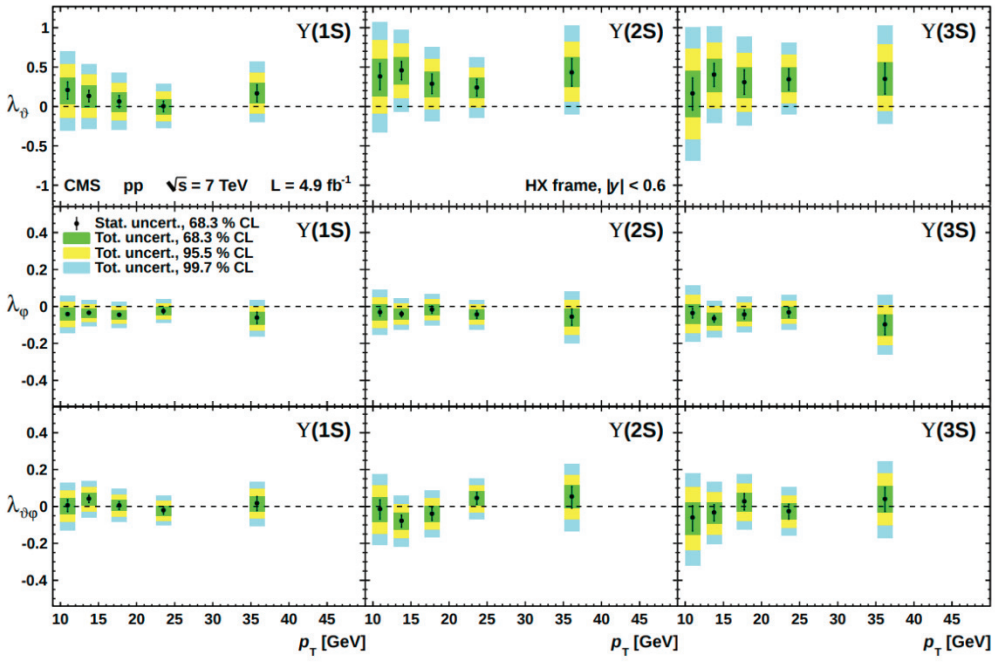

Figure 1.25: Υ(nS) polarization parameters λ_θ, λ_φ, and $\lambda_{\theta\varphi}$ as a function of transverse momentum in pp collisions at $\sqrt{s} = 7$ TeV with CMS [116] in Helicity reference frame. Figure taken from [116].

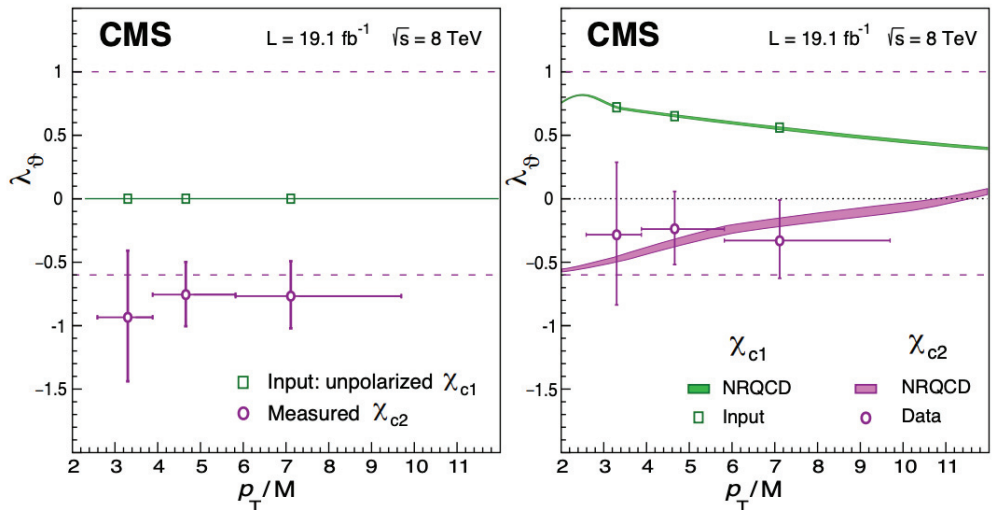

Figure 1.26: The polarization parameter $\lambda_\theta^{\chi_{c2}}$ values measured when the $\lambda_\theta^{\chi_{c1}}$ values are fixed to the unpolarized (left) or the NRQCD (right) scenarios as a function of p_T/M of the J/ψ [130]. The purple band on the right is the NRQCD prediction for $\lambda_\theta^{\chi_{c2}}$ [131]. Figures taken from Ref. [130].

The analysis reported in this thesis (Chapter 7) will contribute to the study of quarkonium polarization, providing a new measurement of the Υ(1S) polarization as a function of p_{T} in pp collisions at $\sqrt{s}$ =13 TeV, at forward rapidity, in both the Helicity and Collins-Soper reference frames, exploiting the dimuon decay channel.

Chapter 2

Experimental apparatus

2.1 The Large Hadron Collider

The Large Hadron Collider (LHC) is the largest collider ever built in the world, located at the European Organization for Nuclear Research (CERN) in the France-Switzerland border. Its 27-km ring hosts a system of superconducting magnets and RF cavities to accelerate, deviate, and focus the colliding beams. The accelerator complex with its pre-accelerators is shown in Fig. 2.1. More details can be found in Ref. [132]. Up to now, the LHC delivered pp collisions at the center-of-mass energies of 0.9, 2.76, 5.02, 7, 8 and 13 TeV; p–Pb collisions at 5.02 and 8.16 TeV; Pb–Pb collisions at 2.76 and 5.02 TeV; xenon–xenon (Xe–Xe) collisions at 5.44 TeV. The collected data were analyzed by four main experiments:

- **ATLAS (A Toroidal LHC ApparatuS)** is the largest general purpose particle physics detector in the world, aiming at performing measurements in the electroweak sector of the Standard Model, including the Higgs sector, and looking for any hint of physics beyond the standard model (see Refs. [133**?**]).

- **CMS (Compact Muon Solenoid)** is the second general purpose particle physics detector at the LHC. It has a different detector layout than ATLAS, but shares the same physics goals.

- **LHCb (Large Hadron Collider beauty)** mainly focuses on heavy-flavor physics and in particular precision measurements related to CP violation.

- **ALICE (A Large Ion Collider Experiment)** is a dedicated detector aiming at the study of the quark-gluon-plasma produced in heavy-ion collisions at the LHC, and other phenomena related to QCD at high energy and high density. More details on the ALICE detector are given in Section 2.2.

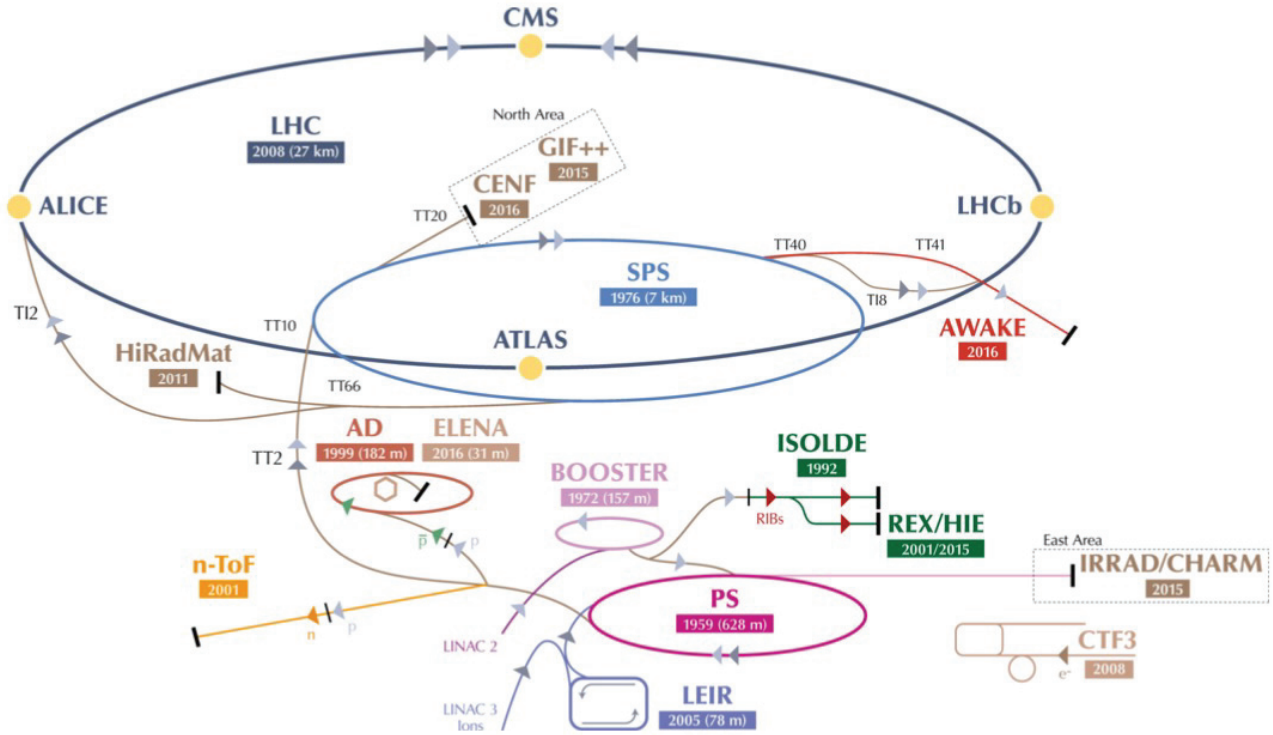

Figure 2.1: Schematic view of the CERN accelerator complex and its four main experiments.

2.2 ALICE

Figure 2.2 shows a schematic layout of the ALICE detector. ALICE has unique features among the LHC experiments, namely for its particle tracking performance down to low transverse momenta and particle identification (PID) in a wide kinematic range employing a variety of technologies. A short summary of the various sub-detectors will be given here. The ones relevant for the presented analyses will be further described in the following sections.

The main part of ALICE is the central barrel, built as a cylinder around the interaction point. The first detector outside the beam pipe is the Inner Tracking System (ITS), which is responsible for determining the primary vertex of a collision, and the secondary vertices corresponding to the decay of long-living particles. Going outer in the radial direction, one finds the Time Projection Chamber (TPC), the main tracking and PID device of ALICE and the largest of its kind in the world. Outside the TPC several, additional tracking and PID detectors are installed: the Transition Radiation Detector (TRD), Time Of Flight (TOF), Electromagentic Calorimeter (EMcal), Di-jet Calorimeter (DCal), Photon Spectrometer (PHOS) and High-Momentum PID (HMPID). Another set of detectors is installed in the forward part of the barrel, for specific purposes: the V0 and T0 detectors, in particular, are used for event triggering and luminosity determination. The muon arm is also installed in the forward region, composed of a hadron absorber with a thickness of about 10 interaction lengths, followed by a series of 10 tracking planes installed on both sides of a dipole magnet providing an integrated field of 3 T·m. The tracking planes are followed by an iron wall of about 7.2 interaction lengths, shielding the stations of the muon trigger. Further away from the main detectors,

the ALICE Diffractive (AD) and the Zero-Degree Calorimeter (ZDC) detectors are installed, both consisting of two parts, located on either side of the interaction point along the beam axis. The AD detectors are located at extremely forward rapidities, and focus on trigger diffractive collisions. The ZDC detectors, located at even smaller angles to the beam, are used to measure the energy of spectator nucleons and act as a centrality estimator in heavy-ion collisions.

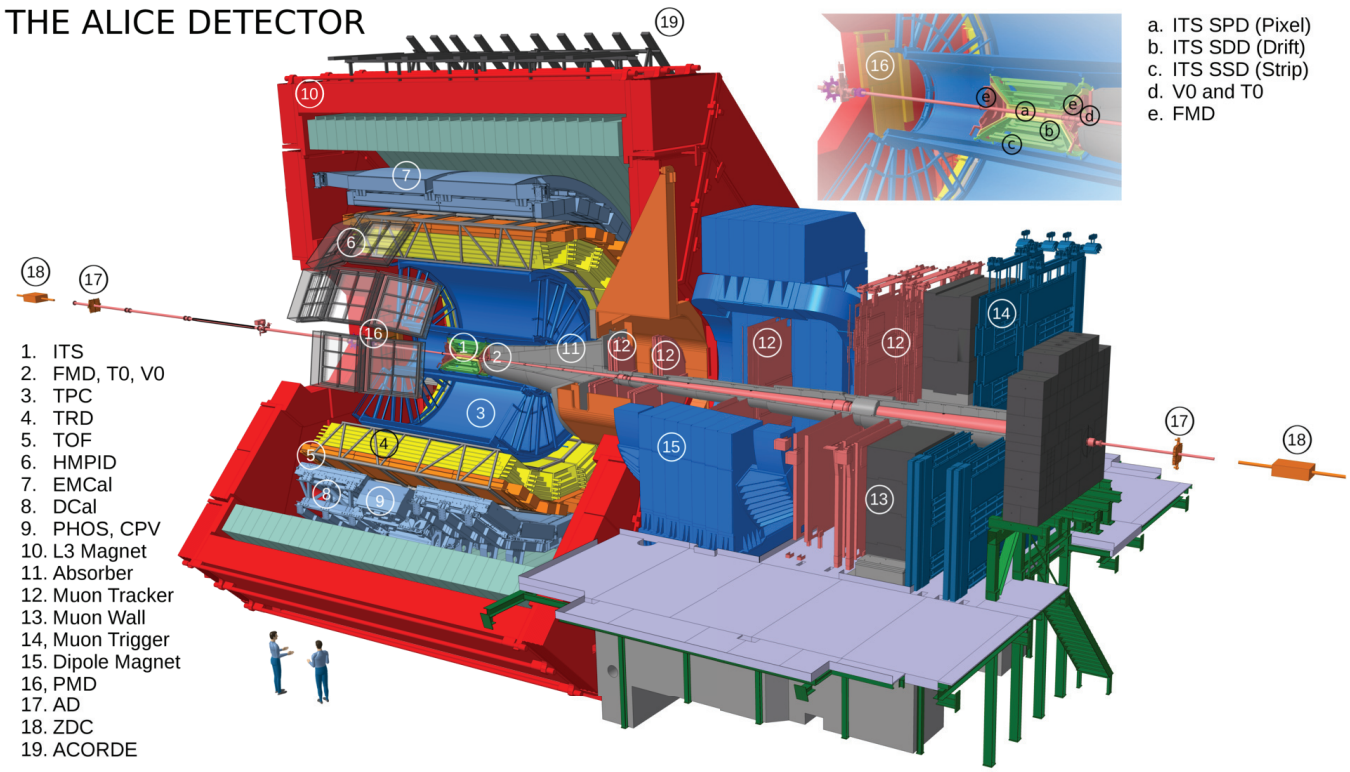

Figure 2.2: Schematic view of the ALICE detector during Run 2. Figure taken from ALICE figure repository.

2.2.1 Inner Tracking System (ITS)

The Inner Tracking System (ITS) includes six cylindrical silicon layers. Although each layer covers the entire azimuth, they have pseudorapidity ranges, as shown in Tab. 2.1. The two innermost layers compose the Silicon Pixel Detector (SPD), which was used in the first analysis reported in this work to estimate the charged-particle multiplicity at midrapidity (see Section 4.2). The third and fourth layers of the ITS form the Silicon Drift Detector (SDD), and the last two layers compose the Silicon Strip Detector (SSD). Both the SDD and the SSD provide position information in two dimensions and a $\mathrm{d}E/\mathrm{d}x$ sample that can be used for PID.

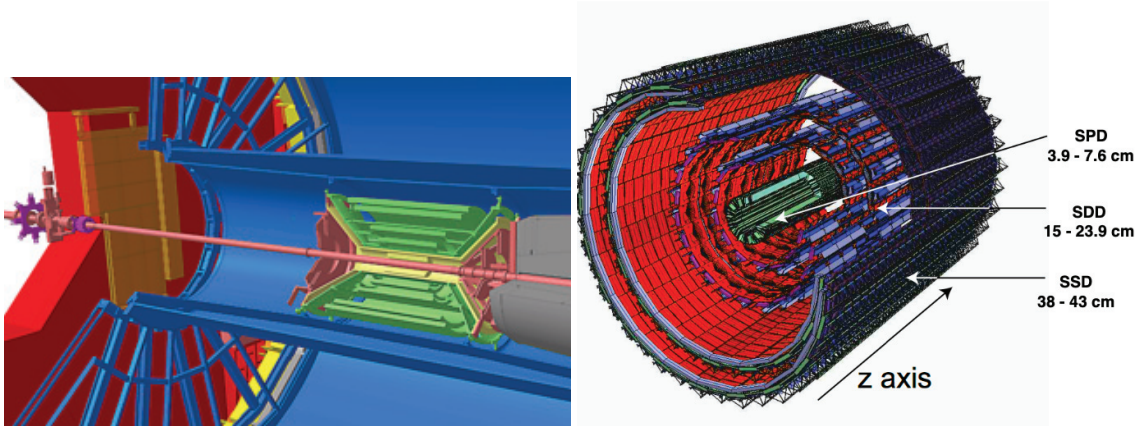

Figure 2.3: Left: layout of the ITS detector during Run 1 and Run 2. Figure taken from ALICE figure repository. Right: The radial positions of the three sub-systems: SPD, SDD, and SSD are indicated. Figures taken from Ref. [134].

Detector	Acceptance		Position r (cm)	Main purpose
	Polar η	Azimuthal Φ		
ITS layer 1, 2 (SPD)	$\|\eta\| < 2.0$, $\|\eta\| < 1.4$	full	$r = 3.9, r = 7.6$	Tracking and vertexing
ITS layer 3, 4 (SDD)	$\|\eta\| < 0.9$, $\|\eta\| < 0.9$	full	$r = 15.0, r = 23.9$	Tracking and PID
ITS layer 5, 6 (SSD)	$\|\eta\| < 1.0$, $\|\eta\| < 1.0$	full	$r = 38.0, r = 43.0$	Tracking and PID

Table 2.1: Dimensions of individual layers of ITS.

2.2.2 V0 detector

The V0 detector is made up of two scintillator hodoscopes (the V0A: $2.8 < \eta < 5.1$ and the V0C: $-3.7 < \eta < -1.7$), one on either side of the interaction point. The minimum-bias (MB) trigger is provided,requiring a signal in both hodoscopes. The V0 can also be used to filter out background caused by interactions between the beam and residual gas in the beam pipe as well as between the beam halo and different accelerator components.

2.2.3 Muon Spectrometer

The Muon Spectrometer (MS), located at forward rapidity ($-4.0 < \eta < -2.5$), is used for the study of low-mass neutral mesons, Z bosons, and quarkonium in the dimuon decay channel. In addition, it allows one to measure the open heavy flavor mesons (D and B mesons) and the W boson in their semi-leptonic decay channel. Fig. 2.4 shows the main components of the spectrometer. The closest element to the interaction region is a front absorber, designed to absorb hadrons emerging in the collision, mainly pions and kaons, before their semi-muonic decays. Five pairs of high-resolution detector planes constitute a tracking system, in the middle of which a large dipole magnet is installed. Beyond the magnet, an iron wall acts as a muon filter shielding two pairs of trigger chamber

planes. Through the longitudinal extension of the MS, an inner beam shield protects the chambers from particles emitted at small angles.

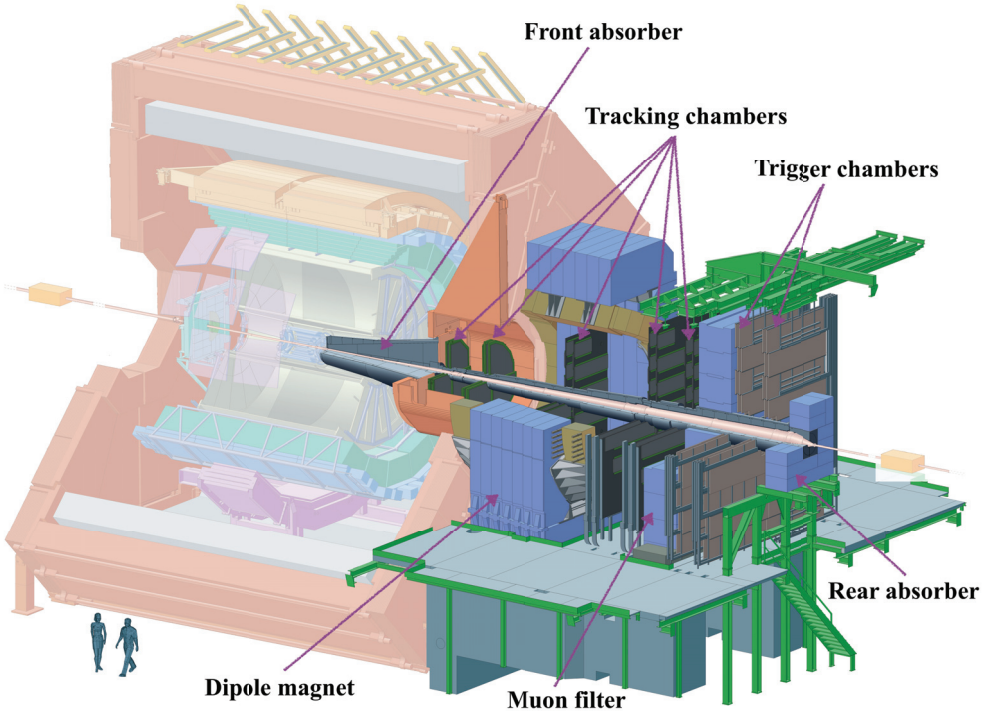

Figure 2.4: Layout of the Muon Spectrometer detector.

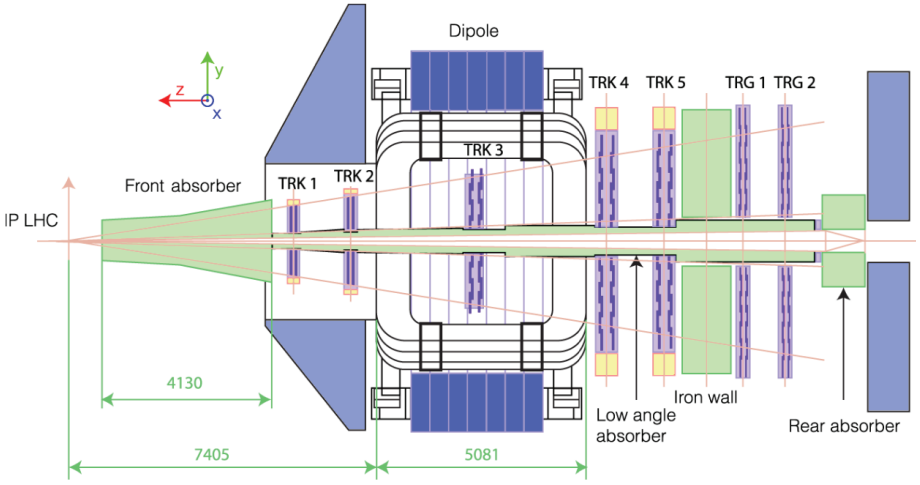

Figure 2.5: Layout of the Muon Spectrometer detector. Figure taken from Ref. [135].

Absorbers and beam shield

The front absorber has a crucial role, being designed to remove hadrons coming from the interaction region without creating further particles flowing towards the tracking chambers, and without affecting muons that come from

the processes of interest for the physics measurements. This absorber, approximately 4 m long, is located inside the L3 magnet. It has a composite structure involving different materials, specifically tuned to limit the small-angle scattering and the energy loss of muons, and to protect other sub-detectors from the secondary particles that are produced in the absorber itself. The spectrometer is also shielded throughout its length by the beam shield, a dense absorber tube made of some 100 t of tungsten, lead and stainless steel, which surrounds the beam pipe. While the front absorber and the beam shield are sufficient to protect the tracking chambers, the trigger chambers need an additional shielding. This is provided by an iron wall about 1 m thick — the muon filter — situated between the last tracking chamber and the first trigger chamber. The front absorber and the muon filter work together to stop muons with momentum of, approximately, less than 4 GeV/*c*.

Dipole magnet

The design of the spectrometer incorporates one of the largest dipole magnets ever constructed with resistive coils. It weighs 850 t with a gap between poles of about 3.5 m and a yoke height of about 9 m. It has a peak field of 0.7 T and a field integral of 3 T·m between the interaction point and the muon filter in order to provide the required resolution on the dimuon mass.

The muon tracking system

The design of the tracking system was driven by two main requirements: a spatial resolution better than 100 μm, and the capability to operate in the high-multiplicity environment corresponding to the most central Pb–Pb collisions at the top LHC energy. There are 10 tracking planes (chambers) in all, arranged in pairs to form five stations: two pairs before the dipole magnet; one inside it; and two after the magnet. Each chamber has two cathode planes to provide a 2D hit information. The segmentation fo the read-out pads is designed to keep the occupancy down to around 5%. In the first station, for example, in the inner region, the one closest to the beam pipe, where the occupancy is the highest, the pads are as small as 4.2×6.3 mm^2. Then, larger pads are used at larger radii because the hit density decreases with the distance from the beam. As a result, there are about 1 million electronics channels overall. To reduce the multiple scattering of the muons, the chambers are built using composite materials such as carbon fibre. This technological choice allows for extremely thin and rigid elements for the detectors, resulting in a chamber thickness as small as 0.03 radiation lengths. The various tracking stations, ranging from a few square metres for station 1 to more than 30 m^2 for station 5, justify two different basic designs for the chambers. The read-out electronics are dispersed across the surface of the quadrant-shaped chambers in the first two stations. The chambers for the other stations have an overlapping slat structure, with the electronics installed on the slat edges. The maximum size of the slats is 40×240 cm^2.

The muon trigger system

The trigger chambers beyond the muon filter form the last main element of the muon spectrometer. The role of the trigger detectors is to select single muons and dimuons produced in the processes of interest (e.g. the dimuon decays of the J/ψ or the Υ resonances), and to reject background originating from muons (mainly low-p_{T}) produced by π and K decays, as well as punch-through hadrons emerging from the front absorber. The trigger system operates based on a predetermined transverse momentum (p_{T}) threshold. When there are two or more tracks with p_{T} above this threshold, the readout electronics of the trigger system can accept or reject each track individually, depending on an estimation of its p_{T}. This process enables the generation of a dimuon trigger signal. To meet the requirement for a position-sensitive trigger detector with a spatial resolution better than 1 cm for p_{T} selection, Resistive Plate Chambers (RPCs) are employed. The main component of the trigger system consists of four RPC planes, with a combined active area of approximately 150 m^2. These planes are arranged in two stations, positioned 1 m apart from each other, and installed behind the muon filter.

2.2.4 ALICE trigger system and data acquisition

The ALICE trigger system is a crucial component of the ALICE experiment at the LHC. It is responsible for selecting and identifying interesting events from a large number of collision events, and must be able to process very different collision environments (e.g. pp, p–Pb, and Pb–Pb collisions). The system consists of the Central Trigger Processor (CTP) and additional Local Trigger Units (LTUs), which work together as a uniform interface to the detector front-end electronics. The trigger decisions in the ALICE experiment are generated by the CTP, which gathers information from all detector signals. The CTP selects events with diverse characteristics, adjusting the rates to meet both the Data Acquisition system (DAQ) bandwidth limitations and the physics requirements. The crucial task of the CTP is to evaluate the trigger inputs at every machine cycle ($\sim$ 25 ns). Owing to the nature of the input signals and the demands of the detectors, the trigger system is categorized into three levels, namely Level 0 (L0), Level 1 (L1), and Level 2 (L2), each with varying latencies [136]:

- L0: the CTP combines signals from the fastest detectors, namely T0, V0, SPD, TOF, PHOS, EMCal (photon trigger), and muon trigger, using both AND and OR logic to satisfy the requirements of a specific trigger class. The trigger decision is made $\sim$ 1.2 μs after the collision.

- L1: the CTP combines signals from slower detectors, such as EMCal (neutral-jet trigger), TRD and ZDC. The trigger decision is made $\sim$ 6.5 μs after L0, casuing by the computation time in TRD and EMCAL, as well as the propagation time to ZDC.

- L2: the trigger decision is taken after $\sim$ 100 μs. This delay is attributed to the timing of the TPC.

The counts for all trigger classes at each level, both before (L0b) and after (L0a) the CTP decision, are stored in the scalers. The CTP may veto events for various reasons, such as a busy cluster in at least one detector, a mismatch between the L0 input and bunch crossing, past-future protection, or downscaling of certain trigger classes to allow more DAQ bandwidth for rare events. If there are no CTP vetoes, the sub-detectors are read out after a successful L2 trigger, and the event is sent to the High Level Trigger (HLT) for more sophisticated trigger criteria implementation [137]. After processing the detector readout data, the HLT either accepts or rejects events.

The accepted events are then subjected to various processes via the DAQ system, which is responsible for facilitating the transfer of data from the detectors to data storage. Once the CTP has decided to acquire a particular event, the trigger signal is sent to the front-end electronics of the detector. The resulting data is transmitted to a group of computers called Local Data Concentrators (LDCs), where the data fragments that correspond to a specific event are processed and combined into sub-events. The Global Data Collector (GDC) collates information from different LDCs to construct the event, which is then forwarded to the CERN storage facilities. During reconstruction, the raw data is processed to generate the Event Summary Data (ESD), which are subsequently filtered to create the Analysis Object Data (AOD). These AOD files provide reduced and specific information, depending on the type of study. In tandem with processing the raw data, the alignment and calibration data from the detectors are compiled and stored in the Offline Condition Database (OCDB).

2.2.5 Analysis framework

The ALICE analysis framework for Run 1 and Run 2 was based on the AliRoot software package. AliRoot was a C++ based framework and it provided a wide range of tools for analyzing the data collected by the ALICE experiment, including event selection, track and vertex reconstruction, particle identification, and event visualization. It also included interfaces for various data analysis packages, such as ROOT, a popular data analysis tool in the high-energy physics community. In addition, AliRoot had a well-developed user community that contributed to the development of new analysis tools and techniques. This community produced a large number of analysis packages, including packages for jet reconstruction, heavy-ion physics, and more. Overall, the AliRoot framework provided a powerful and flexible platform for analyzing the data collected by the ALICE experiment in Run 1 and Run 2.

Chapter 3

Data selection and signal extraction

3.1 Data sample and event selection

The proton-proton data samples used for the analyses discussed in the present document, namely the measurement of the multiplicity-dependent Υ production, and the measurement of the Υ(1S) polarization, both performed at forward rapidity in the dimuon channel, were collected in 2016, 2017 and 2018 at a center-of-mass energy of $\sqrt{s} = 13$ TeV. However, for the multiplicity-dependent analysis, the data sample is selected requiring both a good SPD status and a good muon quality, while for the polarization analysis, only a good muon quality is requested. The same low-p_{T} muon trigger threshold (corresponding approximately to 0.5 GeV/c) is used for various samples considered in the analyses. The data samples and the corresponding anchored Monte Carlo (MC) samples considered for the multiplicity dependent analysis are listed in Tab. 3.1; the data and MC samples considered for the polarization analysis are reported in Tab. 3.2.

The event selection for the two analyses is based on the CMUL7-B-NOPF-MUFAST (CMUL7) trigger, and an additional CINT7-B-NOPF-MUFAST (CINT7) trigger is requested for the events considered in the multiplicity-dependent analysis. The CMUL7 trigger is the unlike-sign dimuon trigger, defined by a coincidence of signals in V0A and V0C systems with a pair of unlike-sign muon tracks, where both muon tracks satisfy the low-p_{T} threshold in the muon spectrometer. The CINT7 trigger is the minimum bias (MB) trigger, defined by a coincidence of signals in V0A and V0C systems.

3.2 Υ signal extraction

The two analyses discussed in the present document share various aspects of the Υ signal extraction strategy, as detailed in this section.

Data sample	MC sample
LHC16h	LHC17f5 (PYTHIA 8.2)
LHC16j	LHC17e5 (PYTHIA 8.2)
LHC16k	LHC17d20a1 (PYTHIA 8.2)
LHC16o	LHC17d16 (PYTHIA 8.2)
LHC16p	LHC17d18 (PYTHIA 8.2)
LHC17i	LHC17k4 (PYTHIA 8.2)
LHC17k	LHC18c13 (PYTHIA 8.2)
LHC17m	LHC17l5 (PYTHIA 8.2)
LHC17o	LHC18a9 (PYTHIA 8.2)
LHC17r	LHC18a1 (PYTHIA 8.2)
LHC18d	LHC18g5 (PYTHIA 8.2)
LHC18e	LHC18g6 (PYTHIA 8.2)
LHC18f	LHC18h2 (PYTHIA 8.2)
LHC18l	LHC18j1 (PYTHIA 8.2)
LHC16k	LHC17d20b1(EPOS-LHC)

Table 3.1: Internal ALICE labels for the data and MC samples used in the analysis of the Υ(nS) production as a function of charged-particle multiplicity.

Data sample	MC sample
LHC16f	LHC21d7
LHC16g	
LHC16h	
LHC16i	
LHC16j	
LHC16k	
LHC16o	
LHC16p	
LHC17h	
LHC17i	
LHC17k	
LHC17l	
LHC17m	
LHC17o	
LHC17r	
LHC18b	
LHC18c	
LHC18d	
LHC18e	
LHC18f	
LHC18g	
LHC18h	
LHC18i	
LHC18j	
LHC18l	
LHC18m	
LHC18o	
LHC18p	

Table 3.2: Internal ALICE labels for the data and MC samples used in the analysis of the Υ(1S) polarization.

3.2.1 Muon track and dimuon selection

The signal corresponding to the bottomonium states of the Υ family is measured exploiting the dimuon decay channel of the resonances. The single muon track candidates are selected according to the following criteria:

- The track must be reconstructed within the nominal acceptance of the spectrometer $-4 < \eta_\mu < -2.5$, to reject tracks at the edges of the spectrometer
- The radial coordinate of the muon candidate at the end of the absorber in the range $17.6 < |R_{\rm abs}| < 89.5$ cm to reduce the contamination from the tracks crossing the thicker parts of the absorber
- The track reconstructed by the tracking stations must match a trigger tracklet with $p_{\rm T}^{\mu} > 0.5$ GeV/c
- The product of the muon total momentum p and its Distance of Closest Approach ($p \times {\rm DCA}$) must be within 6 σ of the distribution, to remove tracks not pointing to the interaction vertex

In addition, dimuon pairs formed by combining tracks satisfying the above selection criteria must fulfill the following requirements:

- Total charge of the pair = 0
- Dimuon pair within the nominal acceptance of the spectrometer $2.5 < y_{\mu\mu} < 4$, to cope with the spectrometer's acceptance

3.2.2 Signal extraction

Muon multiple scattering and energy loss fluctuations in the front absorber, as well as residual mis-alignment of the tracking chambers, result in a tail at low and high invariant mass of the two-body peak of the Υ resonances in the reconstructed dimuon mass spectrum [138]. The Υ raw signal yield is obtained by fitting the opposite-sign dimuon invariant mass distribution with the superposition of three double Crystal Ball functions (CB2) (defined in Eq. 3.1), one for each of the Υ(1S), Υ(2S) and Υ(3S) states, and a product of an exponential and a power-law function to account for the background. The CB2 function consists of a Gaussian core extended with two tails, one on each side. The tails can be described by a simple power law function. The parameters α_L and n_L are used to characterize the left tail, while the parameters α_R and n_R describe the right tail. Due to the complexity of the signal resulting by the superposition of the three CB2 functions, and the limited available statistics, leaving the tail parameters (α_L, n_L, α_R and n_R) free in the fit resulted in a systematical overestimation of the tail component and a non-physical shape of the extended tails. For this reason, the tail parameters were fixed with MC simulations.

$$f(x;\mu,\sigma,\alpha_L,n_L,\alpha_R,n_R) = N \cdot \begin{cases} A\cdot(B-t)^{-n_L}, & t \le \alpha_L \\ \exp(-\frac{1}{2}t^2), & \alpha_L < t < \alpha_R \\ C\cdot(D+t)^{-n_R}, & t \ge \alpha_R \end{cases} \tag{3.1}$$

where,

$$t = \frac{x-\mu}{\sigma}$$
$$A = (\frac{n_L}{|\alpha_L|})^{n_L} \cdot \exp(-\frac{|\alpha_L|^2}{2})$$
$$B = \frac{n_L}{|\alpha_L|} - |\alpha_L|$$
$$C = (\frac{n_R}{|\alpha_R|})^{n_R} \cdot \exp(-\frac{|\alpha_R|^2}{2})$$
$$D = \frac{n_R}{|\alpha_R|} - |\alpha_R|$$

and N is the normalization factor, μ and σ are the mean and width of the Gaussian.

Υ(nS) signal extraction in the multiplicity-dependent analysis

As was verified in the data and the MC, no significant dependence on the charged-particle multiplicity affects the shape of theΥ(nS) peaks, the default set of the tail parameters is obtained in the integrated multiplicity interval. The parameters are listed in Tab. 3.3.

pp 13 TeV MC simulations	
α_L	1.0242
n_L	2.0000
α_R	2.0711
n_R	2.2565

Table 3.3: Tail parameters used in the multiplicity dependent analysis: fixed to the simulations at 13 TeV.

Υ(1S) signal extraction in the polarization analysis

For the polarization analysis, the data are analyzed in sub-samples defined by p_{T} and the angular variables $|\cos\theta|$, $|\varphi|$, and $\tilde{\varphi}$. In this case, a dependence of the tail parameters (see Appendix B.2) and the width of Υ(1S) are found in the MC, as shown in Fig. 3.1 (the other results are shown in Appendix B.3). For this reason, in the invariant mass fits performed in the polarization analysis, the width was fixed according to Eq. 3.2, i.e. by scaling the measured width for the angle-integrated spectrum with the MC ratio between the widths in a given angular interval and in the integrated spectrum, while the tail parameters were always fixed to the parameters extracted from the MC.

$$\sigma^{\mathrm{i,Data}}_{\Upsilon(1S)} = \sigma^{\mathrm{i,MC}}_{\Upsilon(1S)} \times (\frac{\sigma^{\mathrm{Data}}_{\Upsilon(1S)}}{\sigma^{\mathrm{MC}}_{\Upsilon(1S)}})_{\mathrm{Integrated}} \tag{3.2}$$

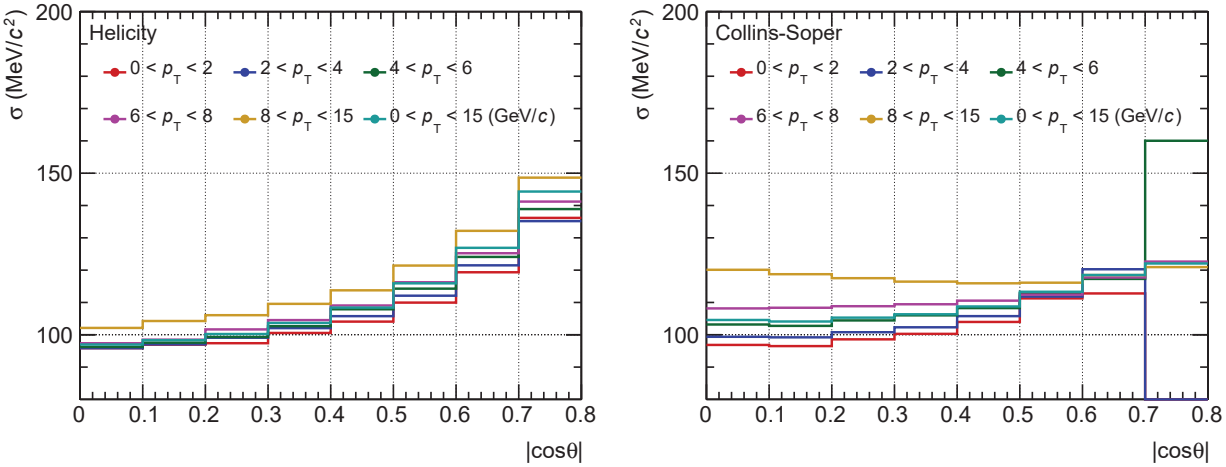

Figure 3.1: The width of Υ(1S) as a function of $|\cos\theta|$ in p_{T} intervals in both Helicity (left) and Collins-Soper (right) frames with MC simulations.

3.2.3 Fit strategy

The fit to the dimuon invariant mass distribution is performed in four iterative steps, as described below. At step N+1, the free parameters are initialized with the values obtained at step N. Only fits satisfying convergence conditions of the minimization strategy are kept. The different steps defining the procedure are illustrated in Fig. 3.2.

- Step 1: fit to the dimuon invariant mass out of the mass window defining the signal range ($m_{\mu\mu} = [8.5, 11]$ GeV/c^2), with the background parameters kept free.
- Step 2: fit to the dimuon invariant mass for the Υ(1S) signal, with the superposition of the background and a Gaussian, excluding the Υ(2S) and Υ(3S) signal range ($m_{\mu\mu} = [9.9, 11]$ GeV/c^2), with all parameters kept free. In this and the following steps, for the multiplicity-dependent analysis the width of Υ(1S) is kept free in the integrated multiplicity, but fixed to the value obtained in the multiplicity-integrated sample when analyzing the other multiplicity intervals; for the polarization analysis, the width is fixed to the scaled MC value.
- Step 3: fit to the dimuon invariant mass for Υ(1S) with the superposition of the background and a CB2, still excluding the Υ(2S) and Υ(3S) ($m_{\mu\mu} = [9.9, 11]$ GeV/c^2). The CB2 tail parameters are fixed to MC, while the other parameters are kept free.
- Step 4: fit to the whole dimuon invariant-mass distribution with the superposition of the background and three CB2 functions with fixed tail parameters, and the mass-pole and the sigma parameters of the

Υ(2S) and Υ(3S) fixed to the ones of the Υ(1S) according to the ratio between the mass-pole parameters reported in the PDG (as described in Eq. 3.3 and 3.4). The other parameters are kept free.

$$m_{\Upsilon(2S)} = m_{\Upsilon(1S)} \times \frac{m^{PDG}_{\Upsilon(2S)}}{m^{PDG}_{\Upsilon(1S)}}, \quad m_{\Upsilon(3S)} = m_{\Upsilon(1S)} \times \frac{m^{PDG}_{\Upsilon(3S)}}{m^{PDG}_{\Upsilon(1S)}} \tag{3.3}$$

$$\sigma_{\Upsilon(2S)} = \sigma_{\Upsilon(1S)} \times \frac{m^{PDG}_{\Upsilon(2S)}}{m^{PDG}_{\Upsilon(1S)}}, \quad \sigma_{\Upsilon(3S)} = \sigma_{\Upsilon(1S)} \times \frac{m^{PDG}_{\Upsilon(3S)}}{m^{PDG}_{\Upsilon(1S)}} \tag{3.4}$$

Where $m_{\Upsilon(nS)}$ and $\sigma_{\Upsilon(nS)}$ denote the mass and the width of Υ(nS) (n = 1, 2 or 3), respectively.

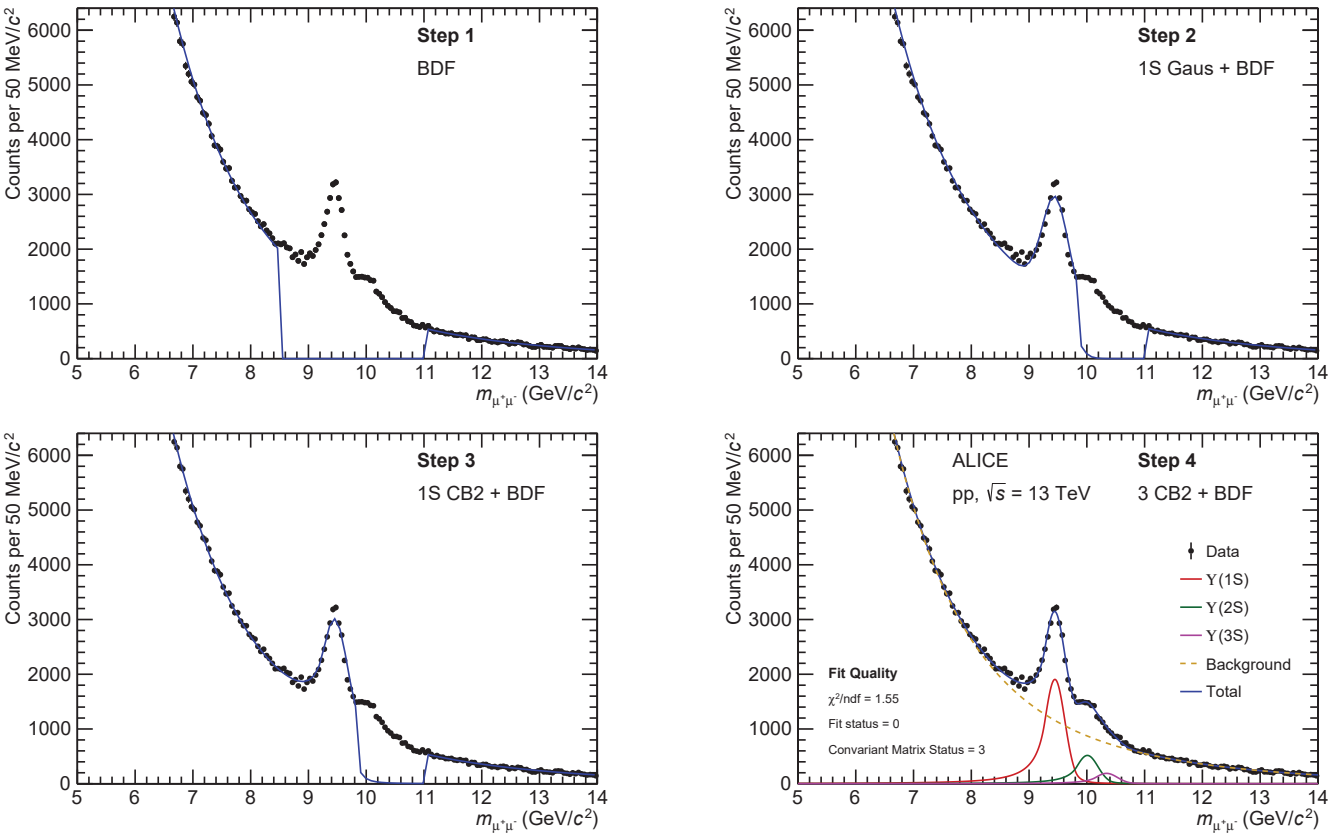

Figure 3.2: An example of the dimuon invariant mass fit procedure: three CB2 functions used to describe the Υ signals and a product of an exponential and a power-law function used to account for the background.

At the end of the fit procedure, the number of Υ(nS) is computed as the integral of the corresponding CB2 function, and the corresponding statistical uncertainty is estimated from the uncertainties on the parameters optimized by the fit.

Chapter 4

Charged-particle multiplicity estimation

The estimation of the charged-particle multiplicity is a mandatory step for the first analysis discussed in the present document, namely the analysis of Υ production at forward rapidity as a function of the charged-particle multiplicity. This analysis is performed on INEL> 0 events, defined by the presence of at least one charged-particle track in $|\eta| < 1$. Moreover, in order to limit any correlation with the measured signal, the pseudorapidity charged-particle multiplicity density (d$N_{\rm ch}$/dη) is measured considering the tracks reconstructed at mid-rapidity.

4.1 Event selection for multiplicity determination

In order to ensure the best possible multiplicity estimation from the number of tracks of the charged particles reconstructed with the SPD, a series of selection criteria (pileup rejection and SPD vertex selection) is applied on events, satisfying the minimum bias trigger level.

Pileup rejection

In high luminosity colliders, it is common to encounter pileup events where multiple separate events are produced within a single bunch crossing. Due to the simultaneous nature of these interactions within the same bunch crossing, the detector is unable to resolve them individually. In this study, the rejection of pileup events was achieved using the Physics Selection framework developed by the ALICE collaboration [139], which includes a dedicated task designed to apply criteria for identifying and removing pileup events. These criteria have been optimized for each specific period and are applied based on the SPD selection criteria and V0 timing.

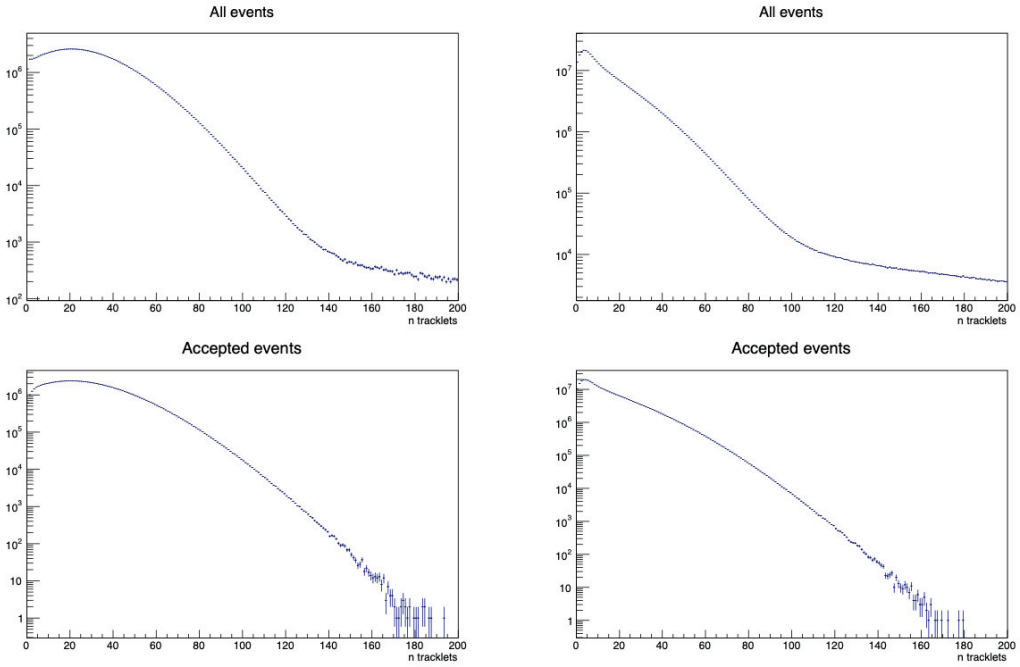

Figure 4.1: The distribution of SPD tracklets for the CMUL7 trigger (left column) and CINT7 trigger (right column) both before and after pileup rejection. Figures taken from [140].

SPD vertex selection

The multiplicity determination requires events with a reconstructed primary vertex from the SPD satisfying the following vertex quality selection criteria (also called vertex quality assurance, vertex QA):

- $N_{\mathrm{contributors}} > 0$: the selected events are required to have a reconstructed primary vertex with at least one primary vertex contributor
- $\sigma(z_{\mathrm{vtx}}) < 0.25$ cm: the resolution of the z-coordinate of the SPD vertex must be better than 0.25 cm
- $|z_{\mathrm{vtx}}| < 10$ cm: the selected events are required to have SPD vertex reconstructed within $|z_{\mathrm{vtx}}| < 10$ cm

4.2 Charged-particle multiplicity estimation

The charged-particle multiplicity, $\mathrm{d}N_{\mathrm{ch}}/\mathrm{d}\eta$, is measured by counting the number of SPD tracklets reconstructed in $|\eta| < 1$. A tracklet is a segment of a track which is reconstructed in the Silicon Pixel Detector (SPD), the two innermost layers of the ITS. The details about the tracklets reconstruction algorithm can be found in [141]. The acceptance of SPD depends both on the position of the vertex, and on the SPD modules status, since inactive SPD modules result in a reduced acceptance. As a consequence, a z-vertex (z_{vtx}) dependence is observed for the number of reconstructed tracklets (see Fig. 4.2). In order to take into account the SPD acceptance variation with

time in the data sample considered, a data-driven event-by-event correction method is applied, similar to the one described in [82]. This method consists in equalizing the measured $\langle N_{\rm trk}\rangle(z_{\rm vtx})$ profile to a reference value, which is at a specific z-vertex position ($z_{\rm vtx}^{\rm ref}$). In this analysis, the maximum $\langle N_{\rm trk}\rangle$ is taken as a reference, i.e. $\langle N_{\rm trk}^{\rm raw}\rangle(z_{\rm vtx}^{\rm ref}) = max(\langle N_{\rm trk}^{\rm raw}\rangle(z_{\rm vtx}))$. More details about the choice of the reference value can see Ref. [142]. Then the correction term is smeared with a Poissonian distribution to mimic the event-by-event fluctuations. The tracklet multiplicity after the equalization procedure is referred to as the "corrected" tracklet multiplicity, $N_{\rm trk}^{\rm cor}(z_{\rm vtx})$. The procedure is illustrated in Eq. 4.1, where the number of missing tracklets ($\Delta N(z_{\rm vtx})$) is computed using Eq. 4.2.

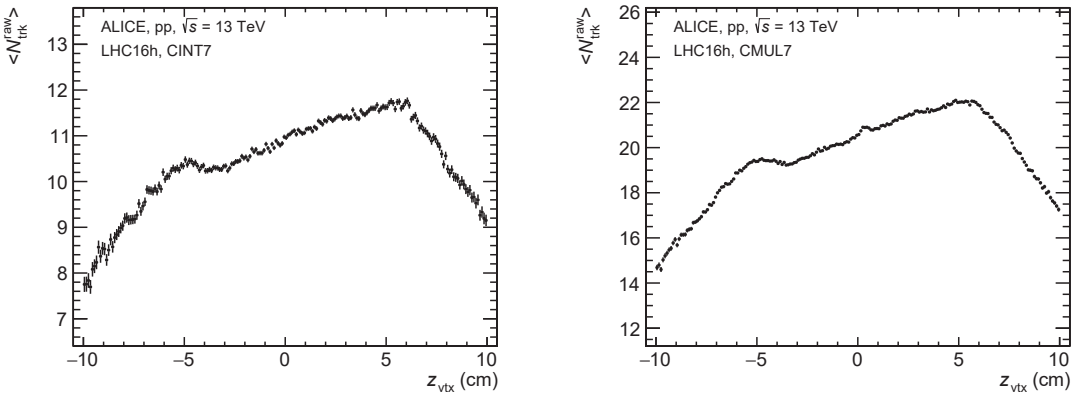

Figure 4.2: An example of average number of tracklets as a function of $z_{\rm vtx}$ for both CINT7 (left) and CMUL7 (right) triggered events.

$$N_{\rm trk}^{\rm cor}(z_{\rm vtx}) = N_{\rm trk}^{\rm raw}(z_{\rm vtx}) + \Delta N_{\rm rand}(z_{\rm vtx}) \tag{4.1}$$

$$\Delta N_{\rm rand}(z_{\rm vtx}) = N_{\rm trk}^{\rm raw}(z_{\rm vtx}) \frac{\langle N_{\rm trk}^{\rm raw}\rangle(z_{\rm vtx}^{\rm ref}) - \langle N_{\rm trk}^{\rm raw}\rangle(z_{\rm vtx})}{\langle N_{\rm trk}^{\rm raw}\rangle(z_{\rm vtx})} \tag{4.2}$$

4.2.1 Choice of reference value and data-driven correction

The reference profile for the $z_{\rm vtx}$-dependence of $\langle N_{\rm trk}\rangle$ may in principle depend on the events considered to evaluate it. From Fig. 4.2, in particular, one can see that the profile extracted from CINT7 and CMUL7 events have slightly different shapes, their ratio being shown in Fig. 4.3 for the LHC16h period (more results are available in Appendix A.2), likely due to the slight correlation between the condition implemented in the dimuon trigger and the topology of the underlying event (more details in Ref. [142]). Since the multiplicity estimation is based on the CINT7 (MB) trigger, which is the less biased trigger, the reference profile corresponding to the CINT7 events has been finally retained as an input for the data-driven correction.

The reference profile for the $z_{\rm vtx}$-dependence of $\langle N_{\rm trk}\rangle$ also depend on the data sample period, see Fig. 4.4: different shapes associated with different maximum values are observed. After inspection, the data sample considered

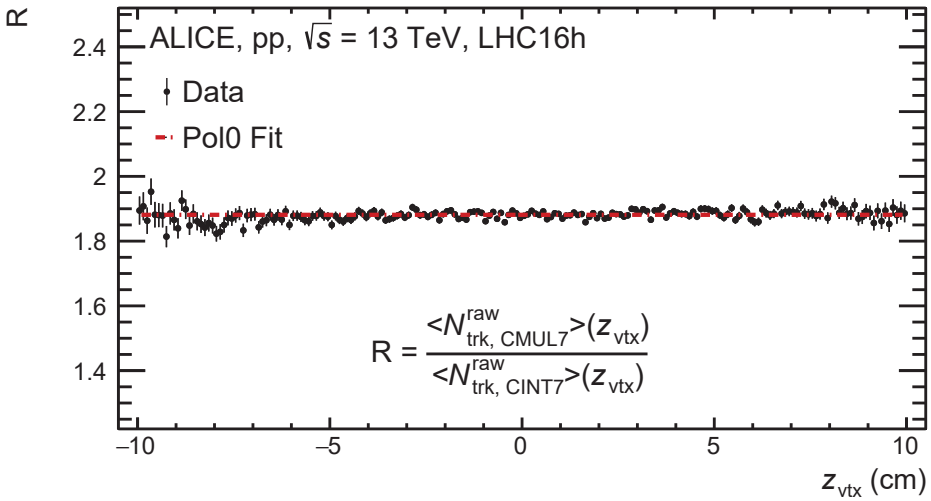

Figure 4.3: An example of the ratio of the average number of raw tracklets as a function of $z_{\rm vtx}$ between CMUL7 and CINT7 triggered events for LHC16h.

for the analysis was then split into three groups, namely G1 (corresponding to 16h+16j+16k+16o+16p+17 i+17k), G2 (corresponding to 17m+17o+17r+18d+18e+18f) and G3 (corresponding to 18l). The raw profiles corresponding to each group are shown in Fig. 4.5. Table 4.1 reports the maximum $\langle N_{\rm trk}\rangle$ values and the corresponding number of triggered events in each selected group. The integrated sample of each group has been used as a baseline for the data-driven correction, and the maximum value among the three profiles ($\langle N_{\rm trk}\rangle^{\rm max} = 11.73$) is used as a uniform reference for all corrections.

Group	Period	$\langle N_{\rm trk}\rangle^{\rm max}$	$N_{\rm events}^{\rm CMUL7}$	$N_{\rm events}^{\rm CINT7}$
G1	16h + 16j + 16k + 16o + 16p + 17i + 17k	11.73	143.2M	43.6M
G2	17m + 17o + 17r + 18d + 18e + 18f	11.64	187.0M	63.9M
G3	18l	10.85	25.1M	9.9M

Table 4.1: $\langle N_{\rm trk}\rangle^{\rm max}$ values and number of CINT7 and CMUL7 triggered events in each group.

After the correction, $\langle N_{\rm trk}\rangle$ is independent of $z_{\rm vtx}$ for CINT7 triggered events, as shown in Fig. 4.6. The effect of this correction on the distribution of the number of tracklets is shown in Fig. 4.7 for both CINT7 and CMUL7 triggered events, and each of the three groups defined for the data sample. As it can be seen, the correction shifts the tracklet distribution towards higher tracklet multiplicities, due to the recovering of the inefficiencies allowed by the data-driven correction. The same data-driven correction procedure is then applied in the MC simulations: to ensure that the same multiplicity classes are considered in data and MC, the same $N_{\rm trk}^{\rm cor}(z_{\rm vtx})$ profile and reference value are considered as in the data. Fig. 4.8 shows the average number of tracklet or charged-particle multiplicity $\langle N_{\rm trk}^{\rm raw}\rangle$, $\langle N_{\rm trk}^{\rm cor}\rangle$ and $\langle N_{\rm ch}\rangle$ (in the left panel) and the probability distributions of $N_{\rm trk}^{\rm raw}$, $N_{\rm trk}^{\rm cor}$ and $N_{\rm ch}$ (in the right panel), in MC.

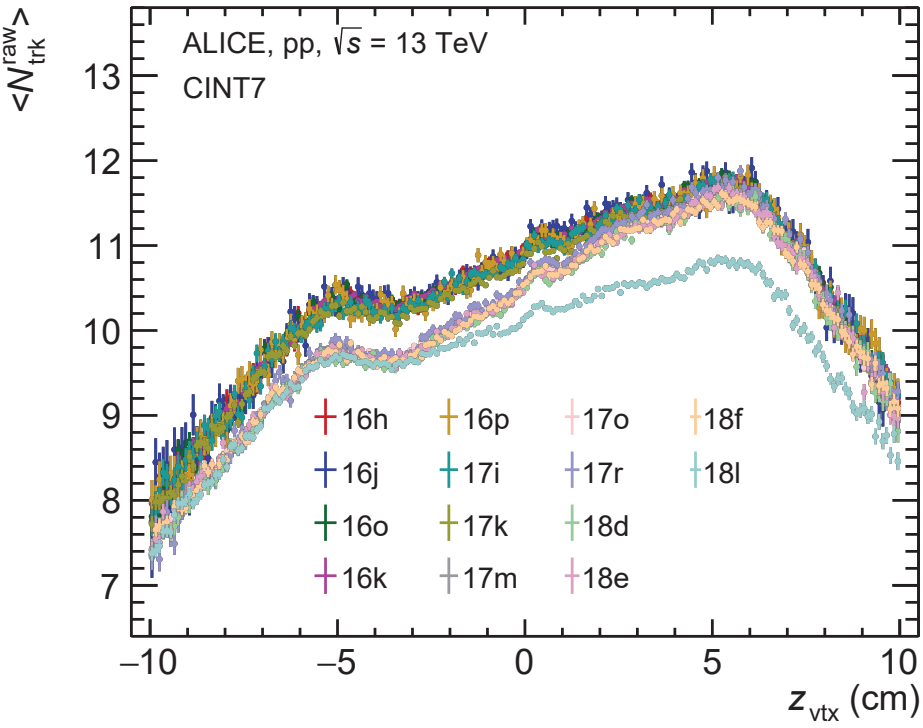

Figure 4.4: Average number of raw tracklets as a function of z_{vtx} for CINT7 triggered events for each period.

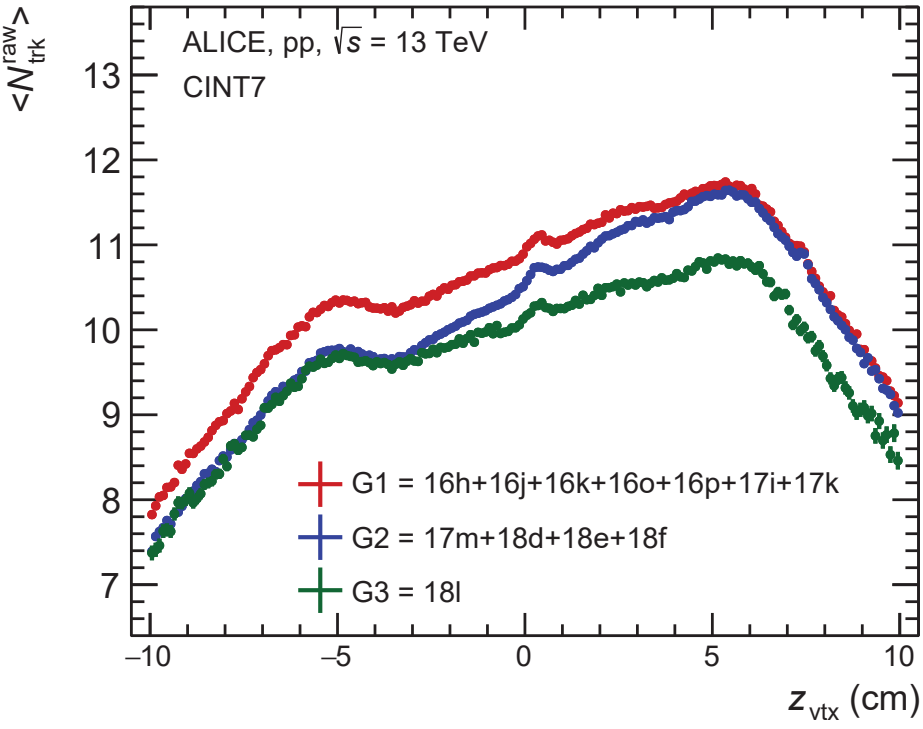

Figure 4.5: Average number of raw tracklets as a function of z_{vtx} for CINT7 triggered events for each group.

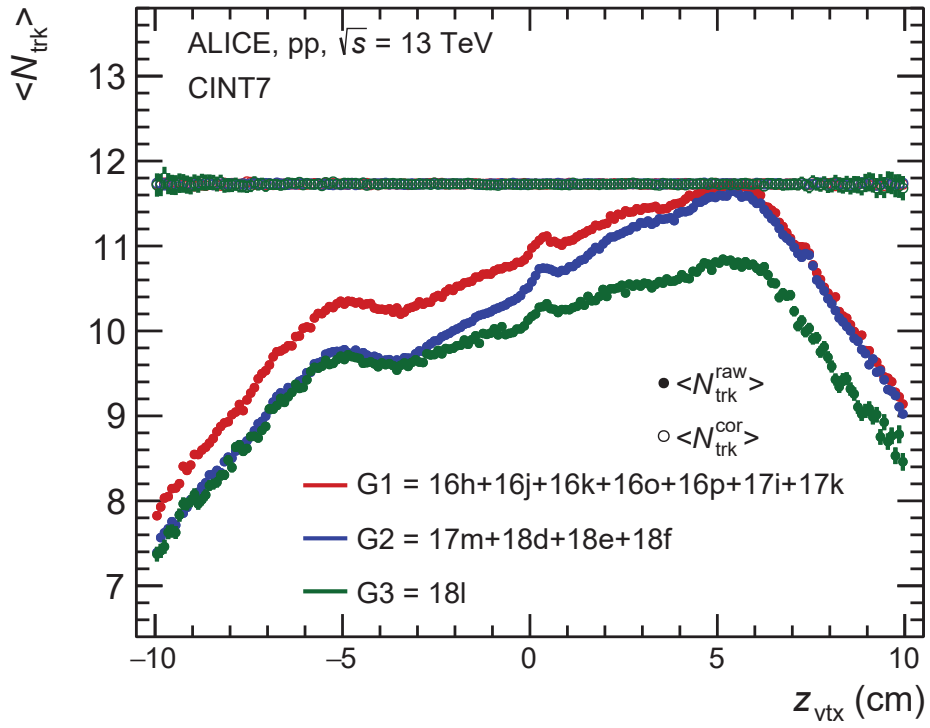

Figure 4.6: Average number of raw (corrected) tracklets as a function of z_{vtx} for CINT7-triggered events for each group.

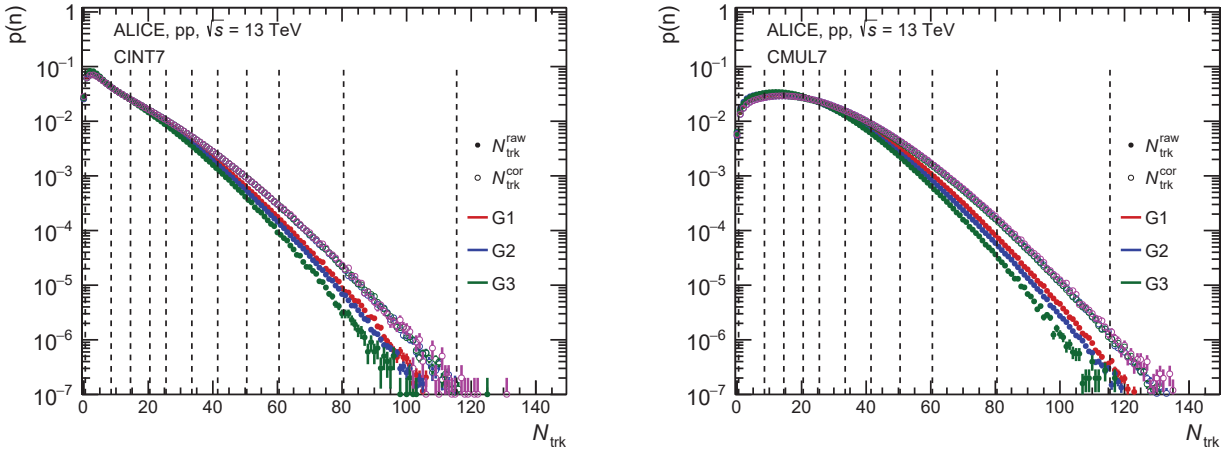

Figure 4.7: Probability distributions of $N_{\mathrm{trk}}^{\mathrm{raw/cor}}$ for CINT7- and CMUL7-triggered events in each group.

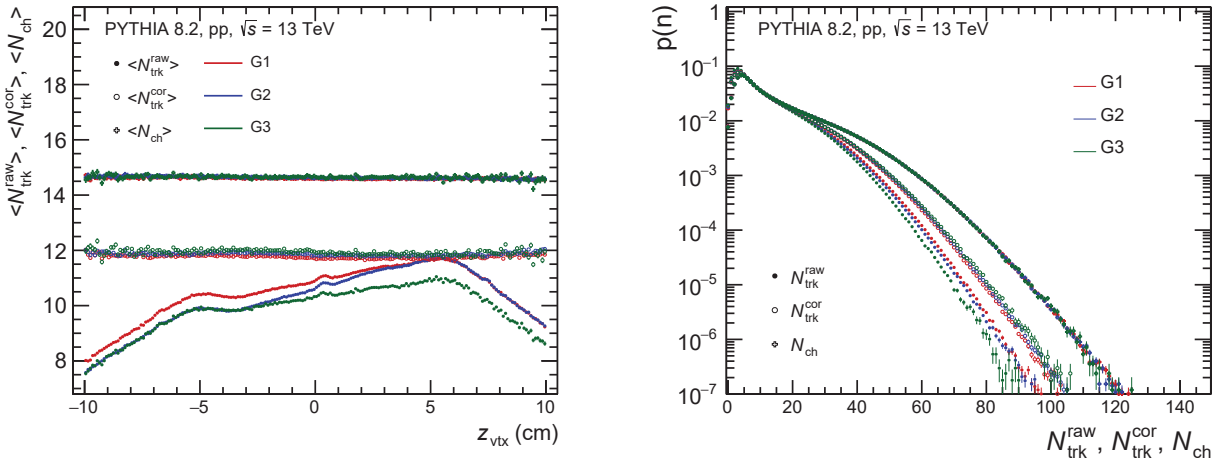

Figure 4.8: Left: the average number of tracklet and charged-particle multiplicity $\langle N_{\rm trk}^{\rm raw}\rangle$, $\langle N_{\rm trk}^{\rm cor}\rangle$ and $\langle N_{\rm ch}\rangle$ as a function of $z_{\rm vtx}$; Right: probability distributions of $N_{\rm trk}^{\rm raw}$, $N_{\rm trk}^{\rm cor}$ and $N_{\rm ch}$, in MC.

4.2.2 $N_{\rm ch}$–$N_{\rm trk}^{\rm cor}$ correlation factor evaluation

Once the number of reconstructed tracklet is corrected for the detector inefficiencies, one can try to estimate the corresponding number of primary charged particles corresponding to the tracklets reconstructed in the event. This estimation must take into account that the production of secondary particles, either coming from the decay of primary particles or their interaction with the detector volumes, leads to a difference between the number of reconstructed tracklets and the number of primary charged particles ($N_{\rm ch}$), as detailed in Ref. [143]. The correlation between the corrected tracklet multiplicity $N_{\rm trk}^{\rm cor}$ and the number of generated primary charged particles $N_{\rm ch}$ has been studied [84] using Monte Carlo (MC) simulations based on the PYTHIA 8.2 [91] event generator. The propagation of the simulated particles in the detector apparatus, a crucial step to describe secondary particle production, is performed with GEANT 3 [144], followed by the same reconstruction procedure as for real data. Once the $N_{\rm ch}$ distribution is found, the self-normalized multiplicity is defined as the ratio of the charged-particle multiplicity density in the analysis multiplicity interval, $\mathrm{d}N_{\rm ch}/\mathrm{d}\eta$, to the average one:

$$\frac{\mathrm{d}N_{\rm ch}/\mathrm{d}\eta}{\langle \mathrm{d}N_{\rm ch}/\mathrm{d}\eta\rangle_{\rm INEL>0}} = \frac{f(\langle N_{\rm trk}^{\rm cor}\rangle)}{\Delta\eta \times \langle \mathrm{d}N_{\rm ch}/\mathrm{d}\eta\rangle_{\rm INEL>0}}, \tag{4.3}$$

where $\Delta\eta = 2$ is the width of the pseudorapidity region considered for the measurement of the charged-particle multiplicity. The average charged particle multiplicity $\langle \mathrm{d}N_{\rm ch}/\mathrm{d}\eta\rangle$, for the pp collisions at $\sqrt{s} = 13$ TeV [145], is found to be 7.02 ± 0.11 (1.6% syst.). The function $f(\langle N_{\rm trk}^{\rm cor}\rangle)$ is used to parametrize the correlation between $N_{\rm trk}^{\rm cor}$ and $N_{\rm ch}$.

Correlation between $N_{\rm trk}^{\rm cor}$ and $N_{\rm ch}$

According to Eq. 4.3, the charged-particle multiplicity density in the analysis multiplicity interval, $\mathrm{d}N_{\rm ch}/\mathrm{d}\eta$, can be expressed as

$$\frac{\mathrm{d}N_{\mathrm{ch}}}{\mathrm{d}\eta} = \frac{\langle N_{\mathrm{ch}} \rangle}{\Delta\eta} = \frac{f(\langle N_{\mathrm{trk}}^{\mathrm{cor}} \rangle)}{\Delta\eta} \tag{4.4}$$

The function $f(\langle N_{\mathrm{trk}}^{\mathrm{cor}} \rangle)$, defined as an ad-hoc polynomial (see Appendix A.3) parametrizes the correlation between $N_{\mathrm{trk}}^{\mathrm{cor}}$ and N_{ch} in the full $N_{\mathrm{trk}}^{\mathrm{cor}}$ range, as shown in Fig. 4.9. The $\langle N_{\mathrm{ch}} \rangle$ values corresponding to the various $N_{\mathrm{trk}}^{\mathrm{cor}}$ intervals (taken from Ref. [80]) considered for the analysis, are reported in Tab. 4.2.

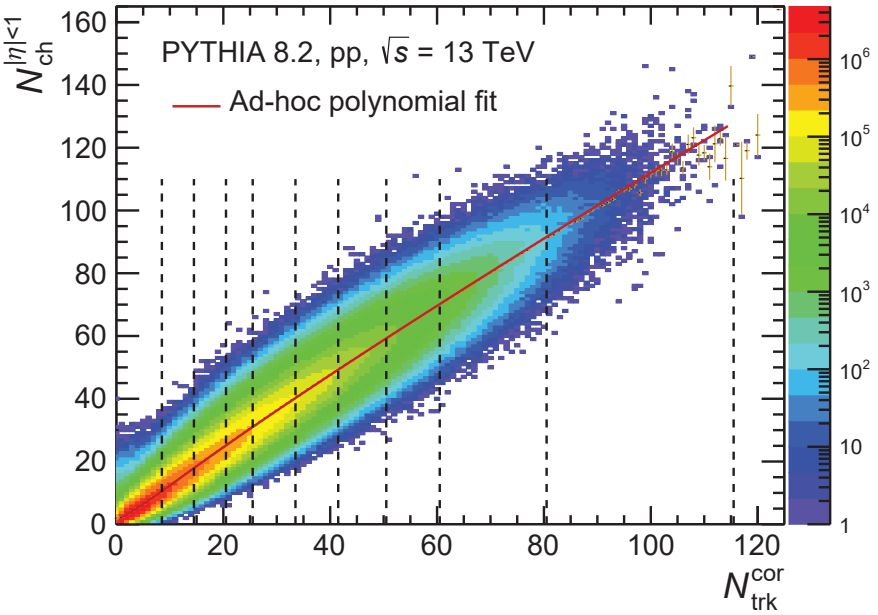

Figure 4.9: $N_{\mathrm{ch}} - N_{\mathrm{trk}}^{\mathrm{cor}}$ correlation map fitted with an ad-hoc polynominal function.

$N_{\mathrm{trk}}^{\mathrm{cor}}$ range	$\langle N_{\mathrm{ch}} \rangle$
$[1, 8]$	5.610 ± 0.000
$[9, 14]$	13.886 ± 0.000
$[15, 20]$	21.258 ± 0.001
$[21, 25]$	27.889 ± 0.001
$[26, 33]$	35.112 ± 0.001
$[34, 41]$	44.189 ± 0.001
$[42, 50]$	53.487 ± 0.002
$[51, 60]$	63.682 ± 0.004
$[61, 80]$	76.744 ± 0.011
$[21, 33]$	31.384 ± 0.001

Table 4.2: $\langle N_{\mathrm{ch}} \rangle$ measurement in the corrected tracklet multiplicity classes. The uncertainty quoted in this table is from the fit.

4.2.3 Systematic uncertainty on charged-particle multiplicity

The systematic uncertainty on the self-normalized charged-particle multiplicity $\mathrm{d}N_{\mathrm{ch}}/\mathrm{d}\eta/\langle \mathrm{d}N_{\mathrm{ch}}/\mathrm{d}\eta \rangle$ contains four contributions, detailed in Tab. 4.3: the calculation of $\langle N_{\mathrm{ch}} \rangle$ in each multiplicity interval; the fitting functions used

to parametrize the correlation between the tracklets and the charged-particle multiplicities; the charged-particle multiplicity averaged over all $\mathrm{INEL} > 0$ events ($\langle \mathrm{d}N_{\mathrm{ch}}/\mathrm{d}\eta \rangle$) and a correction to account for the vertex quality selection, affecting only the first multiplicity bin, $\epsilon^{1}_{\mathrm{INEL}>0,\ \langle N_{\mathrm{ch}} \rangle}$.

The systematic uncertainties for the calculation of the $\langle N_{\mathrm{ch}} \rangle$ come from the residual dependence of $\langle N_{\mathrm{ch}} \rangle$ on z_{vtx}, the dependence on the specific MC simulations, and the data-driven correction to the input profiles. The systematic uncertainty on the correlation encoded in the function f (ad-hoc polynominal function), introduced in Eq. 4.4, is estimated by varying the z_{vtx} range ([-10, -5], [-5, 0], [0, 5], [5, 10], and [-10, 10] cm) for the MC events considered for its optimization (the systematics corresponding to the choice of the analytical form of the f function is studied separately, in the following), as well as the event generators (PYTHIA 8.2 Monash 2013, and EPOS-LHC) used in the simulations. The reference profile of the number of tracklets as a function of z_{vtx} is also varied in the equalization procedure, considering both the profile obtained from the data and the one from the MC (PYTHIA 8.2 or EPOS-LHC). The multiplicity $\langle N_{\mathrm{ch}} \rangle$ is calculated as the average, and its systematic uncertainty as the standard deviation, of the distribution of the N_{ch} values obtained by considering the combined options described above. The resulting systematic uncertainty on $\langle N_{\mathrm{ch}} \rangle$ ranges within 0.4–2%, depending on the multiplicity class (more details see Appendix A.4.1).

To estimate the systematic uncertainty coming from the specific choice of the f function, the correlation between the tracklets and the charged-particle multiplicities is also studied with a linear fit function ($N_{\mathrm{ch}} = \alpha \times N^{\mathrm{cor}}_{\mathrm{trk}}$), on top of the polynomial approach described above, both globally (for the whole multiplicity range) and separately in the specific multiplicity intervals considered in the analysis. The α factors and their uncertainties are computed by applying the same procedure as for the polynomial fit. In each multiplicity class, the difference originating by the usage of either the global or the bin-by-bin α factor is considered as an additional systematic uncertainty on the self-normalized multiplicity, "$N^{\mathrm{cor}}_{\mathrm{trk}}$ vs N_{ch} non-linearity" in Table 4.3, amounting to $0.14-7$%, depending on the multiplicity class (more details see Appendix A.4.2).

$\langle \mathrm{d}N_{\mathrm{ch}}/\mathrm{d}\eta \rangle$ represents the charged-particle multiplicity averaged over all $\mathrm{INEL} > 0$ events. The value and its systematic uncertainty (1.6%) are taken from an independent analysis [145].

In addition, the lowest multiplicity class is affected by the vertex quality selection, which removes very-low-multiplicity events. This effect is accounted for by dividing the $\langle N_{\mathrm{ch}} \rangle$ value extracted for the first multiplicity interval by a correction factor $\epsilon^{1}_{\mathrm{INEL}>0,\ \langle N_{\mathrm{ch}} \rangle}$ (1.039), introducing an associated systematic uncertainty of 0.3%. The efficiency of the $\mathrm{INEL} > 0$ event selection, for any multiplicity class other than the lowest one is close to unity, and has negligible uncertainty (more details see Appendix A.4.4). All the aforementioned systematic uncertainties are added in quadrature and summarized in Table 4.3. Whenever the source has a dependence on multiplicity, the minimum and maximum uncertainties are indicated.

Source	%
$\langle N_{\rm ch}\rangle$	$0.4-2$
$N_{\rm trk}^{\rm cor}$ vs. $N_{\rm ch}$ non-linearity	$0.14-7$
$\langle {\rm d}N_{\rm ch}/{\rm d}\eta\rangle^*$	1.6
$\varepsilon^1_{{\rm INEL}>0,\ \langle N_{\rm ch}\rangle}$	0.3
${\rm d}N_{\rm ch}/{\rm d}\eta/\langle {\rm d}N_{\rm ch}/{\rm d}\eta\rangle$	$1.7-7$

Table 4.3: Summary of the systematic uncertainty sources in percentage on the self-normalized multiplicity. When the systematic uncertainty depends on the multiplicity class, the corresponding range is given. The quantity labelled with * is taken from an independent analysis [145]. All the mentioned systematic uncertainties are added in quadrature to the self-normalized multiplicity.

$N_{\rm trk}^{\rm cor}$	$\frac{{\rm d}N_{\rm ch}/{\rm d}\eta}{\langle {\rm d}N_{\rm ch}/{\rm d}\eta\rangle}$
$1-8$	0.38 ± 0.03
$9-14$	0.99 ± 0.02
$15-20$	1.51 ± 0.03
$21-25$	1.99 ± 0.04
$21-33$	2.24 ± 0.04
$26-33$	2.51 ± 0.04
$34-41$	3.16 ± 0.07
$42-50$	3.8 ± 0.1
$51-60$	4.5 ± 0.2
$61-80$	5.5 ± 0.3

Table 4.4: List of the event classes considered in the analysis, defined in terms of the $N_{\rm trk}^{\rm cor}$ measured in the SPD ($|\eta|<1$). For each event class, the average self-normalized charged-particle multiplicity is indicated together with its systematic uncertainty (statistical uncertainties are negligible).

4.2.4 Self-normalized charged-particle multiplicity

The self-normalized multiplicity in each $N_{\rm trk}^{\rm cor}$ interval is computed by using Eq. 4.5:

$$\frac{{\rm d}N^i_{\rm ch}/{\rm d}\eta}{\langle {\rm d}N_{\rm ch}/{\rm d}\eta\rangle} = \frac{\langle N_{\rm ch}\rangle^i}{\langle dN_{\rm ch}/d\eta\rangle \times \Delta\eta \times \varepsilon^i_{{\rm INEL}>0,\langle N_{\rm ch}\rangle}}\ , \tag{4.5}$$

where $\varepsilon^i_{{\rm INEL}>0,\langle N_{\rm ch}\rangle}$ is the correction factor for ${\rm INEL}>0$ selection in the $i^{\rm th}$ selected corrected tracklet multiplicity class. This value was checked to be negligible for all the multiplicity classes except for the first multiplicity class, $\varepsilon^1_{{\rm MB,INEL}>0,\langle N_{\rm ch}\rangle}$ = 1.039 $\pm$ 0.003 (0.3% syst.). Finally, the statistical uncertainty is calculated by a squared sum of all the terms in Eq. 4.5. The systematical uncertainty is computed by a squared sum of all contributions in Table 4.3. The final values are presented in Table 4.4.

Chapter 5

Υ production as a function of multiplicity

5.1 Analysis strategy

The self-normalized yield of Υ, i.e. the yield in a given multiplicity class i normalized to the multiplicity-integrated value, is evaluated as:

$$\frac{\mathrm{d}N^{i}_{\Upsilon}/\mathrm{d}y}{\langle \mathrm{d}N_{\Upsilon}/\mathrm{d}y \rangle} = \frac{N^{i}_{\Upsilon}}{N_{\Upsilon}} \times \frac{N^{\mathrm{eq}}_{\mathrm{MB}}}{N^{\mathrm{eq},i}_{\mathrm{MB}}} \times \frac{(A \times \varepsilon)_{\Upsilon}}{(A \times \varepsilon)^{i}_{\Upsilon}} \times \frac{\varepsilon^{i}_{\mathrm{MB}}}{\varepsilon_{\mathrm{MB}}} \times \frac{\varepsilon_{\Upsilon}}{\varepsilon^{i}_{\Upsilon}}, \tag{5.1}$$

where N_{Υ} and $N^{\mathrm{eq}}_{\mathrm{MB}}$ are the number of reconstructed Υ candidates and the equivalent number of MB events for the dimuon-triggered sample analyzed, respectively. The ratio $N^{\mathrm{eq},i}_{\mathrm{MB}}/N^{\mathrm{eq}}_{\mathrm{MB}}$ is the fraction of the MB cross section corresponding to multiplicity class i, and is calculated from the MB-triggered sample, as $N^{i}_{\mathrm{MB}}/N_{\mathrm{MB}}$, as detailed in Ref. [80]. The $A \times \varepsilon$ correction for N_{Υ} is independent of multiplicity in the measured intervals, therefore, this factor cancels out for the self-normalized yield measurement. The $1/\varepsilon_{\mathrm{MB}}$ (or $1/\varepsilon^{i}_{\mathrm{MB}}$) and $1/\varepsilon_{\Upsilon}$ (or $1/\varepsilon^{i}_{\Upsilon}$) factors are meant to account for the possible event and signal losses due to the event selections.

5.2 Signal extraction

5.2.1 Υ yields in the dimuon-triggered sample

The number of Υ mesons in the selected multiplicity class is extracted from a log-likelihood binned fit to the invariant mass ($m_{\mu^+\mu^-}$) distribution. In the integrated multiplicity class, the fit is performed modeling the 2-body decay peaks of the three Υ(1S), Υ(2S), and Υ(3S) states with three CB2 functions with fixed tail parameters, and three alternative parametrizations of the underlying continuum background, namely a variable-width Gaussian (VWG) [146], the product of two exponentials, or the product of an exponential and a power law function; and three alternative invariant mass fit ranges — [6, 13], [5, 14], and [7, 12] GeV/c^2. The distribution of the corresponding results is shown in Fig. 5.1. In addition, when extracting the signal in multiplicity classes, the Υ(1S) mean mass

and width, extracted from the multiplicity-integrated fit, are varied within their uncertainties. The mass and the width of the Υ(2S) and Υ(3S) fixed to the ones of the Υ(1S) according to the ratio between the mass-pole parameters reported in the PDG (as described in Eq. 3.3 and 3.4). More details of the fit procedure has been explained in Section 3.2.3. The raw number of the Υ(1S) in the integrated-multiplicity class with various combined fit options is shown in Fig. 5.2. Last but not least, the last control variable, the signal significance, which is typically expressed in terms of the number of standard deviations (σ) above the background fluctuation, is discussed. A significance at 3σ is defined as:

$$\Sigma_{3\sigma}^{\Upsilon(\mathrm{nS})} = \mathrm{S}/\sqrt{\mathrm{S}+\mathrm{B}}\Big|_{3\sigma}^{\Upsilon(\mathrm{nS})}$$

where S represents the integral of the fitted signal function over the invariant mass interval $[\mu - 3\sigma, \mu + 3\sigma]$, and B represents the integral of the fitted background function over the same interval.

With this definition, the significance is used to validate the choice of boundaries for the intervals in terms of corrected tracklet multiplicity. If the significance of the Υ(nS) (n=1, 2 or 3) signal is too low in a particular interval, it would imply that it is not possible to reliably extract a signal in that interval. In such cases, the fitting tests would fail to converge, indicating the inability to distinguish the signal from the background. In this analysis, considering the significance condition ($\Sigma_{3\sigma}^{\Upsilon(\mathrm{nS})} > 3$, n=1, 2 or 3) for each Υ state in the selected multiplicity interval, the highest $N_{\mathrm{trk}}^{\mathrm{cor}}$ intervals in which the measurement is significant are $[61, 80]$ for Υ(1S) and Υ(2S) and $[21, 33]$ for Υ(3S). The raw number of Υ(1S), Υ(2S) and Υ(3S) are then reported in Tab. 5.1.

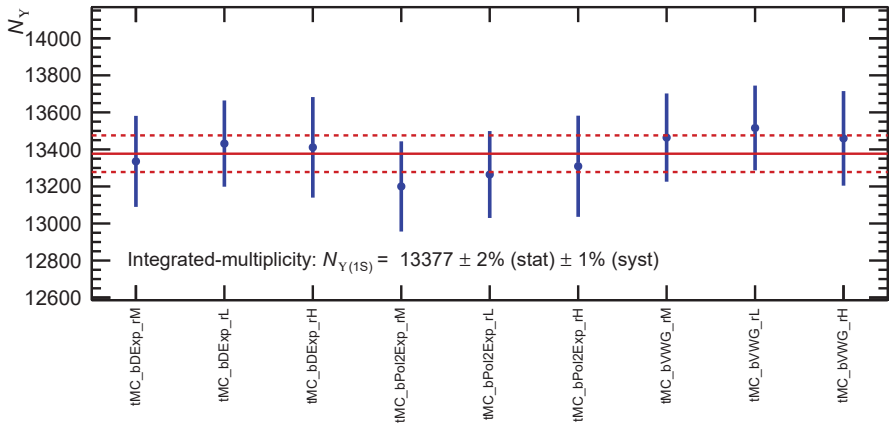

Figure 5.1: Raw number of Υ(1S) in the integrated-multiplicity class with various combined options. The solid line is the central value and the dashed lines show the 1σ deviation to the central value, which is the systematic uncertainty for the signal extraction in the multiplicity classes.

The raw yield ratio of N_Υ^i/N_Υ for each multiplicity class i is computed with all variations of three background shapes — a VWG, the product of two exponentials, and the product of an exponential and a power law function — and three alternative invariant mass fit ranges — [6, 13], [5, 14], and [7, 12] GeV/c^2, which are combined for the same set of tail parameters, σ and mass. The corresponding systematic uncertainty, are calculated as the average

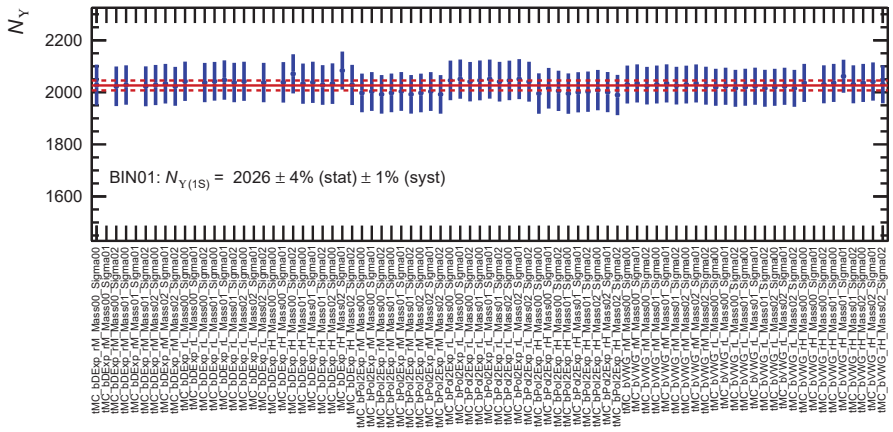

Figure 5.2: Raw number of Υ(1S) in the multiplicity class $[1, 8]$ with various combined options. The solid line is the central value and the dashed lines show the 1σ deviation to the central value.

$N_{\rm trk}^{\rm cor}$ range	$N_{\Upsilon(1S)} \pm \text{stat}(\%) \pm \text{syst}(\%)$	$N_{\Upsilon(2S)} \pm \text{stat}(\%) \pm \text{syst}(\%)$	$N_{\Upsilon(3S)} \pm \text{stat}(\%) \pm \text{syst}(\%)$
Integrated	$13377 \pm 2 \pm 1$	$3728 \pm 5 \pm 1$	$1513 \pm 10 \pm 5$
$[1, 8]$	$2032 \pm 4 \pm 1$	$558 \pm 11 \pm 2$	$318 \pm 17 \pm 5$
$[9, 14]$	$2358 \pm 4 \pm 1$	$592 \pm 12 \pm 3$	$353 \pm 18 \pm 7$
$[15, 20]$	$2266 \pm 4 \pm 3$	$595 \pm 12 \pm 5$	$419 \pm 16 \pm 7$
$[21, 25]$	$1723 \pm 4 \pm 2$	$521 \pm 12 \pm 3$	–
$[21, 33]$	$3923 \pm 3 \pm 1$	$1176 \pm 8 \pm 2$	$283 \pm 30 \pm 12$
$[26, 33]$	$2187 \pm 4 \pm 3$	$651 \pm 11 \pm 4$	–
$[34, 41]$	$1331 \pm 5 \pm 1$	$380 \pm 15 \pm 2$	–
$[42, 50]$	$787 \pm 7 \pm 2$	$139 \pm 30 \pm 7$	–
$[51, 60]$	$353 \pm 10 \pm 4$	$144 \pm 19 \pm 5$	–
$[61, 80]$	$156 \pm 15 \pm 6$	$56 \pm 33 \pm 7$	–

Table 5.1: Raw number of Υ(nS) in the corrected tracklet multiplicity classes. The "–" quoted in the table means that the significance in the corresponding multiplicity class is too small (< 3) and the signal is not measured.

and the standard deviation of the results corresponding to the various options considered for the signal extraction, as shown in Fig. 5.3. The results are also reported in Tab. 5.2.

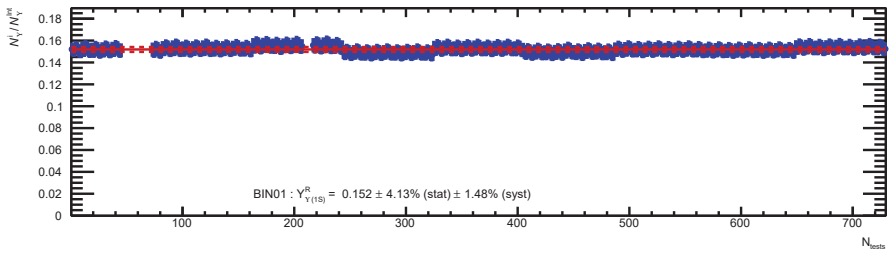

Figure 5.3: Raw yield ratio of $N^{1}_{\Upsilon(1S)}/N_{\Upsilon(1S)}$ in the first multiplicity class, corresponding to $[1, 8]$, with various combined options: three background shapes — a VWG, the product of two exponentials, and the product of an exponential and a power law function; and three alternative invariant mass fit ranges — [6, 13], [5, 14], and [7, 12] GeV/c^2, which are combined for the same set of tail parameters, σ and mass. The solid line is the central value and the dashed line means 1σ deviation to the central value, which is the systematic uncertainty for the signal extraction.

$\mathrm{Multi.Class}(i)$	$N^{\mathrm{cor}}_{\mathrm{trk}}$ range	$\frac{N^{i}_{\Upsilon(1S)}}{N_{\Upsilon(1S)}} \pm \mathrm{stat}(\%) \pm \mathrm{syst}(\%)$	$\frac{N^{i}_{\Upsilon(2S)}}{N_{\Upsilon(2S)}} \pm \mathrm{stat}(\%) \pm \mathrm{syst}(\%)$	$\frac{N^{i}_{\Upsilon(3S)}}{N_{\Upsilon(3S)}} \pm \mathrm{stat}(\%) \pm \mathrm{syst}(\%)$
1	$[1, 8]$	$0.152 \pm 4 \pm 1$	$0.150 \pm 12 \pm 3$	$0.211 \pm 20 \pm 7$
2	$[9, 14]$	$0.176 \pm 4 \pm 2$	$0.159 \pm 12 \pm 3$	$0.234 \pm 21 \pm 9$
3	$[15, 20]$	$0.169 \pm 4 \pm 3$	$0.160 \pm 13 \pm 5$	$0.278 \pm 19 \pm 9$
4	$[21, 25]$	$0.129 \pm 5 \pm 2$	$0.140 \pm 13 \pm 3$	–
$4 + 5$	$[21, 33]$	$0.293 \pm 4 \pm 1$	$0.315 \pm 9 \pm 2$	$0.187 \pm 32 \pm 13$
5	$[26, 33]$	$0.164 \pm 4 \pm 3$	$0.175 \pm 12 \pm 4$	–
6	$[34, 41]$	$0.100 \pm 5 \pm 2$	$0.102 \pm 15 \pm 3$	–
7	$[42, 50]$	$0.059 \pm 7 \pm 2$	$0.037 \pm 30 \pm 7$	–
8	$[51, 60]$	$0.026 \pm 10 \pm 4$	$0.039 \pm 20 \pm 5$	–
9	$[61, 80]$	$0.012 \pm 15 \pm 6$	$0.015 \pm 34 \pm 7$	–

Table 5.2: Raw yield ratio of $\frac{N^{i}_{\Upsilon(nS)}}{N_{\Upsilon(nS)}}$ in the corrected tracklet multiplicity classes. The "–" quoted in the table means that the significance in the corresponding multiplicity class is too small (< 3) and the signal is not measured.

5.2.2 Υ yields in the corresponding MB-triggered sample

The dimuon-triggered sample is used to measure Υ(nS) states in dimuon decay channel. To calculate the corresponding Υ(nS) yields in MB-triggered sample, the equivalent number of MB events ($N^{\mathrm{eq}}_{\mathrm{MB}}$) for the dimuon-triggered sample is calculated. The ratio $N^{\mathrm{eq},i}_{\mathrm{MB}}/N^{\mathrm{eq}}_{\mathrm{MB}}$ is the fraction of the MB cross section corresponding to multiplicity class i and integrated-multiplicity class. It has been verified that this ratio can be directly calculated from the MB-triggered sample, as $N^{i}_{\mathrm{MB}}/N_{\mathrm{MB}}$ (more details see Ref. [80]), resulting in a negligible difference (0.02%) with respect to the approach considered in the present analysis.

Multi.Class(i)	$N_{\rm trk}^{\rm cor}$ range	$\frac{N_{\rm MB}}{N_{\rm MB}^i}$
1	$[1, 8]$	2.08
2	$[9, 14]$	5.10
3	$[15, 20]$	8.28
4	$[21, 25]$	15.37
$4 + 5$	$[21, 33]$	7.93
5	$[26, 33]$	16.39
6	$[34, 41]$	34.17
7	$[42, 50]$	71.36
8	$[51, 60]$	182.95
9	$[61, 80]$	482.68

Table 5.3: $\frac{N_{\rm MB}}{N_{\rm MB}^i}$ in the multiplicity classes.

5.3 Event selection efficiency correction

The MB-triggered events used in this analysis are considered with the vertex quality selection (vertex QA), see Section 4.1. In order to obtain the Υ(nS) production rate in $\rm INEL > 0$ collisions, the efficiency of the applied vertex QA and MB trigger efficiency for $\rm INEL > 0$ selection have been taken into account. The event selection efficiency correction ($\varepsilon_{\rm MB}$), entering Eq. 5.1, includes contributions from vertex QA ($\varepsilon_{\rm vtx,QA}$), the MB trigger efficiency for $\rm INEL > 0$ selection ($\varepsilon_{\rm MB,INEL>0}$), and pileup rejection ($\varepsilon_{\rm pu}$), as in Ref. [80]. Finally, it is worth noticing that the integrated number of MB events includes events with zero tracklets ($\rm INEL = 0$ events): to remove this contamination, a specific correction factor ($\varepsilon_{\rm INEL=0}$) is applied, as estimated from MC simulations. Finally, Eq. 5.1 can be expressed as Eq. 5.2.

$$\frac{{\rm d}N_{\Upsilon}^i/{\rm d}y}{\langle {\rm d}N_{\Upsilon}/{\rm d}y\rangle} = \frac{N_{\Upsilon}^i}{N_{\Upsilon}} \times \frac{N_{\rm MB}}{N_{\rm MB}^i} \times \varepsilon_{\rm vtx,QA} \times \frac{\varepsilon_{\rm MB,INEL>0}^i}{\varepsilon_{\rm MB,INEL>0}} \times \frac{1}{\varepsilon_{\rm INEL=0}} \times \varepsilon_{\rm pu} \tag{5.2}$$

5.3.1 Vertex quality selection

The number of MB-trigger events and the number of Υ(nS) with or without using vertex QA, associated with the efficiencies, are reported in Tab. 5.4. The vertex QA efficiency, due to the vertex cuts for MB events and Υ signals, is then defined as Eq. 5.3 in the integrated-multiplicity class.

	With vertex QA	Without vertex QA	ε
$N_{\rm MB}$	$1.18866e+08$	$1.26572e+08$	0.94 ± 0.00
$N_{\Upsilon(1S)}$	13840 ± 244	14266 ± 239	0.97 ± 0.02
$N_{\Upsilon(2S)}$	3857 ± 174	3938 ± 173	0.98 ± 0.06
$N_{\Upsilon(3S)}$	1760 ± 157	1844 ± 159	0.95 ± 0.12

Table 5.4: The number of MB-triggered events and the number of Υ(nS) in the integrated-multiplicity class.

$$\varepsilon_{\mathrm{vtx,QA}} = \frac{(N_{\Upsilon}/N_{\mathrm{MB}})_{\mathrm{w/\ vertex\ QA}}}{(N_{\Upsilon}/N_{\mathrm{MB}})_{\mathrm{w/o\ vertex\ QA}}} \tag{5.3}$$

The computed values are: $\varepsilon^{\Upsilon(1S)}_{\mathrm{vtx,QA}} = 1.03 \pm 0.03\ (\mathrm{stat.})$, $\varepsilon^{\Upsilon(2S)}_{\mathrm{vtx,QA}} = 1.02 \pm 0.07\ (\mathrm{stat.})$, $\varepsilon^{\Upsilon(3S)}_{\mathrm{vtx,QA}} = 1.02 \pm 0.13\ (\mathrm{stat.})$.

5.3.2 MB trigger efficiency correction

The MB trigger efficiency ($\varepsilon_{\mathrm{MB,INEL>0}}$) is close to unity for all the multiplicity classes, except for the lowest and the integrated classes: this effect must be taken into account since it affects the corresponding Υ yields. The correction factor for the lowest multiplicity class has been calculated as Eq. 5.4.

$$\varepsilon^{1}_{\mathrm{MB,INEL>0,yield}} = \frac{N_{\mathrm{events}}(N_{\mathrm{ch}} \geq 1 + \mathrm{vertex\ QA} + \mathrm{MB\ trigger})}{N_{\mathrm{events}}(N_{\mathrm{ch}} \geq 1 + \mathrm{vertex\ QA})} \tag{5.4}$$

In the lowest multiplicity, the calculated value with associated systematic uncertainty is $\varepsilon^{1}_{\mathrm{MB,INEL>0,yield}} = 0.914 \pm 0.008\ (1.0\%)$. In the integrated multiplicity class, the correction factor is $\varepsilon_{\mathrm{MB,INEL>0}} = 0.95 \pm 0.005\ (0.5\%)$ (see Appendix A.4.3).

Event generator	$N_{\mathrm{events}}\ (N_{\mathrm{ch}} \geq 1 + \mathrm{vertex\ QA} + \mathrm{MB\ trigger})$	$N_{\mathrm{events}}\ (N_{\mathrm{ch}} \geq 1 + \mathrm{vertex\ QA})$	$\varepsilon^{1}_{\mathrm{MB,INEL>0,yield}}$
PYTHIA 8.2	$1.0607e+08$	$1.17045e+08$	0.906
EPOS − LHC	$2.06606e+07$	$2.24057e+07$	0.922

Table 5.5: Efficiency for MB-triggered event correction in the lowest multiplicity class in MC simulations.

5.3.3 Correction for the contamination from MB INEL = 0 events

A strict MB trigger $\mathrm{INEL} > 0$ condition can only be applied on MC samples, while the data sample includes a contamination of $\mathrm{INEL} = 0$ events. In addition, the efficiency correction of vertex QA, obtained from data (fraction of Υ(nS) states and MB events rejected, see Sec. 5.3.1), will reintroduce any contamination that was rejected. Therefore, the correction for the contamination effect has been computed together with the one on the vertex QA. The calculated contamination value from MC is:

Contamination without vertex QA:

$$f_1 = \frac{N_{\mathrm{events}}(\mathrm{INEL} = 0 + \mathrm{MB\ trigger})}{N_{\mathrm{events}}(\mathrm{INEL} \geq 0 + \mathrm{MB\ trigger})} = 2\% \tag{5.5}$$

or:

Contamination with vertex QA:

$$f_2 = \frac{N_{\text{events}}(\text{INEL} = 0 + \text{MB trigger} + \text{vtx, QA})}{N_{\text{events}}(\text{INEL} \geq 0 + \text{MB trigger} + \text{vtx, QA})} = 0.8\% \tag{5.6}$$

From these values, there are two methods used to correct for the vertex QA and the contamination, starting from the number of MB in data after MB-trigger and vertex QA, which corresponds to $N_{\text{data}} = N_{\text{INEL}\geq 0+\text{MB trigger+vtx,QA}}$.

1. Correct for vertex QA from data first and then correct for the contamination w/o vertex QA (Method 1):

$$N_{\text{data}} * \frac{N_{\text{INEL}\geq 0+\text{MB trigger}}}{N_{\text{INEL}\geq 0+\text{MB trigger+vtx,QA}}} * (1 - \frac{N_{\text{INEL}=0+\text{MB trigger}}}{N_{\text{INEL}\geq 0+\text{MB trigger}}}) = N_{\text{data}} * \frac{1}{\varepsilon_{\text{vtx,QA}}^{\text{MB,Data}}} * (1 - f_1) = N_{\text{data}} * 1.04$$

2. Correct for the contamination with vertex QA first and then correct for vertex QA from MC (Method 2):

$$N_{\text{data}} * (1 - \frac{N_{\text{INEL}=0+\text{MB trigger+vtx,QA}}}{N_{\text{INEL}\geq 0+\text{MB trigger+vtx,QA}}}) * \frac{N_{\text{INEL}>0+\text{MB trigger}}}{N_{\text{INEL}>0+\text{MB trigger+vtx,QA}}} = N_{\text{data}} * (1 - f_2) * \frac{1}{\varepsilon_{\text{vtx,QA}}^{\text{MB,MC}}} = N_{\text{data}} * 1.03$$

The vertex QA MB triggered efficiencies from data and MC are respectively: $\varepsilon_{\text{vtx,QA}}^{\text{MB,Data}} = 0.94$, $\varepsilon_{\text{vtx,QA}}^{\text{MB,MC}} = 0.96$ (MC: refers to PYTHIA 8 generator).

For both cases, the small vertex QA effect on Υ should also be corrected for, as is currently done in the analysis (Section 5.3.1). Since so far the vertex QA correction is extracted from data, the first method, correcting for the contamination after vertex QA correction is considered. The contamination $\text{INEL} = 0$ correction efficiency is: $\varepsilon_{\text{INEL}=0} = \frac{1}{1-f_1} = 1.02$. In this case, the vertex QA correction used so far in the analysis will not change.

The difference between the two methods (Method 1 vs 2) should be added to the systematic uncertainty on the integrated yield. From the results above, it is 1%. And there is 1% difference between the two MC generators (PYTHIA 8 vs. EPOSLHC). The final correction efficiency for contamination $\text{INEL} = 0$ with associated systematic uncertainty is: $\varepsilon_{\text{INEL}=0} = 1.02 \pm 0.02$ (2%).

5.3.4 Efficiency for pileup rejection

The pileup efficiency factor was found to be close to unity in multiplicity bins, resulting in a negligible effect on the final results, as details in Ref. [147].

5.4 Systematic uncertainty on the self-normalized Υ yields

The systematic uncertainty on the self-normalized Υ(nS) yield includes four contributions, as summarized in Table 5.6. The raw yield ratio of $N_{\Upsilon}^{i}/N_{\Upsilon}$ for each multiplicity class i, and the corresponding systematic uncertainty, are calculated as the average and the standard deviation of the results corresponding to the various options considered

for the signal extraction. The MB trigger efficiency ($\varepsilon_{\mathrm{MB,INEL>0}}$) affects the Υ yields of the lowest and the integrated multiplicity classes with an associated systematic uncertainty of 1% ($\varepsilon^{1}_{\mathrm{MB,INEL>0,yield}}$) and 0.5% ($\varepsilon_{\mathrm{MB,INEL>0}}$), respectively. The contamination efficiency factor $\varepsilon_{\mathrm{MB,INEL=0}}$, mentioned above, is characterized by an associated systematic uncertainty of 2%, while the systematic uncertainty for the vertex quality correction ($\varepsilon_{\mathrm{vtx}}$) and the pileup rejection ($\varepsilon_{\mathrm{pu}}$) are both found to be negligible. All the aforementioned systematic uncertainties are added in quadrature in the final results.

Source	%
$N^{i}_{\Upsilon(1\mathrm{S})}/N_{\Upsilon(1\mathrm{S})}$	$1-6$
$N^{i}_{\Upsilon(2\mathrm{S})}/N_{\Upsilon(2\mathrm{S})}$	$3-7$
$N^{i}_{\Upsilon(3\mathrm{S})}/N_{\Upsilon(3S)}$	$7-13$
$\varepsilon^{1}_{\mathrm{MB,INEL>0,yield}}$	1
$\varepsilon_{\mathrm{MB,INEL>0}}$	0.5
$\varepsilon_{\mathrm{MB,INEL=0}}$	2

Table 5.6: Summary of the systematic uncertainties for the self-normalized Υ yields. When the systematic uncertainty depends on the multiplicity class, the corresponding range is given.

5.5 Results and discussion

The self-normalized yields, $\mathrm{d}N_{\Upsilon}/\mathrm{d}y/\langle \mathrm{d}N_{\Upsilon}/\mathrm{d}y\rangle$, as a function of the self-normalized charged-particle multiplicity density, $\mathrm{d}N_{\mathrm{ch}}/\mathrm{d}\eta/\langle \mathrm{d}N_{\mathrm{ch}}/\mathrm{d}\eta\rangle$, for the three Υ(1S), Υ(2S), and Υ(3S) states, measured for the first time in pp collisions at $\sqrt{s} = 13$ TeV for $p_{\mathrm{T}} > 0$, are shown in Fig. 5.4. The bottom panel of Fig. 5.4 shows the double ratio of the self-normalized Υ yields to the self-normalized multiplicity: the almost linear scaling observed in the top panel of the figure results in a flat trend of the double ratios for the three states, within the current uncertainties. The measurements are compared with the available theoretical models as shown in Fig. 5.5. For multiplicities up to 4 times the mean multiplicity, no relevant difference is observed between the PYTHIA 8.2 configurations, including feed-down, with or without color reconnection (CR) which fairly describe the observed linear scaling. The implementation of the MPI mechanism corresponds to the simple scaling ($N_{\mathrm{MPI}} \propto N_{\mathrm{hard\ process}} \propto N_{\mathrm{ch}}$. The PYTHIA 8.2 color reconnection scenario is a final-state effect at play with MPI where strings are merged based on a QCD full color flow calculation with a loose modeling of dynamical effect via a global saturation [148]. CR might have an impact both on the charged particle multiplicity and the correlation to the produced hard probe. At larger multiplicities, PYTHIA 8.2 computations for the Υ(1S) deviate from the linear scaling, suggesting a weakening of the dependence of the self-normalized bottomonium yield on the charged-particle multiplicity for increasing values of the latter. Computations from coherent particle production (CPP) [86] are also displayed: in this framework, high-multiplicity hadronic colli-

sions are parameterized on equal footing regardless of the specific pp, p–A, or A–A system, allowing one to take into account features associated to nuclear effects. This is done by means of a phenomenological parameterization for mean multiplicities of light hadrons and quarkonia, assuming a linear dependence with the number of binary nucleon–nucleon interactions in p–A collisions. This model also takes into account the possible mutual boosting of the gluon densities and saturation scales in the colliding protons, induced by MPIs in a high-multiplicity environment, affecting the hard process production mechanisms (prompt production) [149]. The model is defined for $\mathrm{d}N_{\mathrm{ch}}/\mathrm{d}\eta/\langle\mathrm{d}N_{\mathrm{ch}}/\mathrm{d}\eta\rangle > 1$, corresponding to at least one nucleon–nucleon collision, therefore the model predictions and curves start at $\mathrm{d}N_{\mathrm{ch}}/\mathrm{d}\eta/\langle\mathrm{d}N_{\mathrm{ch}}/\mathrm{d}\eta\rangle > 1$. Its uncertainties are inherited from the experimental uncertainties of the p–A measurements used to extract the model parameters. The CPP computations qualitatively describe the observed behavior within the current large theoretical and experimental uncertainties. In the computation with the CGC approach of Ref. [88], the probability to produce charmonia and bottomonia increases via a sizeable contribution of the multipomeron mechanism and especially the 3-pomeron term. It is enhanced, at high energy, thanks to additional *t*-channel gluons due to the increased gluon densities. The 3-pomeron CGC computation overestimates the measured dependence of Υ(1S) for the highest multiplicities reached, while no firm conclusion can be established for the excited states due to the large experimental uncertainties. It has to be noted that, despite the recent progress in the simultaneous computation or modelization of the soft and the hard components of hadronic interactions, there is a general lack of predictions available for bottomonium studies, except the PYTHIA 8.2, CPP and CGC in the 3-pomeron approach computations considered in this thesis. In particular, at the time of writing, predictions concerning bottomonium production are neither available in EPOS [75], nor in the already cited percolation model [89]. Computations from CPP are not available for the Υ(3S) due to a lack of experimental measurements needed to extract the model parameters.

Figure 5.6 presents the Υ excited-to-ground state self-normalized yield ratios as a function of the self-normalized charged-particle multiplicity. A large fraction of the systematic uncertainties affecting the self-normalized yield of Υ(nS) states, dominated by signal extraction, cancels in the excited-to-ground state ratios (more details see Appendix A.5). The excited-to-ground state ratio of Υ(2S) to Υ(1S), shown in Fig. 5.6 (top panel), is compatible with unity within the current uncertainties up to six times the mean charged-particle multiplicity. The measurement is compared with computations from PYTHIA 8.2, predicting a ratio close to unity at high multiplicity, independently of the considered color reconnection scenario. Calculations from CPP and 3-pomeron CGC are also compatible with a ratio close to unity, within large uncertainties. The measurement is also compared with computations from the comover model [99, 100] in which quarkonia are dissociated by interactions with final-state comoving particles. Dissociation rate is linked to the binding energy of the considered quarkonium state, and to the comover density. This last parameter also determines the uncertainties of the model. Feed-down contributions are taken into account in the computation. A decrease of 20% to 40% over the covered multiplicity range is predicted by this approach for the Υ(2S)-to-Υ(1S) ratio. It is worth noting that the CMS experiment reports a decrease of the direct Υ(2S)-to-Υ(1S)

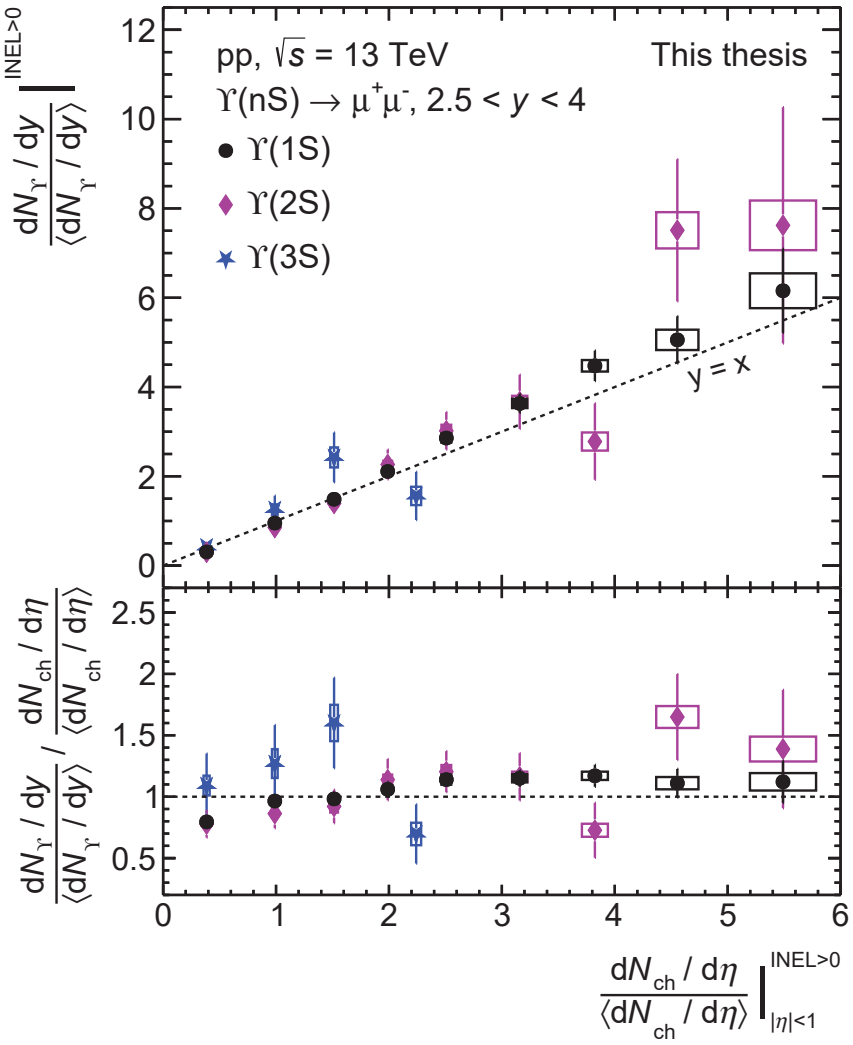

Figure 5.4: Self-normalized yield of Υ(nS) states as a function of the self-normalized charged-particle multiplicity for $p_{\mathrm{T}} > 0$ GeV/c. The error bars represent the statistical uncertainty on the Υ yields, while the quadratic sum of the point-by-point systematic uncertainties on the Υ yield as well as on $\mathrm{d}N_{\mathrm{ch}}/\mathrm{d}\eta$ / $\langle \mathrm{d}N_{\mathrm{ch}}/\mathrm{d}\eta \rangle$ is depicted as boxes. The dashed line shown in the top panel represents a linear function with the slope equal to unity.

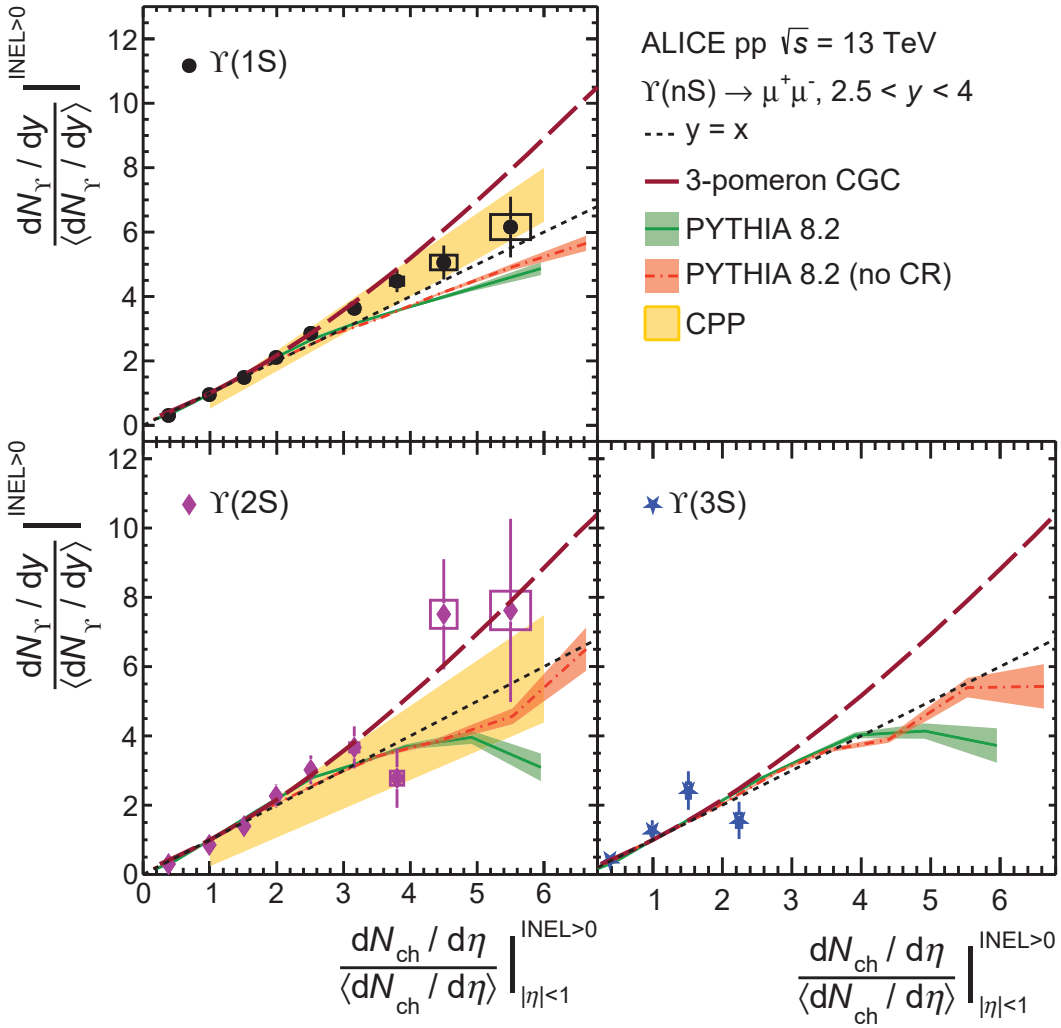

Figure 5.5: Self-normalized yield of Υ(nS) states as a function of the self-normalized charged-particle multiplicity for $p_{\mathrm{T}} > 0$ GeV/c, compared to 3-pomeron CGC approach [88], PYTHIA 8.2 [73] and CPP [86]. The dashed line represents a linear function with the slope equal to unity.

ratio as a function of the number of tracks when both quantities are measured in the central rapidity region in pp collisions at $\sqrt{s} = 2.76$ TeV [96] and 7 TeV [101]. On the contrary, when the measurement is performed with a rapidity gap between the Υ(nS) states ($|y| < 1.93$) and the transverse energy measurement as an estimator of event activity ($|\eta| > 4$), a much less pronounced decrease is observed in the ratio between the production yields of the two states [96]. Figure 5.6 (bottom panel) shows the excited-to-ground state ratio of Υ(3S) to Υ(1S). The measurement is compatible with unity within the large uncertainties and with the almost flat trend predicted by PYTHIA 8.2, regardless of the considered color reconnection scenario, and by 3-pomeron CGC computations. It is interesting to note that, on the contrary, the comover scenario predicts a dissociation of Υ(3S) states leading to a large suppression at high charged-particle multiplicity (~ 6 times the mean multiplicity). For the Υ(2S) and Υ(3S) states, the discrepancy between data and the predictions of the comover model amounts to 1.8 and 1.7 sigmas, at most. Firm conclusions on the presence or absence of a final state Υ dissociation due to comoving particles would require further investigation based on larger data samples. The ALICE collaboration reported excited-to ground state ratio in the charm sector: $\psi(2S)$-to-J/ψ ratio [83]. This ratio is found to be compatible with 1 with the current systematic and statistical uncertainties up to 6 times the mean multiplicity. The excited-to-ground state ratio in the charm and the beauty sector suggests no or small dependence of the measured correlation with the binding energy of the state.

Figure 5.7 (top panel) presents the results discussed in this thesis for the Υ(1S), Υ(2S), and Υ(3S), compared with other quarkonium measurements by ALICE, namely J/ψ measurements in the forward rapidity region at 5.02 TeV [80], 7 TeV [82], and 13 TeV [80], exploiting the same multiplicity estimator as in the present analysis (event classification based on the SPD tracklet multiplicity). A corresponding measurement is also available for the $\psi(2S)$ [83], showing a similar trend of the production yield with multiplicity as for the J/ψ. The Υ(1S) self-normalized production yield also presents a similar scaling with the self-normalized charged-particle multiplicity density as the J/ψ, independently of the collision energy at which the J/ψ measurement is performed. This is further investigated, at $\sqrt{s} = 13$ TeV, in Fig. 5.7 (bottom panel), by presenting the double ratio of Υ(1S) to J/ψ self-normalized yield as a function of the self-normalized charged-particle multiplicity. The double ratio is close to unity for $\mathrm{d}N_{\mathrm{ch}}/\mathrm{d}\eta/\langle \mathrm{d}N_{\mathrm{ch}}/\mathrm{d}\eta\rangle > 1$, indicating no modification of the correlation with respect to mass and quark content up to six times the mean multiplicity. The ratio is also compared to the various available models, namely PYTHIA 8.2 with and without CR [73], the comovers model [99, 100], the model by CPP [86], and the computation of the 3-pomeron contribution in the CGC approach [88]. The considered models, except for 3-pomeron CGC, provide predictions close to unity over the whole charged-particle multiplicity range considered, suggesting that both initial- and final-state effects act on Υ(1S) and J/ψ in a similar way. The first data point in Fig. 5.7 (bottom panel) departs from the main trend discussed above by about two standard deviations, hinting that the double ratio is smaller than unity for $\mathrm{d}N_{\mathrm{ch}}/\mathrm{d}\eta/\langle \mathrm{d}N_{\mathrm{ch}}/\mathrm{d}\eta\rangle < 1$. A possible mechanism explaining this behaviour invokes an event activity bias: events containing a Υ(1S) are, on average, biased towards higher event activities than events containing a J/ψ, this behavior being driven by the mass difference of the two particles. The same mechanism could be expected when going from Υ(1S) to Υ(2S),

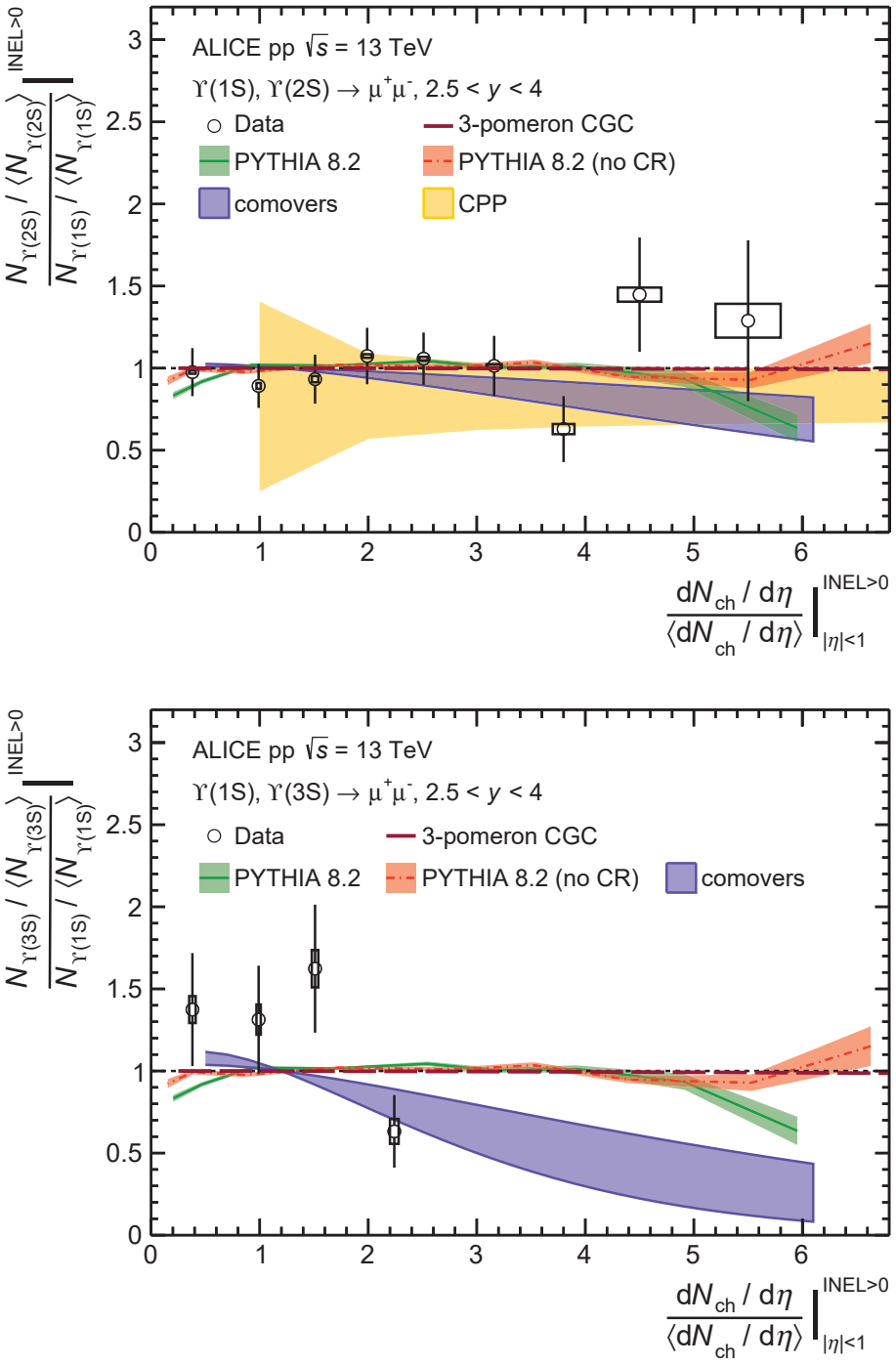

Figure 5.6: Top: Excited-to-ground state self-normalized yield ratio (Υ(2S) over Υ(1S)) as a function of self-normalized charged-particle multiplicity, compared to model predictions from 3-pomeron CGC approach [88], PYTHIA 8.2 [73], comovers [99, 100], and CPP [86] predictions; Bottom: Excited-to-ground state self-normalized yield ratio (Υ(3S) over Υ(1S)) as a function of self-normalized multiplicity, compared to PYTHIA 8.2 and comovers predictions.

and Υ(3S) states, currently not visible due to the relatively small mass difference between the three states, and the limited statistical significance of the higher-state measurements. In the 3-pomeron CGC computation, the increase of the Υ(1S) yield as a function of charged-particle multiplicity is expected to be faster than for J/ψ due to mass dependent higher twist effects, expected to be small and mainly visible at high multiplicities. This accounts for the upward deviation from unity seen at large multiplicities in the 3-pomeron CGC computations. This interpretation is not favored by the measurement.

J/ψ measurements are also performed in ALICE in another kinematic range, with the J/ψ decaying into dielectrons at central rapidity ($|y| < 0.9$). In this case, the charged-particle multiplicity density is measured using two alternative estimators, defined respectively in the central rapidity region (SPD-based selection) or at forward rapidity (V0-based selection) [84]. The corresponding results are also shown in Fig. 5.7 (top panel). No difference is observed in the multiplicity dependence of the J/ψ production measured at central rapidity, corresponding to the two multiplicity estimators, up to five times the mean multiplicity. Conversely, a clear difference is observed between the central rapidity J/ψ measurement and the forward rapidity J/ψ as also expected from several models [80, 84]. At forward rapidity, the Υ(1S) and J/ψ measurements show a similar linear behavior, whereas the Υ(2S) is compatible with both faster than linear and linear behaviors within the current uncertainties, and a larger data sample is needed to draw firm conclusions.

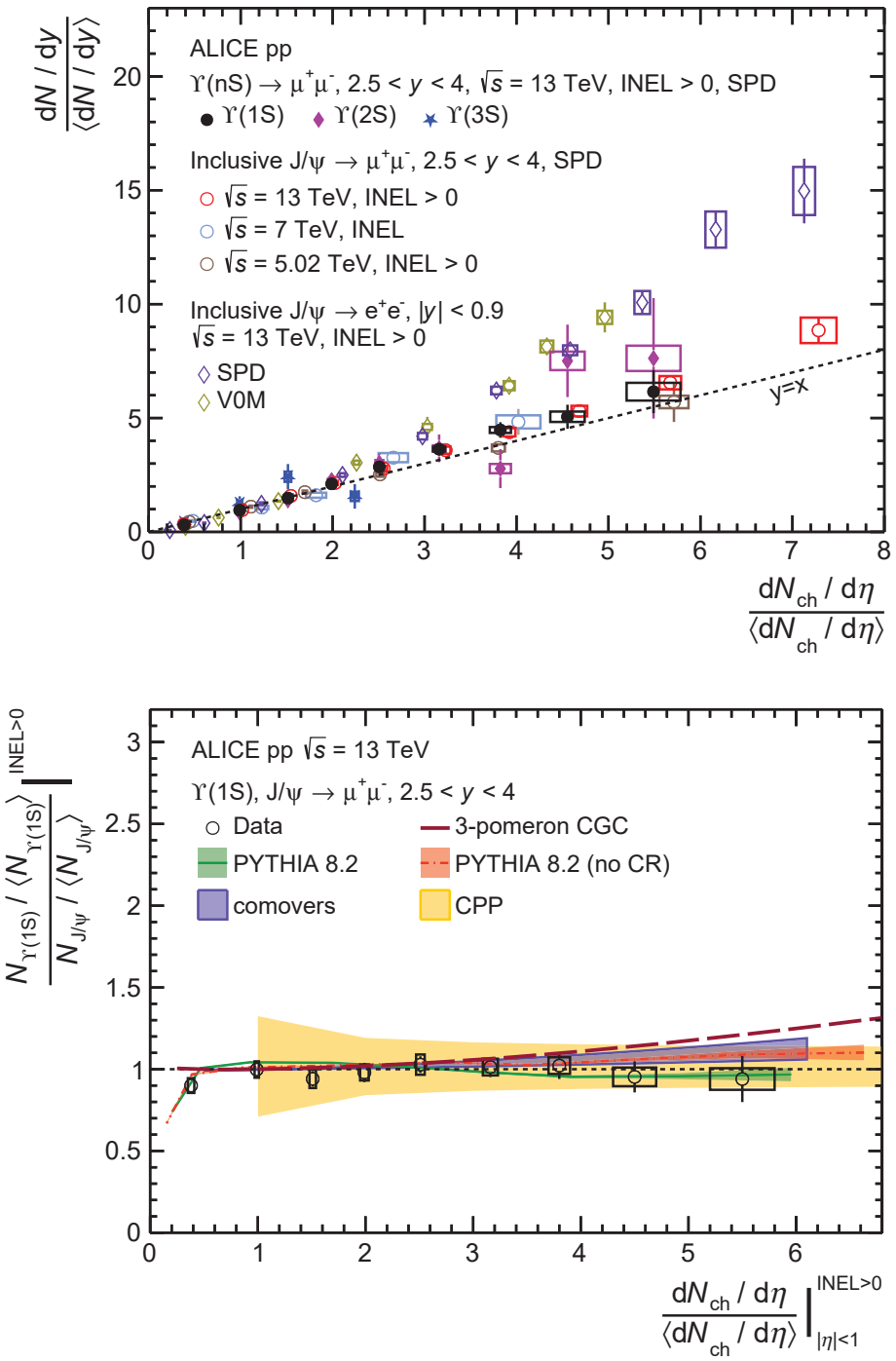

Figure 5.7: Top: Self-normalized yield of Υ as a function of self-normalized charged-particle multiplicity, compared to inclusive J/ψ measured in the forward rapidity region at 5.02 TeV [80], 7 TeV [82], and 13 TeV [80], and to inclusive J/ψ measured in the central rapidity region at 13 TeV [84]. The error bars represent the statistical uncertainty on the quarkonium yields, while the quadratic sum of the point-by-point systematic uncertainties on the quarkonium yields as well as on $\mathrm{d}N_{\mathrm{ch}}/\mathrm{d}\eta$ / $\langle \mathrm{d}N_{\mathrm{ch}}/\mathrm{d}\eta \rangle$ is depicted as boxes. Bottom: Self-normalized yield ratio of Υ(1S) over J/ψ as a function of self-normalized charged-particle multiplicity, compared to model computations from 3-pomeron CGC approach [88], PYTHIA 8.2 [73], comovers [99, 100], and CPP [86].

Chapter 6

Upsilon polarization

A second analysis has been performed in the context of the present PhD thesis. It is based on the same data sample as the analysis discussed in the previous chapters, and concerns the measurement of the polarization for the Υ(1S) meson in pp collisions at $\sqrt{s} = 13$ TeV. Contrary to the analysis focusing on the multiplicity dependence, only the ground state has been considered here, the only one for which the signal extraction was possible with a large enough statistical significance.

6.1 Analysis strategy

The analysis of the polarization of the Υ(1S) meson has been performed following a strategy including three main steps:

- **Signal extraction**: the number of Υ(1S) candidates is obtained via a fit procedure on the dimuon ($\mu^+\mu^-$) invariant mass distribution in each angular interval considered in the analysis.

- **Acceptance $\times$ efficiency correction**: the raw number of Υ(1S) extracted from the fit procedure is corrected for a factor quantifying the geometrical acceptance and reconstruction efficiency effects, estimated via a MC simulation.

- **Polarization parameters determination**: the polarization parameters λ_θ, λ_φ and $\lambda_{\theta\varphi}$ are extracted by fitting the acceptance- and efficiency-corrected angular distributions of Υ(1S), in both the Helicity and Collins-Soper reference frames.

6.2 Signal extraction

Figure 6.1 shows the two-dimensional maps — ($\cos\theta$, p_{T}), (φ, p_{T}) and ($\tilde{\varphi}$, p_{T}) in both Helicity and Collins-Soper reference frames. For each ($\cos\theta$, p_{T}) ((or φ, p_{T}) or ($\tilde{\varphi}$, p_{T})) cell, the raw Υ(1S) yield is extracted.

The signal extraction for the polarization analysis follows the same strategy as described in Section 3.2, with the Υ signal obtained from a fit to the dimuon invariant mass distribution. In order to improve the signal extraction procedure and taking into account the symmetries of the angular distributions (see Figs. 6.1 and 6.8), the analysis regions were limited to $|\cos\theta|$ between 0 and 1, $|\varphi|$ between 0 and π and $\tilde{\varphi}$ between 0 and 2π. Fig. 6.2 and 6.3 show the example of fits to the invariant mass distributions as a function of $|\cos\theta|$ in $2 < p_{\mathrm{T}} < 4$ GeV/c. In this p_{T} region, due to the limited data in the edges of $|\cos\theta|$ (between 0.8 to 1), it is hard to converge the fit to the dimuon invariant mass distributions.

After the signal extraction, the raw number of Υ(1S) as a function of $|\cos\theta|$, $|\varphi|$ and $\tilde{\varphi}$ in different p_{T} intervals are respectively shown in Fig. 6.4, 6.5, and 6.6 in both Helicity and Collins-Soper reference frames. From those plots, one can see that the number of Υ(1S) in the selected angular variable interval shows different behavior between Helicity and Collins-Soper frames, this could be explained that the $A \times \varepsilon$ varies with the choice of reference frames (see Section 6.3). Finally, it is confirmed the sum of the number of Υ(1S) for each chosen p_{T} interval are comparable among these three angular variables, as shown in Fig. 6.7.

6.3 A $\times$ ε correction

The acceptance-times-efficiency (A $\times$ ε) denotes the product of two variables: one is the acceptance, which is related to the geometrical coverage of the experimental apparatus and to the kinematics of particle decay; the other one is the efficiency, which is related to the detector performances and to the reconstruction algorithm. It also takes into account the contributions of the trigger, tracking, and matching efficiencies in the specific situation of the ALICE muon spectrometer. Then raw number of Υ(1S) is corrected by corrected the raw number of using the proportion of Υ(1S) that can be reconstructed in the kinematic region under consideration provided by the A $\times$ ε. Finally, the corrected number of Υ(1S) is defined, as shown in Eq. 6.1.

$$N^{\mathrm{corr}}_{\Upsilon(1\mathrm{S})}(p_{\mathrm{T}}, \mathrm{angular}) = \frac{N^{\mathrm{raw}}_{\Upsilon(1\mathrm{S})}(p_{\mathrm{T}}, \mathrm{angular})}{\mathrm{A} \times \varepsilon(p_{\mathrm{T}}, \mathrm{angular})} \tag{6.1}$$

The A $\times$ ε is evaluated from a pure signal MC simulation (LHC21d7, generated in a run-by-run basis and proportional to the dimuon pairs reconstructed from data in each run), which MC input shapes (p_{T} and y shapes) were tuned on LHCb data [150]. In each p_{T} and angular interval, the A $\times$ ε correction factor is computed as the ratio of the number of reconstructed Υ(1S) ($N^{\mathrm{rec}}_{\Upsilon(1\mathrm{S})}$) divided by the number of generated Υ(1S) ($N^{\mathrm{gen}}_{\Upsilon(1\mathrm{S})}$), as shown in Eq. 6.2 (angular in the equation refers to $|\cos\theta|$, $|\varphi|$ or $\tilde{\varphi}$). Figure 6.8 shows the $A \times \varepsilon$ two-dimensional maps in the

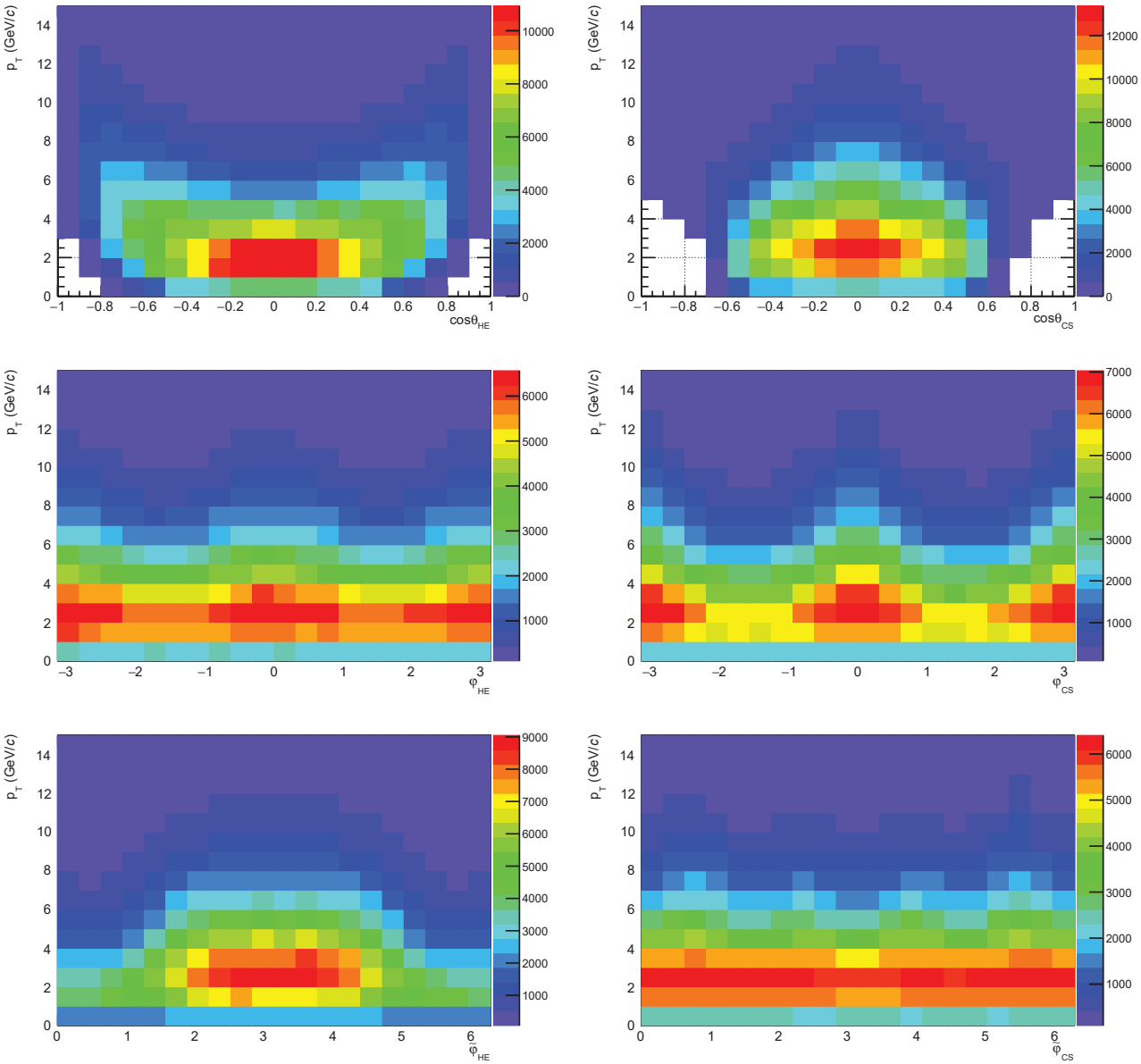

Figure 6.1: Two-dimensional maps populated with dimuons in the Helicity (left) and Collins-Soper (right) frames. From top to bottom, it shows the $\cos\theta$, φ and $\tilde{\varphi}$ vs p_{T}.

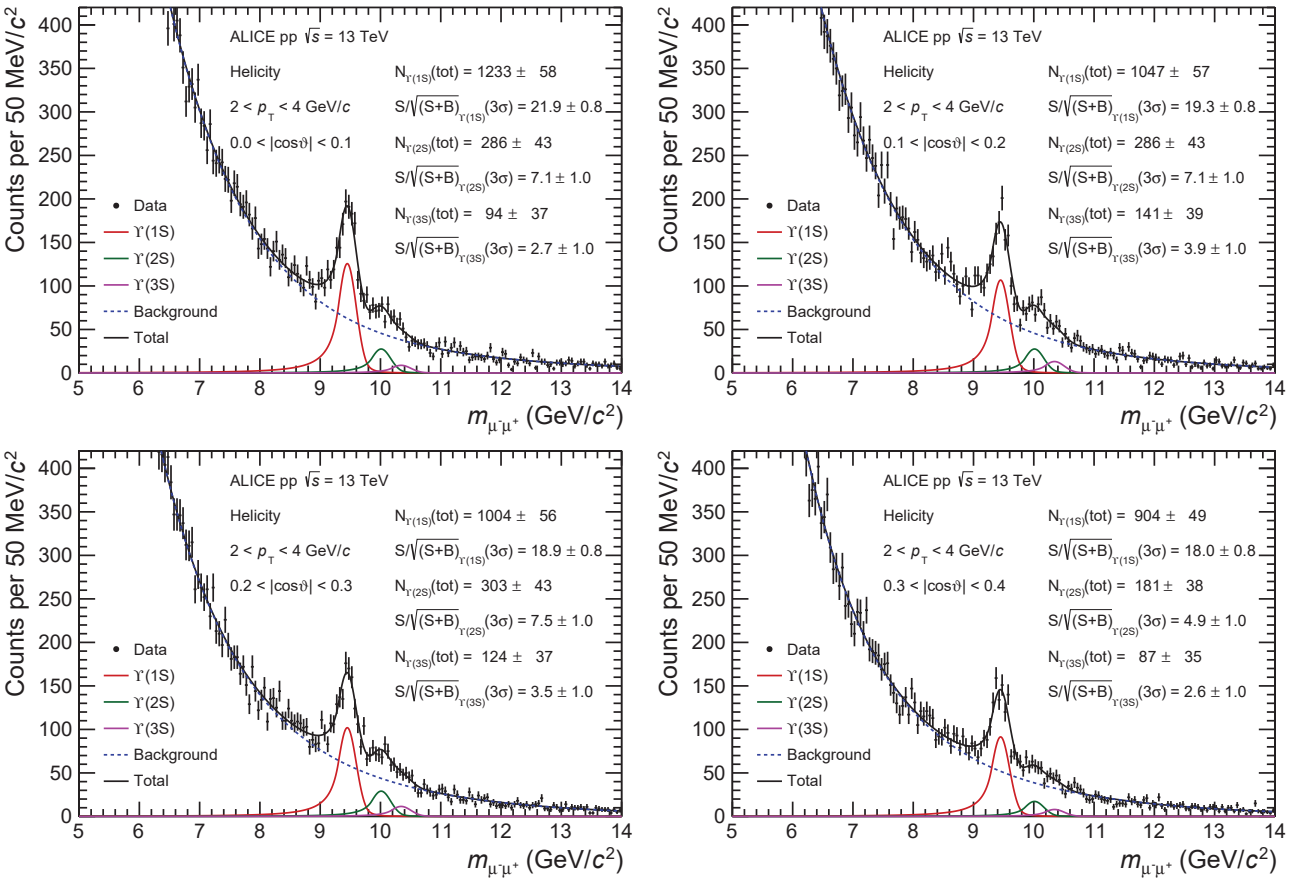

Figure 6.2: An example of Υ(1S) signal extraction as a function of $|\cos\theta|$ ($0 < |\cos\theta| < 0.4$) in $2 < p_{\mathrm{T}} < 4$ GeV/c in the Helicity reference frame.

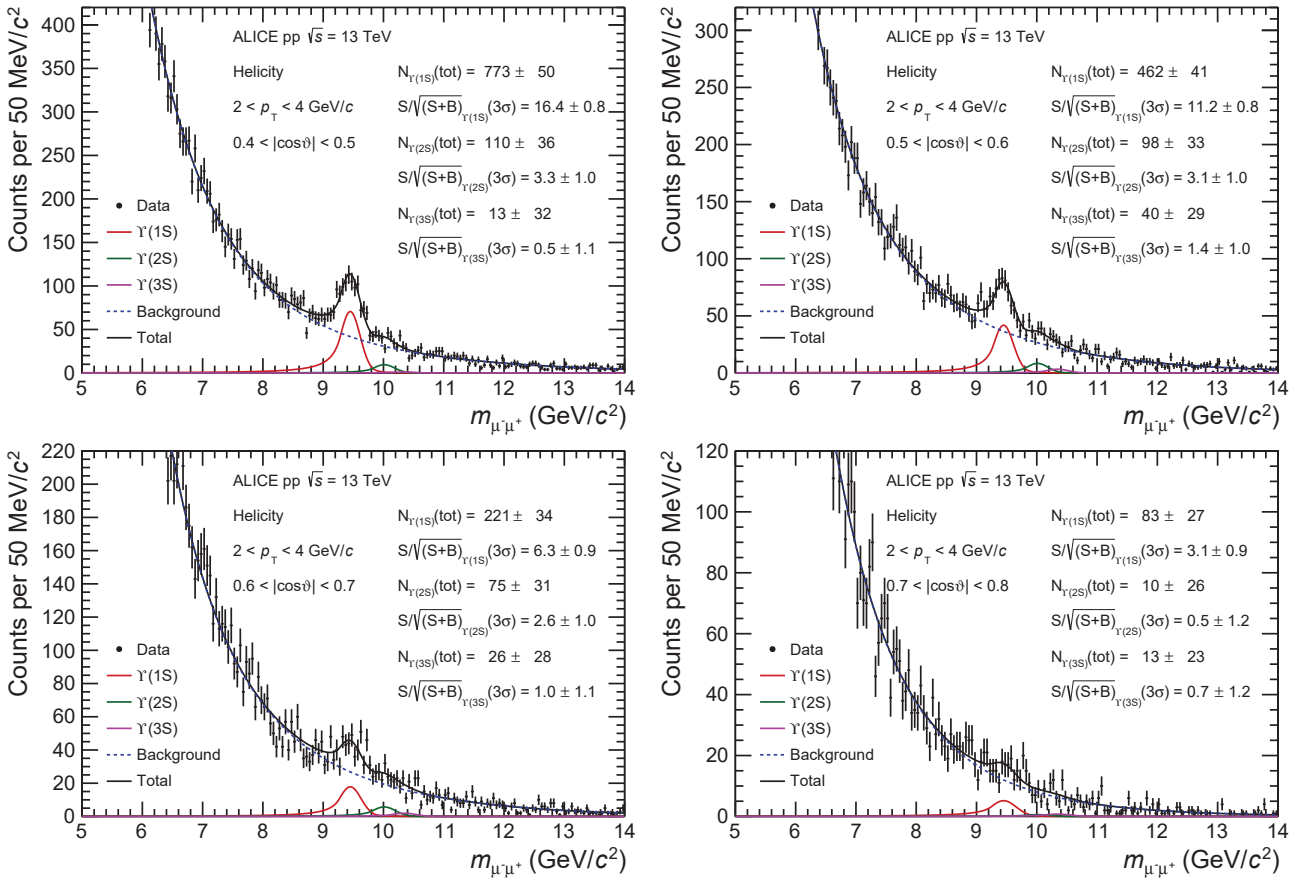

Figure 6.3: An example of Υ(1S) signal extraction as a function of $|\cos\theta|$ ($0.4 < |\cos\theta| < 0.8$) in $2 < p_{\mathrm{T}} < 4$ GeV/c in the Helicity reference frame.

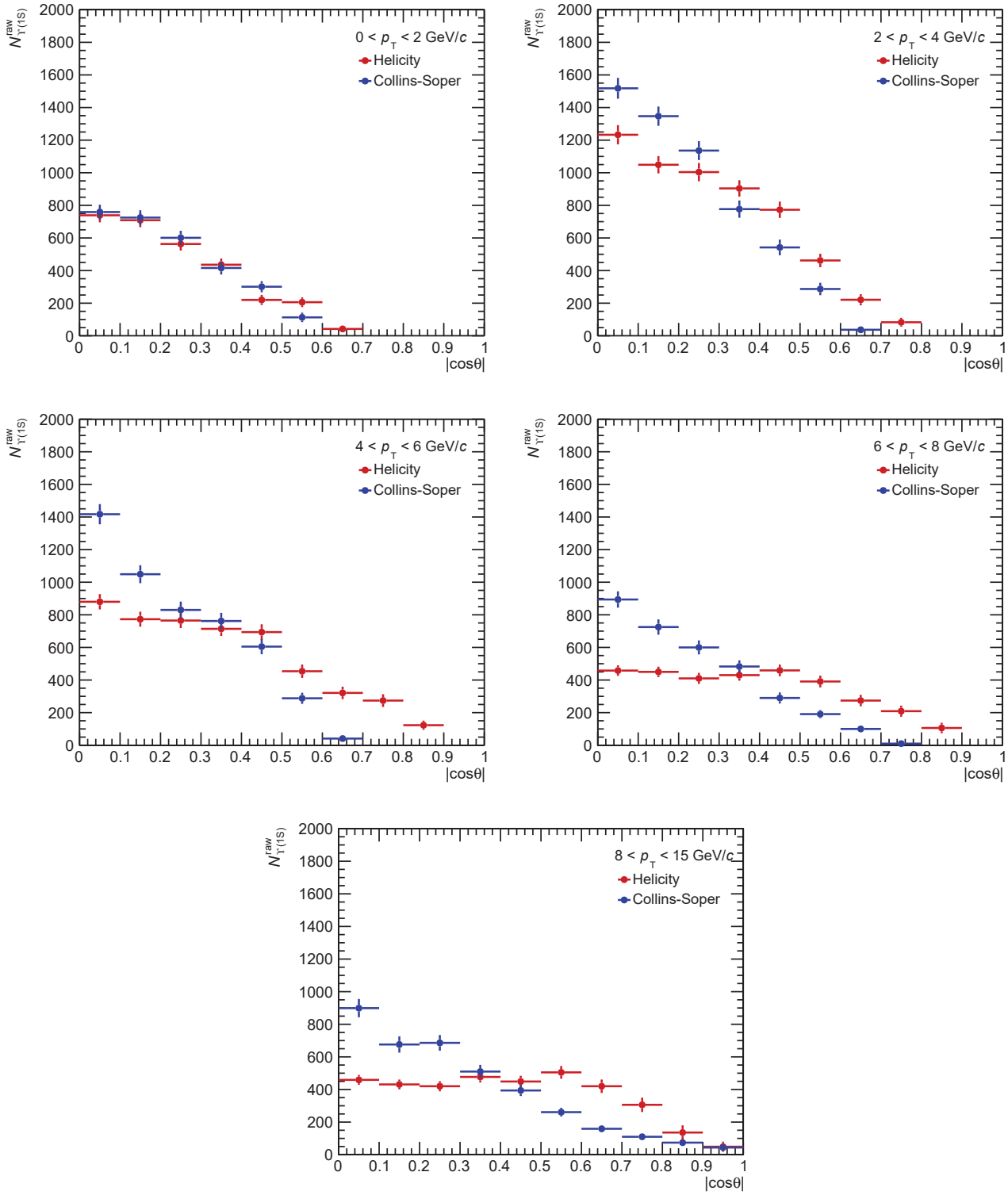

Figure 6.4: Raw number of Υ(1S) as a function of $|\cos\theta|$ in different p_{T} intervals in both Helicity and Collins-Soper reference frames.

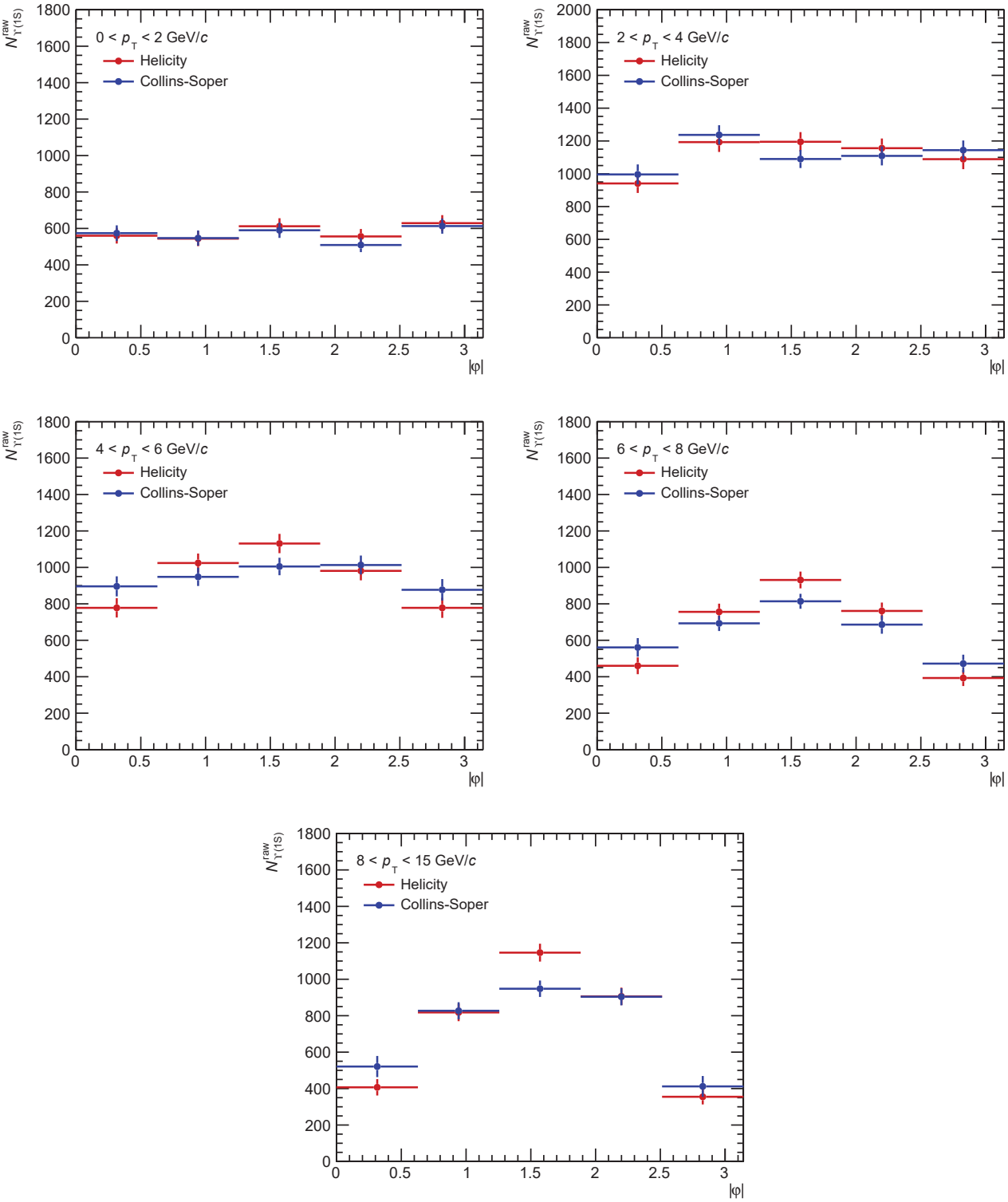

Figure 6.5: Raw number of Υ(1S) as a function of $|\varphi|$ in different p_{T} intervals in both Helicity and Collins-Soper reference frames.

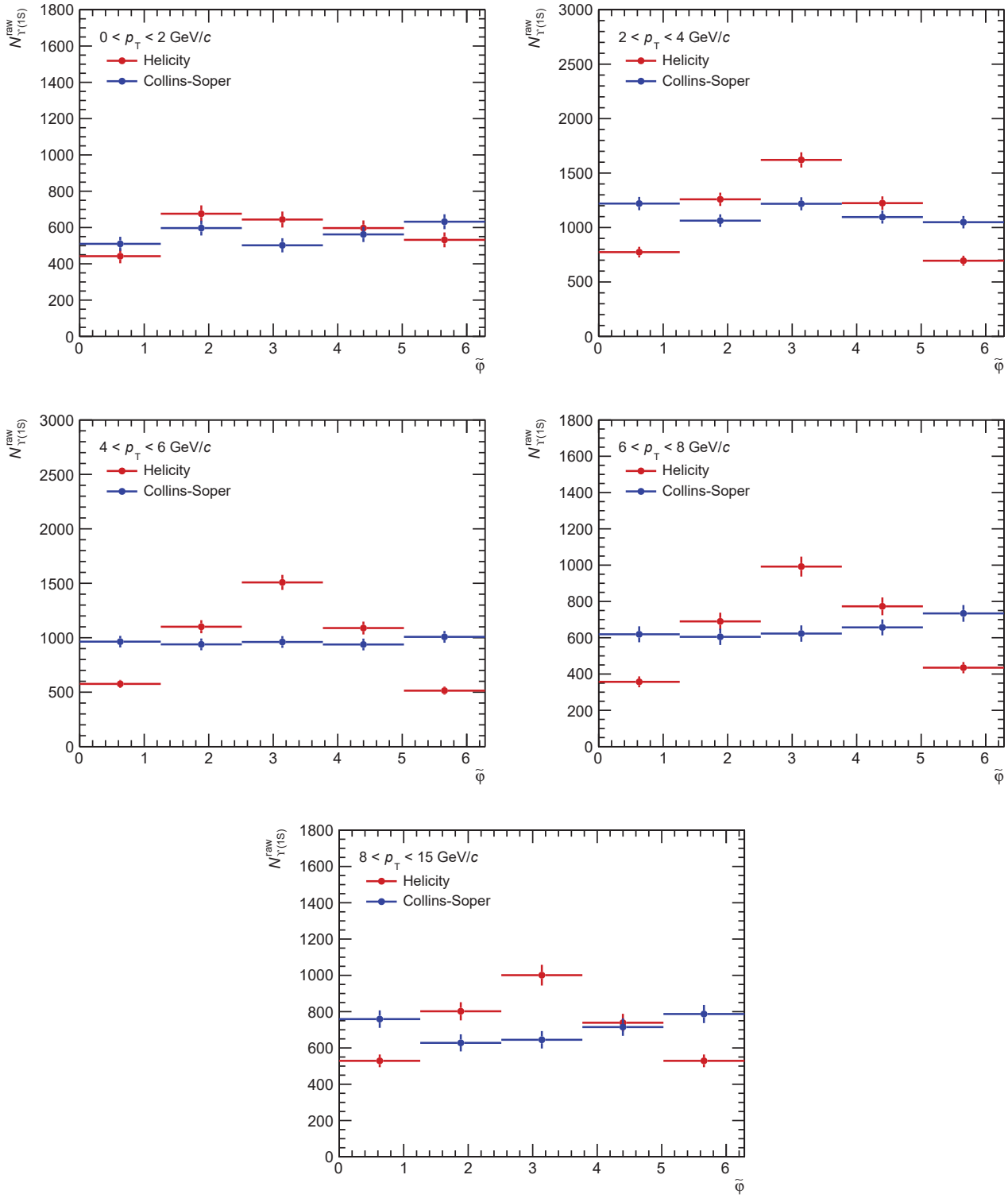

Figure 6.6: Raw number of Υ(1S) as a function of $\tilde{\varphi}$ in different p_{T} intervals in both Helicity and Collins-Soper reference frames.

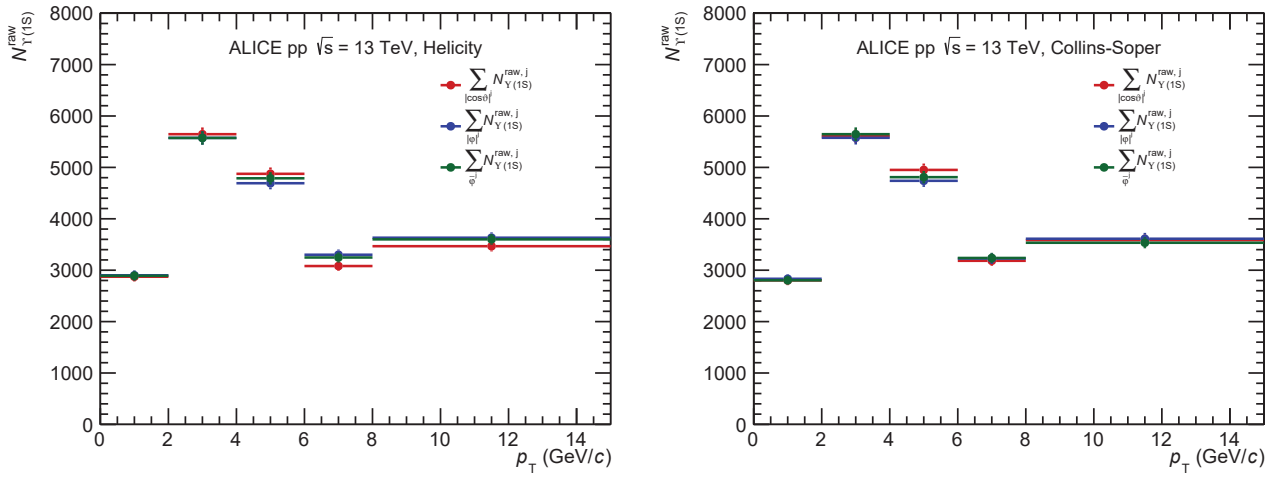

Figure 6.7: Raw number of Υ(1S) in different p_{T} intervals in both the Helicity (left) and Collins-Soper (right) reference frames.

Helicity and Collins-Soper frames for the different angular variables as a function of p_{T} and a symmetrical behavior is observed for both $\cos\theta$ and φ variables.

The $A\times\,\varepsilon$ factor is then performed as a function of $|\cos\theta|$ in p_{T} regions, as shown in Fig. 6.9. The $A\times\,\varepsilon$ factor as a function of the other variables φ and $\tilde{\varphi}$ is shown in Appendix B.4. It is obvious that the $A\times\varepsilon$ is rather small (<0.1) at the edges of $|\cos\theta|$ at low p_{T}. The regions of low $A\times\varepsilon$ constitute a limitation to the signal extraction procedure and it is not always possible to achieve a converging fit to the dimuon invariant mass spectra for the selected angular intervals with very low statistics. Therefore, the binning in the angular variables has to be carefully chosen: a sufficient number of dimuon events for each bin is required to properly fit the corresponding invariant mass spectra. In this analysis, only angular intervals with a Υ(1S) significance $\mathrm{S}/\sqrt{\mathrm{S}+\mathrm{B}}>5$, integrated in the dimuon mass range $[\mu-3\sigma,\mu+3\sigma]$ (μ and σ are the mass and width of Υ(1S), respectively), and the $A\times\varepsilon>0.1$ (see Fig. 6.9), are considered. Finally, the ranges and bins of the $|\cos\theta|$ variable used in this analysis are presented in Tab. 6.1. For the other angular variables, $|\varphi|$ and $\tilde{\varphi}$, 5 bins in $|\varphi|$ from 0 to π and 5 bins in $\tilde{\varphi}$ from 0 to 2π are used. It is noted that in each p_{T} region, events with the $|\cos\theta|>X$ ("X" is chosen as the maximum $|\cos\theta|$ value in each p_{T} region) are excluded, creating a fiducial area within which the λ_θ, λ_φ and $\lambda_{\theta\varphi}$ are extracted.

$$A\times\varepsilon(p_{\mathrm{T}},\mathrm{angular})=\frac{N^{\mathrm{rec}}_{\Upsilon(1S)}(p_{\mathrm{T}},\mathrm{angular})}{N^{\mathrm{gen}}_{\Upsilon(1S)}(p_{\mathrm{T}},\mathrm{angular})} \tag{6.2}$$

The corrected number of Υ(1S) in the considered kinematic region is then extracted according to Eq. 6.1. Fig. 6.10 and 6.11 present A $\times\,\varepsilon$ corrected number of Υ(1S) distribution as a function of $|\cos\theta|$, $|\varphi|$ and $\tilde{\varphi}$ in $2<p_{\mathrm{T}}<4$ GeV/c in both Helicity and Collins-Soper reference frames. More results see Appendix B.6.

After the $A\times\varepsilon$ correction, the sum of the number of Υ(1S) for each chosen p_{T} interval are comparable among

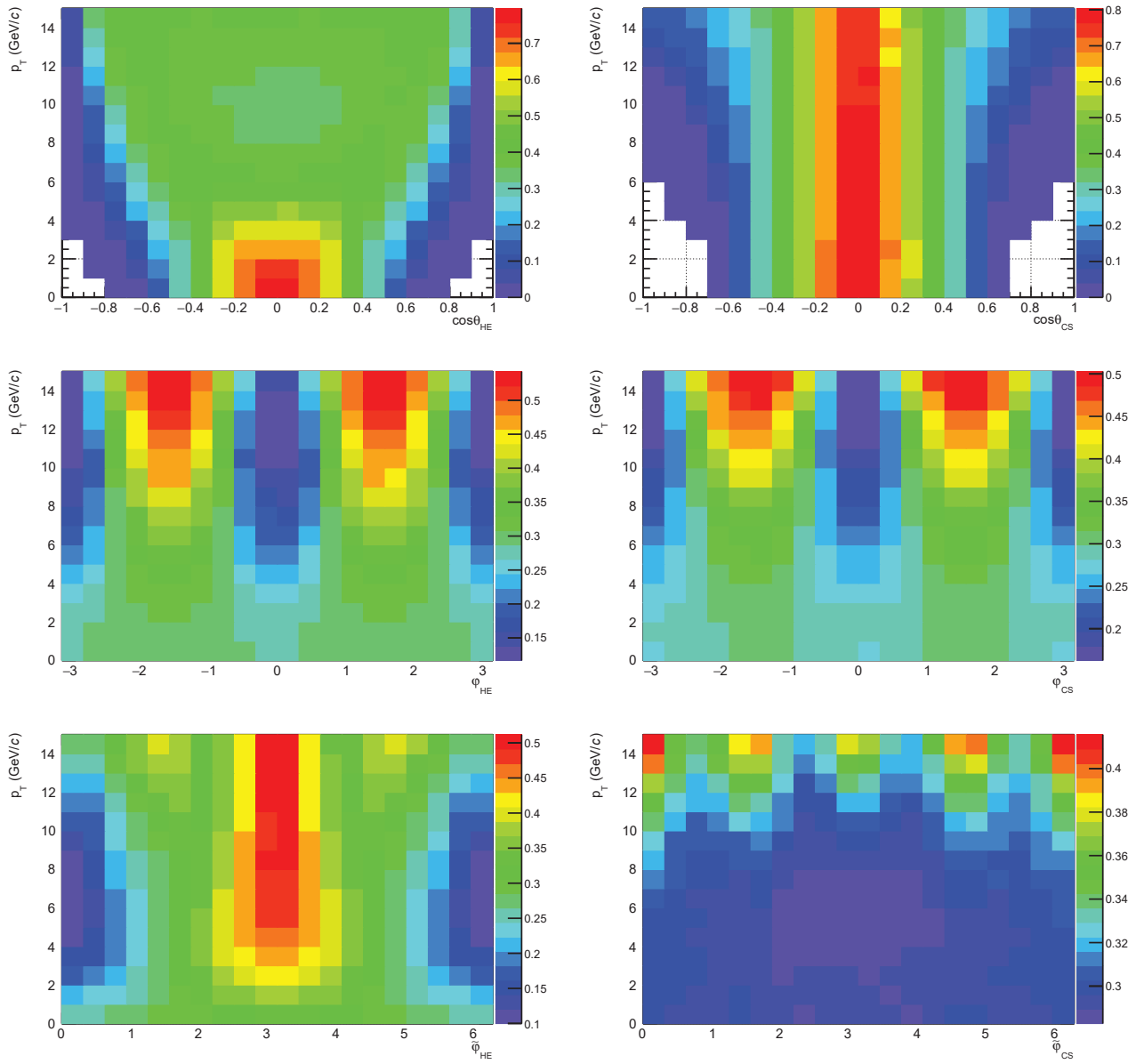

Figure 6.8: $A \times \varepsilon$ maps in the Helicity (left) and Collins-Soper (right) frames. From top to bottom, it shows the $\cos\theta$, φ and $\tilde{\varphi}$ vs p_{T}.

$p_{\mathrm{T}}(\mathrm{GeV/c})$	$\lvert\cos\theta\rvert$, HE	$\lvert\cos\theta\rvert$, CS
$[0, 2]$	6 bins in $[0, 0.6]$	5 bins in $[0, 0.5]$
$[2, 4]$	7 bins in $[0, 0.7]$	6 bins in $[0, 0.6]$
$[4, 6]$	8 bins in $[0, 0.8]$	6 bins in $[0, 0.6]$
$[6, 8]$	8 bins in $[0, 0.8]$	6 bins in $[0, 0.6]$
$[8, 15]$	8 bins in $[0, 0.8]$	7 bins in $[0, 0.7]$

Table 6.1: $\lvert\cos\theta\rvert$ intervals used in the analysis for both Helicity and Collins-Soper reference frames.

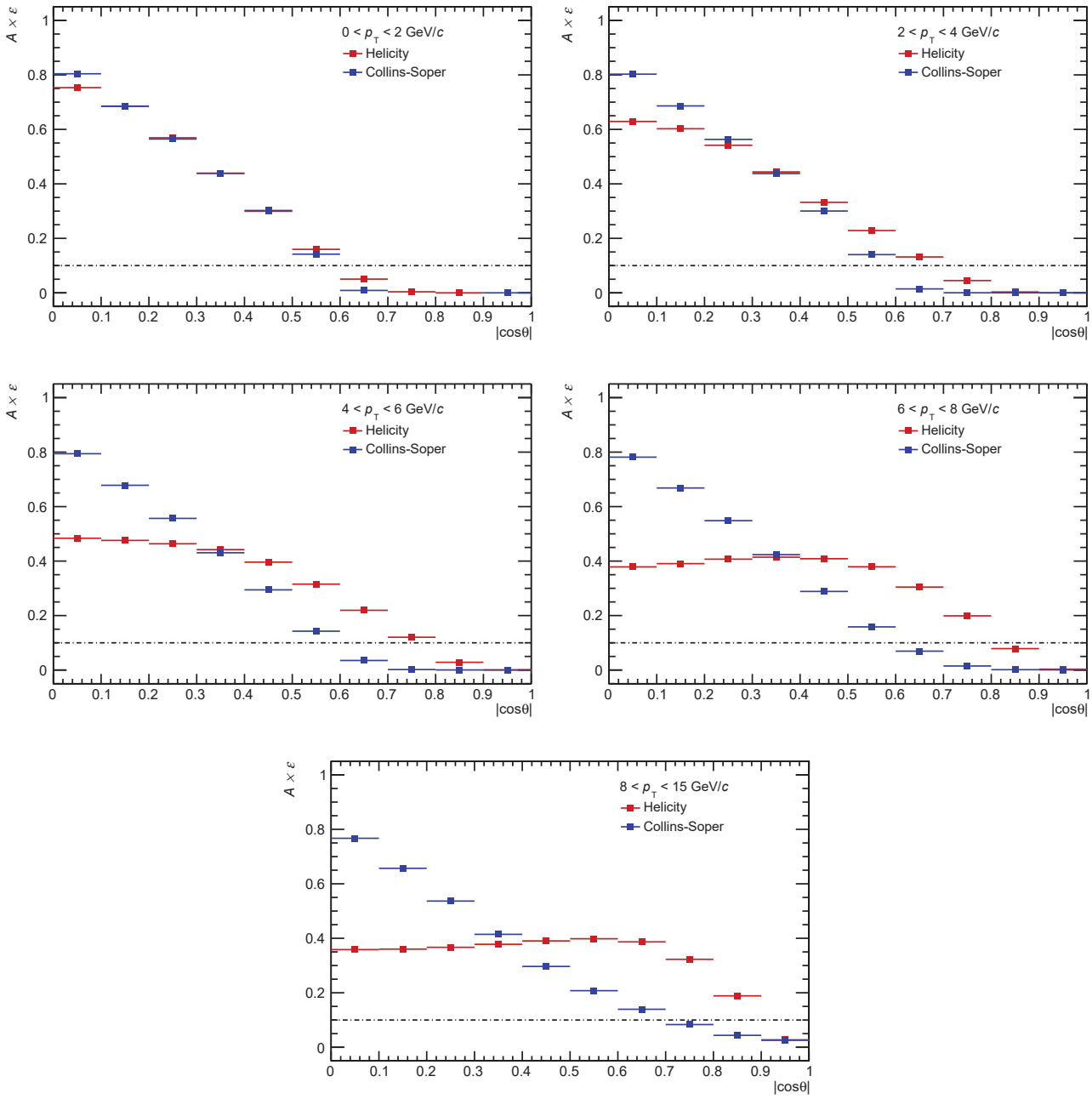

Figure 6.9: A $\times$ ε as a function of $|\cos\theta|$ in both Helicity and Collins-Soper reference frames. The dashed line means the A $\times$ ε equals to 0.1.

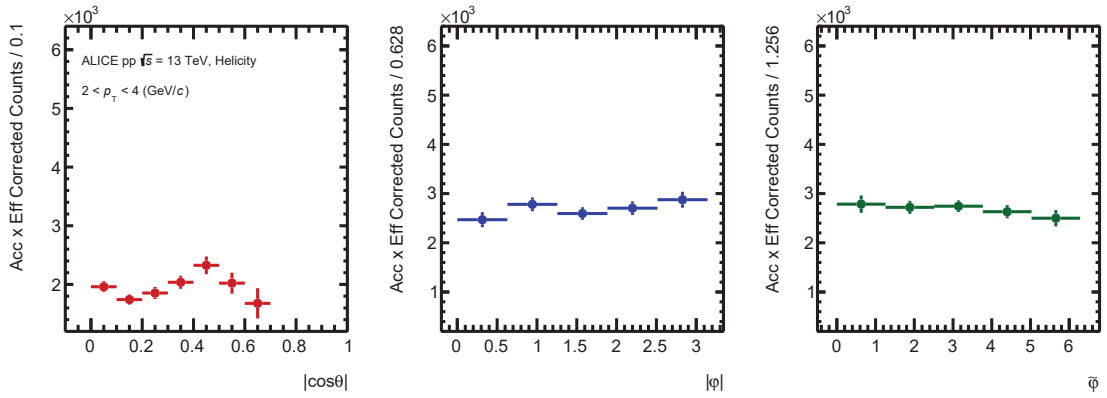

Figure 6.10: An example of the corrected number of Υ(1S) as a function of $|\cos\theta|$, $|\varphi|$ and $\tilde{\varphi}$ in $2 < p_{\mathrm{T}} < 4$ GeV/c interval in Helicity reference frame.

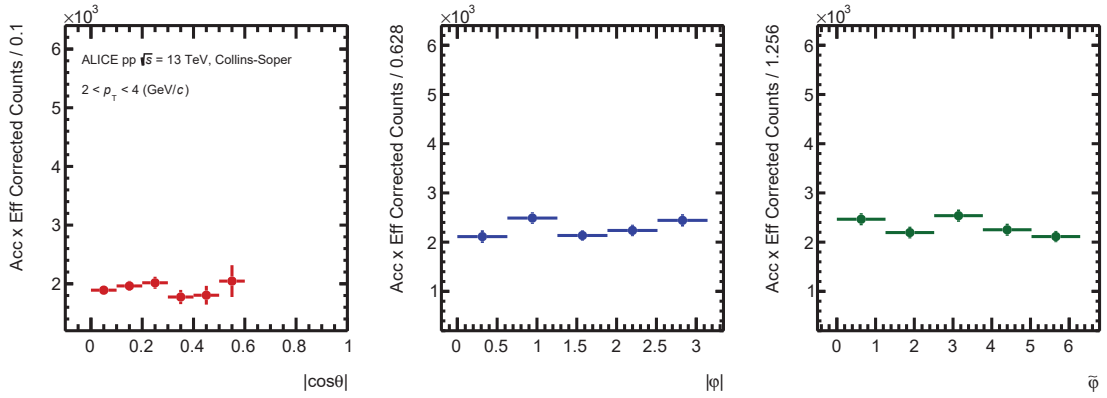

Figure 6.11: An example of corrected number of Υ(1S) as a function of $|\cos\theta|$, $|\varphi|$ and $\tilde{\varphi}$ in $2 < p_{\mathrm{T}} < 4$ GeV/c interval in Collins-Soper reference frame.

the three angular variables, as shown in Fig. 6.12.

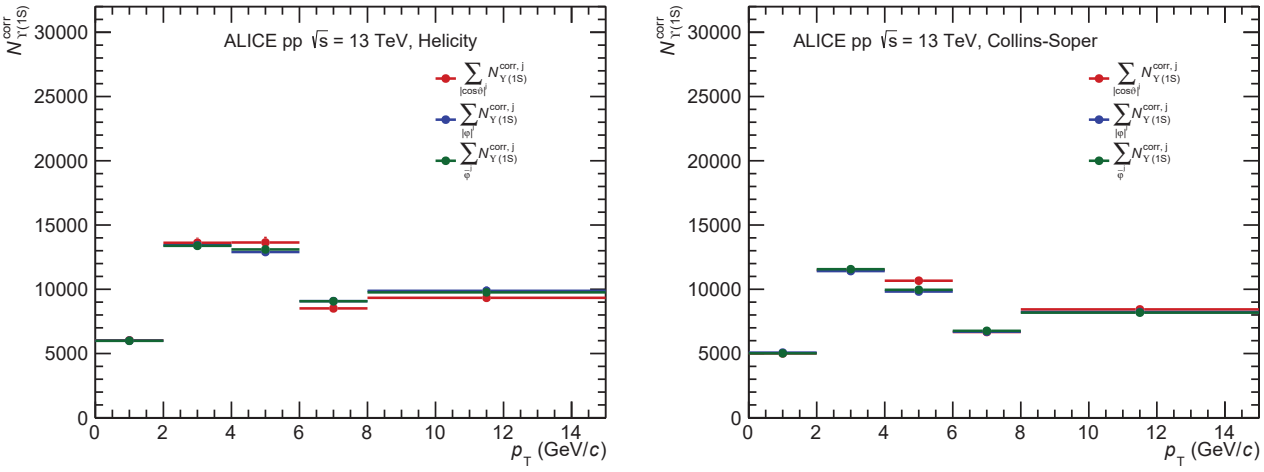

Figure 6.12: The corrected number of Υ(1S) in different p_{T} intervals in both Helicity (left) and Collins-Soper (right) reference frames.

6.4 Polarization parameter determination

The Υ(1S) polarization parameters are obtained performing a simultaneous fit on the $|\cos\theta|$, $|\varphi|$, and $\tilde{\varphi}$ corrected distributions with the functions described by Eq. 1.16, 1.17, and 1.19. Performing the fit simultaneously in the Helicity and Collins-Soper reference frames would result in the optimization of six free parameters; however, the existence of the frame-invariant quantity $\tilde{\lambda}$, defined in Eq. 1.26, allows one to reduce the number of free parameters from six to five (providing smaller and more reliable uncertainties on the parameters) by imposing the condition expressed by Eq. 6.3. An example of a simultaneous fit is shown in Fig. 6.13. The polarization parameters as a function of p_{T} are performed in Fig. 6.14.

$$\tilde{\lambda} = \frac{\lambda_\theta^{\mathrm{HE}} + 3\lambda_\varphi^{\mathrm{HE}}}{1 - \lambda_\varphi^{\mathrm{HE}}} = \frac{\lambda_\theta^{\mathrm{CS}} + 3\lambda_\varphi^{\mathrm{CS}}}{1 - \lambda_\varphi^{\mathrm{CS}}} \tag{6.3}$$

In order to check the stability of the fit procedure, the analysis was also performed without forcing the fit to satisfy the invariant quantity $\tilde{\lambda}$. This allowed to verify that, fitting the corrected spectra independently for the two reference frames, the results are in agreement with what is found with the default approach (see Appendix B.7).

6.5 Systematic uncertainties

Three main sources of systematic uncertainties are considered in the analysis:

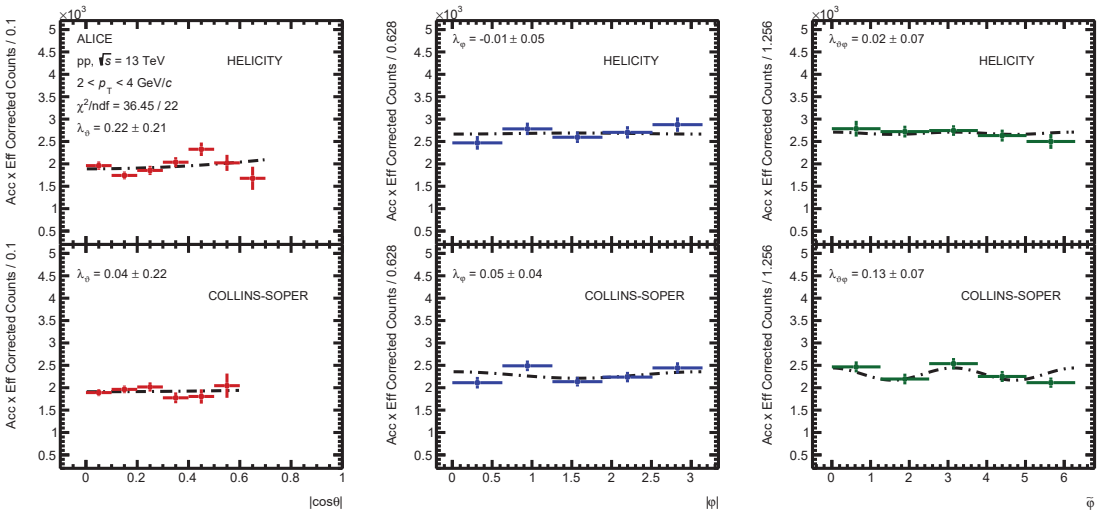

Figure 6.13: An example of polarization parameters determination in $2 < p_{\mathrm{T}} < 4$ GeV/c with a simultaneous fit in both Helicity and Collins-Soper reference frames.

- Systematic uncertainty on the signal extraction, associated to the choice of the background function and the fitting range;

- Systematic uncertainty on the signal extraction, associated to the choice of the width of the function describing the Υ(1S) signal;

- Systematic uncertainty on the estimation of the geometrical acceptance and the reconstruction efficiency ($A \times \varepsilon$), depending on the input MC shapes.

  The three sources are discussed in details in the following subsections.

6.5.1 Systematic uncertainty on the background description and the fit range

Several choices are possible for the functions describing the background, as well as for the fitting range, in the fit of the invariant mass spectrum from which the Υ(1S) signal is estimated. To estimate the systematic uncertainty associated to this choice, three alternative parametrizations of the underlying continuum background, namely a variable-width Gaussian (VWG), the product of two exponentials, or the product of an exponential and a power law function, and three fitting ranges ($5-14$, $6-13$ and $7-12$ GeV/c^2) are considered in the analysis.

The central value ($\overline{\lambda_{\mathrm{i}}}$) and the corresponding statistical uncertainty ($\sigma^{\mathrm{stat}}_{\overline{\lambda_{\mathrm{i}}}}$) for each polarization parameter have then estimated considering the N different tests, as:

$$\overline{\lambda_{\mathrm{i}}} = \frac{\sum_{\mathrm{j}} \lambda_{\mathrm{i}}^{(\mathrm{j})}}{N} \text{ and } \sigma^{\mathrm{stat}}_{\overline{\lambda_{\mathrm{i}}}} = \frac{\sum_{\mathrm{j}} \sigma^{(\mathrm{j})}_{\lambda_{\mathrm{i}}}}{N} \ , \tag{6.4}$$

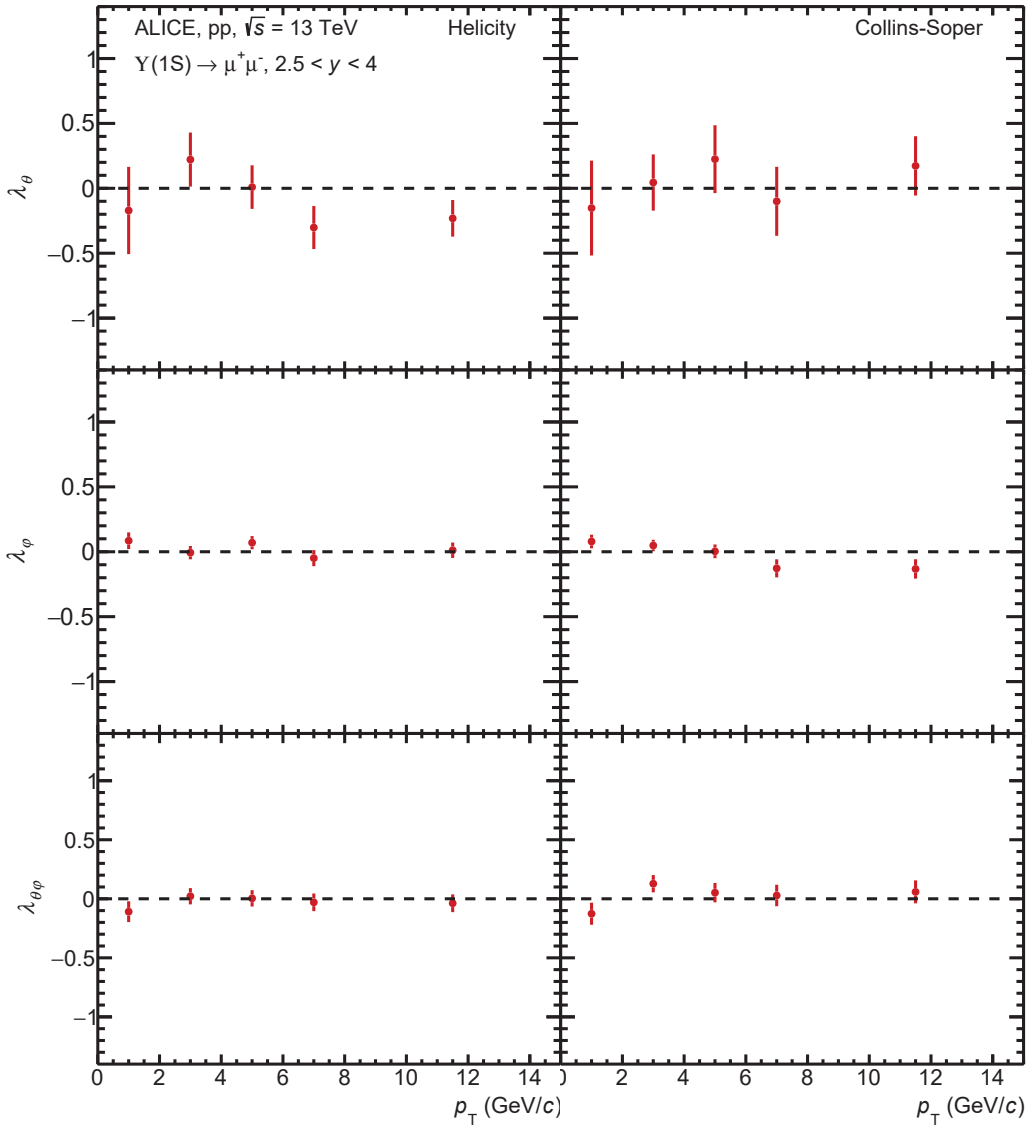

Figure 6.14: Υ(1S) polarization parameters as a function of p_{T} in both Helicity and Collins-Soper reference frames.

where the index j indicates each specific combination of background function and fitting range considered for the signal extraction, and $\mathrm{i} = 0$, 1 and 2 corresponds to $|\cos\theta|$, $|\varphi|$, and $\tilde{\varphi}$, respectively. The corresponding systematic uncertainty is computed by adding in quadrature with respect to the central value:

$$\sigma^{\mathrm{syst}}_{\lambda_\mathrm{i}} = \sqrt{\frac{\sum_\mathrm{j}[\lambda^{(\mathrm{j})}_\mathrm{i} - \overline{\lambda_\mathrm{i}}]^2}{N-1}}. \tag{6.5}$$

Figure 6.15 reports the simultaneous fit for various choices of the background function and the fitting range. In Fig. 6.16, it shows the polarization parameters as a function of transverse momentum associated with the uncertainty on the signal extraction.

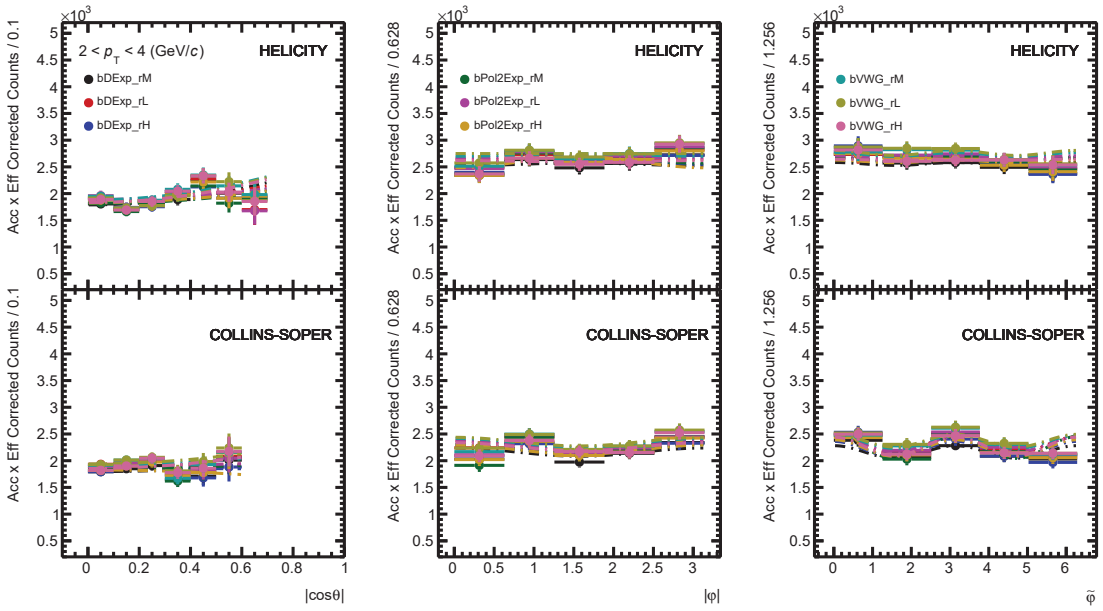

Figure 6.15: An example of polarization parameters determination for various choice of the background functions and fitting mass ranges in both Helicity and Collins-Soper reference frames. bDExp, bPol2Exp and bVWG refer to the background shapes: bDExp corresponding to the product of two exponentials; bPol2Exp corresponding to the product of an exponential and a power law and bVWG corresponding to the variable-width Gaussian. rL, rM and rH refer to the fitting ranges: rL corresponding to $[5, 14]$ GeV/c^2; rM corresponding to $[6, 13]$ GeV/c^2 and rH corresponding to $[7, 12]$ GeV/c^2.

6.5.2 Systematic uncertainty on the choice of the Υ(1S) width

In order to help the fit in the single $|\varphi|$ and $\tilde{\varphi}$ intervals to converge, the mass of the Υ(1S) is fixed to the value obtained in the fit to the integrated spectrum, since there is no reason for the mass pole to have any dependence on the angular variables. Such a dependence could however exist for the width of the reconstructed peak, due to the correlation between the angular variables and the average transverse momentum of the decay muons: this

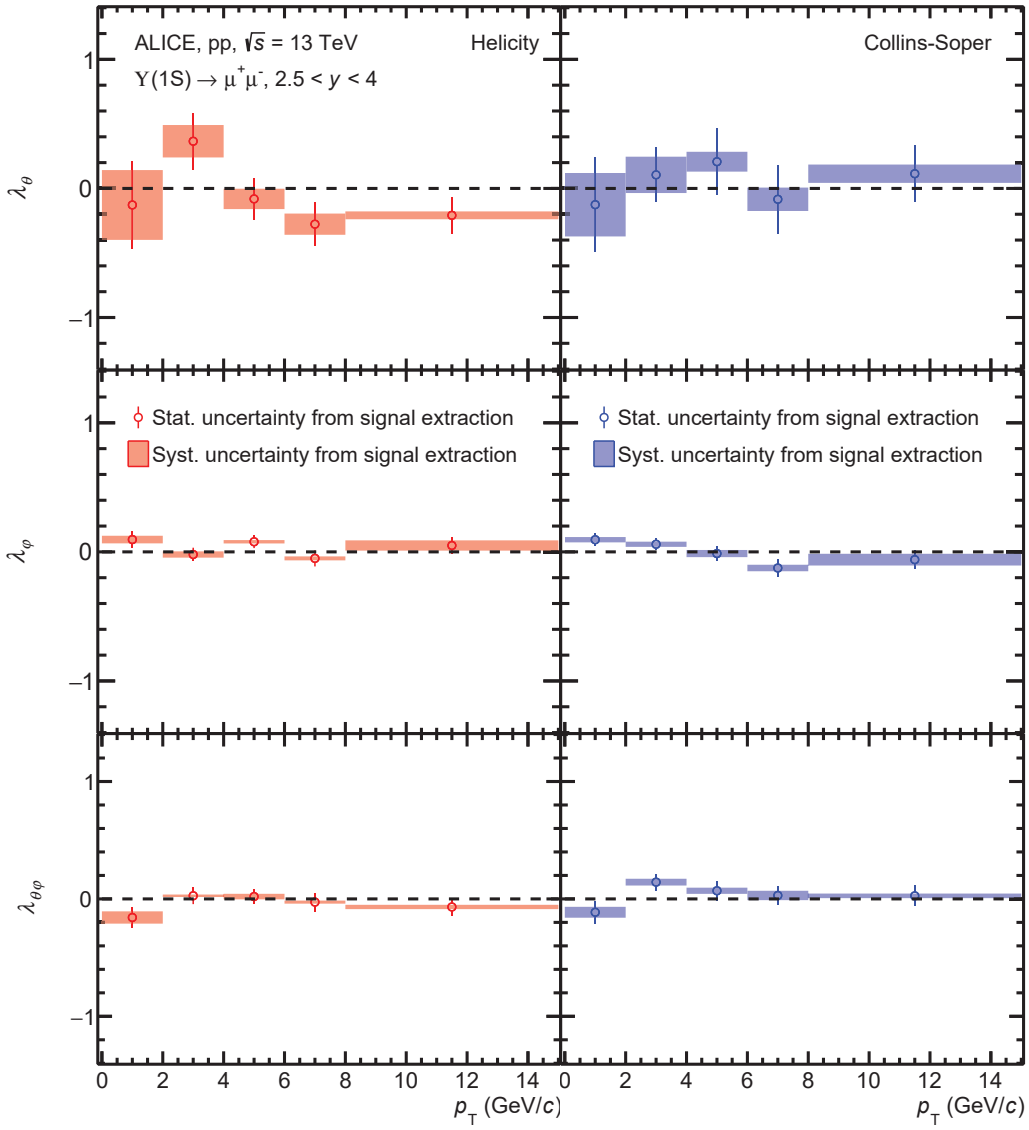

Figure 6.16: Polarization parameters as a function of p_{T} in both Helicity (red) and Collins-Soper (blue) frames, the error bars represent the statistical uncertainty from signal extraction, while the boxes represent the systematic uncertainty from signal extraction.

dependence has been studied in the analysis, profiting from the large size of the available data sample, performing the analysis both fixing or keeping free the Υ(1S) width in the signal extraction in the single $|\varphi|$ and $\tilde{\varphi}$ intervals. However, for the $|\cos\theta|$ variable, the value of the width optimized by the fit was found to fluctuate too much, especially in the low p_{T} intervals (see Fig. 6.17), affecting the reliability of the Υ(1S) signal extraction. For this reason, in the $|\cos\theta|$, the data-driven free-width approach was replaced by a MC-driven width-variation approach, where the variation was chosen to be 5% of the MC value.

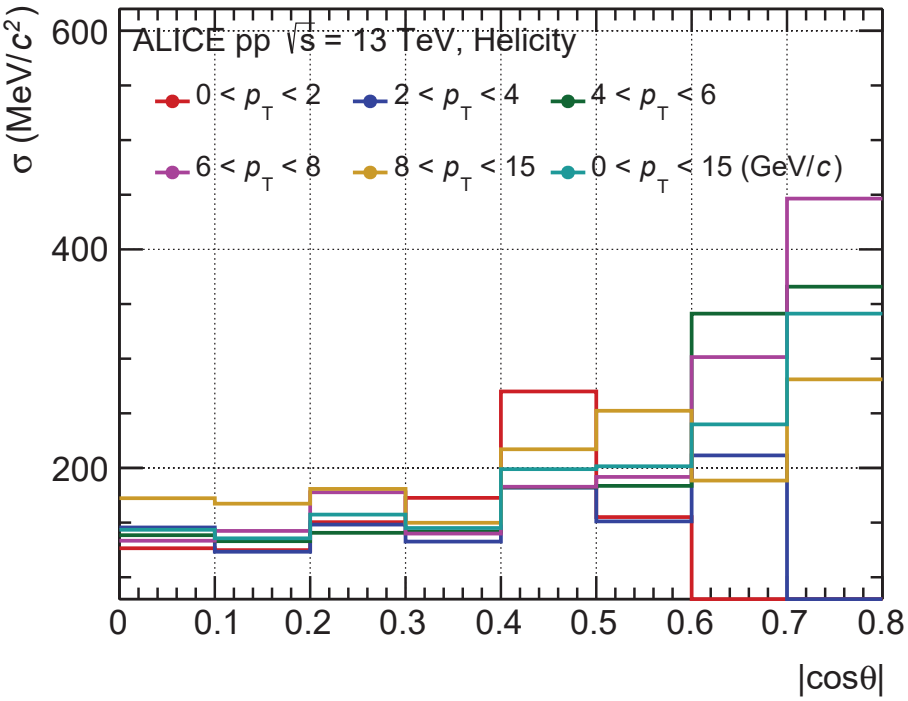

Figure 6.17: The width of Υ(1S) as a function of $|\cos\theta|$ in p_{T} intervals in Helicity reference frame with data.

The systematic uncertainty choice of the Υ(1S) width was evaluated as the semi-difference between the results obtained with the data- or MC-driven variation of the Υ(1S) width, and the results obtained keeping the Υ(1S) width fixed, see Fig. 6.18.

6.5.3 Systematic uncertainty on the $A \times \varepsilon$ correction factor

Another source of systematic uncertainty is represented by the estimation of the $A \times \varepsilon$ correction, which depends on the choice of the input kinematic distributions considered in the MC simulations. In particular, the impact of the p_{T} and y input shapes on the final polarization results has been studied considering the extreme options for the p_{T} and y shapes, compatible with the LHCb data [150] (see Fig. 6.19), resulting in 4 combinations in total. For each of these combinations, the default MC has been re-weighted, and a new $A \times \varepsilon$ extracted and used to correct the raw number of Υ(1S) of the analysis, leading to new values for the results on the polarization parameters. The difference with respect to λ_θ, λ_φ, and $\lambda_{\theta\varphi}$ obtained with the default $A \times \varepsilon$ is taken as the corresponding systematic uncertainty,

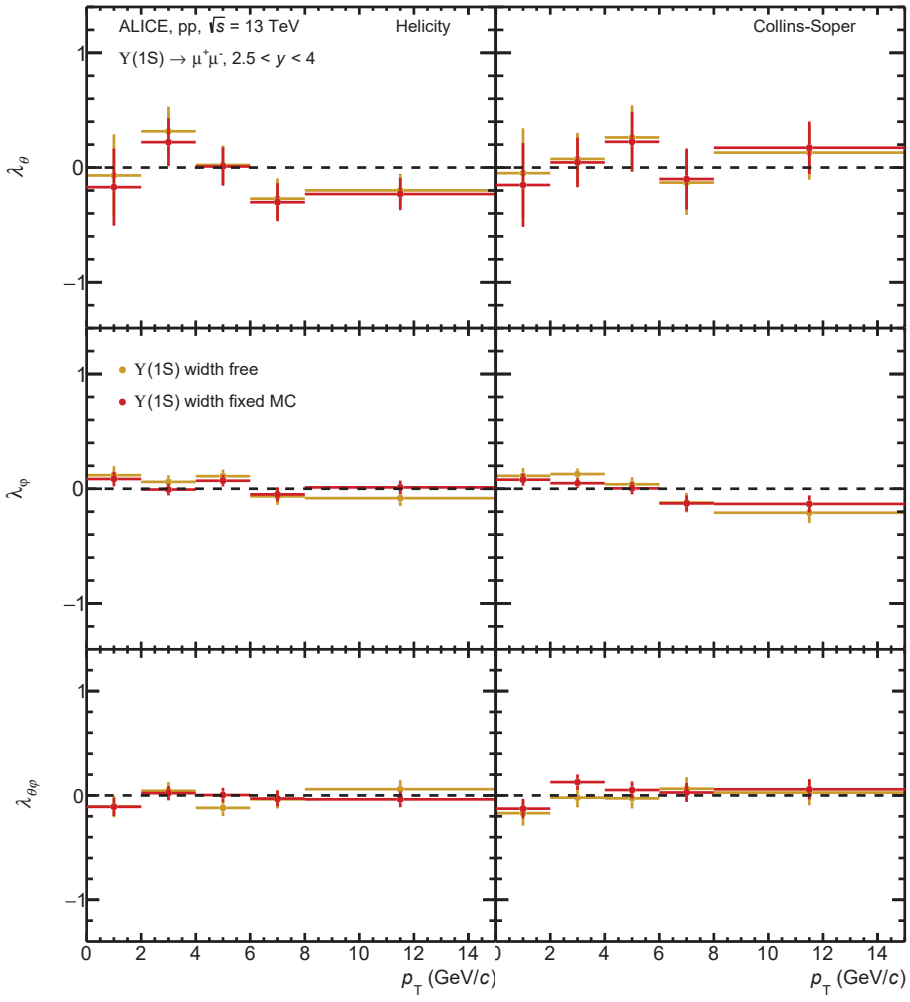

Figure 6.18: Polarization parameters as a function of p_{T} in Helicity and Collins-Soper reference frames with width free and fixed during the signal extraction.

and the maximum variation of the polarization parameters is 0.04, as shown in Fig. 6.20.

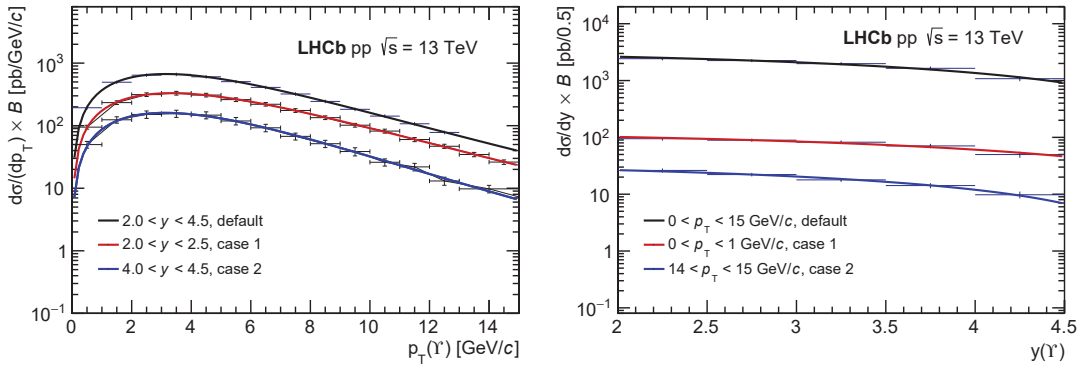

Figure 6.19: Comparison between the Υ(1S) y and p_{T} distributions from LHCb results [150].

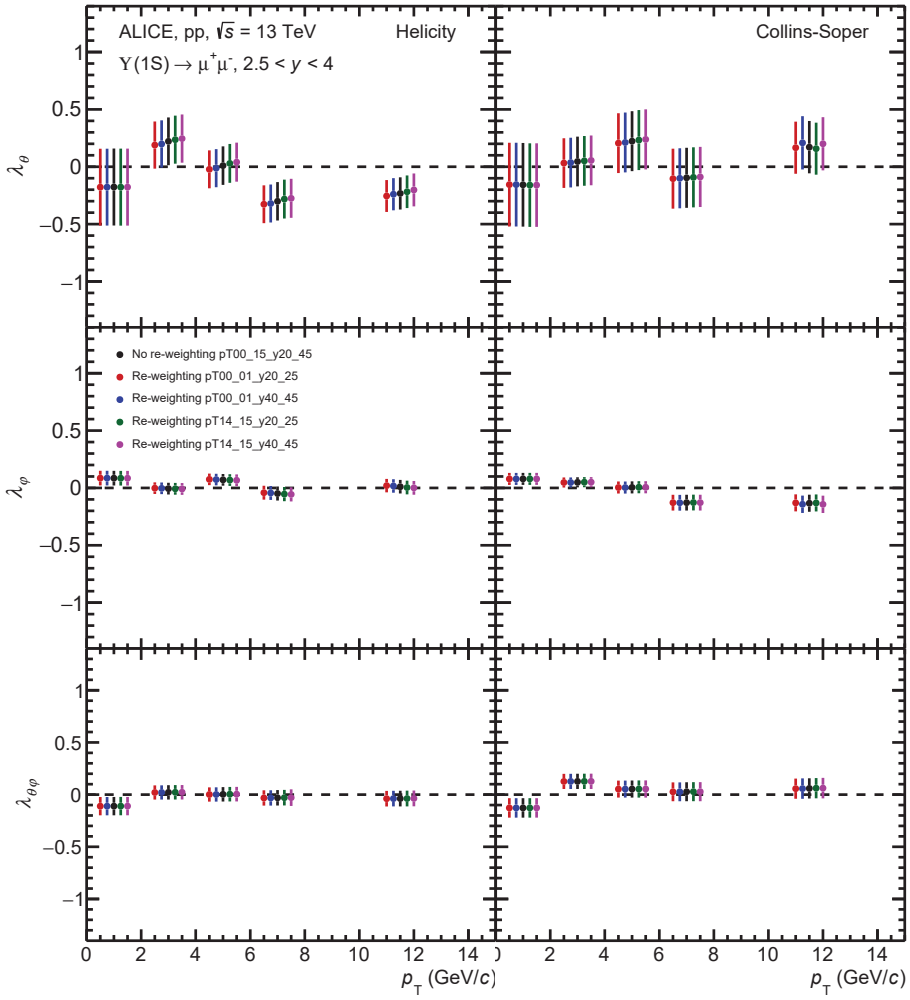

Figure 6.20: Comparison between the three polarization parameters obtained using the alternative Υ(1S) y and p_{T} distributions

The various systematic uncertainties considered in the analysis are summarized in Tab. 6.2, and the systematic uncertainties are added in quadrature in the final results.

Polarization parameters	p_{T} (GeV/c)	Helicity			Collins-Soper		
		Signal	Input MC	Width	Signal	Input MC	Width
λ_θ	$0 < p_{\mathrm{T}} < 2$	0.27	0.00	0.05	0.25	0.00	0.05
	$2 < p_{\mathrm{T}} < 4$	0.13	0.03	0.05	0.14	0.02	0.02
	$4 < p_{\mathrm{T}} < 6$	0.08	0.03	0.01	0.08	0.02	0.02
	$6 < p_{\mathrm{T}} < 8$	0.08	0.03	0.02	0.09	0.01	0.02
	$8 < p_{\mathrm{T}} < 15$	0.03	0.03	0.02	0.07	0.04	0.02
λ_φ	$0 < p_{\mathrm{T}} < 2$	0.03	0.01	0.02	0.02	0.00	0.02
	$2 < p_{\mathrm{T}} < 4$	0.02	0.01	0.03	0.02	0.00	0.04
	$4 < p_{\mathrm{T}} < 6$	0.01	0.00	0.02	0.03	0.01	0.02
	$6 < p_{\mathrm{T}} < 8$	0.02	0.00	0.01	0.03	0.00	0.00
	$8 < p_{\mathrm{T}} < 15$	0.04	0.00	0.05	0.05	0.01	0.04
$\lambda_{\theta\varphi}$	$0 < p_{\mathrm{T}} < 2$	0.05	0.00	0.00	0.05	0.00	0.02
	$2 < p_{\mathrm{T}} < 4$	0.01	0.00	0.01	0.03	0.00	0.07
	$4 < p_{\mathrm{T}} < 6$	0.02	0.00	0.06	0.03	0.00	0.04
	$6 < p_{\mathrm{T}} < 8$	0.01	0.00	0.00	0.04	0.00	0.02
	$8 < p_{\mathrm{T}} < 15$	0.02	0.00	0.05	0.02	0.00	0.02

Table 6.2: Summary of the systematic uncertainties.

6.6 Results and discussion

The polarization parameters λ_θ, λ_φ, and $\lambda_{\theta\varphi}$ for the Υ(1S) meson, measured in both Helicity and Collins-Soper frames, for the data collected in pp collisions at $\sqrt{s} = 13$ TeV with ALICE at the LHC, are shown in Fig. 6.21. All the polarization parameters are compatible with zero within uncertainties, consistently with the results found by the LHCb experiment in pp collisions at $\sqrt{s} = 8$ TeV in a similar rapidity range [129], shown in Fig. 6.22, and the NLO NRQCD calculations [151].

Apart from the NLO NRQCD calculations, the predictions from the ICEM model with the κ_{T} factorization approach [152] are available for the Υ(1S) polarization, at least for the prompt component (direct and feed down contributions). Fig. 6.23 shows that the ICEM predictions for the polarization of prompt Υ(1S) is different from zero at low p_{T}, with a significant frame dependence of the λ_θ parameter: while the Υ(1S) polarization is predicted to be slightly transverse in the Helicity frame (left panel), it is predicted to be slightly longitudinal in the Collins-Soper frame (right panel). On the contrary, at high p_{T}, the polarization becomes compatible with zero for both Helicity and Collins-Soper frames, close to the LHCb measurements [129]. A similar behavior is observed for the prompt J/Ψ with the same ICEM calculation [124].

Up to now, all the polarization measurements of J/ψ and Υ in pp collisions at the LHC either exhibit a small polarization or no significant polarization within the uncertainties. ALICE has also measured the inclusive Υ(1S) and the inclusive J/ψ in Pb–Pb collisions at $\sqrt{s_{\mathrm{NN}}} = 5.02$ TeV [153]. The values for the Υ(1S) are compatible with the

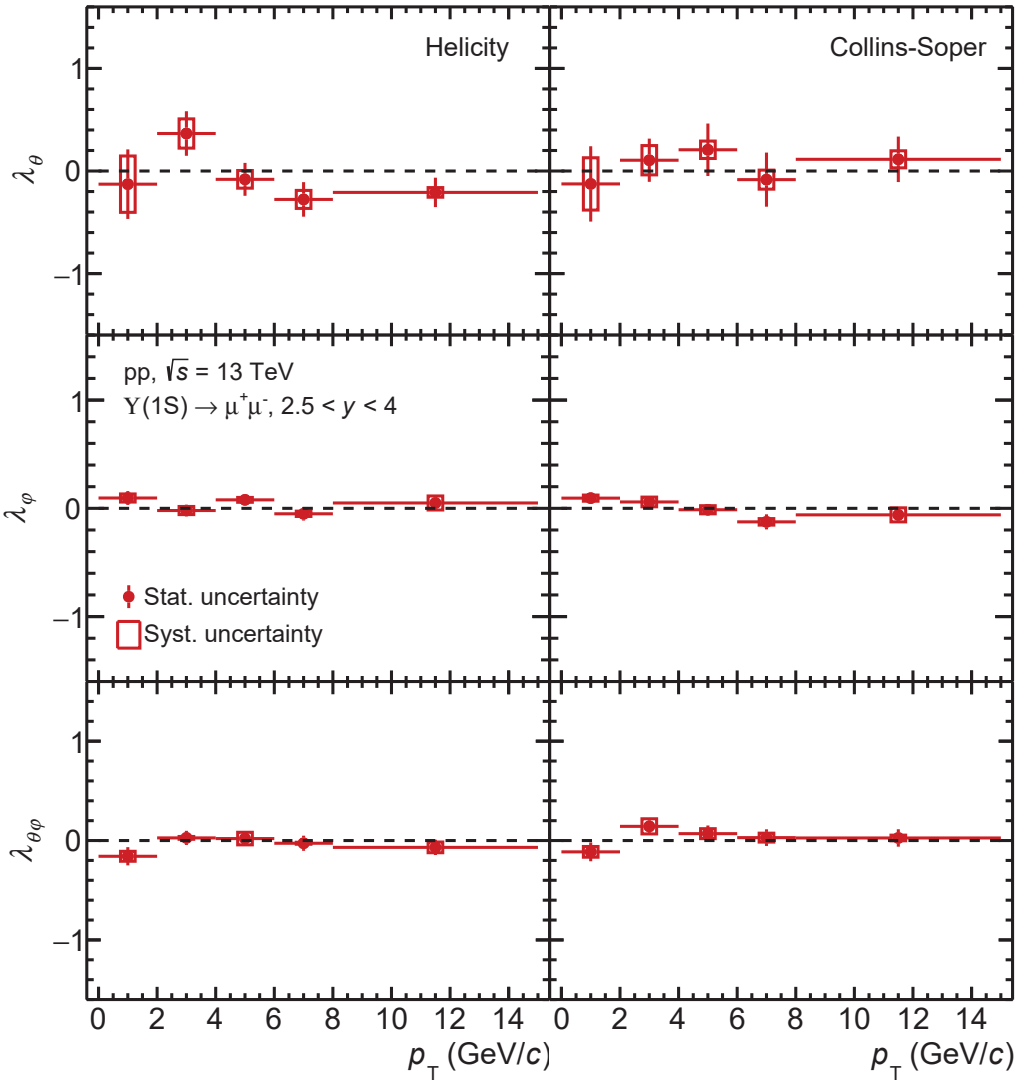

Figure 6.21: Υ(1S) polarization parameters as a function of p_{T} in both Helicity and Collins-Soper frames, the error bars represent the statistical uncertainty, while the boxes represent the systematic uncertainty.

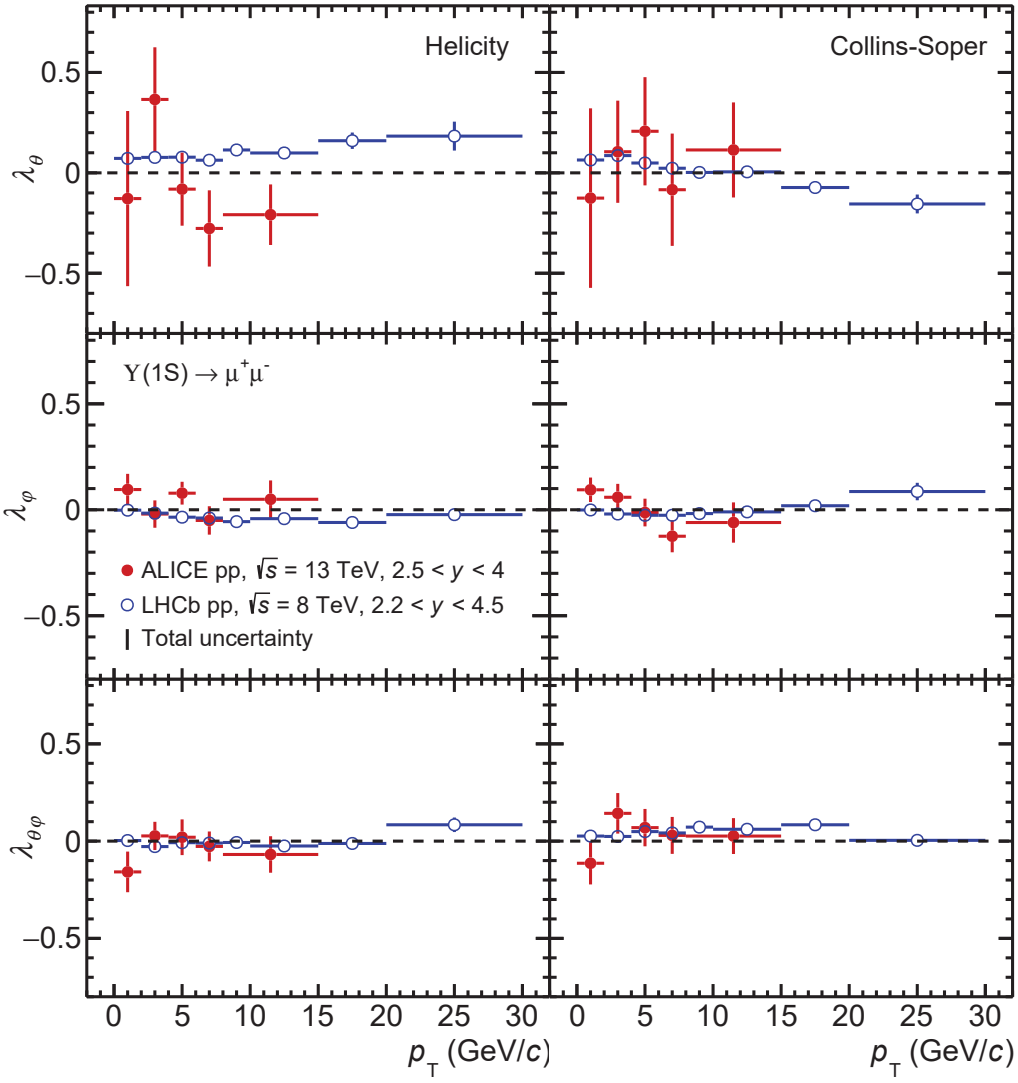

Figure 6.22: Υ(1S) polarization parameters as a function of p_{T} in both Helicity and Collins-Soper frames for ALICE and LHCb measurements [129], the error bars represent the quadrature for the statistical and systematic uncertainties.

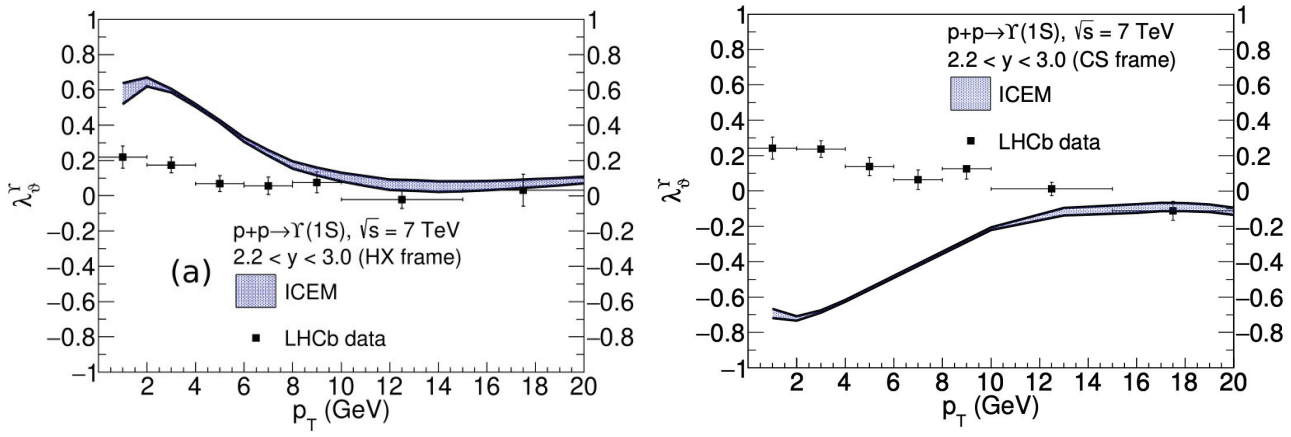

Figure 6.23: Υ(1S) polarization parameter λ_θ as a function of p_{T} in both Helicity (left) and Collins-Soper (right) frames for LHCb measurements at 7 TeV [129], compared to the ICEM model [152]. Figures taken from Ref. [152].

absence of polarization within the large uncertainties of the measurement, while for the J/ψ the measurements of the λ_θ parameter in the Helicity frame indicates a slight transverse polarization (2σ) at low p_{T}, and weak longitudinal polarization (2σ) in Collins-Soper frame. When increasing the p_{T}, the λ_θ gets close to zero.

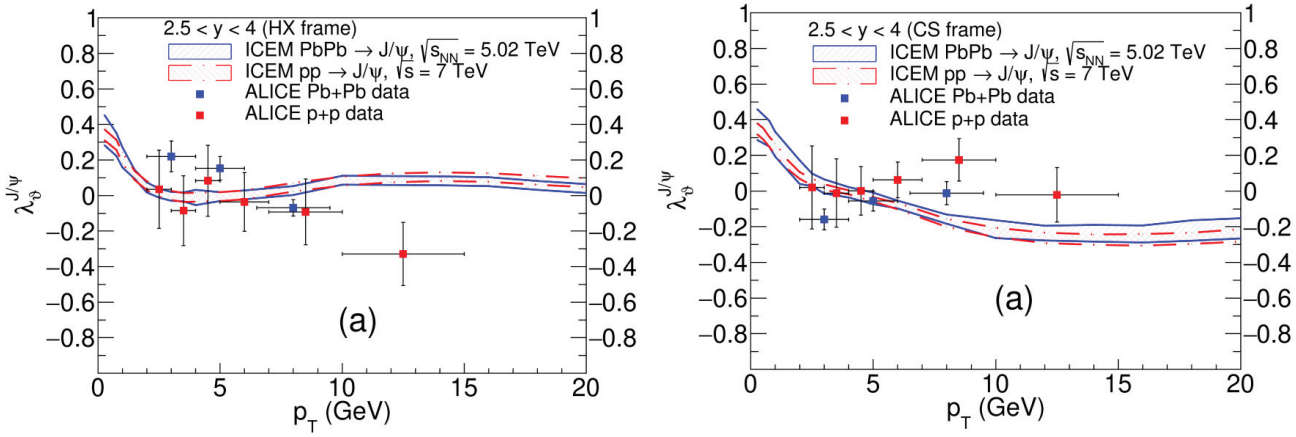

Figure 6.24: Direct J/ψ polarization parameter λ_θ in both Helicity (left) and Collins-Soper (right) frames in the ICEM model with the collinear factorization approach [154], compared to the ALICE inclusive J/Ψ polarization measurements in pp [127] and Pb–Pb [153] collisions. Figures taken from Ref. [154].

The direct comparison between the polarization measurements for quarkonium in pp and Pb–Pb collisions can provide valuable constraints on the theoretical models. To this end, Fig. 6.24 shows the ALICE inclusive J/ψ polarization measurements in pp collisions at $\sqrt{s} = 7$ TeV [127] (the J/ψ polarization results in pp collisions are comparable at 7 and 8 TeV) and Pb–Pb collisions at $\sqrt{s_{\mathrm{NN}}} = 5.02$ TeV, compared to the ICEM model with the collinear factorization approach [154], including cold nuclear matter effects on the J/ψ production in Pb–Pb collisions. The ICEM model predicts no remarkable difference between the pp and Pb–Pb collisions (it should be noted, however, that the predictions are limited to direct J/ψ production that no feed-down contributions being included in

the calculations). According to these predictions, the presence of the hot medium does not seem to affect the direct J/ψ polarization. The role of the feed-down contributions to the polarization needs to be investigated both for the charmonium and bottomonium. For bottomonium states, in particular, the measurements on polarization in Pb–Pb collisions with high precision still have to appear and are waited for Run 3.

Chapter 7

Conclusions

In this thesis, the measurements of Υ(nS) production as a function of charged-particle multiplicity and Υ(1S) polarization in pp collisions at $\sqrt{s} = 13$ TeV were presented and discussed. The Υ(nS) states were measured in the dimuon decay channel in the forward rapidity region $2.5 < y < 4.0$.

In the first part of the thesis, the measurement of Υ(nS) production as a function of charged-particle multiplicity at central rapidity ($|\eta| < 1$) is reported. The Υ(nS) states are measured in the dimuon decay channel in the forward rapidity region $2.5 < y < 4.0$, while the charged-particle multiplicity measurement is performed at central rapidity $|\eta| < 1$. In this rapidity configuration, the self-normalized Υ yield as a function of self-normalized charged-particle multiplicity density is compatible with a linear correlation with a slope of unity within the current uncertainties. This behavior is qualitatively reproduced by PYTHIA 8.2 up to four times the mean multiplicity regardless of the considered color reconnection scenario, as well as by computations from CPP and the 3-pomeron CGC approach. At higher multiplicities, the 3-pomeron CGC tends to overestimate the observed trend, while PYTHIA 8.2 underestimates it. The ratios of the self-normalized yields of Υ(2S) and Υ(3S) to Υ(1S) are compatible with unity in the explored multiplicity range within uncertainties, and in agreement with the predictions of PYTHIA 8.2, CPP and 3-pomeron CGC. However, due to the large uncertainties, the present measurement can neither confirm nor exclude a final state suppression of the Υ(2S) and Υ(3S) states at high multiplicity, as predicted by the comover scenario. The self-normalized yield ratio of Υ(1S) over J/ψ as a function of the self-normalized charged-particle multiplicity is close to unity for $\mathrm{d}N_{\mathrm{ch}}/\mathrm{d}\eta/\langle \mathrm{d}N_{\mathrm{ch}}/\mathrm{d}\eta \rangle > 1$ and described both by computations involving initial state effects (CPP, and PYTHIA 8.2 without color reconnection), and final state effects, such as the model by comovers and PYTHIA 8.2 with color reconnection. The 3-pomeron CGC approach is disfavored. An improved statistical precision of the measurements of excited states in the charmonium sector, with respect to the currently available ones [83], would also contribute in properly assessing the validity of the comover model.

In the second part of the thesis a new measurement of the Υ(1S) polarization is presented, evaluated through the estimation of the polarization parameters λ_θ, λ_φ and $\lambda_{\theta\varphi}$, which quantify the anisotropies in the angular distribu-

tions of the decay products, extracted in the Helicity and Collins-Soper reference frames. No significant Υ(1S) polarization is observed in both Helicity and Collins-Soper frames, as expected from the NLO QCD calculations [155]. This result is consistent with the measurement performed by LHCb in pp collisions at $\sqrt{s}$ =8 TeV in a similar kinematic region [129] within the large uncertainties of the ALICE results. It should be noted that, the more precise measurements of quarkonium polarization in pp collisions conducted by LHCb have revealed a slight transverse polarization for the Υ(1S) measured at $2.2 < y < 4.5$ [129] and a significant longitudinal polarization for the J/ψ measured at $2.5 < y < 4.0$ [26]. To further understand the behaviors observed in charmonium and bottomonium, a more complete theoretical picture of quarkonium polarization is needed.

As a final remark, it should be noted that the measurements reported in this thesis on bottomonium states have a limited statistical significance, preventing firm conclusions to be drawn on the origin of the measured correlation (initial vs. final state effects) and not allowing for strong constraints to be put on the available theoretical model. A better understanding of quarkonium production and polarization in a dense hadronic environment, from pp to nucleus-nucleus collisions, is a challenge requiring higher-precision and more differential measurements, which will be reached with the upgraded ALICE apparatus [156–160] starting from LHC Run 3.

Chapter 8

Summary

During my PhD, I was involved in two part of analyses: the first part is about the study of the production of Υ mesons as a function of charged-particle multiplicity in pp collisions at $\sqrt{s}$ = 13 TeV with the ALICE detector at the CERN-LHC. This analysis has been approved by the ALICE collaboration and reported in some international conferences and has be submitted to Physics Letters B. The second part is related to the study of the Υ(1S) polarization in pp collisions at $\sqrt{s} = 13$ TeV. This result was approved by ALICE as a preliminary result and presented in some international conferences or workshops, too. In the next step, the paper proposal would be followed up and the paper draft would be written. Meanwhile, I have accomplished my service task, the rivetization of charmonia production as a function of charged-particle multiplicity in pp collisions at both $\sqrt{s} = 7$ and 13 TeV (see Appendix C). This service task is a work of general interest for the whole collaboration which is required from every student enrolled in a PhD program within the ALICE collaboration.

Main conference or workshop contributions:

Oral contributions:

July, 6-13, 2022: “Quarkonium polarization in Pb–Pb and pp collisions with ALICE”, The 41st International Conference on High Energy Physics (ICHEP 2022), Italy

May, 2-6, 2022: “Υ polarization in pp and J/ψ polarization as a function of event plane in Pb–Pb with ALICE at the LHC”, The 29th International Workshop on Deep-Inelastic Scattering and Related Subjects (DIS 2022), Spain

October, 17-23, 2021: “Quarkonia excited state suppression in pp and p—Pb collisions with ALICE”, Journées de Rencontres Jeunes Chercheurs 2021 (JRJC 2021), France

July, 5-8, 2021: “Multiplicity dependence of production at forward rapidity in pp collisions at $\sqrt{s}$ = 13 TeV with ALICE”, Rencontres QGP-France 2021, France

May, 17-22, 2021: “Quarkonia excited state suppression in pp and p—Pb collisions with ALICE”, Online Strangeness in Quark Matter Conference 2021 (SQM 2021), Online

November, 6-9, 2020: “Open and hidden heavy-flavour production as a function of multiplicity in small systems at the LHC”, The 6th China LHC Physics Workshop (CLHCP 2020), Online

November, 3-6, 2018: “Quarkonium production as a function of charged particles multiplicity in pp collisions measured by ALICE at the LHC”, The 7th Asian Triangle Heavy-Ion Conference (ATHIC 2018), China

Poster contributions:

April, 4-10, 2022: “Υ(1S) polarization in pp collisions at $\sqrt{s}$ = 13 TeV with ALICE”, The 29th International Conference On Ultra-relativistic Nucleus-Nucleus Collisions (QM 2022), Online

November, 25-28, 2021: “Multiplicity dependence of production at forward rapidity in pp collisions at $\sqrt{s}$ = 13 TeV with ALICE”, The 7th China LHC Physics Workshop (CLHCP 2021), Online

November, 17-18, 2021: “Multiplicity dependence of production at forward rapidity in pp collisions at $\sqrt{s}$ = 13 TeV with ALICE”, The 148th LHCC Meeting — OPEN Session, Online

January, 10-15, 2021: “Quarkonia production and excited state suppression in pp and p–Pb with ALICE”, The $\mathrm{VI}^{\mathrm{th}}$ International Conference on Initial Stages of High-Energy Nuclear Collisions (IS 2021), Online

May, 25-30, 2020: “Υ production as a function of charged-particle multiplicity in pp collisions at $\sqrt{s} = 13$ TeV with ALICE”, 8th Edition of the Large Hadron Collider Physics Conference (LHCP 2020), Online

May, 13-19, 2018: “Charmonium production in proton-proton collisions with ALICE”, The 27th International Conference on Ultra-relativistic Nucleus-Nucleus Collisions (Quark Matter 2018), Italy

Conference proceeding: “Quarkonia production as a function of charged-particle multiplicity in pp collisions at $\sqrt{s} = 13$ TeV with ALICE”, PoS LHCP2020 (2021) 224

Bibliography

[1] **ALICE** Collaboration, "The ALICE experiment – A journey through QCD", arXiv:2211.04384 [nucl-ex].

[2] **E598** Collaboration, J. J. Aubert *et al.*, "Experimental Observation of a Heavy Particle J", *Phys. Rev. Lett.* **33** (1974) 1404–1406.

[3] **SLAC-SP-017** Collaboration, J. E. Augustin *et al.*, "Discovery of a Narrow Resonance in e^+e^- Annihilation", *Phys. Rev. Lett.* **33** (1974) 1406–1408.

[4] **Particle Data Group** Collaboration, M. Tanabashi *et al.*, "Review of Particle Physics", *Phys. Rev. D* **98** (2018) 030001.

[5] **E288** Collaboration, S. W. Herb *et al.*, "Observation of a Dimuon Resonance at 9.5 GeV in 400 GeV Proton-Nucleus Collisions", *Phys. Rev. Lett.* **39** (1977) 252–255.

[6] **E288** Collaboration, W. R. Innes *et al.*, "Observation of Structure in the Υ Region", *Phys. Rev. Lett.* **39** (1977) 1240–1242.

[7] K. Ueno *et al.*, "Evidence for the Υ'' and a Search for New Narrow Resonances", *Phys. Rev. Lett.* **42** (1979) 486–489.

[8] **Particle Data Group** Collaboration, P. Zyla *et al.*, "Review of Particle Physics", *PTEP* **2020** (2020) 083C01.

[9] H. Fritzsch, "Producing Heavy Quark Flavors in Hadronic Collisions: A Test of Quantum Chromodynamics", *Phys. Lett. B* **67** (1977) 217–221.

[10] G. T. Bodwin, E. Braaten, and G. P. Lepage, "Rigorous QCD analysis of inclusive annihilation and production of heavy quarkonium", *Phys. Rev. D* **51** (1995) 1125–1171, arXiv:hep-ph/9407339.

[11] M. B. Einhorn and S. D. Ellis, "Hadronic Production of the New Resonances: Probing Gluon Distributions", *Phys. Rev. D* **12** (1975) 2007.

[12] J. P. Lansberg, "On the mechanisms of heavy-quarkonium hadroproduction", *Eur. Phys. J. C* **61** (2009) 693–703, arXiv:0811.4005 [hep-ph].

[13] R. Vogt, "Quarkonium Production and Polarization in an Improved Color Evaporation Model", *Nucl. Phys. A* **982** (2019) 751–754.

[14] **ALICE** Collaboration, S. Acharya *et al.*, "Energy dependence of forward-rapidity J/ψ and $\psi(2\mathrm{S})$ production in pp collisions at the LHC", *Eur. Phys. J. C* **77** (2017) 392, arXiv:1702.00557 [hep-ex].

[15] **CMS** Collaboration, A. M. Sirunyan *et al.*, "Measurement of quarkonium production cross sections in pp collisions at $\sqrt{s} = 13$ TeV", *Phys. Lett. B* **780** (2018) 251–272, arXiv:1710.11002 [hep-ex].

[16] Y.-Q. Ma, K. Wang, and K.-T. Chao, "J/ψ (ψ') production at the Tevatron and LHC at $\mathcal{O}(\alpha_s^4 v^4)$ in nonrelativistic QCD", *Phys. Rev. Lett.* **106** (2011) 042002, arXiv:1009.3655 [hep-ph].

[17] Y.-Q. Ma and R. Venugopalan, "Comprehensive Description of J/ψ Production in Proton-Proton Collisions at Collider Energies", *Phys. Rev. Lett.* **113** (2014) 192301, arXiv:1408.4075 [hep-ph].

[18] M. Cacciari, S. Frixione, N. Houdeau, M. L. Mangano, P. Nason, and G. Ridolfi, "Theoretical predictions for charm and bottom production at the LHC", *JHEP* **10** (2012) 137, arXiv:1205.6344 [hep-ph].

[19] H. Han, Y.-Q. Ma, C. Meng, H.-S. Shao, Y.-J. Zhang, and K.-T. Chao, "Υ(nS) and $\chi_b(nP)$ production at hadron colliders in nonrelativistic QCD", *Phys. Rev. D* **94** (2016) 014028, arXiv:1410.8537 [hep-ph].

[20] **ALICE** Collaboration, S. Acharya *et al.*, "Inclusive quarkonium production in pp collisions at $\sqrt{s}$ = 5.02 TeV", *Eur. Phys. J. C* **83** (2023) 61, arXiv:2109.15240 [nucl-ex].

[21] **LHCb** Collaboration, R. Aaij *et al.*, "Study of J/ψ Production in Jets", *Phys. Rev. Lett.* **118** (2017) 192001, arXiv:1701.05116 [hep-ex].

[22] M. Butenschoen and B. A. Kniehl, "J/ψ polarization at Tevatron and LHC: Nonrelativistic-QCD factorization at the crossroads", *Phys. Rev. Lett.* **108** (2012) 172002, arXiv:1201.1872 [hep-ph].

[23] **CMS** Collaboration, S. Chatrchyan *et al.*, "Measurement of the Prompt J/ψ and ψ(2S) Polarizations in pp Collisions at $\sqrt{s}$ = 7 TeV", *Phys. Lett. B* **727** (2013) 381–402, arXiv:1307.6070 [hep-ex].

[24] K.-T. Chao, Y.-Q. Ma, H.-S. Shao, K. Wang, and Y.-J. Zhang, "J/ψ Polarization at Hadron Colliders in Nonrelativistic QCD", *Phys. Rev. Lett.* **108** (2012) 242004, arXiv:1201.2675 [hep-ph].

[25] H.-S. Shao and K.-T. Chao, "Spin correlations in polarizations of P-wave charmonia χ_{cJ} and impact on J/ψ polarization", *Phys. Rev. D* **90** (2014) 014002, arXiv:1209.4610 [hep-ph].

[26] **LHCb** Collaboration, R. Aaij *et al.*, "Measurement of J/ψ polarization in pp collisions at $\sqrt{s} = 7$ TeV", *Eur. Phys. J. C* **73** (2013) 2631, arXiv:1307.6379 [hep-ex].

[27] J. F. Amundson, O. J. P. Eboli, E. M. Gregores, and F. Halzen, "Quantitative tests of color evaporation: Charmonium production", *Phys. Lett. B* **390** (1997) 323–328, arXiv:hep-ph/9605295.

[28] J. P. Lansberg, "J/ψ production at $\sqrt{s}$ = 1.96 and 7 TeV: Color-Singlet Model, NNLO* and polarisation", *J. Phys. G* **38** (2011) 124110, arXiv:1107.0292 [hep-ph].

[29] T. Matsui and H. Satz, "J/ψ Suppression by Quark-Gluon Plasma Formation", *Phys. Lett. B* **178** (1986) 416–422.

[30] A. Rothkopf, "Heavy Quarkonium in Extreme Conditions", *Phys. Rept.* **858** (2020) 1–117, arXiv:1912.02253 [hep-ph].

[31] S. Digal, P. Petreczky, and H. Satz, "Quarkonium feed down and sequential suppression", *Phys. Rev. D* **64** (2001) 094015, arXiv:hep-ph/0106017.

[32] **ALICE** Collaboration, J. Adam *et al.*, "Centrality dependence of inclusive J/ψ production in p-Pb collisions at $\sqrt{s_{\rm NN}} = 5.02$ TeV", *JHEP* **11** (2015) 127, arXiv:1506.08808 [nucl-ex].

[33] Y.-p. Liu, Z. Qu, N. Xu, and P.-f. Zhuang, "J/ψ Transverse Momentum Distribution in High Energy Nuclear Collisions at RHIC", *Phys. Lett. B* **678** (2009) 72–76, arXiv:0901.2757 [nucl-th].

[34] X. Zhao and R. Rapp, "Medium Modifications and Production of Charmonia at LHC", *Nucl. Phys. A* **859** (2011) 114–125, arXiv:1102.2194 [hep-ph].

[35] P. Braun-Munzinger and J. Stachel, "(Non)thermal aspects of charmonium production and a new look at J/ψ suppression", *Phys. Lett. B* **490** (2000) 196–202, arXiv:nucl-th/0007059.

[36] R. L. Thews, M. Schroedter, and J. Rafelski, "Enhanced J/ψ production in deconfined quark matter", *Phys. Rev. C* **63** (2001) 054905, arXiv:hep-ph/0007323.

[37] A. Andronic, P. Braun-Munzinger, K. Redlich, and J. Stachel, "The thermal model on the verge of the ultimate test: particle production in Pb–Pb collisions at the LHC", *J. Phys. G* **38** (2011) 124081, arXiv:1106.6321 [nucl-th].

[38] P. Braun-Munzinger and J. Stachel, "On charm production near the phase boundary", *Nucl. Phys. A* **690** (2001) 119–126, arXiv:nucl-th/0012064.

[39] H. Satz, "Quarkonium Binding and Dissociation: The Spectral Analysis of the QGP", *Nucl. Phys. A* **783** (2007) 249–260, arXiv:hep-ph/0609197.

[40] **ALICE** Collaboration, K. Aamodt *et al.*, "Centrality dependence of the charged-particle multiplicity density at mid-rapidity in Pb–Pb collisions at $\sqrt{s_{\rm NN}} = 2.76$ TeV", *Phys. Rev. Lett.* **106** (2011) 032301, arXiv:1012.1657 [nucl-ex].

[41] **NA50** Collaboration, B. Alessandro *et al.*, "A New measurement of J/ψ suppression in Pb–Pb collisions at 158 GeV per nucleon", *Eur. Phys. J. C* **39** (2005) 335–345, arXiv:hep-ex/0412036.

[42] **NA60** Collaboration, R. Arnaldi *et al.*, "J/ψ production in indium-indium collisions at 158-GeV/nucleon", *Phys. Rev. Lett.* **99** (2007) 132302.

[43] **PHENIX** Collaboration, A. Adare *et al.*, "J/ψ Production vs Centrality, Transverse Momentum, and Rapidity in Au+Au Collisions at $\sqrt{s_{\rm NN}} = 200$ GeV", *Phys. Rev. Lett.* **98** (2007) 232301, arXiv:nucl-ex/0611020.

[44] **PHENIX** Collaboration, A. Adare *et al.*, "J/ψ suppression at forward rapidity in Au+Au collisions at $\sqrt{s_{\rm NN}} = 200$ GeV", *Phys. Rev. C* **84** (2011) 054912, arXiv:1103.6269 [nucl-ex].

[45] **STAR** Collaboration, L. Adamczyk *et al.*, "Energy dependence of J/ψ production in Au+Au collisions at $\sqrt{s_{\rm NN}} = 39$, 62.4 and 200 GeV", *Phys. Lett. B* **771** (2017) 13–20, arXiv:1607.07517 [hep-ex].

[46] **STAR** Collaboration, B. I. Abelev *et al.*, "J/ψ production at high transverse momentum in p+p and Cu+Cu collisions at $\sqrt{s_{\rm NN}} =$ = 200 GeV", *Phys. Rev. C* **80** (2009) 041902, arXiv:0904.0439 [nucl-ex].

[47] N. Brambilla *et al.*, "Heavy Quarkonium: Progress, Puzzles, and Opportunities", *Eur. Phys. J. C* **71** (2011) 1534, arXiv:1010.5827 [hep-ph].

[48] **ALICE** Collaboration, S. Acharya *et al.*, "Centrality and transverse momentum dependence of inclusive J/ψ production at midrapidity in Pb–Pb collisions at $\sqrt{s_{\rm NN}}$=5.02 TeV", *Phys. Lett. B* **805** (2020) 135434, arXiv:1910.14404 [nucl-ex].

[49] **ATLAS** Collaboration, M. Aaboud *et al.*, "Prompt and non-prompt J/ψ and $\psi(2S)$ suppression at high transverse momentum in 5.02 TeV Pb+Pb collisions with the ATLAS experiment", *Eur. Phys. J. C* **78** (2018) 762, arXiv:1805.04077 [nucl-ex].

[50] **CMS** Collaboration, A. M. Sirunyan *et al.*, "Relative Modification of Prompt ψ(2S) and J/ψ Yields from pp to Pb–Pb Collisions at $\sqrt{s_{\rm NN}} = 5.02$ TeV", *Phys. Rev. Lett.* **118** (2017) 162301, arXiv:1611.01438 [nucl-ex].

[51] **ALICE** Collaboration, J. Adam *et al.*, "J/ψ suppression at forward rapidity in Pb–Pb collisions at $\sqrt{s_{\rm NN}} = 5.02$ TeV", *Phys. Lett. B* **766** (2017) 212–224, arXiv:1606.08197 [nucl-ex].

[52] **ALICE** Collaboration, "ψ(2S) suppression in Pb–Pb collisions at the LHC", arXiv:2210.08893 [nucl-ex].

[53] X. Du and R. Rapp, "Sequential Regeneration of Charmonia in Heavy-Ion Collisions", *Nucl. Phys. A* **943** (2015) 147–158, arXiv:1504.00670 [hep-ph].

[54] A. Andronic, P. Braun-Munzinger, M. K. Köhler, K. Redlich, and J. Stachel, "Transverse momentum distributions of charmonium states with the statistical hadronization model", *Phys. Lett. B* **797** (2019) 134836, arXiv:1901.09200 [nucl-th].

[55] A. Andronic, P. Braun-Munzinger, K. Redlich, and J. Stachel, "Decoding the phase structure of QCD via particle production at high energy", *Nature* **561** (2018) 321–330, arXiv:1710.09425 [nucl-th].

[56] **CMS** Collaboration, A. M. Sirunyan *et al.*, "Measurement of prompt and nonprompt charmonium suppression in Pb–Pb collisions at 5.02 TeV", *Eur. Phys. J. C* **78** (2018) 509, arXiv:1712.08959 [nucl-ex].

[57] **NA50** Collaboration, B. Alessandro *et al.*, "ψ' production in Pb–Pb collisions at 158 GeV per nucleon", *Eur. Phys. J. C* **49** (2007) 559–567, arXiv:nucl-ex/0612013.

[58] **CMS** Collaboration, S. Chatrchyan *et al.*, "Suppression of non-prompt J/ψ, prompt J/ψ, and Υ(1S) in Pb–Pb collisions at $\sqrt{s_{\mathrm{NN}}}$ = 2.76 TeV", *JHEP* **05** (2012) 063, arXiv:1201.5069 [nucl-ex].

[59] **CMS** Collaboration, S. Chatrchyan *et al.*, "Observation of sequential Υ suppression in Pb–Pb collisions", *Phys. Rev. Lett.* **109** (2012) 222301, arXiv:1208.2826 [nucl-ex].

[60] **CMS** Collaboration, V. Khachatryan *et al.*, "Suppression of Υ(1S), Υ(2S) and Υ(3S) production in Pb–Pb collisions at $\sqrt{s_{\mathrm{NN}}}$ = 2.76 TeV", *Phys. Lett. B* **770** (2017) 357–379, arXiv:1611.01510 [nucl-ex].

[61] **CMS** Collaboration, A. M. Sirunyan *et al.*, "Measurement of nuclear modification factors of Υ(1S), Υ(2S), and Υ(3S) mesons in Pb–Pb collisions at $\sqrt{s_{\mathrm{NN}}} = 5.02$ TeV", *Phys. Lett. B* **790** (2019) 270–293, arXiv:1805.09215 [hep-ex].

[62] **ALICE** Collaboration, B. B. Abelev *et al.*, "Suppression of Υ(1S) at forward rapidity in Pb–Pb collisions at $\sqrt{s_{\mathrm{NN}}} = 2.76$ TeV", *Phys. Lett. B* **738** (2014) 361–372, arXiv:1405.4493 [nucl-ex].

[63] **ALICE** Collaboration, S. Acharya *et al.*, "Υ suppression at forward rapidity in Pb–Pb collisions at $\sqrt{s_{\mathrm{NN}}}$ = 5.02 TeV", *Phys. Lett. B* **790** (2019) 89–101, arXiv:1805.04387 [nucl-ex].

[64] **ALICE** Collaboration, S. Acharya *et al.*, "Υ production and nuclear modification at forward rapidity in Pb–Pb collisions at $\sqrt{s_{\mathrm{NN}}}$=5.02TeV", *Phys. Lett. B* **822** (2021) 136579, arXiv:2011.05758 [nucl-ex].

[65] E. G. Ferreiro and J.-P. Lansberg, "Is bottomonium suppression in proton-nucleus and nucleus-nucleus collisions at LHC energies due to the same effects?", *JHEP* **10** (2018) 094, arXiv:1804.04474 [hep-ph].

[66] B. Krouppa and M. Strickland, "Predictions for bottomonia suppression in 5.023 TeV Pb–Pb collisions", *Universe* **2** (2016) 16, arXiv:1605.03561 [hep-ph].

[67] X. Du, M. He, and R. Rapp, "Color Screening and Regeneration of Bottomonia in High-Energy Heavy-Ion Collisions", *Phys. Rev. C* **96** (2017) 054901, arXiv:1706.08670 [hep-ph].

[68] X. Yao, W. Ke, Y. Xu, S. A. Bass, and B. Müller, "Coupled Boltzmann Transport Equations of Heavy Quarks and Quarkonia in Quark-Gluon Plasma", *JHEP* **01** (2021) 046, arXiv:2004.06746 [hep-ph].

[69] Z. Citron *et al.*, "Future physics opportunities for high-density QCD at the LHC with heavy-ion and proton beams", *CERN Yellow Rep. Monogr.* **7** (2019) 1159–1410, arXiv:1812.06772 [hep-ph].

[70] C. Loizides, "Experimental overview on small collision systems at the LHC", *Nucl. Phys. A* **956** (2016) 200–207, arXiv:1602.09138 [nucl-ex].

[71] T. Sjöstrand and M. van Zijl, "A Multiple Interaction Model for the Event Structure in Hadron Collisions", *Phys. Rev. D* **36** (1987) 2019.

[72] **ALICE** Collaboration, J. Adam *et al.*, "Charged-particle multiplicities in proton–proton collisions at $\sqrt{s}$ = 0.9 to 8 TeV", *Eur. Phys. J. C* **77** (2017) 33, arXiv:1509.07541 [nucl-ex].

[73] T. Sjöstrand, S. Mrenna and P. Z. Skands, "A Brief Introduction to PYTHIA 8.1", *Comput. Phys. Commun.* **178** (2008) 852–867, arXiv:0710.3820 [hep-ph].

[74] S. G. Weber, A. Dubla, A. Andronic, and A. Morsch, "Elucidating the multiplicity dependence of J/ψ production in proton–proton collisions with PYTHIA 8", *Eur. Phys. J. C* **79** (2019) 36, arXiv:1811.07744 [nucl-th].

[75] T. Pierog, I. Karpenko, J. M. Katzy, E. Yatsenko, and K. Werner, "EPOS LHC: Test of collective hadronization with data measured at the CERN Large Hadron Collider", *Phys. Rev. C* **92** (2015) 034906, arXiv:1306.0121 [hep-ph].

[76] E. Cuautle, E. Dominguez, and I. Maldonado, "Extraction of multiple parton interactions and color reconnection from forward-backward multiplicity correlations", *Eur. Phys. J. C* **79** (2019) 626, arXiv:1907.08706 [hep-ph].

[77] J.-P. Lansberg, "New Observables in Inclusive Production of Quarkonia", *Phys. Rept.* **889** (2020) 1–106, arXiv:1903.09185 [hep-ph].

[78] A. Andronic *et al.*, "Heavy-flavour and quarkonium production in the LHC era: from proton–proton to heavy-ion collisions", *Eur. Phys. J. C* **76** (2016) 107, arXiv:1506.03981 [nucl-ex].

[79] S. Porteboeuf and R. Granier de Cassagnac, "J/ψ yield vs. multiplicity in proton-proton collisions at the LHC", *Nucl. Phys. B Proc. Suppl.* **214** (2011) 181–184, arXiv:1012.0719 [hep-ex].

[80] **ALICE** Collaboration, S. Acharya *et al.*, "Forward rapidity J/ψ production as a function of charged-particle multiplicity in pp collisions at $\sqrt{s}$ = 5.02 and 13 TeV", *JHEP* **06** (2022) 015, arXiv:2112.09433 [nucl-ex].

[81] **ALICE** Collaboration, J. Adam *et al.*, "Measurement of charm and beauty production at central rapidity versus charged-particle multiplicity in proton-proton collisions at $\sqrt{s} = 7$ TeV", *JHEP* **09** (2015) 148, arXiv:1505.00664 [nucl-ex].

[82] **ALICE** Collaboration, B. Abelev *et al.*, "J/ψ Production as a Function of Charged Particle Multiplicity in pp Collisions at $\sqrt{s} = 7$ TeV", *Phys. Lett. B* **712** (2012) 165–175, arXiv:1202.2816 [hep-ex].

[83] **ALICE** Collaboration, S. Acharya *et al.*, "Measurement of ψ(2S) production as a function of charged-particle pseudorapidity density in pp collisions at $\sqrt{s}$ = 13 TeV and p-Pb collisions at $\sqrt{s_{\rm NN}}$ = 8.16 TeV with ALICE at the LHC", *JHEP* **06** (2023) 147, arXiv:2204.10253 [nucl-ex].

[84] **ALICE** Collaboration, S. Acharya *et al.*, "Multiplicity dependence of J/ψ production at midrapidity in pp collisions at $\sqrt{s}$ = 13 TeV", *Phys. Lett. B* **810** (2020) 135758, arXiv:2005.11123 [nucl-ex].

[85] **ALICE** Collaboration, J. Adam *et al.*, "Measurement of D-meson production versus multiplicity in p-Pb collisions at $\sqrt{s_{\rm NN}} = 5.02$ TeV", *JHEP* **08** (2016) 078, arXiv:1602.07240 [nucl-ex].

[86] B. Z. Kopeliovich, H. J. Pirner, I. K. Potashnikova, K. Reygers, and I. Schmidt, "Heavy quarkonium in the saturated environment of high-multiplicity pp collisions", *Phys. Rev. D* **101** (2020) 054023, arXiv:1910.09682 [hep-ph].

[87] Y.-Q. Ma, P. Tribedy, R. Venugopalan, and K. Watanabe, "Event engineering studies for heavy flavor production and hadronization in high multiplicity hadron-hadron and hadron-nucleus collisions", *Phys. Rev. D* **98** (2018) 074025, arXiv:1803.11093 [hep-ph].

[88] E. Levin, I. Schmidt, and M. Siddikov, "Multiplicity dependence of quarkonia production in the CGC approach", *Eur. Phys. J. C* **80** (2020) 560, arXiv:1910.13579 [hep-ph].

[89] E. G. Ferreiro and C. Pajares, "High multiplicity pp events and J/ψ production at LHC", *Phys. Rev. C* **86** (2012) 034903, arXiv:1203.5936 [hep-ph].

[90] K. Werner, B. Guiot, I. Karpenko, and T. Pierog, "Analysing radial flow features in p-Pb and p-p collisions at several TeV by studying identified particle production in EPOS3", *Phys. Rev. C* **89** (2014) 064903, arXiv:1312.1233 [nucl-th].

[91] T. Sjöstrand, S. Ask, J. R. Christiansen, R. Corke, N. Desai, P. Ilten, S. Mrenna, S. Prestel, C. O. Rasmussen, and P. Z. Skands, "An introduction to PYTHIA 8.2", *Comput. Phys. Commun.* **191** (2015) 159–177, arXiv:1410.3012 [hep-ph].

[92] **STAR** Collaboration, J. Adam *et al.*, "J/ψ production cross section and its dependence on charged-particle multiplicity in p + p collisions at $\sqrt{s}$ = 200 GeV", *Phys. Lett. B* **786** (2018) 87–93, arXiv:1805.03745 [hep-ex].

[93] B. Z. Kopeliovich, H. J. Pirner, I. K. Potashnikova, K. Reygers, and I. Schmidt, "J/ψ in high-multiplicity pp collisions: Lessons from pA collisions", *Phys. Rev. D* **88** (2013) 116002, arXiv:1308.3638 [hep-ph].

[94] L. Frankfurt, M. Strikman, D. Treleani, and C. Weiss, "Evidence for color fluctuations in the nucleon in high-energy scattering", *Phys. Rev. Lett.* **101** (2008) 202003, arXiv:0808.0182 [hep-ph].

[95] M. Strikman, "Transverse structure of the nucleon and multiparton interactions", *Prog. Theor. Phys. Suppl.* **187** (2011) 289–296.

[96] **CMS** Collaboration, S. Chatrchyan *et al.*, "Event Activity Dependence of Υ(nS) Production in $\sqrt{s_{\mathrm{NN}}}$ = 5.02 TeV p-Pb and $\sqrt{s}$ = 2.76 TeV pp Collisions", *JHEP* **04** (2014) 103, arXiv:1312.6300 [nucl-ex].

[97] B. Krouppa, R. Ryblewski, and M. Strickland, "Bottomonia suppression in 2.76 TeV Pb–Pb collisions", *Phys. Rev. C* **92** (2015) 061901, arXiv:1507.03951 [hep-ph].

[98] **ALICE** Collaboration, S. Acharya *et al.*, "Υ suppression at forward rapidity in Pb–Pb collisions at $\sqrt{s_{\mathrm{NN}}}$ = 5.02 TeV", *Phys. Lett. B* **790** (2019) 89–101, arXiv:1805.04387 [nucl-ex].

[99] E. G. Ferreiro, "Excited charmonium suppression in proton–nucleus collisions as a consequence of comovers", *Phys. Lett. B* **749** (2015) 98–103, arXiv:1411.0549 [hep-ph].

[100] A. Esposito, E. G. Ferreiro, A. Pilloni, A. D. Polosa, and C. A. Salgado, "The nature of $X(3872)$ from high-multiplicity pp collisions", *Eur. Phys. J. C* **81** (2021) 669, arXiv:2006.15044 [hep-ph].

[101] **CMS** Collaboration, A. M. Sirunyan *et al.*, "Investigation into the event-activity dependence of Υ(nS) relative production in proton-proton collisions at $\sqrt{s}$ = 7 TeV", *JHEP* **11** (2020) 001, arXiv:2007.04277 [hep-ex].

[102] **ALICE** Collaboration, S. Acharya *et al.*, "Υ production in p–Pb collisions at $\sqrt{s_{\mathrm{NN}}}$ = 8.16 TeV", *Phys. Lett. B* **806** (2020) 135486, arXiv:1910.14405 [nucl-ex].

[103] Faccioli, Pietro and Lourenco, Carlos and Seixas, Joao and Wöhri, Hermine K., "Towards the experimental clarification of quarkonium polarization", *Eur. Phys. J. C* **69** (2010) 657–673, arXiv:1006.2738 [hep-ph].

[104] D. M. Brink and G. R. Satchler, *Angular momentum*. Clarendon Press, 3 ed., 1993.

[105] P. Faccioli, C. Lourenco, J. Seixas, and H. K. Wohri, "Model-independent constraints on the shape parameters of dilepton angular distributions", *Phys. Rev. D* **83** (2011) 056008, arXiv:1102.3946 [hep-ph].

[106] J. C. Collins and D. E. Soper, "Angular Distribution of Dileptons in High-Energy Hadron Collisions", *Phys. Rev. D* **16** (1977) 2219.

[107] K. Gottfried and J. D. Jackson, "On the Connection between production mechanism and decay of resonances at high-energies", *Nuovo Cim.* **33** (1964) 309–330.

[108] **CDF** Collaboration, D. Acosta *et al.*, "Measurement of the J/ψ meson and $b-$hadron production cross sections in $p\bar{p}$ collisions at $\sqrt{s} = 1960$ GeV", *Phys. Rev. D* **71** (2005) 032001, arXiv:hep-ex/0412071.

[109] **CDF** Collaboration, D. Acosta *et al.*, "Υ Production and Polarization in $p\bar{p}$ Collisions at $\sqrt{s} = 1.8$ TeV", *Phys. Rev. Lett.* **88** (2002) 161802.

[110] **D0** Collaboration, V. M. Abazov *et al.*, "Measurement of inclusive differential cross sections for Υ(1S) production in $p\bar{p}$ collisions at $\sqrt{s}$ = 1.96 TeV", *Phys. Rev. Lett.* **94** (2005) 232001, arXiv:hep-ex/0502030.

[111] **CMS** Collaboration, S. Chatrchyan *et al.*, "J/ψ and ψ(2S) production in pp collisions at $\sqrt{s} = 7$ TeV", *JHEP* **02** (2012) 011, arXiv:1111.1557 [hep-ex].

[112] **LHCb** Collaboration, R. Aaij *et al.*, "Measurement of Υ production in pp collisions at $\sqrt{s}$ = 7 TeV", *Eur. Phys. J. C* **72** (2012) 2025, arXiv:1202.6579 [hep-ex].

[113] **CMS** Collaboration, V. Khachatryan *et al.*, "Upsilon Production Cross-Section in pp Collisions at $\sqrt{s}$ = 7 TeV", *Phys. Rev. D* **83** (2011) 112004, arXiv:1012.5545 [hep-ex].

[114] B. Gong, J.-X. Wang, and H.-F. Zhang, "QCD corrections to Υ production via color-octet states at the Tevatron and LHC", *Phys. Rev. D* **83** (2011) 114021, arXiv:1009.3839 [hep-ph].

[115] **CDF** Collaboration, A. Abulencia *et al.*, "Polarization of J/ψ and ψ(2S) Mesons Produced in $p\bar{p}$ Collisions at $\sqrt{s}$ = 1.96 TeV", *Phys. Rev. Lett.* **99** (2007) 132001, arXiv:0704.0638 [hep-ex].

[116] **CMS** Collaboration, S. Chatrchyan *et al.*, "Measurement of the Υ(1S), Υ(2S) and Υ(3S) Polarizations in pp Collisions at $\sqrt{s} = 7$ TeV", *Phys. Rev. Lett.* **110** (2013) 081802, arXiv:1209.2922 [hep-ex].

[117] **CDF** Collaboration, T. Affolder *et al.*, "Measurement of J/ψ and ψ(2S) Polarization in $p\bar{p}$ Collisions at $\sqrt{s} = 1.8$ TeV", *Phys. Rev. Lett.* **85** (2000) 2886–2891, arXiv:hep-ex/0004027.

[118] **D0** Collaboration, V. M. Abazov *et al.*, "Measurement of the polarization of the Υ(1S) and Υ(2S) states in $p\bar{p}$ collisions at $\sqrt{s}$ = 1.96 TeV", *Phys. Rev. Lett.* **101** (2008) 182004, arXiv:0804.2799 [hep-ex].

[119] E. Braaten, B. A. Kniehl, and J. Lee, "Polarization of prompt J/ψ at the Tevatron", *Phys. Rev. D* **62** (2000) 094005, arXiv:hep-ph/9911436.

[120] S. P. Baranov, "Highlights from the k_{T} factorization approach on the quarkonium production puzzles", *Phys. Rev. D* **66** (2002) 114003.

[121] E. Braaten and J. Lee, "Polarization of Υ(nS) at the Tevatron", *Phys. Rev. D* **63** (2001) 071501, arXiv:hep-ph/0012244.

[122] **STAR** Collaboration, J. Adam *et al.*, "Measurement of inclusive J/ψ polarization in $p + p$ collisions at $\sqrt{s}$ =200 GeV by the STAR experiment", *Phys. Rev. D* **102** (2020) 092009, arXiv:2007.04732 [hep-ex].

[123] Y.-Q. Ma, T. Stebel, and R. Venugopalan, "J/ψ polarization in the CGC+NRQCD approach", *JHEP* **12** (2018) 057, arXiv:1809.03573 [hep-ph].

[124] V. Cheung and R. Vogt, "Production and polarization of prompt J/ψ in the improved color evaporation model using the k_T-factorization approach", *Phys. Rev. D* **98** (2018) 114029, arXiv:1808.02909 [hep-ph].

[125] B. Gong, L.-P. Wan, J.-X. Wang, and H.-F. Zhang, "Polarization for Prompt J/ψ and ψ(2S) Production at the Tevatron and LHC", *Phys. Rev. Lett.* **110** (2013) 042002, arXiv:1205.6682 [hep-ph].

[126] H.-F. Zhang, Z. Sun, W.-L. Sang, and R. Li, "Impact of η_c hadroproduction data on charmonium production and polarization within NRQCD framework", *Phys. Rev. Lett.* **114** (2015) 092006, arXiv:1412.0508 [hep-ph].

[127] **ALICE** Collaboration, B. Abelev *et al.*, "J/ψ polarization in pp collisions at $\sqrt{s} = 7$ TeV", *Phys. Rev. Lett.* **108** (2012) 082001, arXiv:1111.1630 [hep-ex].

[128] **ALICE** Collaboration, S. Acharya *et al.*, "Measurement of the inclusive J/ψ polarization at forward rapidity in pp collisions at $\sqrt{\mathrm{s}} = 8$ TeV", *Eur. Phys. J. C* **78** (2018) 562, arXiv:1805.04374 [hep-ex].

[129] **LHCb** Collaboration, R. Aaij *et al.*, "Measurement of the Υ polarizations in pp collisions at $\sqrt{s}$ = 7 and 8 TeV", *JHEP* **12** (2017) 110, arXiv:1709.01301 [hep-ex].

[130] **CMS** Collaboration, A. M. Sirunyan *et al.*, "Constraints on the χ_{c1} versus χ_{c2} Polarizations in Proton-Proton Collisions at $\sqrt{s} = 8$ TeV", *Phys. Rev. Lett.* **124** (2020) 162002, arXiv:1912.07706 [hep-ex].

[131] P. Faccioli, C. Lourenço, M. Araújo, J. a. Seixas, I. Krätschmer, and V. Knünz, "From identical S- and P-wave p_{T} spectra to maximally distinct polarizations: probing NRQCD with χ states", *Eur. Phys. J. C* **78** (2018) 268, arXiv:1802.01106 [hep-ph].

[132] "LHC Machine", *JINST* **3** (2008) S08001.

[133] S. L. Glashow, J. Iliopoulos, and L. Maiani, "Weak Interactions with Lepton-Hadron Symmetry", *Phys. Rev. D* **2** (1970) 1285–1292.

[134] **ALICE** Collaboration, K. Aamodt *et al.*, "Alignment of the ALICE Inner Tracking System with cosmic-ray tracks", *JINST* **5** (2010) P03003, arXiv:1001.0502 [physics.ins-det].

[135] **ALICE** Collaboration, "Addendum of the Letter of Intent for the upgrade of the ALICE experiment : The Muon Forward Tracker", tech. rep., CERN, Geneva, 2013. https://cds.cern.ch/record/1592659.

[136] **ALICE** Collaboration, B. B. Abelev *et al.*, "Performance of the ALICE Experiment at the CERN LHC", *Int. J. Mod. Phys. A* **29** (2014) 1430044, arXiv:1402.4476 [nucl-ex].

[137] **ALICE** Collaboration, H. Engel, T. Alt, T. Breitner, A. G. Ramirez, T. Kollegger, M. Krzewicki, J. Lehrbach, D. Rohr, and U. Kebschull, "The ALICE high-level trigger read-out upgrade for LHC Run 2", *JINST* **11** (2016) C01041.

[138] **ALICE** Collaboration, "Quarkonium signal extraction in ALICE", *ALICE-PUBLIC-2015-006* (2015) . http://cds.cern.ch/record/2060096.

[139] **ALICE** Collaboration, "Alice analysis repository", *GITHUB-ALICESW-ALIPHYSICS* . https://github.com/alisw/AliPhysics/.

[140] T. Chowdhury, *Study of Υ production as a function of charged-particle multiplicity in proton-proton collisions at $\sqrt{s}$ = 13 TeV with ALICE at the LHC*. Phd thesis, Université Clermont Auvergne, 2019. http://cds.cern.ch/record/2691433.

[141] J. Martin Blanco, *Study of J/ψ production dependence with the charged particle multiplicity in p-Pb collisions at $\sqrt{s_{\rm NN}}$ = 5.02 TeV and pp collisions at $\sqrt{s}$ = 8 TeV with the ALICE experiment at the LHC*. Phd thesis, Université de Nantes, 2016. https://cds.cern.ch/record/2651031.

[142] D. Thakur, *Multiplicity dependence of Forward Rapidity J/ψ Production in Proton+Proton Collisions with ALICE at the LHC and Study of Particle Production in High-Energy Collisions*. Phd thesis, Indian Institute of Technology Indore, 2019. https://cds.cern.ch/record/2689357.

[143] **ALICE** Collaboration, J. Adam *et al.*, "Pseudorapidity and transverse-momentum distributions of charged particles in proton–proton collisions at $\sqrt{s} = 13$ TeV", *Phys. Lett. B* **753** (2016) 319–329, arXiv:1509.08734 [nucl-ex].

[144] R. Brun, F. Bruyant, F. Carminati, S. Giani, M. Maire, A. McPherson, G. Patrick, and L. Urban, "GEANT Detector Description and Simulation Tool", *CERN Program Library* (1994) .

[145] **ALICE** Collaboration, S. Acharya *et al.*, "Pseudorapidity distributions of charged particles as a function of mid- and forward rapidity multiplicities in pp collisions at $\sqrt{s}$ = 5.02, 7 and 13 TeV", *Eur. Phys. J. C* **81** (2021) 630, arXiv:2009.09434 [nucl-ex].

[146] **ALICE** Collaboration, S. Acharya *et al.*, "Measurement of Υ(1S) elliptic flow at forward rapidity in Pb–Pb collisions at $\sqrt{s_{\rm NN}} = 5.02$ TeV", *Phys. Rev. Lett.* **123** (2019) 192301, arXiv:1907.03169 [nucl-ex].

[147] M. Guittière, "ψ(2S) production as a function of charged-particle pseudorapidity density in pp collisions at $\sqrt{s}$ = 13 TeV", *ALICE Analysis Note* (2020) .

[148] J. R. Christiansen and P. Z. Skands, "String Formation Beyond Leading Colour", *JHEP* **08** (2015) 003, arXiv:1505.01681 [hep-ph].

[149] B. Z. Kopeliovich, H. J. Pirner, I. K. Potashnikova, and I. Schmidt, "Mutual boosting of the saturation scales in colliding nuclei", *Phys. Lett. B* **697** (2011) 333–338, arXiv:1007.1913 [hep-ph].

[150] **LHCb** Collaboration, R. Aaij *et al.*, "Measurement of Υ production in pp collisions at $\sqrt{s}$= 13 TeV", *JHEP* **07** (2018) 134, arXiv:1804.09214 [hep-ex].

[151] B. Gong, L.-P. Wan, J.-X. Wang, and H.-F. Zhang, "Complete next-to-leading-order study on the yield and polarization of Υ(1S, 2S, 3S) at the Tevatron and LHC", *Phys. Rev. Lett.* **112** (2014) 032001, arXiv:1305.0748 [hep-ph].

[152] V. Cheung and R. Vogt, "Production and polarization of prompt Υ(nS) in the improved color evaporation model using the k_{T}-factorization approach", *Phys. Rev. D* **99** (2019) 034007, arXiv:1811.11570 [hep-ph].

[153] **ALICE** Collaboration, S. Acharya *et al.*, "First measurement of quarkonium polarization in nuclear collisions at the LHC", *Phys. Lett. B* **815** (2021) 136146, arXiv:2005.11128 [nucl-ex].

[154] V. Cheung and R. Vogt, "Quarkonium polarization in Pb+Pb collisions in the improved color evaporation model", *Phys. Rev. C* **105** (2022) 055202, arXiv:2203.10154 [hep-ph].

[155] Y. Feng, B. Gong, C.-H. Chang, and J.-X. Wang, "Complete study on polarization of Υ(nS) hadroproduction at QCD next-to-leading order", *Chin. Phys. C* **45** (2021) 013117, arXiv:2009.03028 [hep-ph].

[156] **ALICE** Collaboration, B. Abelev *et al.*, "Technical Design Report for the Upgrade of the ALICE Inner Tracking System", *J. Phys. G* **41** (2014) 087002.

[157] **ALICE** Collaboration, G. Martinez-Garcia and W. Riegler, "Technical Design Report for the Muon Forward Tracker", tech. rep., CERN-LHCC-2015-001, ALICE-TDR-018, 2015. https://cds.cern.ch/record/1981898.

[158] **ALICE** Collaboration, R. Münzer, "Upgrade of the ALICE Time Projection Chamber", *Nucl. Instrum. Meth. A* **958** (2020) 162058.

[159] **ALICE** Collaboration, P. Antonioli, A. Kluge, and W. Riegler, "Upgrade of the ALICE Readout and Trigger System", tech. rep., CERN-LHCC-2013-019, ALICE-TDR-015, 2013. https://cds.cern.ch/record/1603472.

[160] **ALICE** Collaboration, P. Buncic, M. Krzewicki, and P. Vande Vyvre, "Technical Design Report for the Upgrade of the Online-Offline Computing System", tech. rep., CERN-LHCC-2015-006, ALICE-TDR-019, 2015. https://cds.cern.ch/record/2011297.

[161] Y. Ding, "Υ(1S) polarization in pp collisions at $\sqrt{s} = 13$ TeV", *ALICE Physics Analysis Group Meeting* (2021) .

[162] Y. Ding, "Υ(1S) polarization in pp collisions at $\sqrt{s} = 13$ TeV", *ALICE Physics Analysis Group Meeting* (2022) .

[163] G. Marchesini, B. R. Webber, G. Abbiendi, I. G. Knowles, M. H. Seymour, and L. Stanco, "HERWIG: A Monte Carlo event generator for simulating hadron emission reactions with interfering gluons. Version 5.1 - April 1991", *Comput. Phys. Commun.* **67** (1992) 465–508.

[164] J. Bellm *et al.*, "Herwig 7.2 release note", *Eur. Phys. J. C* **80** (2020) 452, arXiv:1912.06509 [hep-ph].

[165] J. Bellm *et al.*, "Herwig 7.0/Herwig++ 3.0 release note", *Eur. Phys. J. C* **76** (2016) 196, arXiv:1512.01178 [hep-ph].

[166] G. Bíró, G. G. Barnaföldi, G. Papp, M. Gyulassy, P. Lévai, X.-N. Wang, and B.-W. Zhang, "Introducing HIJING++: the Heavy Ion Monte Carlo Generator for the High-Luminosity LHC Era", *PoS* **HardProbes2018** (2019) 045, arXiv:1901.04220 [physics.comp-ph].

[167] P. Skands, S. Carrazza, and J. Rojo, "Tuning PYTHIA 8.1: the Monash 2013 Tune", *Eur. Phys. J. C* **74** (2014) 3024, arXiv:1404.5630 [hep-ph].

[168] **CMS** Collaboration, V. Khachatryan *et al.*, "Event generator tunes obtained from underlying event and multiparton scattering measurements", *Eur. Phys. J. C* **76** (2016) 155, arXiv:1512.00815 [hep-ex].

[169] **ATLAS** Collaboration, "Summary of ATLAS Pythia 8 tunes", *ATL-PHYS-PUB-2012-003* (2012) . http://cdsweb.cern.ch/record/1474107.

[170] C. Bierlich *et al.*, "Confronting experimental data with heavy-ion models: RIVET for heavy ions", *Eur. Phys. J. C* **80** (2020) 485, arXiv:2001.10737 [hep-ph].

[171] E. Maguire, L. Heinrich, and G. Watt, "HEPData: a repository for high energy physics data", *J. Phys. Conf. Ser.* **898** (2017) 102006, arXiv:1704.05473 [hep-ex].

[172] M. Dobbs and J. B. Hansen, "The HepMC C++ Monte Carlo event record for High Energy Physics", *Comput. Phys. Commun.* **134** (2001) 41–46.

Appendix A

Upsilon production as a function of multiplicity

A.1 Run list for multiplicity dependent Υ(nS) production analysis

LHC16h (pass1) AOD 208, 72 runs:

255467, 255466, 255465, 255463, 255447, 255442, 255440, 255415, 255402, 255398, 255352, 255351, 255350, 255283, 255280, 255276, 255275, 255256, 255255, 255253, 255252, 255251, 255249, 255248, 255247, 255242, 255240, 255182, 255180, 255177, 255176, 255173, 255171, 255167, 255162, 255159, 255154, 255111, 255091, 255086, 255085, 255082, 255079, 255076, 255075, 255074, 255073, 255071, 255068, 255042, 255010, 255009, 255008, 254984, 254983, 254654, 254653, 254652, 254651, 254649, 254648, 254646, 254644, 254640, 254632, 254630, 254629, 254621, 254608, 254606, 254604, 254419

LHC16j (pass1) AOD 208, 49 runs:

256420, 256418, 256417, 256415, 256373, 256372, 256371, 256368, 256366, 256365, 256364, 256363, 256362, 256361, 256356, 256311, 256307, 256302, 256298, 256297, 256295, 256292, 256290, 256289, 256287, 256284, 256283, 256282, 256281, 256231, 256228, 256227, 256223, 256222, 256219, 256215, 256213, 256212, 256210, 256204, 256169, 256161, 256158, 256157, 256156, 256149, 256148, 256147, 256146

LHC16k (pass1) AOD, 171 runs:

258537, 258499, 258498, 258477, 258456, 258454, 258452, 258426, 258399, 258393, 258391, 258388, 258387, 258359, 258336, 258332, 258307, 258306, 258303, 258302, 258301, 258299, 258280, 258278, 258274, 258273, 258271, 258270, 258258, 258257, 258256, 258204, 258203, 258202, 258197, 258178, 258117, 258114, 258113,

258109, 258108, 258107, 258063, 258062, 258060, 258059, 258049, 258048, 258045, 258042, 258041, 258039, 258019, 258017, 258014, 258012, 258008, 257989, 257986, 257979, 257963, 257960, 257958, 257957, 257939, 257937, 257936, 257932, 257912, 257901, 257893, 257892, 257737, 257735, 257734, 257733, 257727, 257725, 257724, 257697, 257694, 257688, 257687, 257685, 257684, 257682, 257644, 257642, 257636, 257635, 257632, 257630, 257606, 257605, 257604, 257601, 257595, 257594, 257592, 257590, 257588, 257587, 257566, 257565, 257564, 257563, 257562, 257561, 257560, 257541, 257540, 257531, 257530, 257492, 257491, 257490, 257488, 257487, 257474, 257468, 257457, 257433, 257364, 257358, 257330, 257322, 257320, 257318, 257260, 257224, 257095, 257092, 257086, 257084, 257083, 257082, 257080, 257077, 257071, 257026, 257021, 257012, 257011, 256944, 256942, 256941, 256697, 256695, 256694, 256691, 256684, 256681, 256677, 256676, 256658, 256620, 256619, 256591, 256567, 256565, 256564, 256561, 256560, 256557, 256556, 256554, 256552, 256512, 256510, 256506, 256504

LHC16o (pass1) AOD 208, 101 runs:
264035, 264033, 263985, 263984, 263981, 263979, 263978, 263977, 263923, 263920, 263917, 263916, 263905, 263866, 263863, 263861, 263830, 263829, 263824, 263823, 263813, 263810, 263803, 263793, 263792, 263790, 263787, 263786, 263785, 263784, 263744, 263743, 263741, 263739, 263738, 263737, 263691, 263690, 263689, 263682, 263662, 263657, 263654, 263653, 263652, 263647, 263529, 263497, 263496, 263490, 263487, 263332, 262858, 262855, 262853, 262849, 262847, 262844, 262842, 262841, 262778, 262777, 262776, 262768, 262760, 262727, 262725, 262723, 262719, 262717, 262713, 262705, 262635, 262632, 262628, 262594, 262593, 262583, 262578, 262574, 262572, 262571, 262570, 262569, 262568, 262567, 262563, 262537, 262533, 262532, 262528, 262492, 262487, 262451, 262430, 262428, 262424, 262423, 262422, 262419, 262418

LHC16p (pass1) AOD 208, 38 runs:
264347, 264346, 264345, 264341, 264336, 264312, 264305, 264281, 264279, 264277, 264273, 264267, 264266, 264265, 264264, 264262, 264261, 264260, 264259, 264238, 264233, 264232, 264198, 264197, 264194, 264188, 264168, 264164, 264138, 264137, 264129, 264110, 264109, 264086, 264085, 264082, 264078, 264076

LHC17i (muon_calo_pass1), AOD, 56 runs:
274442, 274390, 274387, 274385, 274364, 274363, 274360, 274357, 274355, 274329, 274283, 274281, 274280, 274278, 274276, 274271, 274270, 274269, 274268, 274266, 274264, 274263, 274259, 274232, 274212, 274148, 274147, 274125, 274094, 274092, 274064, 274063, 274058, 273986, 273985, 273946, 273942, 273918, 273889, 273887, 273886, 273885, 273825, 273824, 273719, 273711, 273709, 273695, 273690, 273689, 273687, 273654, 273653, 273593, 273592, 273591

LHC17k (muon_calo_pass1), AOD, 100 runs:

276508, 276507, 276506, 276500, 276462, 276461, 276439, 276438, 276437, 276435, 276434, 276432, 276429, 276351, 276348, 276302, 276297, 276294, 276292, 276291, 276290, 276259, 276230, 276205, 276178, 276177, 276170, 276169, 276166, 276145, 276141, 276140, 276108, 276105, 276104, 276102, 276099, 276098, 275664, 275661, 275657, 275650, 275648, 275624, 275559, 275558, 275515, 275472, 275471, 275467, 275459, 275457, 275453, 275452, 275448, 275406, 275404, 275401, 275369, 275361, 275360, 275357, 275332, 275328, 275283, 275247, 275246, 275245, 275188, 275177, 275175, 275174, 275173, 275151, 275150, 275149, 275076, 275075, 275073, 275070, 275068, 275067, 274979, 274978, 274886, 274884, 274883, 274882, 274822, 274817, 274815, 274811, 274807, 274806, 274803, 274802, 274801, 274743, 274736, 274708

LHC17m (muon_calo_pass1), AOD, 117 runs:

280140, 280135, 280134, 280131, 280126, 280118, 280114, 280111, 280108, 280066, 280052, 280051, 280049, 279955, 279954, 279952, 279893, 279890, 279886, 279884, 279880, 279879, 279855, 279854, 279853, 279830, 279827, 279826, 279773, 279749, 279747, 279719, 279718, 279715, 279689, 279688, 279684, 279683, 279682, 279679, 279677, 279676, 279642, 279641, 279600, 279598, 279597, 279583, 279565, 279564, 279563, 279562, 279561, 279560, 279559, 279488, 279487, 279483, 279441, 279439, 279435, 279410, 279391, 279355, 279354, 279349, 279348, 279344, 279342, 279312, 279310, 279309, 279274, 279273, 279270, 279268, 279267, 279265, 279264, 279242, 279238, 279235, 279234, 279208, 279207, 279201, 279199, 279157, 279155, 279130, 279125, 279123, 279122, 279117, 279106, 279075, 279074, 279073, 279068, 279044, 279043, 279041, 279038, 279037, 279036, 279008, 279007, 279005, 278999, 278964, 278963, 278959, 278941, 278939, 278936, 278915, 278914

LHC17o (muon_calo_pass1), AOD203, 170 runs:

281961, 281956, 281953, 281946, 281940, 281939, 281931, 281928, 281918, 281916, 281915, 281894, 281893, 281892, 281755, 281754, 281753, 281751, 281750, 281741, 281713, 281709, 281707, 281706, 281705, 281672, 281667, 281664, 281658, 281655, 281654, 281651, 281645, 281642, 281640, 281635, 281634, 281633, 281592, 281583, 281581, 281580, 281574, 281569, 281568, 281563, 281562, 281557, 281511, 281509, 281477, 281475, 281450, 281449, 281446, 281444, 281441, 281415, 281321, 281301, 281277, 281275, 281244, 281243, 281242, 281241, 281240, 281213, 281212, 281191, 281190, 281181, 281180, 281179, 281081, 281080, 281079, 281062, 281061, 281060, 281036, 281035, 281033, 281032, 280998, 280997, 280996, 280994, 280990, 280947, 280943, 280940, 280936, 280897, 280890, 280881, 280880, 280856, 280848, 280847, 280845, 280844, 280842, 280793, 280792, 280786, 280768, 280767, 280766, 280765, 280764, 280763, 280761, 280756, 280755, 280754, 280753, 280706, 280705, 280681, 280679, 280676, 280671, 280650, 280648, 280647, 280645, 280639, 280637, 280634, 280613, 280583, 280581, 280576, 280575, 280574, 280551, 280550, 280547, 280546, 280519, 280518, 280448, 280447, 280446, 280445, 280443, 280419, 280418, 280415, 280413, 280412, 280406, 280405, 280403, 280375,

280374, 280352, 280351, 280350, 280349, 280348, 280312, 280310, 280290, 280286, 280285, 280284, 280283, 280282

LHC17r (muon_calo_pass1), AOD, 32 runs:
282704, 282703, 282702, 282700, 282677, 282676, 282673, 282671, 282670, 282668, 282667, 282666, 282653, 282651, 282629, 282622, 282620, 282618, 282615, 282609, 282608, 282607, 282606, 282580, 282579, 282575, 282573, 282546, 282545, 282544, 282528, 282504

LHC18d (muon_calo_pass1), AOD, 45 runs:
286350, 286349, 286348, 286345, 286340, 286337, 286336, 286314, 286313, 286312, 286311, 286310, 286309, 286308, 286289, 286288, 286287, 286284, 286282, 286261, 286258, 286257, 286254, 286230, 286229, 286203, 286202, 286201, 286199, 286198, 286159, 286130, 286129, 286127, 286124, 286064, 286028, 286027, 286026, 286025, 286018, 286014, 285980, 285979, 285978

LHC18e (muon_calo_pass1), AOD, 44 runs:
286937, 286936, 286933, 286932, 286931, 286930, 286911, 286910, 286908, 286907, 286877, 286876, 286874, 286852, 286850, 286848, 286846, 286810, 286809, 286805, 286801, 286799, 286731, 286695, 286661, 286653, 286633, 286594, 286592, 286591, 286569, 286568, 286567, 286566, 286509, 286508, 286502, 286501, 286455, 286454, 286428, 286427, 286426, 286380

LHC18f (muon_calo_pass1), AOD, 68 runs:
287977, 287975, 287941, 287923, 287784, 287783, 287658, 287657, 287656, 287654, 287578, 287576, 287575, 287573, 287524, 287521, 287520, 287518, 287517, 287516, 287513, 287486, 287484, 287481, 287480, 287451, 287413, 287389, 287388, 287387, 287385, 287381, 287380, 287360, 287358, 287356, 287355, 287353, 287349, 287347, 287346, 287344, 287343, 287325, 287324, 287323, 287283, 287254, 287251, 287250, 287249, 287248, 287209, 287208, 287204, 287203, 287202, 287201, 287155, 287137, 287077, 287072, 287071, 287066, 287064, 287063, 287021, 287000

LHC18l (muon_calo_pass1), AOD, 85 runs:
289971, 289966, 289943, 289941, 289940, 289935, 289931, 289928, 289888, 289884, 289880, 289857, 289856, 289855, 289852, 289849, 289830, 289816, 289815, 289814, 289811, 289808, 289775, 289757, 289731, 289729, 289724, 289723, 289721, 289666, 289664, 289660, 289659, 289658, 289657, 289654, 289632, 289626, 289625, 289582, 289581, 289579, 289577, 289576, 289574, 289547, 289494, 289493, 289468, 289466, 289465, 289463, 289462, 289444, 289426, 289373, 289370, 289369, 289368, 289367, 289366, 289365, 289363, 289356, 289355,

289354, 289353, 289309, 289308, 289306, 289303, 289300, 289280, 289278, 289277, 289276, 289275, 289254, 289253, 289249, 289247, 289243, 289242, 289241, 289240

A.2 Raw profile ratio between CMUL7 and CINT7 triggered events

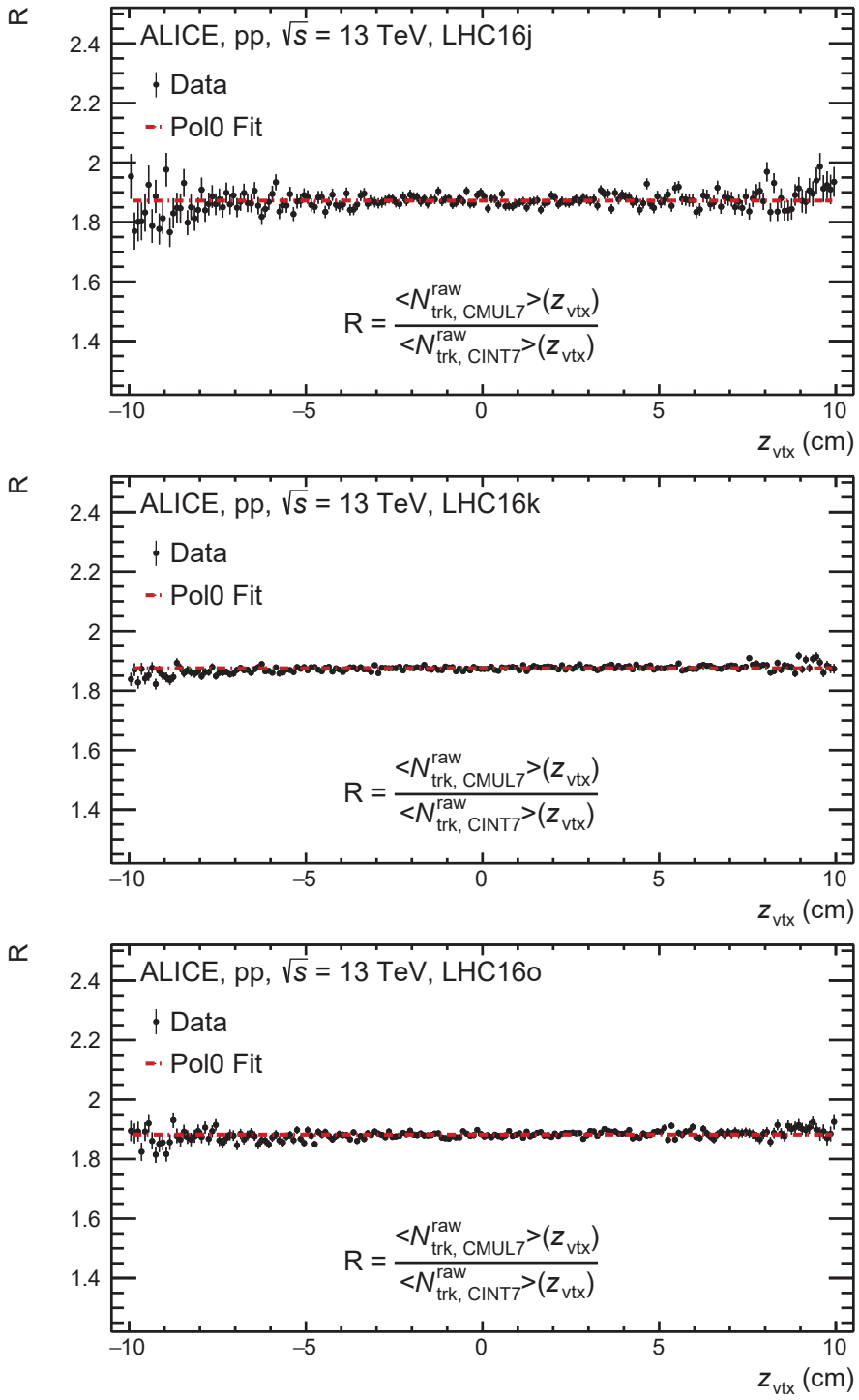

Figure A.1: Ratios of the average number of raw tracklets as a function of z_{vtx} between CMUL7 and CINT7 triggered events for LHC16j, LHC16k, and LHC16o.

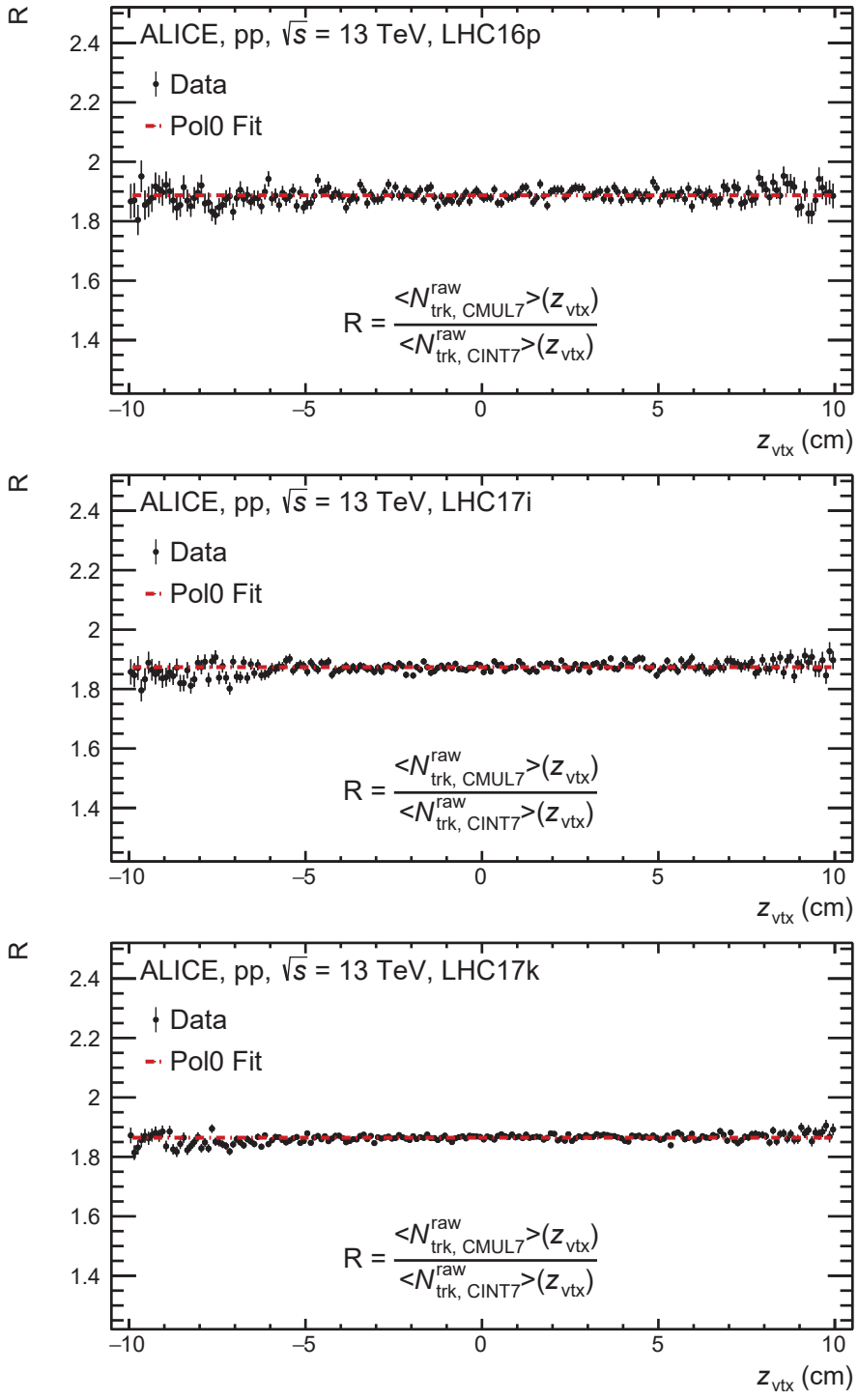

Figure A.2: Ratios of the average number of raw tracklets as a function of z_{vtx} between CMUL7 and CINT7 triggered events for LHC16p, LHC17i, and LHC17k.

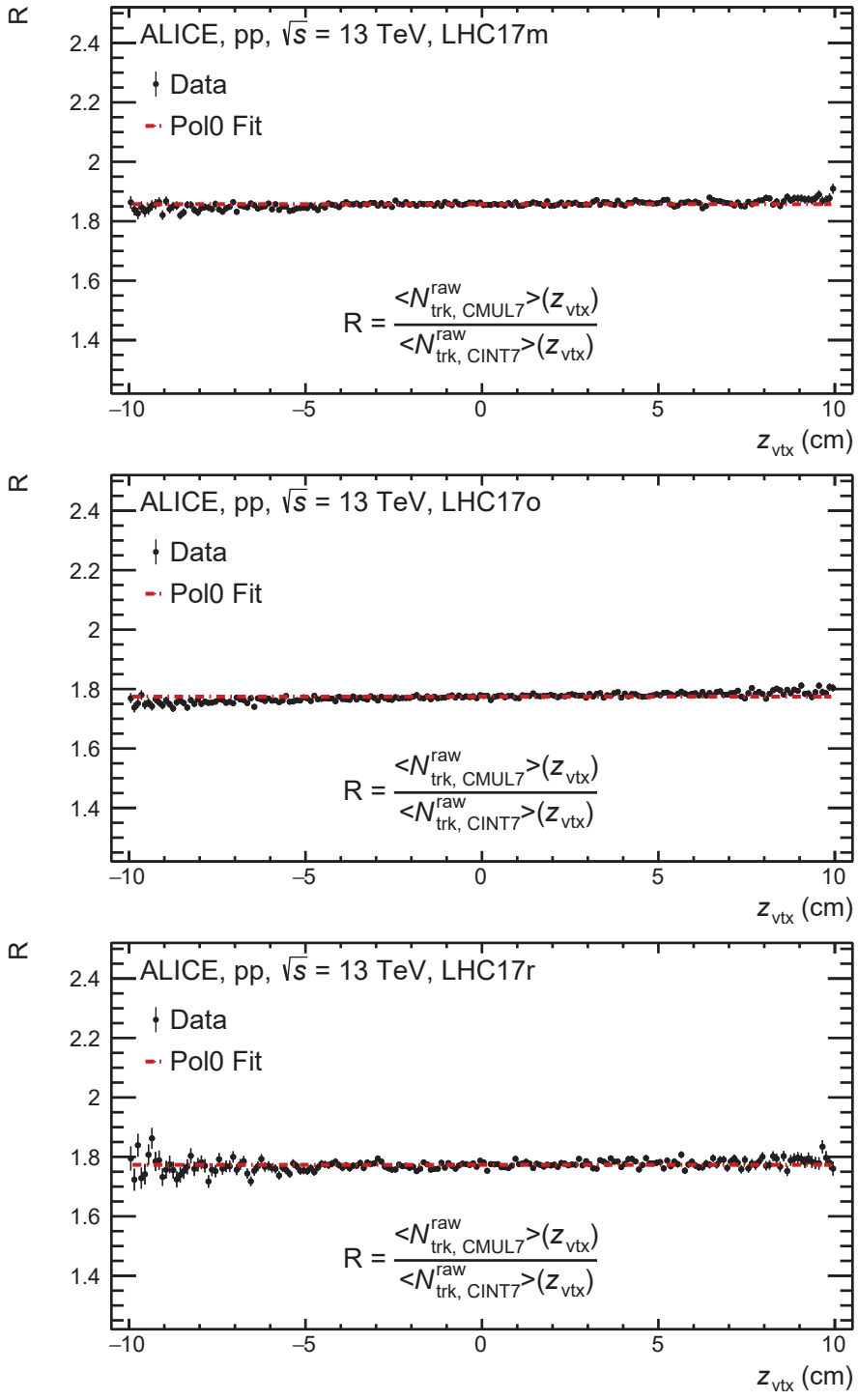

Figure A.3: Ratios of the average number of raw tracklets as a function of z_{vtx} between CMUL7 and CINT7 triggered events for LHC17m, LHC17o, and LHC17r.

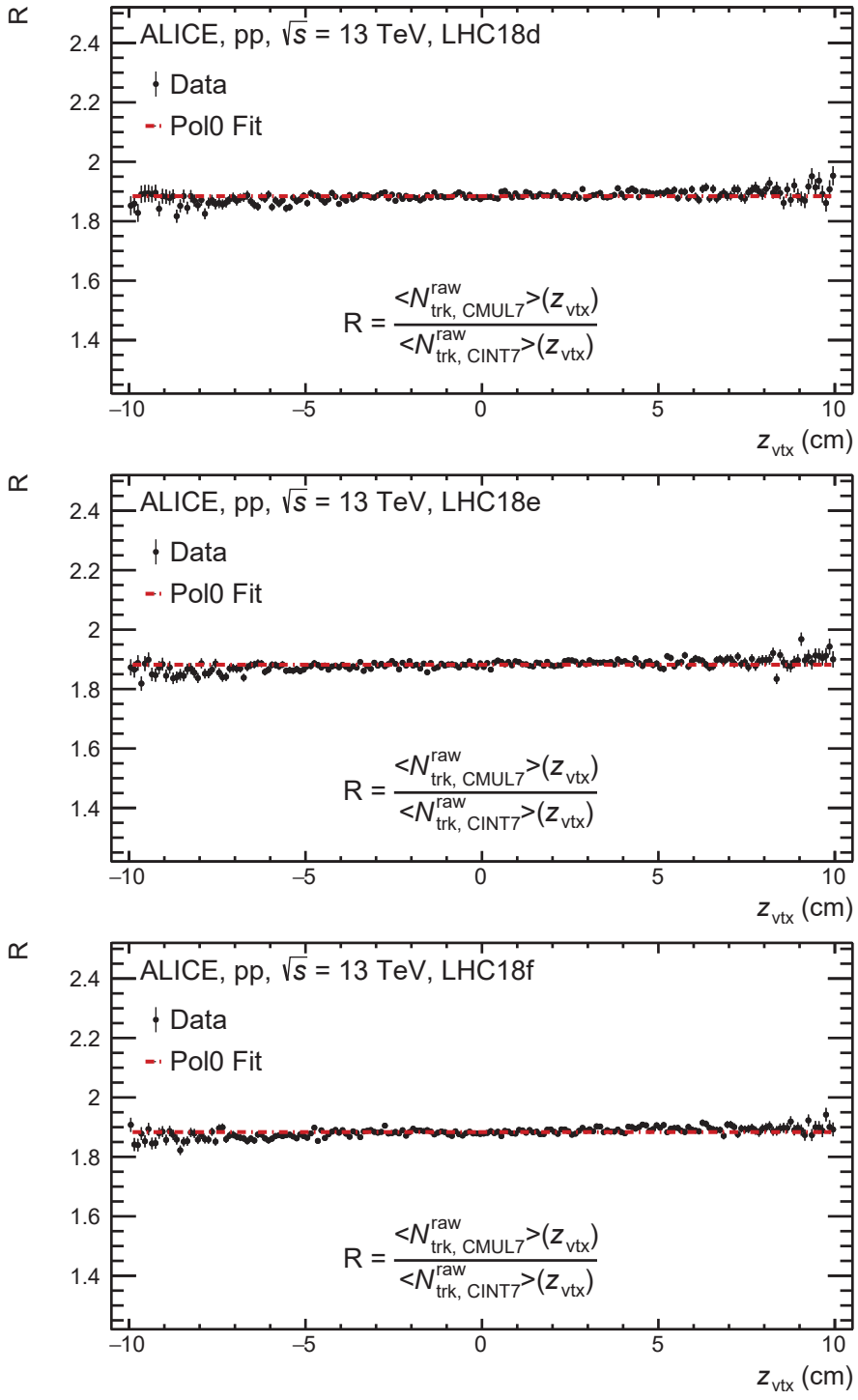

Figure A.4: Ratios of the average number of raw tracklets as a function of z_{vtx} between CMUL7 and CINT7 triggered events for LHC18d, LHC18e, and LHC18f.

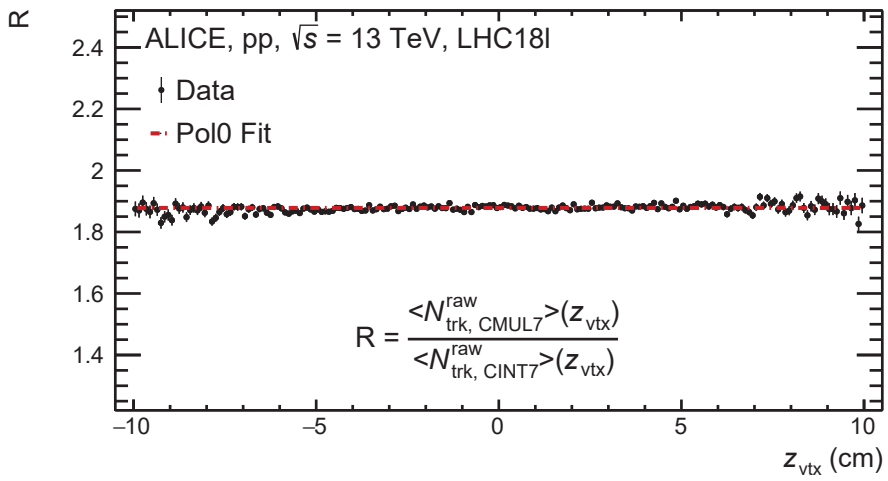

Figure A.5: Ratios of the average number of raw tracklets as a function of $z_{\rm vtx}$ between CMUL7 and CINT7 triggered events for LHC18l.

A.3 Polynomial function

An ad-hoc polynomial fitting function f is used to describe the relation between the number of tracklets and charged-particle multiplicity, namely:

$$f(x) = \begin{cases} ax^c + b, & x < x_0 \\ a_2 x^{c_2} + b_2, & x \geq x_0 \end{cases} \tag{A.1}$$

where,

$$a_2 = (\tfrac{ac}{c_2}) x_0^{c-c_2},\ b_2 = (\tfrac{ac_2 - ac}{c_2}) x_0^c + b$$

A.4 Systematic uncertainty investigation on the charged-particle multiplicity

A.4.1 $\langle N_{\rm ch} \rangle$ systematic uncertainties

The systematic uncertainty evaluation on $\langle N_{ch} \rangle$ has been studied by the polynomial fit combining 20 tests. The sources of the systematic uncertainties are listed as follows:

- $z_{\rm vtx}$ range: [-10, 10], [-10, -5], [-5, 0], [0, 5], and [5, 10] (cm)
- Generator: PYTHIA 8.2 (Monash 2013) and EPOS-LHC

- Reference profile: data profile and MC profile

The following Eq. A.2 and Eq. A.3 are used for the calculation of statistical and systematical uncertainties respectively.

$$\Delta_{\overline{x}}^{\mathrm{stat}} = \frac{1}{n}\sum_{i=1}^{n}\Delta_{x_i}^{\mathrm{stat}} \tag{A.2}$$

$$\sigma_{\overline{x}}^{\mathrm{syst}} = \sqrt{\frac{\sum_{i=1}^{n}(x_i-\overline{x})^2}{n}} \tag{A.3}$$

In the above equations, x_i is the quantity obtained in each test, $\Delta_{x_i}^{\mathrm{stat}}$ is the statistical error in each test and $\overline{x}$ is the mean value of the whole set of tests.

$N_{\mathrm{trk}}^{\mathrm{cor}}$ range	$\langle N_{\mathrm{ch}}\rangle \pm \mathrm{stat}(\%) \pm \mathrm{syst}(\%)$
$Integrated$	$14.58 \pm 0.03 \pm 0.38$
$[1-8]$	$5.62 \pm 0.02 \pm 1.76$
$[9-14]$	$13.89 \pm 0.01 \pm 0.44$
$[15-20]$	$21.25 \pm 0.01 \pm 0.50$
$[21-25]$	$27.93 \pm 0.01 \pm 0.51$
$[21,33]$	$31.46 \pm 0.01 \pm 0.58$
$[26-33]$	$35.21 \pm 0.01 \pm 0.68$
$[34-41]$	$44.34 \pm 0.01 \pm 0.96$
$[42-50]$	$53.69 \pm 0.02 \pm 1.23$
$[51-60]$	$63.94 \pm 0.02 \pm 1.51$
$[61-80]$	$77.08 \pm 0.05 \pm 1.76$
$[81-115]$	$98.97 \pm 0.18 \pm 2.20$

Table A.1: Systematical calculation on $\langle N_{\mathrm{ch}}\rangle$

A.4.2 Linear fit

This method uses a simple linear fit, N_{ch}=$\alpha \times N_{\mathrm{trk}}^{\mathrm{corr}}$ where α is a correction factor, as shown in Fig. A.6 (Full red line). The same function is used to fit in $N_{\mathrm{trk}}^{\mathrm{corr}}$ slices (i) where $N_{\mathrm{trk}}^{\mathrm{corr}}$ corresponds to the MB corrected number of tracklets. Then one α_i factor for each $N_{\mathrm{trk}}^{\mathrm{corr}}$ slice is obtained.

If the correlation between N_{ch} and $N_{\mathrm{trk}}^{\mathrm{corr}}$ would have been perfectly linear, only the global α factor would be needed. But in reality, the correlation between N_{ch} and $N_{\mathrm{trk}}^{\mathrm{corr}}$ is not perfectly linear due to the detector resolution and multiplicity binning, the global fit method can not give us a good N_{ch} estimation. From Fig. A.7, it can be seen that the bin-by-bin α_i is different from the global α_{Global}, mainly at low and high multiplicity classes.

The uncertainty due to the non-linearity has been assigned to the default fit – ad-hoc polynomial fit method. The final α in each bin and integrated case are calculated combining 20 tests (same as what have done in ad-hoc polynomial method). Then the difference between the α_{i} and α_{Global} factors is used as an additional systematic uncertainty, denoted as δ, added in quadrature to the final self-normalized multiplicity. The values for the selected

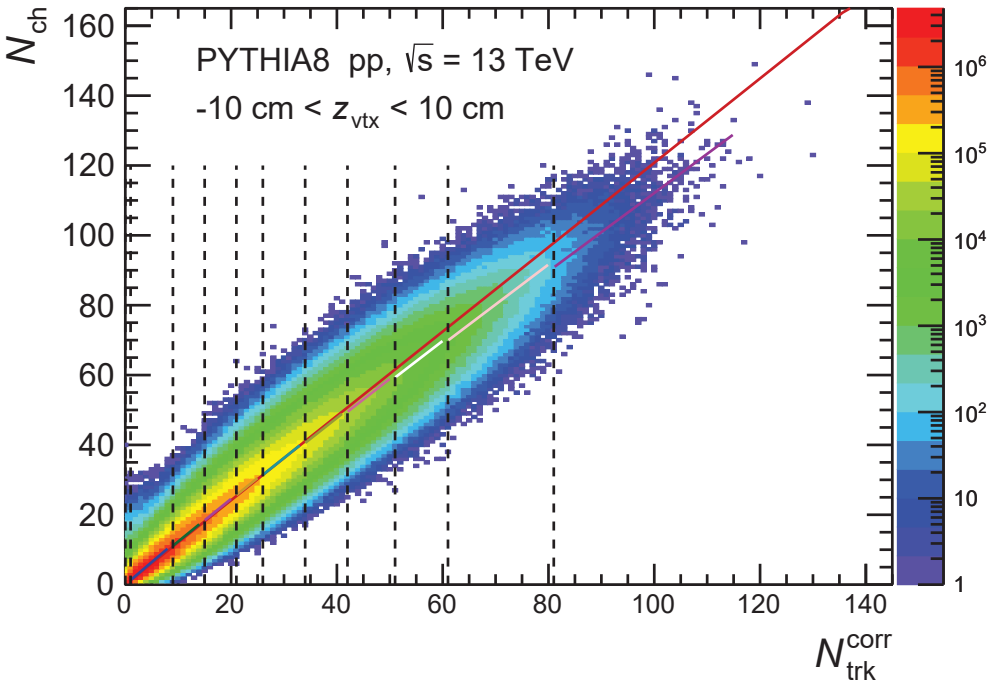

Figure A.6: $\langle N_{\rm ch}\rangle$-$\langle N_{\rm trk}^{\rm corr}\rangle$ correlation plot fitted by a simple linear function.

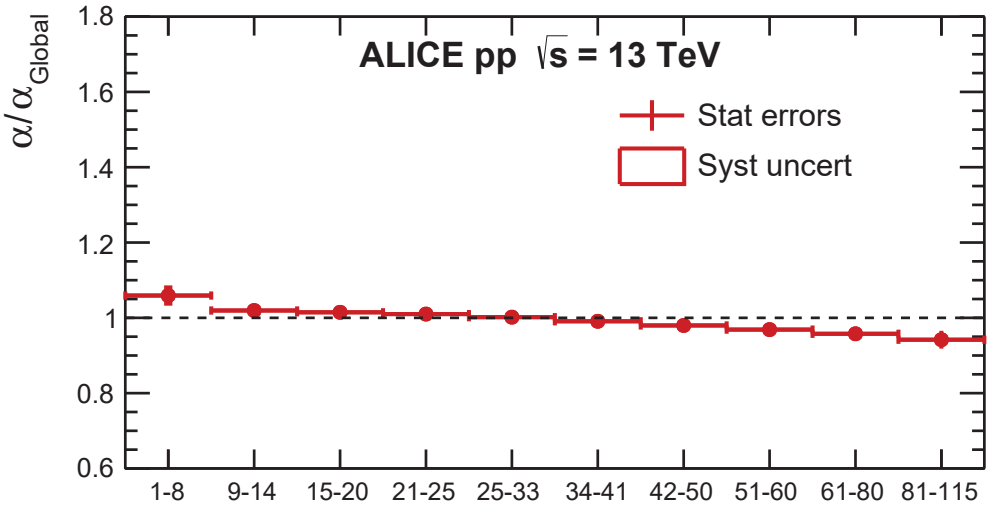

Figure A.7: Comparison between global alpha and alpha in multiplicity intervals.

multiplicity interval are listed in Table. A.2.

$N_{\rm trk}^{\rm cor}$ range	$\alpha \pm {\rm stat}(\%) \pm {\rm syst}(\%)$	$\delta(\%)$
Integrated	$1.21 \pm 0.24 \pm 0.73$	–
$[1, 8]$	$1.30 \pm 2.38 \pm 1.33$	6.7
$[9, 14]$	$1.23 \pm 1.75 \pm 0.49$	2.0
$[15, 20]$	$1.23 \pm 1.34 \pm 0.47$	1.5
$[21, 25]$	$1.22 \pm 1.29 \pm 0.53$	1.0
$[21, 33]$	$1.22 \pm 0.61 \pm 0.62$	1.0
$[26, 33]$	$1.21 \pm 0.77 \pm 0.69$	0.1
$[34, 41]$	$1.20 \pm 0.66 \pm 0.99$	1.0
$[42, 50]$	$1.18 \pm 0.55 \pm 1.29$	2.3
$[51, 60]$	$1.17 \pm 0.47 \pm 1.60$	3.5
$[61, 80]$	$1.16 \pm 0.30 \pm 1.95$	4.8

Table A.2: α factor extraction in the multiplicity and multiplicity-integrated intervals and the δ extraction which is defined as the relative difference in the central values of the α parameter values between α factors in multiplicity and multiplicity-integrated intervals.

A.4.3 Minimum bias trigger efficiency for $\rm INEL > 0$

The efficiency of the MB trigger for events satisfying the $\rm INEL > 0$ selection in the selected multiplicity class (i) ($\varepsilon^{i}_{\rm MB,INEL>0}$) is calculated using Eq. A.4. The number of events with and without MB trigger selection excluding all the event cuts is tabulated in Tab. A.3.

$$\varepsilon^{i}_{\rm MB,INEL>0} = \frac{N_{\rm events}\ \text{with MB}}{N_{\rm events}\ \text{without MB}} \tag{A.4}$$

It is found that the efficiency is very close to unity except for the integrated and first $N_{\rm trk}^{\rm cor}$ class. The values shown in Tab. A.3 are obtained from PYTHIA 8.2. When we change to another MC generator—EPOS, similar results are obtained, while for the integrated and first multiplicity classes, $\varepsilon^{\rm Integrated,EPOS}_{\rm MB,INEL>0} = 0.957$, $\varepsilon^{\rm 1,EPOS}_{\rm MB,INEL>0} = 0.922$. So

$N_{\rm trk}^{\rm cor}$ range	$N_{\rm events}$with MB trigger	$N_{\rm events}$without MB trigger	$\varepsilon^{i}_{\rm MB,INEL>0}$
Integrated	$2.14630e+08$	$2.26557e+08$	0.947
$[1, 8]$	$1.10079e+08$	$1.21504e+08$	0.906
$[9, 14]$	$4.08487e+07$	$4.13048e+07$	0.989
$[15, 20]$	$2.46486e+07$	$2.46894e+07$	0.998
$[21, 25]$	$1.38237e+07$	$1.38278e+07$	1.000
$[21, 33]$	$2.76091e+07$	$2.76140e+07$	1.000
$[26, 33]$	$1.37854e+07$	$1.37862e+07$	1.000
$[34, 41]$	$6.89421e+06$	$6.89427e+06$	1.000
$[42, 50]$	$3.17017e+06$	$3.17018e+06$	1.000
$[51, 60]$	$1.07190e+06$	$1.07190e+06$	1.000
$[61, 80]$	298280	298280	1.000

Table A.3: $\varepsilon_{\rm MB,INEL>0}$ in the multiplicity class for PYTHIA 8.2

the final efficiency for integrated and first multiplicity classes should be: $\varepsilon^{\rm Integrated}_{\rm MB,INEL>0} = 0.95 \pm 0.005$ $(0.5\%$ syst$)$, $\varepsilon^{1}_{\rm MB,INEL>0} = 0.91 \pm 0.008$ $(1.0\%$ syst$)$, where the central value is taken from the average of PYTHIA 8.2 and EPOS results, the systematic uncertainties is taken from the half of the difference between these two MC generators, respectively. The efficiency for the other multiplicity classes are equal to unity.

A.4.4 Correction factor for relative charged-particles in the first multiplicity class

The MB efficiency for events satisfying the $\rm INEL > 0$ selection is negligible for all multiplicity classes except for the first multiplicity class where the efficiency is 0.91. Moreover, the first multiplicity class is affected by the vertex QA cuts as these cuts mostly remove the lower multiplicity events. A correction must be applied to account for this by comparing the mean number of charged particles with these event cuts with and without the MB trigger selection. The correction factor is defined as Eq. A.5:

$$\epsilon^{1}_{\rm INEL>0,\langle N_{\rm ch}\rangle} = \frac{\langle N_{\rm ch}\rangle(N_{\rm ch} \geq 1 + {\rm MB} + {\rm vtxQA})}{\langle N_{\rm ch}\rangle(N_{\rm ch} \geq 1 + {\rm vtxQA})} \tag{A.5}$$

MC generator	$\langle N_{\rm ch}\rangle$ $(N_{\rm ch} \geq 1 + {\rm MB} + {\rm vtxQA})$	$\langle N_{\rm ch}\rangle$ $(N_{\rm ch} \geq 1 + {\rm vtxQA})$	$\epsilon^{1}_{\rm INEL>0,\langle N_{\rm ch}\rangle}$
PYTHIA 8.2	5.701	5.500	1.0365
EPOS	5.658	5.429	1.0421

Table A.4: $\epsilon^{1}_{\rm INEL>0,\langle N_{\rm ch}\rangle}$ factor for the lowest multiplicity class.

So, the efficiency factor for the first bin is $\epsilon^{1}_{\rm INEL>0,\langle N_{\rm ch}\rangle}$ = 1.039 $\pm$ 0.003 (0.3% syst), where the central value is taken from the average of PYTHIA 8.2 and EPOS results, the systematic uncertainty is taken from the half of the difference between these two generators.

A.5 Double ratio of excited-to-ground Υ state

In this sector, we will focus on the extraction of the self-normalized double ratio of Υ(2S) (or Υ(3S)) to Υ(1S) as a function of multiplicity. Two methods for the extraction of double ratio will be discussed in the following.

The first method is to vary the single ratio firstly, ($N_{\Upsilon(2S)}/N^{\rm Int}_{\Upsilon(2S)}$ and $N_{\Upsilon(1S)}/N^{\rm Int}_{\Upsilon(1S)}$), as shown in Fig. A.8, and then do the ratio. In this case, it will include the correlated terms for the fitting procedure and results in a bit large systematic uncertainty for the double ratio result. And this method is referred as to "single-fit".

The second method is that the double ratio is computed fit-by-fit directly, with the same procedure applied to the single ratio, like Fig. A.8 and it leads to a reduction of the systematic uncertainties from the signal extraction, shown in Fig. A.9, which means that the correlated terms for the signal extraction will be canceled. And this method

is referred as to ”fit-by-fit”.

The raw double ratio results are reported in Table A.5 and A.6. However, for corrected double ratio of the self-normalized yield between the excited and ground state, only the vertex quality selection ($\varepsilon_{\mathrm{vtx,QA}}$) is dependent of the state and do not cancel in the double ratio, and the formula Eq. A.6 is used to calculate the final double ratio. The final results between these above mentioned methods are presented in Table A.7 and A.8. In addition, if taking final self-normalized yield of excited and ground Υ states and doing the double ratio, in this case, we would double counting the efficiency correction systematic uncertainty, which is considered for each state already and also the correlated terms during the fitting procedure are also taken into account. Finally, the systematic uncertainty at this moment are over-estimated too much, and it is referred to “relative-ratio”. And more details is shown at the ALICE related Physics Analysis Group meeting [161].

Finally, the result from the ”fit-by-fit” method would be used in this analysis.

$$R = \frac{N_{\Upsilon(\mathrm{nS})}/ < N_{\Upsilon(\mathrm{nS})} >}{N_{\Upsilon(\mathrm{1S})}/ < N_{\Upsilon(\mathrm{1S})} >} = \frac{N_{\Upsilon(\mathrm{nS})}/N^{\mathrm{Int}}_{\Upsilon(\mathrm{nS})}}{N_{\Upsilon(\mathrm{1S})}/N^{\mathrm{Int}}_{\Upsilon(\mathrm{1S})}} \times \frac{\varepsilon^{\Upsilon(\mathrm{nS})}_{\mathrm{vtx,QA}}}{\varepsilon^{\Upsilon(\mathrm{1S})}_{\mathrm{vtx,QA}}}, n = 2, 3 \tag{A.6}$$

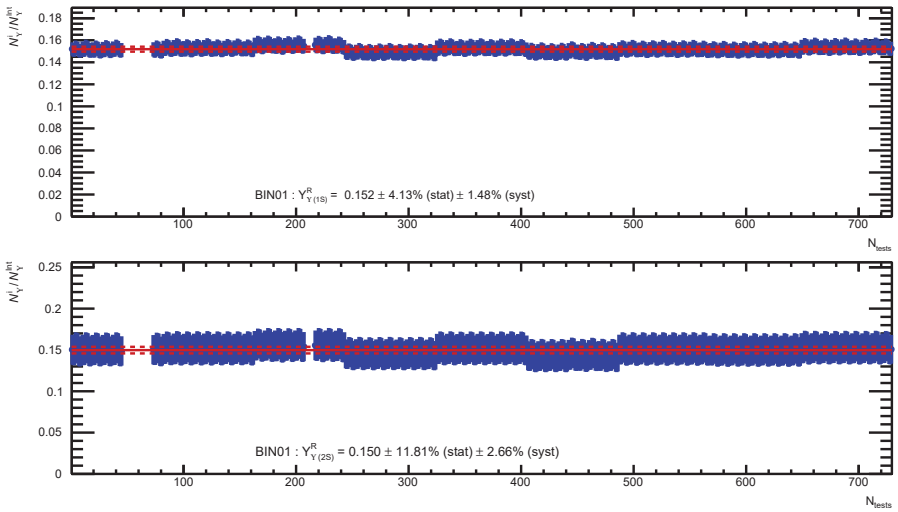

Figure A.8: Raw single ratio of $N_{\Upsilon(\mathrm{2S})}/N^{\mathrm{Int}}_{\Upsilon(\mathrm{2S})}$ (top), and $N_{\Upsilon(\mathrm{1S})}/N^{\mathrm{Int}}_{\Upsilon(1S)}$ (bottom) in the $N^{\mathrm{cor}}_{\mathrm{trk}}$ range $[1, 8]$.

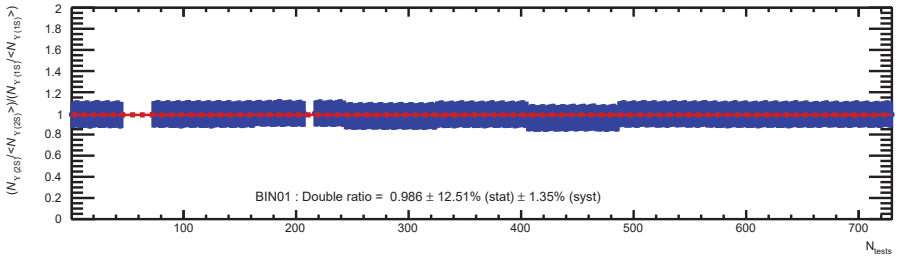

Figure A.9: Raw double ratio of $\frac{N_{\Upsilon(\mathrm{2S})}/N^{\mathrm{Int}}_{\Upsilon(\mathrm{2S})}}{N_{\Upsilon(\mathrm{1S})}/N^{\mathrm{Int}}_{\Upsilon(\mathrm{1S})}}$ in the $N^{\mathrm{cor}}_{\mathrm{trk}}$ range $[1, 8]$.

	$\frac{N_{2S}/N_{2S}^{Int}}{N_{1S}/N_{1S}^{Int}}_{fit-by-fit} \pm stat \pm syst$	$\frac{N_{2S}/N_{2S}^{Int}}{N_{1S}/N_{1S}^{Int}}_{single-fit} \pm stat \pm syst$
$[1,8]$	$0.986 \pm 12.51\% \pm 1.35\%$	$0.987 \pm 12.51\% \pm 3.04\%$
$[9,14]$	$0.901 \pm 13.13\% \pm 1.88\%$	$0.903 \pm 13.12\% \pm 3.81\%$
$[15,20]$	$0.942 \pm 13.71\% \pm 2.09\%$	$0.947 \pm 13.70\% \pm 5.84\%$
$[21,25]$	$1.085 \pm 13.68\% \pm 1.38\%$	$1.085 \pm 13.68\% \pm 3.45\%$
$[26,33]$	$1.068 \pm 12.59\% \pm 1.38\%$	$1.067 \pm 12.58\% \pm 4.72\%$
$[34,41]$	$1.024 \pm 16.16\% \pm 1.37\%$	$1.020 \pm 16.15\% \pm 3.14\%$
$[42,50]$	$0.635 \pm 30.93\% \pm 5.16\%$	$0.627 \pm 30.89\% \pm 7.36\%$
$[51,60]$	$1.462 \pm 22.50\% \pm 2.70\%$	$1.500 \pm 22.46\% \pm 6.62\%$
$[61,80]$	$1.302 \pm 37.07\% \pm 7.74\%$	$1.250 \pm 37.00\% \pm 9.72\%$

Table A.5: Extracted values for raw double ratio between Υ(2S) and Υ(1S).

	$\frac{N_{3S}/N_{3S}^{Int}}{N_{1S}/N_{1S}^{Int}}_{fit-by-fit} \pm stat \pm syst$	$\frac{N_{3S}/N_{3S}^{Int}}{N_{1S}/N_{1S}^{Int}}_{single-fit} \pm stat \pm syst$
$[1,8]$	$1.387 \pm 20.58\% \pm 6.25\%$	$1.388 \pm 20.58\% \pm 7.42\%$
$[9,14]$	$1.326 \pm 20.97\% \pm 7.26\%$	$1.330 \pm 20.96\% \pm 8.84\%$
$[15,20]$	$1.639 \pm 19.67\% \pm 6.92\%$	$1.645 \pm 19.64\% \pm 9.60\%$
$[21,33]$	$0.638 \pm 31.89\% \pm 11.75\%$	$0.638 \pm 31.86\% \pm 12.79\%$

Table A.6: Extracted values for raw double ratio between Υ(3S) and Υ(1S).

	$\frac{N_{2S}/<N_{2S}>}{N_{1S}/<N_{1S}>}_{fit-by-fit} \pm stat \pm syst$	$\frac{N_{2S}/<N_{2S}>}{N_{1S}/<N_{1S}>}_{single-fit} \pm stat \pm syst$	$\frac{N_{2S}/<N_{2S}>}{N_{1S}/<N_{1S}>}_{relative-ratio} \pm stat \pm syst$
$[1,8]$	$0.976 \pm 14.56\% \pm 1.35\%$	$0.977 \pm 14.56\% \pm 3.04\%$	$0.977 \pm 14.88\% \pm 4.51\%$
$[9,14]$	$0.892 \pm 15.10\% \pm 1.88\%$	$0.894 \pm 15.09\% \pm 3.81\%$	$0.894 \pm 14.72\% \pm 4.61\%$
$[15,20]$	$0.933 \pm 15.61\% \pm 2.09\%$	$0.938 \pm 15.60\% \pm 5.84\%$	$0.937 \pm 15.59\% \pm 6.49\%$
$[21,25]$	$1.074 \pm 15.58\% \pm 1.38\%$	$1.074 \pm 15.58\% \pm 3.45\%$	$1.074 \pm 15.86\% \pm 4.61\%$
$[26,33]$	$1.058 \pm 14.63\% \pm 1.38\%$	$1.057 \pm 14.62\% \pm 4.72\%$	$1.057 \pm 14.75\% \pm 5.79\%$
$[34,41]$	$1.014 \pm 17.80\% \pm 1.37\%$	$1.010 \pm 17.79\% \pm 3.14\%$	$1.010 \pm 17.54\% \pm 4.64\%$
$[42,50]$	$0.629 \pm 31.82\% \pm 5.16\%$	$0.621 \pm 31.78\% \pm 7.36\%$	$0.621 \pm 31.73\% \pm 7.85\%$
$[51,60]$	$1.448 \pm 23.70\% \pm 2.70\%$	$1.485 \pm 23.67\% \pm 6.62\%$	$1.485 \pm 23.62\% \pm 7.04\%$
$[61,80]$	$1.289 \pm 37.81\% \pm 7.74\%$	$1.238 \pm 37.74\% \pm 9.72\%$	$1.238 \pm 37.93\% \pm 9.66\%$

Table A.7: Extracted values for corrected double yield ratio between Υ(2S) and Υ(1S).

	$\frac{N_{3S}/<N_{3S}>}{N_{1S}/<N_{1S}>}_{fit-by-fit} \pm stat \pm syst$	$\frac{N_{3S}/<N_{3S}>}{N_{1S}/<N_{1S}>}_{single-fit} \pm stat \pm syst$	$\frac{N_{3S}/<N_{3S}>}{N_{1S}/<N_{1S}>}_{relative-ratio} \pm stat \pm syst$
$[1,8]$	$1.374 \pm 24.38\% \pm 6.25\%$	$1.375 \pm 24.38\% \pm 7.42\%$	$1.373 \pm 24.31\% \pm 7.83\%$
$[9,14]$	$1.313 \pm 24.71\% \pm 7.26\%$	$1.317 \pm 24.70\% \pm 8.84\%$	$1.317 \pm 25.19\% \pm 9.66\%$
$[15,20]$	$1.623 \pm 23.62\% \pm 6.92\%$	$1.629 \pm 23.59\% \pm 9.60\%$	$1.629 \pm 23.56\% \pm 9.93\%$
$[21,33]$	$0.632 \pm 34.47\% \pm 11.75\%$	$0.632 \pm 34.44\% \pm 12.79\%$	$0.632 \pm 34.89\% \pm 13.33\%$

Table A.8: Extracted values for corrected double yield ratio between Υ(3S) and Υ(1S).

A.6 Final results

$N_{\rm trk}^{\rm cor}$ range	$\frac{{\rm d}N_{\rm ch}/{\rm d}\eta}{\langle {\rm d}N_{\rm ch}/{\rm d}\eta\rangle} \pm \sigma^{\rm syst}$	$\frac{{\rm d}N_{\Upsilon{\rm (1S)}}/{\rm d}y}{\langle {\rm d}N_{\Upsilon{\rm (1S)}}/{\rm d}y\rangle} \pm \Delta^{\rm stat} \pm \sigma^{\rm syst}$	$\frac{N_{\Upsilon{\rm (1S)}}/\langle N_{\Upsilon{\rm (1S)}}\rangle}{{\rm d}N_{\rm ch}/{\rm d}\eta/\langle {\rm d}N_{\rm ch}/{\rm d}\eta\rangle} \pm \Delta^{\rm stat} \pm \sigma^{\rm syst}$
$[1, 8]$	0.38 ± 0.03	$0.306 \pm 0.015 \pm 0.009$	$0.805 \pm 0.039 \pm 0.024$
$[9, 14]$	0.99 ± 0.02	$0.954 \pm 0.048 \pm 0.029$	$0.964 \pm 0.048 \pm 0.029$
$[15, 20]$	1.51 ± 0.03	$1.487 \pm 0.074 \pm 0.059$	$0.985 \pm 0.049 \pm 0.039$
$[21, 25]$	1.99 ± 0.04	$2.108 \pm 0.126 \pm 0.063$	$1.059 \pm 0.063 \pm 0.032$
$[26, 33]$	2.51 ± 0.04	$2.857 \pm 0.143 \pm 0.114$	$1.138 \pm 0.057 \pm 0.045$
$[34, 41]$	3.16 ± 0.07	$3.632 \pm 0.218 \pm 0.109$	$1.149 \pm 0.069 \pm 0.034$
$[42, 50]$	3.8 ± 0.1	$4.475 \pm 0.358 \pm 0.134$	$1.178 \pm 0.094 \pm 0.035$
$[51, 60]$	4.5 ± 0.2	$5.056 \pm 0.506 \pm 0.253$	$1.124 \pm 0.112 \pm 0.056$
$[61, 80]$	5.5 ± 0.3	$6.157 \pm 0.924 \pm 0.369$	$1.119 \pm 0.168 \pm 0.067$

Table A.9: Self-normalized yield of Υ(1S) as a function of self-normalized charged-particle multiplicity.

$N_{\rm trk}^{\rm cor}$ range	$\frac{{\rm d}N_{\rm ch}/{\rm d}\eta}{\langle {\rm d}N_{\rm ch}/{\rm d}\eta\rangle} \pm \sigma^{\rm syst}$	$\frac{{\rm d}N_{\Upsilon{\rm (2S)}}/{\rm d}y}{\langle {\rm d}N_{\Upsilon{\rm (2S)}}/{\rm d}y\rangle} \pm \Delta^{\rm stat} \pm \sigma^{\rm syst}$	$\frac{N_{\Upsilon{\rm (2S)}}/\langle N_{\Upsilon{\rm (2S)}}\rangle}{{\rm d}N_{\rm ch}/{\rm d}\eta/\langle {\rm d}N_{\rm ch}/{\rm d}\eta\rangle} \pm \Delta^{\rm stat} \pm \sigma^{\rm syst}$
$[1, 8]$	0.38 ± 0.03	$0.299 \pm 0.042 \pm 0.012$	$0.787 \pm 0.111 \pm 0.032$
$[9, 14]$	0.99 ± 0.02	$0.854 \pm 0.120 \pm 0.034$	$0.863 \pm 0.121 \pm 0.034$
$[15, 20]$	1.51 ± 0.03	$1.395 \pm 0.209 \pm 0.070$	$0.924 \pm 0.138 \pm 0.046$
$[21, 25]$	1.99 ± 0.04	$2.265 \pm 0.340 \pm 0.091$	$1.138 \pm 0.171 \pm 0.046$
$[26, 33]$	2.51 ± 0.04	$3.019 \pm 0.423 \pm 0.151$	$1.203 \pm 0.169 \pm 0.060$
$[34, 41]$	3.16 ± 0.07	$3.669 \pm 0.624 \pm 0.147$	$1.161 \pm 0.197 \pm 0.047$
$[42, 50]$	3.8 ± 0.1	$2.779 \pm 0.861 \pm 0.195$	$0.731 \pm 0.227 \pm 0.051$
$[51, 60]$	4.5 ± 0.2	$7.511 \pm 1.577 \pm 0.376$	$1.669 \pm 0.350 \pm 0.084$
$[61, 80]$	5.5 ± 0.3	$7.621 \pm 2.667 \pm 0.533$	$1.386 \pm 0.485 \pm 0.097$

Table A.10: Self-normalized yield of Υ(2S) as a function of self-normalized charged-particle multiplicity.

$N_{\rm trk}^{\rm cor}$ range	$\frac{{\rm d}N_{\rm ch}/{\rm d}\eta}{\langle {\rm d}N_{\rm ch}/{\rm d}\eta\rangle} \pm \sigma^{\rm syst}$	$\frac{{\rm d}N_{\Upsilon{\rm (3S)}}/{\rm d}y}{\langle {\rm d}N_{\Upsilon{\rm (3S)}}/{\rm d}y\rangle} \pm \Delta^{\rm stat} \pm \sigma^{\rm syst}$	$\frac{N_{\Upsilon{\rm (3S)}}/\langle N_{\Upsilon{\rm (3S)}}\rangle}{{\rm d}N_{\rm ch}/{\rm d}\eta/\langle {\rm d}N_{\rm ch}/{\rm d}\eta\rangle} \pm \Delta^{\rm stat} \pm \sigma^{\rm syst}$
$[1, 8]$	0.38 ± 0.03	$0.420 \pm 0.101 \pm 0.029$	$1.105 \pm 0.266 \pm 0.076$
$[9, 14]$	0.99 ± 0.02	$1.256 \pm 0.314 \pm 0.113$	$1.269 \pm 0.317 \pm 0.114$
$[15, 20]$	1.51 ± 0.03	$2.423 \pm 0.557 \pm 0.218$	$1.605 \pm 0.369 \pm 0.144$
$[21, 33]$	2.24 ± 0.04	$1.561 \pm 0.546 \pm 0.203$	$0.697 \pm 0.244 \pm 0.091$

Table A.11: Self-normalized yield of Υ(3S) as a function of charged-particle multiplicity.

$N_{\rm trk}^{\rm cor}$ range	$\frac{{\rm d}N_{\rm ch}/{\rm d}\eta}{\langle {\rm d}N_{\rm ch}/{\rm d}\eta\rangle} \pm \sigma^{\rm syst}$	$\frac{N_{\Upsilon{\rm (2S)}}/\langle N_{\Upsilon{\rm (2S)}}\rangle}{N_{\Upsilon{\rm (1S)}}/\langle N_{\Upsilon{\rm (1S)}}\rangle} \pm \Delta^{\rm stat} \pm \sigma^{\rm syst}$	$\frac{N_{\Upsilon{\rm (3S)}}/\langle N_{\Upsilon{\rm (3S)}}\rangle}{N_{\Upsilon{\rm (1S)}}/\langle N_{\Upsilon{\rm (1S)}}\rangle} \pm \Delta^{\rm stat} \pm \sigma^{\rm syst}$
$[1, 8]$	0.38 ± 0.03	$0.976 \pm 0.146 \pm 0.010$	$1.374 \pm 0.344 \pm 0.082$
$[9, 14]$	0.99 ± 0.02	$0.892 \pm 0.134 \pm 0.018$	$1.313 \pm 0.328 \pm 0.092$
$[15, 20]$	1.51 ± 0.03	$0.933 \pm 0.149 \pm 0.019$	$1.623 \pm 0.390 \pm 0.114$
$[21, 25]$	1.99 ± 0.04	$1.074 \pm 0.172 \pm 0.011$	-
$[21, 33]$	2.24 ± 0.04	-	$0.632 \pm 0.221 \pm 0.076$
$[26, 33]$	2.51 ± 0.04	$1.058 \pm 0.159 \pm 0.011$	-
$[34, 41]$	3.16 ± 0.07	$1.014 \pm 0.183 \pm 0.010$	-
$[42, 50]$	3.8 ± 0.1	$0.629 \pm 0.201 \pm 0.031$	-
$[51, 60]$	4.5 ± 0.2	$1.448 \pm 0.348 \pm 0.043$	-
$[61, 80]$	5.5 ± 0.3	$1.289 \pm 0.490 \pm 0.103$	-

Table A.12: Double yield ratios of Υ(2S) and Υ(3S) over Υ(1S) as a function of self-normalized charged-particle multiplicity.

$N_{\mathrm{trk}}^{\mathrm{cor}}$ range	$\frac{\mathrm{d}N_{\mathrm{ch}}/\mathrm{d}\eta}{\langle \mathrm{d}N_{\mathrm{ch}}/\mathrm{d}\eta \rangle} \pm \sigma^{\mathrm{syst}}$	$\frac{N_{\Upsilon(1\mathrm{S})}/\langle N_{\Upsilon(1\mathrm{S})} \rangle}{N_{\mathrm{J}/\psi}/\langle N_{\mathrm{J}/\psi} \rangle} \pm \Delta^{\mathrm{stat}} \pm \sigma^{\mathrm{syst}}$
$[1, 8]$	0.38 ± 0.03	$0.900 \pm 0.045 \pm 0.045$
$[9, 14]$	0.99 ± 0.02	$0.998 \pm 0.050 \pm 0.050$
$[15, 20]$	1.51 ± 0.03	$0.941 \pm 0.047 \pm 0.056$
$[21, 25]$	1.99 ± 0.04	$0.980 \pm 0.059 \pm 0.049$
$[26, 33]$	2.51 ± 0.04	$1.028 \pm 0.051 \pm 0.062$
$[34, 41]$	3.16 ± 0.07	$1.013 \pm 0.061 \pm 0.051$
$[42, 50]$	3.8 ± 0.1	$1.022 \pm 0.082 \pm 0.051$
$[51, 60]$	4.5 ± 0.2	$0.953 \pm 0.095 \pm 0.057$
$[61, 80]$	5.5 ± 0.3	$0.940 \pm 0.141 \pm 0.066$

Table A.13: Double yield ratio of Υ(1S) over J/ψ as a function of charged-particle multiplicity.

Appendix B

Upsilon polarization

B.1 Run list for the Υ polarization analysis

LHC16f (pass1) AOD234, 6 runs:

253978, 253961, 253958, 253957, 253956, 253951

LHC16g (pass1) AOD234, 16 runs:

254332, 254331, 254304, 254302, 254293, 254205, 254204, 254199, 254193, 254178, 254175, 254174, 254149, 254148, 254147, 254128

LHC16h (pass1) AOD234, 65 runs:

255467, 255466, 255465, 255463, 255447, 255442, 255440, 255415, 255402, 255398, 255352, 255351, 255350, 255283, 255280, 255276, 255275, 255256, 255255, 255253, 255252, 255251, 255249, 255248, 255247, 255242, 255240, 255182, 255180, 255177, 255176, 255173, 255171, 255167, 255162, 255159, 255154, 255111, 255091, 255086, 255085, 255082, 255079, 255010, 255009, 255008, 254984, 254983, 254654, 254653, 254652, 254651, 254649, 254648, 254646, 254644, 254640, 254632, 254630, 254629, 254621, 254608, 254606, 254604, 254419

LHC16i (pass1) AOD234, 13 runs:

255618, 255617, 255616, 255615, 255614, 255592, 255591, 255583, 255577, 255543, 255542, 255540, 255539

LHC16j (pass1) AOD234, 49 runs:

256420, 256418, 256417, 256415, 256373, 256372, 256371, 256368, 256366, 256365, 256364, 256363, 256362, 256361, 256356, 256311, 256307, 256302, 256298, 256297, 256295, 256292, 256290, 256289, 256287, 256284, 256283, 256282, 256281, 256231, 256228, 256227, 256223, 256222, 256219, 256215, 256213, 256212, 256210,

256204, 256169, 256161, 256158, 256157, 256156, 256149, 256148, 256147, 256146

LHC16k (pass1) AOD, 171 runs:

258537, 258499, 258498, 258477, 258456, 258454, 258452, 258426, 258399, 258393, 258391, 258388, 258387, 258359, 258336, 258332, 258307, 258306, 258303, 258302, 258301, 258299, 258280, 258278, 258274, 258273, 258271, 258270, 258258, 258257, 258256, 258204, 258203, 258202, 258197, 258178, 258117, 258114, 258113, 258109, 258108, 258107, 258063, 258062, 258060, 258059, 258049, 258048, 258045, 258042, 258041, 258039, 258019, 258017, 258014, 258012, 258008, 257989, 257986, 257979, 257963, 257960, 257958, 257957, 257939, 257937, 257936, 257932, 257912, 257901, 257893, 257892, 257737, 257735, 257734, 257733, 257727, 257725, 257724, 257697, 257694, 257688, 257687, 257685, 257684, 257682, 257644, 257642, 257636, 257635, 257632, 257630, 257606, 257605, 257604, 257601, 257595, 257594, 257592, 257590, 257588, 257587, 257566, 257565, 257564, 257563, 257562, 257561, 257560, 257541, 257540, 257531, 257530, 257492, 257491, 257490, 257488, 257487, 257474, 257468, 257457, 257433, 257364, 257358, 257330, 257322, 257320, 257318, 257260, 257224, 257095, 257092, 257086, 257084, 257083, 257082, 257080, 257077, 257071, 257026, 257021, 257012, 257011, 256944, 256942, 256941, 256697, 256695, 256694, 256691, 256684, 256681, 256677, 256676, 256658, 256620, 256619, 256591, 256567, 256565, 256564, 256561, 256560, 256557, 256556, 256554, 256552, 256512, 256510, 256506, 256504

LHC16o (pass1) AOD234, 75 runs:

264035, 264033, 263985, 263984, 263981, 263979, 263978, 263977, 263923, 263920, 263917, 263916, 263905, 263866, 263863, 263861, 263830, 263829, 263824, 263823, 263813, 263810, 263803, 263793, 263792, 263790, 263787, 263786, 263785, 263784, 263744, 263743, 263741, 263739, 263738, 263737, 263691, 263690, 263689, 263682, 263662, 263657, 263654, 263653, 263652, 263647, 263529, 263497, 263496, 263490, 263487, 263332, 262858, 262855, 262853, 262849, 262847, 262844, 262842, 262841, 262778, 262777, 262776, 262768, 262760, 262727, 262725, 262723, 262719, 262717, 262713, 262705, 262635, 262632, 262628

LHC16p (pass1) AOD234, 38 runs:

264347, 264346, 264345, 264341, 264336, 264312, 264305, 264281, 264279, 264277, 264273, 264267, 264266, 264265, 264264, 264262, 264261, 264260, 264259, 264238, 264233, 264232, 264198, 264197, 264194, 264188, 264168, 264164, 264138, 264137, 264129, 264110, 264109, 264086, 264085, 264082, 264078, 264076

LHC17h (muon_calo_pass2), AOD, 98 runs:

273103, 273101, 273100, 273099, 273077, 273010, 273009, 272985, 272983, 272976, 272949, 272947, 272939, 272935, 272934, 272933, 272932, 272905, 272903, 272880, 272873, 272871, 272870, 272836, 272835, 272834,

272833, 272829, 272828, 272784, 272783, 272782, 272762, 272760, 272749, 272747, 272746, 272692, 272691, 272620, 272619, 272608, 272607, 272585, 272577, 272575, 272574, 272521, 272469, 272468, 272466, 272463, 272462, 272461, 272414, 272413, 272411, 272400, 272394, 272360, 272359, 272335, 272194, 272156, 272155, 272154, 272153, 272152, 272151, 272123, 272101, 272100, 272076, 272075, 272042, 272041, 272040, 272039, 272038, 272036, 272020, 271970, 271969, 271962, 271955, 271953, 271946, 271925, 271921, 271912, 271886, 271879, 271878, 271874, 271873, 271871, 271870, 271868

LHC17i (muon_calo_pass1), AOD, 56 runs:
274442, 274390, 274387, 274385, 274364, 274363, 274360, 274357, 274355, 274329, 274283, 274281, 274280, 274278, 274276, 274271, 274270, 274269, 274268, 274266, 274264, 274263, 274259, 274232, 274212, 274148, 274147, 274125, 274094, 274092, 274064, 274063, 274058, 273986, 273985, 273946, 273942, 273918, 273889, 273887, 273886, 273885, 273825, 273824, 273719, 273711, 273709, 273695, 273690, 273689, 273687, 273654, 273653, 273593, 273592, 273591

LHC17k (muon_calo_pass2), AOD, 100 runs:
276508, 276507, 276506, 276500, 276462, 276461, 276439, 276438, 276437, 276435, 276434, 276432, 276429, 276351, 276348, 276302, 276297, 276294, 276292, 276291, 276290, 276259, 276230, 276205, 276178, 276177, 276170, 276169, 276166, 276145, 276141, 276140, 276108, 276105, 276104, 276102, 276099, 276098, 275664, 275661, 275657, 275650, 275648, 275624, 275559, 275558, 275515, 275472, 275471, 275467, 275459, 275457, 275453, 275452, 275448, 275406, 275404, 275401, 275369, 275361, 275360, 275357, 275332, 275328, 275283, 275247, 275246, 275245, 275188, 275177, 275175, 275174, 275173, 275151, 275150, 275149, 275076, 275075, 275073, 275070, 275068, 275067, 274979, 274978, 274886, 274884, 274883, 274882, 274822, 274817, 274815, 274811, 274807, 274806, 274803, 274802, 274801, 274743, 274736, 274708

LHC17l (pass1), AOD234, 118 runs:
278216, 278215, 278191, 278189, 278167, 278166, 278165, 278164, 278163, 278130, 278127, 278126, 278123, 278122, 278121, 277996, 277991, 277989, 277988, 277987, 277952, 277930, 277907, 277904, 277903, 277901, 277900, 277899, 277898, 277897, 277876, 277870, 277848, 277847, 277842, 277841, 277836, 277834, 277801, 277800, 277799, 277795, 277794, 277749, 277747, 277746, 277725, 277577, 277576, 277575, 277574, 277537, 277536, 277531, 277530, 277479, 277478, 277476, 277473, 277472, 277470, 277418, 277417, 277389, 277386, 277384, 277383, 277360, 277314, 277312, 277310, 277293, 277262, 277256, 277197, 277196, 277194, 277193, 277189, 277188, 277184, 277183, 277182, 277181, 277180, 277155, 277121, 277117, 277091, 277087, 277082, 277079, 277076, 277073, 277037, 277017, 277016, 277015, 276972, 276971, 276970, 276969, 276920, 276917, 276916, 276762, 276675, 276674, 276672, 276671, 276670, 276669, 276644, 276608, 276557, 276553, 276552,

276551

LHC17m (muon_calo_pass1), AOD, 116 runs:
280140, 280135, 280134, 280131, 280126, 280118, 280114, 280111, 280108, 280066, 280052, 280051, 280049, 279955, 279954, 279952, 279893, 279890, 279886, 279884, 279880, 279879, 279855, 279854, 279853, 279830, 279827, 279826, 279773, 279749, 279747, 279719, 279718, 279715, 279689, 279688, 279684, 279682, 279679, 279677, 279676, 279642, 279641, 279600, 279598, 279597, 279583, 279565, 279564, 279563, 279562, 279561, 279560, 279559, 279488, 279487, 279483, 279441, 279439, 279435, 279410, 279391, 279355, 279354, 279349, 279348, 279344, 279342, 279312, 279310, 279309, 279274, 279273, 279270, 279268, 279267, 279265, 279264, 279242, 279238, 279235, 279234, 279208, 279207, 279201, 279199, 279157, 279155, 279130, 279125, 279123, 279122, 279117, 279106, 279075, 279074, 279073, 279068, 279044, 279043, 279041, 279038, 279037, 279036, 279008, 279007, 279005, 278999, 278964, 278963, 278959, 278941, 278939, 278936, 278915 278914

LHC17o (muon_calo_pass1), AOD203, 164 runs:
281961, 281956, 281953, 281946, 281940, 281939, 281931, 281928, 281918, 281916, 281915, 281894, 281893, 281892, 281755, 281754, 281753, 281751, 281750, 281741, 281713, 281709, 281707, 281706, 281705, 281651, 281645, 281642, 281640, 281635, 281634, 281633, 281592, 281583, 281581, 281580, 281574, 281569, 281568, 281563, 281562, 281557, 281511, 281509, 281477, 281475, 281450, 281449, 281446, 281444, 281441, 281415, 281321, 281301, 281277, 281275, 281244, 281243, 281242, 281241, 281240, 281213, 281212, 281191, 281190, 281181, 281180, 281179, 281081, 281080, 281079, 281062, 281061, 281060, 281036, 281035, 281033, 281032, 280998, 280997, 280996, 280994, 280990, 280947, 280943, 280940, 280936, 280897, 280890, 280881, 280880, 280856, 280848, 280847, 280845, 280844, 280842, 280793, 280792, 280786, 280768, 280767, 280766, 280765, 280764, 280763, 280761, 280756, 280755, 280754, 280753, 280706, 280705, 280681, 280679, 280676, 280671, 280650, 280648, 280647, 280645, 280639, 280637, 280634, 280613, 280583, 280581, 280576, 280575, 280574, 280551, 280550, 280547, 280546, 280519, 280518, 280448, 280447, 280446, 280445, 280443, 280419, 280418, 280415, 280413, 280412, 280406, 280405, 280403, 280375, 280374, 280352, 280351, 280350, 280349, 280348, 280312, 280310, 280290, 280286, 280285, 280284, 280283, 280282

LHC17r (muon_calo_pass1), AOD, 32 runs:
282704, 282703, 282702, 282700, 282677, 282676, 282673, 282671, 282670, 282668, 282667, 282666, 282653, 282651, 282629, 282622, 282620, 282618, 282615, 282609, 282608, 282607, 282606, 282580, 282579, 282575, 282573, 282546, 282545, 282544, 282528, 282504

LHC18b (muon_calo_pass1), AOD, 32 runs:

285396, 285365, 285364, 285347, 285328, 285327, 285291, 285290, 285289, 285287, 285286, 285224, 285222, 285203, 285202, 285200, 285165, 285127, 285125, 285108, 285106, 285066, 285065, 285064, 285015, 285014, 285013, 285012, 285011, 285010, 285009, 285008

LHC18c (muon_calo_pass1), AOD, 48 runs:
285958, 285957, 285946, 285917, 285893, 285892, 285869, 285851, 285830, 285812, 285811, 285810, 285806, 285805, 285804, 285781, 285778, 285777, 285756, 285755, 285754, 285753, 285752, 285751, 285722, 285698, 285697, 285664, 285663, 285662, 285659, 285643, 285642, 285641, 285640, 285639, 285603, 285602, 285601, 285599, 285578, 285577, 285576, 285575, 285557, 285515, 285497, 285496

LHC18d (muon_calo_pass1), AOD, 44 runs:
286350, 286349, 286348, 286345, 286340, 286337, 286336, 286314, 286313, 286312, 286311, 286310, 286309, 286308, 286289, 286288, 286287, 286284, 286282, 286261, 286257, 286254, 286230, 286229, 286203, 286202, 286201, 286199, 286198, 286159, 286130, 286129, 286127, 286124, 286064, 286028, 286027, 286026, 286025, 286018, 286014, 285980, 285979, 285978

LHC18e (muon_calo_pass1), AOD, 43 runs:
286937, 286936, 286933, 286932, 286931, 286930, 286911, 286910, 286908, 286907, 286877, 286876, 286874, 286852, 286850, 286848, 286846, 286810, 286809, 286801, 286799, 286731, 286695, 286661, 286653, 286633, 286594, 286592, 286591, 286569, 286568, 286567, 286566, 286509, 286508, 286502, 286501, 286455, 286454, 286428, 286427, 286426, 286380

LHC18f (muon_calo_pass1), AOD, 62 runs:
287977, 287941, 287923, 287783, 287658, 287657, 287656, 287654, 287578, 287576
287575, 287573, 287524, 287521, 287520, 287517, 287516, 287513, 287484, 287481
287451, 287389, 287388, 287387, 287385, 287381, 287380, 287360, 287358, 287356
287355, 287353, 287349, 287347, 287346, 287344, 287343, 287325, 287324, 287323
287283, 287254, 287251, 287250, 287249, 287248, 287209, 287208, 287204, 287203
287202, 287201, 287155, 287137, 287077, 287072, 287071, 287066, 287064, 287063
287021, 287000

LHC18g (muon_calo_pass1), AOD, 6 runs:
288750, 288748, 288743, 288690, 288689, 288688

LHC18g (muon_calo_pass1), AOD, 1 run:

288804

LHC18i (muon_calo_pass1), AOD, 10 runs:

288909, 288908, 288903, 288897, 288893, 288892, 288868, 288864, 288862, 288861

LHC18j (muon_calo_pass1), AOD, 1 run:

288943

LHC18l (muon_calo_pass1), AOD, 79 runs:

289971, 289966, 289943, 289941, 289940, 289935, 289931, 289928, 289888, 289884, 289880, 289857, 289856, 289855, 289852, 289849, 289830, 289816, 289815, 289814, 289811, 289808, 289775, 289757, 289731, 289729, 289724, 289723, 289721, 289666, 289664, 289660, 289659, 289658, 289657, 289654, 289632, 289626, 289625, 289582, 289581, 289579, 289577, 289576, 289574, 289494, 289493, 289468, 289466, 289465, 289462, 289444, 289426, 289373, 289370, 289369, 289368, 289367, 289366, 289365, 289363, 289356, 289355, 289354, 289353, 289309, 289308, 289306, 289303, 289300, 289280, 289278, 289277, 289276, 289275, 289254, 289253, 289249, 289247

LHC18m (muon_calo_pass1), AOD, 172 runs:

292397, 292298, 292274, 292273, 292270, 292269, 292265, 292242, 292241, 292240, 292192, 292168, 292167, 292166, 292164, 292163, 292162, 292161, 292160, 292140, 292115, 292114, 292109, 292108, 292107, 292106, 292081, 292080, 292077, 292075, 292062, 292061, 292060, 292040, 292012, 291982, 291953, 291948, 291945, 291944, 291943, 291942, 291803, 291796, 291795, 291769, 291760, 291756, 291755, 291729, 291706, 291698, 291697, 291694, 291692, 291690, 291665, 291661, 291657, 291614, 291590, 291485, 291484, 291482, 291481, 291457, 291456, 291453, 291451, 291447, 291446, 291420, 291419, 291417, 291416, 291402, 291400, 291399, 291397, 291375, 291373, 291363, 291362, 291361, 291360, 291286, 291285, 291284, 291283, 291282, 291265, 291263, 291041, 291037, 291035, 291006, 291005, 291004, 291003, 291002, 290979, 290976, 290975, 290948, 290944, 290943, 290935, 290932, 290895, 290894, 290892, 290862, 290853, 290848, 290790, 290787, 290776, 290774, 290769, 290766, 290764, 290721, 290699, 290696, 290692, 290687, 290665, 290660, 290658, 290645, 290632, 290627, 290615, 290614, 290613, 290612, 290590, 290553, 290550, 290549, 290544, 290540, 290539, 290538, 290501, 290499, 290469, 290459, 290458, 290456, 290428, 290427, 290425, 290423, 290421, 290420, 290418, 290411, 290404, 290401, 290375, 290374, 290350, 290327, 290324, 290323, 290300, 290297, 290293, 290254, 290223, 290222

LHC18o (muon_calo_pass2), AOD, 39 runs:

293898, 293896, 293893, 293891, 293886, 293856, 293831, 293830, 293829, 293809, 293807, 293806, 293805, 293802, 293799, 293776, 293774, 293773, 293741, 293740, 293698, 293696, 293695, 293692, 293691, 293588, 293587, 293497, 293496, 293494, 293475, 293474, 293424, 293413, 293392, 293391, 293388, 293386, 293368

LHC18p (muon_calo_pass2), AOD, 78 runs:

294925, 294916, 294884, 294883, 294880, 294877, 294875, 294852, 294818, 294817, 294816, 294815, 294813, 294809, 294775, 294774, 294772, 294769, 294749, 294747, 294743, 294742, 294741, 294722, 294721, 294718, 294716, 294715, 294710, 294703, 294653, 294636, 294634, 294633, 294632, 294593, 294591, 294590, 294588, 294587, 294586, 294563, 294558, 294556, 294553, 294531, 294530, 294529, 294527, 294526, 294525, 294524, 294503, 294502, 294310, 294308, 294307, 294305, 294242, 294241, 294212, 294210, 294208, 294205, 294201, 294200, 294199, 294156, 294155, 294154, 294152, 294131, 294128, 294013, 294012, 294011, 294010, 294009

B.2 Tail parameters from MC

Examples of the tail parameters from the MC simulation are shown in Figs. B.1, B.2, B.3, B.4, and B.5 in the Collins-Soper frames. Similar results can be observed in the Helicity reference frame, which are not shown here.

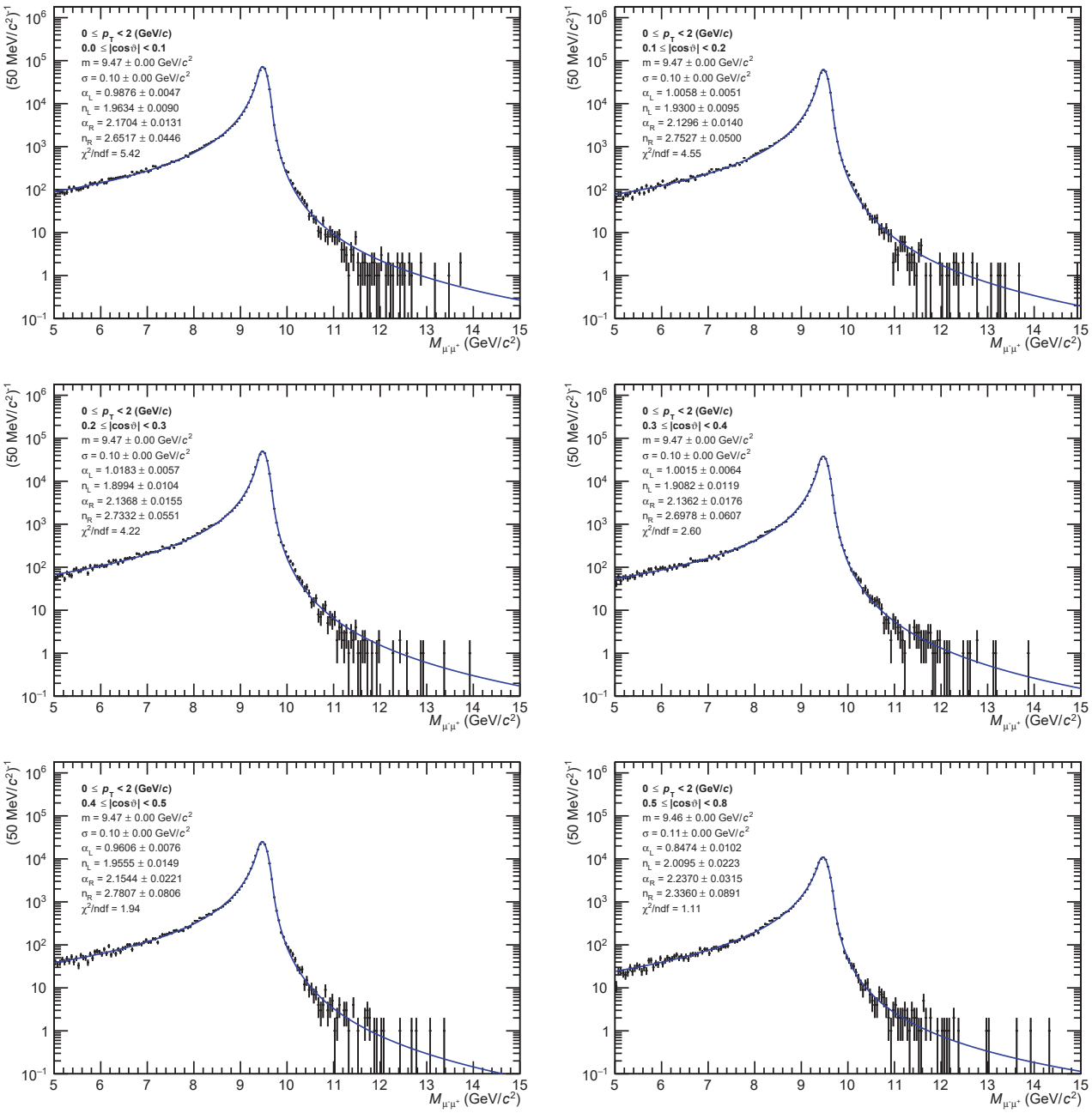

Figure B.1: Tail parameters as a function of $|\cos\theta|$ in $0 < p_{\mathrm{T}} < 2$ GeV/c in the Collins-Soper reference frame.

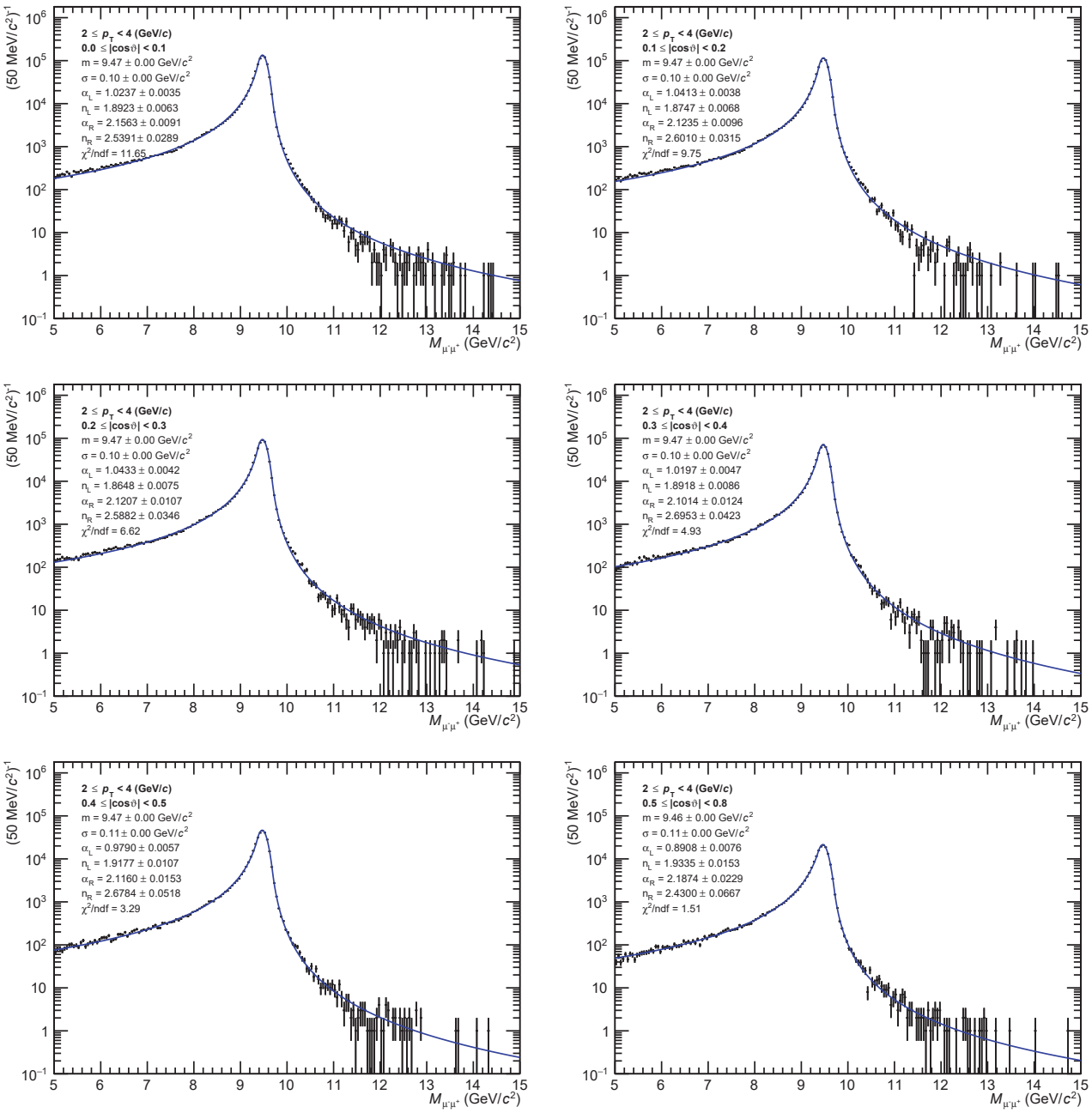

Figure B.2: Tail parameters as a function of $|\cos\theta|$ in $2 < p_{\mathrm{T}} < 4$ GeV/c in the Collins-Soper reference frame.

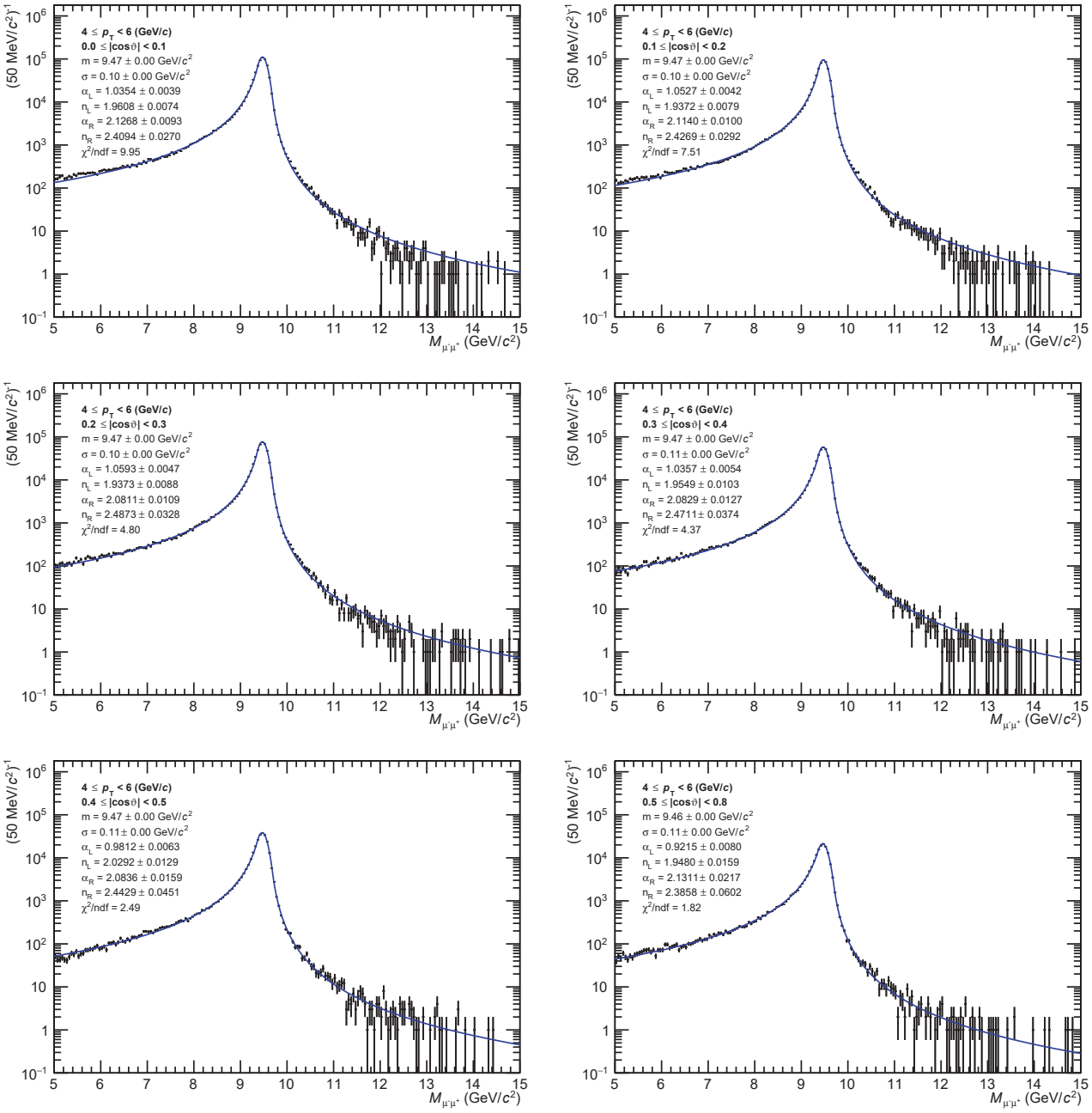

Figure B.3: Tail parameters as a function of $|\cos\theta|$ in $4 < p_{\mathrm{T}} < 6$ GeV/c in the Collins-Soper reference frame.

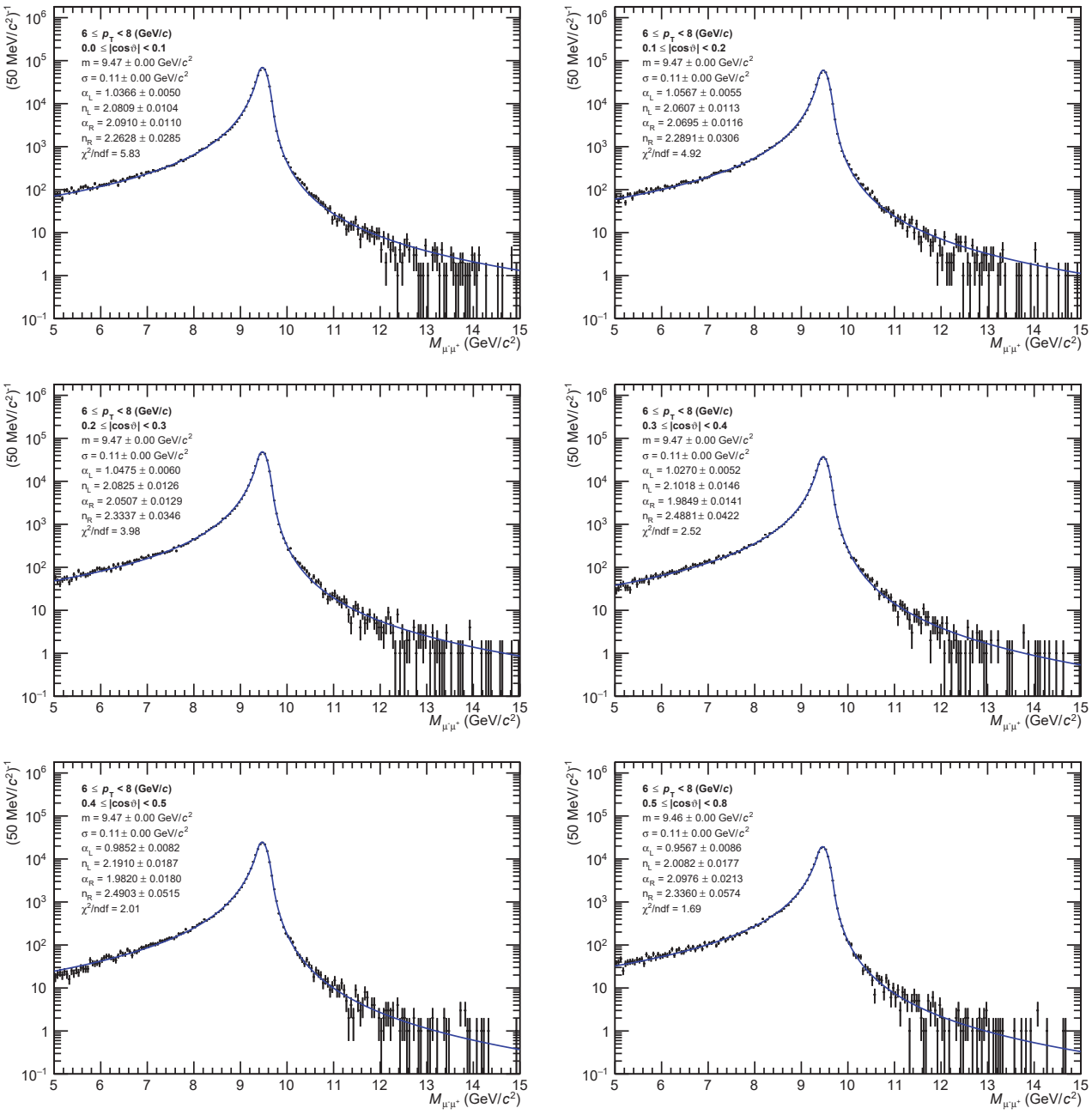

Figure B.4: Tail parameters as a function of $|\cos\theta|$ in $6 < p_{\mathrm{T}} < 8$ GeV/c in the Collins-Soper reference frame.

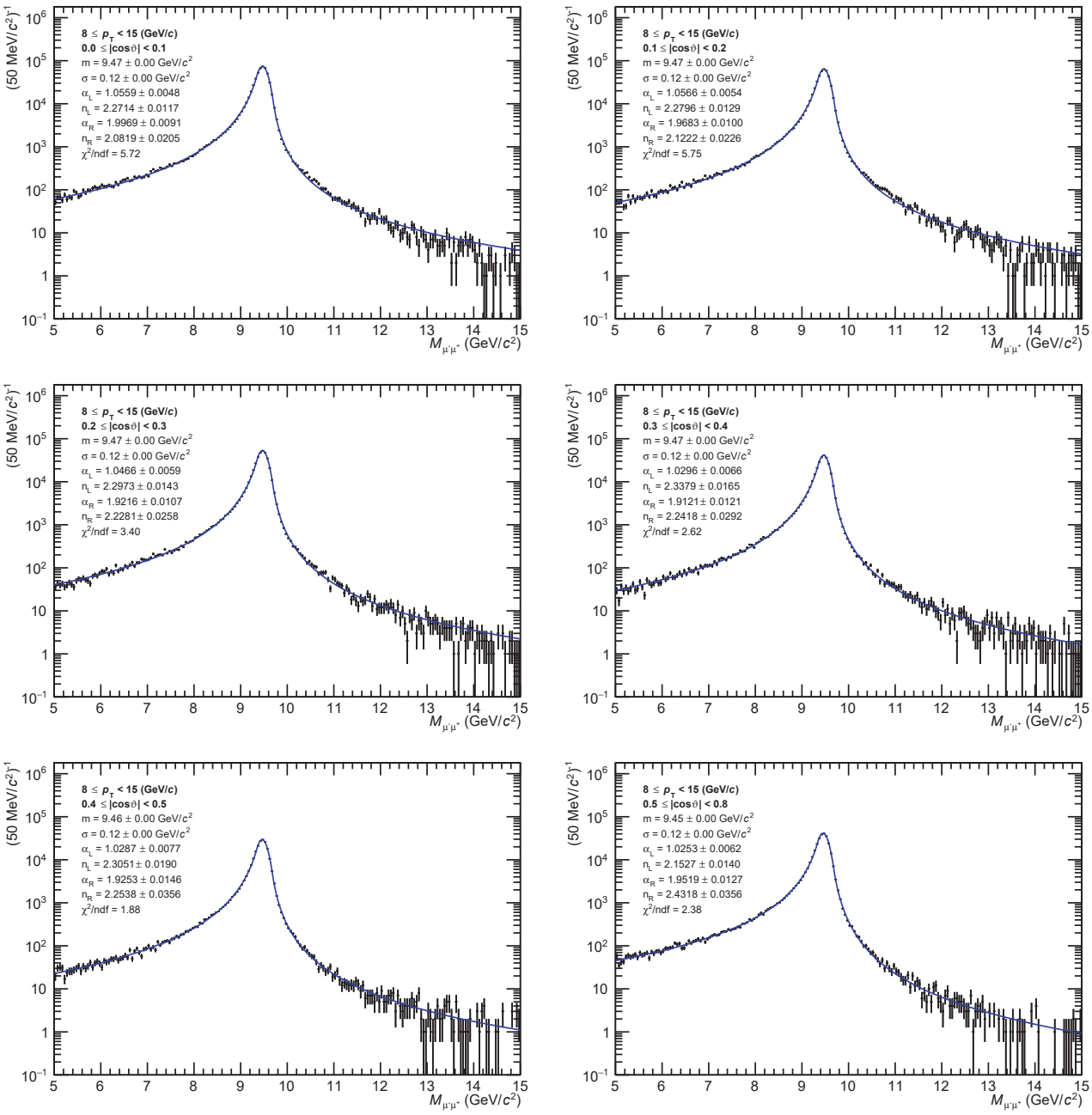

Figure B.5: Tail parameters as a function of $|\cos\theta|$ in $8 < p_{\mathrm{T}} < 15$ GeV/c in the Collins-Soper reference frame.

B.3 Signal width from MC

The Υ(1S) width (σ) as a function of angular variable $|\varphi|$ ($\tilde{\varphi}$) in p_{T} intervals in both the Helicity (left) and Collins-Soper (right) reference frames in MC simulations, are shown in Fig. B.6 (Fig. B.7).

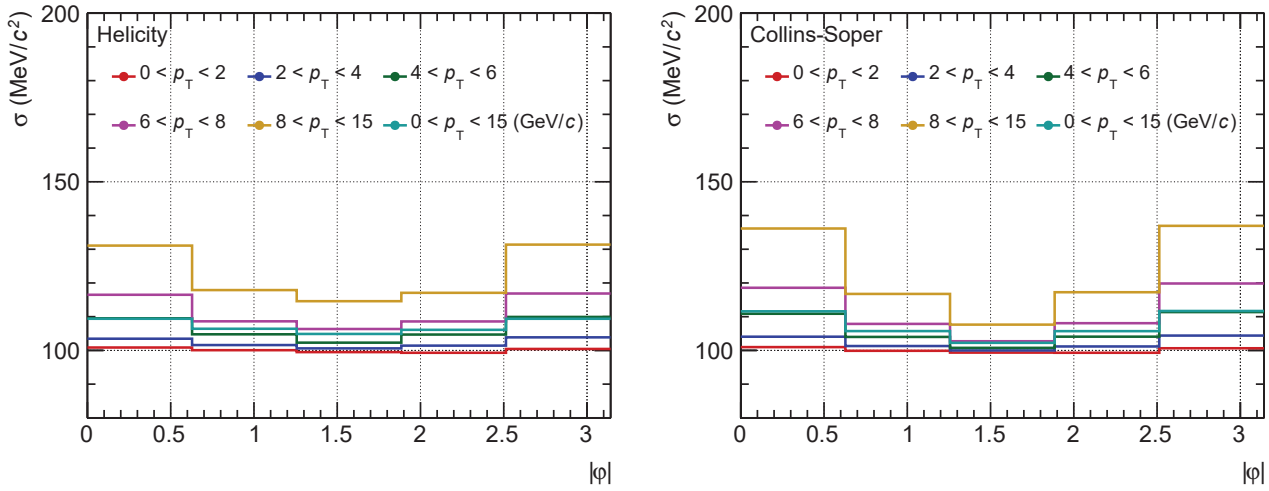

Figure B.6: The width of Υ(1S) as a function of $|\varphi|$ in p_{T} intervals in both the Helicity (left) and Collins-Soper (right) reference frames in MC simulations.

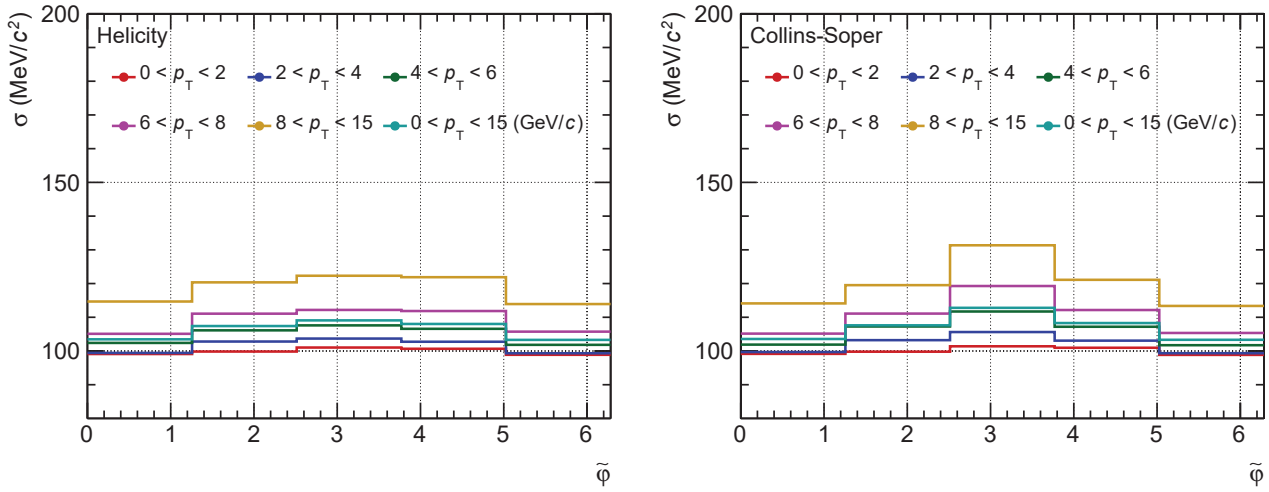

Figure B.7: The width of Υ(1S) as a function of $\tilde{\varphi}$ in p_{T} intervals in both the Helicity (left) and Collins-Soper (right) frames in MC simulations.

B.4 Acceptance-times-efficiency for φ and $\tilde{\varphi}$

The $A \times \varepsilon$ factor as a function of $|\varphi|$ and $\tilde{\varphi}$ in p_{T} regions is shown in Fig. B.8 and B.9, respectively.

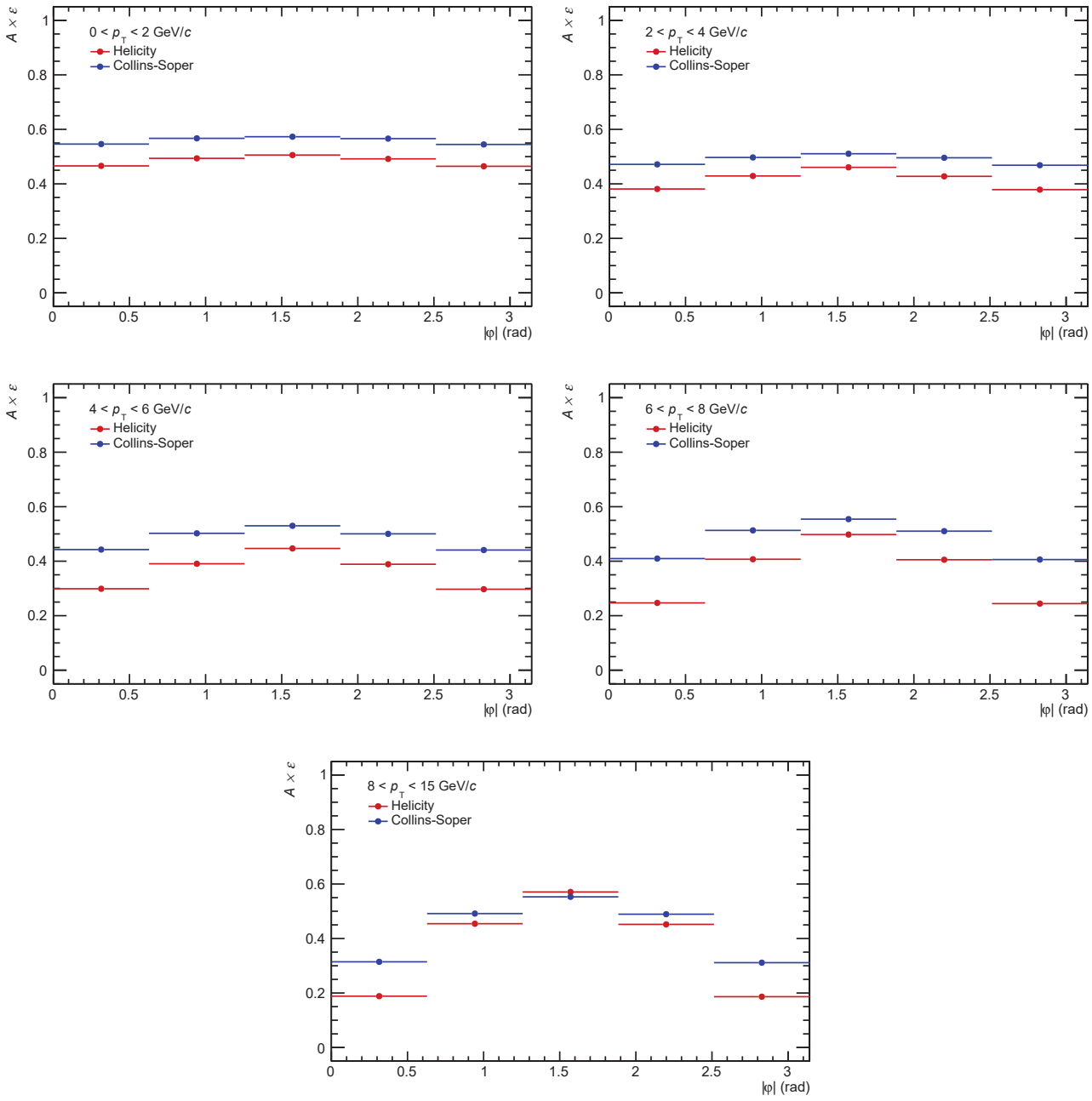

Figure B.8: A $\times$ ε as a function of $|\varphi|$ in both Helicity and Collins-Soper reference frames.

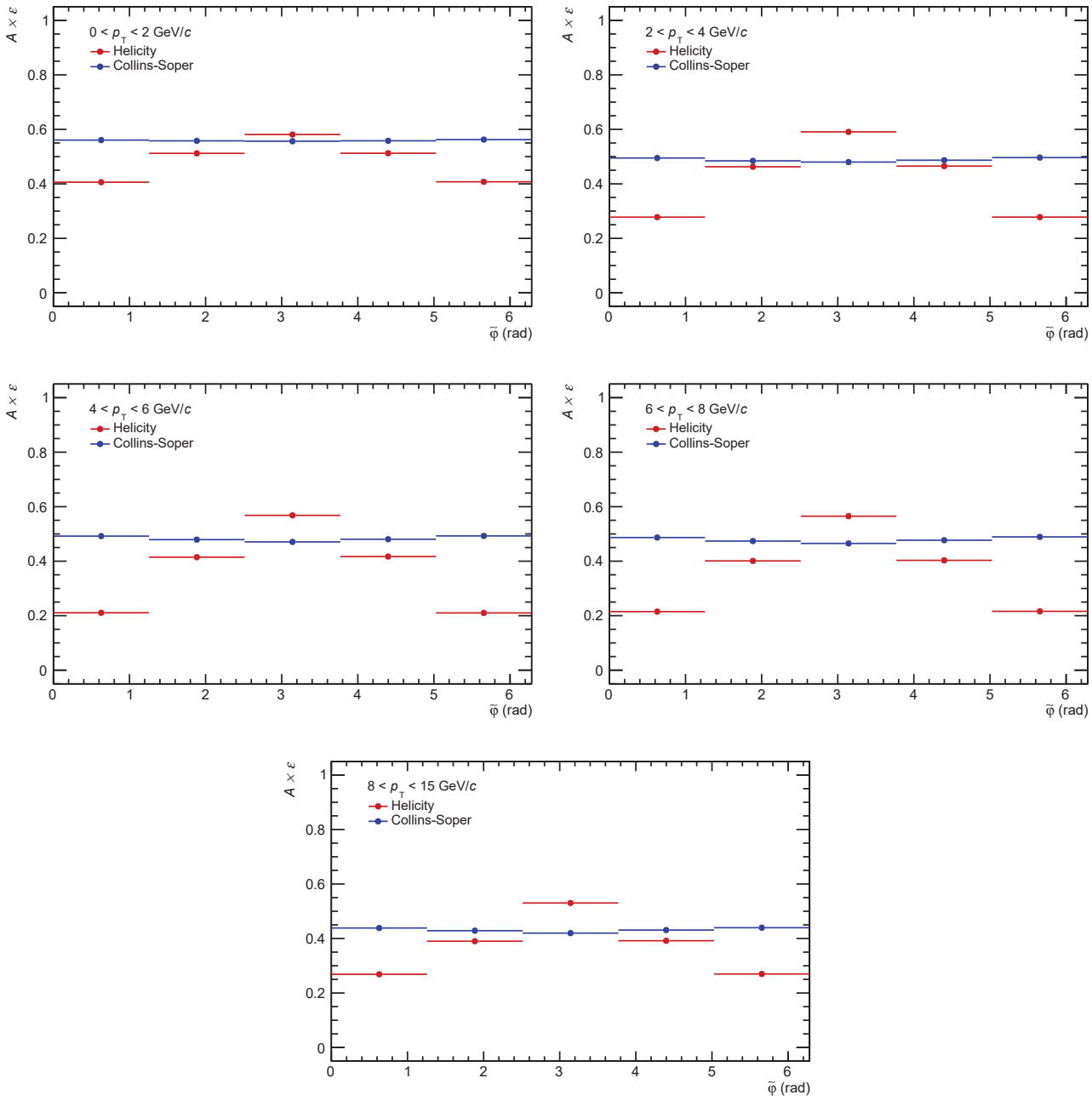

Figure B.9: A $\times$ ε as a function of $\tilde{\varphi}$ in both Helicity and Collins-Soper reference frames.

B.5 Cross check for the $|\cos\theta|$ range effect

The details of the $|\cos\theta|$ range effect were presented in [162]. When choosing the loose $|\cos\theta|$ range (using uniform $|\cos\theta|$ bin size in all p_{T} ranges and using wider range $[0.5, 0.8]$ as the last bin to ensure enough statistics in each bin) and the restricted range (constraints on the significance and A $\times$ ε), the two results are compatible within uncertainties, as shown in Fig. B.10.

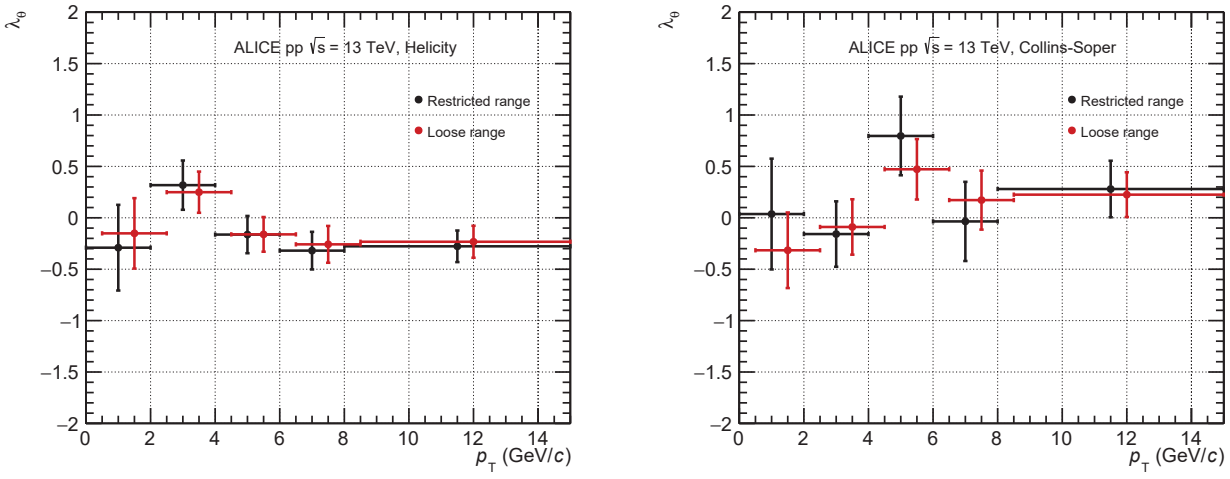

Figure B.10: Comparison of λ_θ as a function of transverse momentum between loose and restricted $|\cos\theta|$ range in both the Helicity (left) and Collins-Soper reference frames (right).

B.6 Corrected number of Υ(1S) in p_{T} ranges in both the Helicity and Collins-Soper reference frames

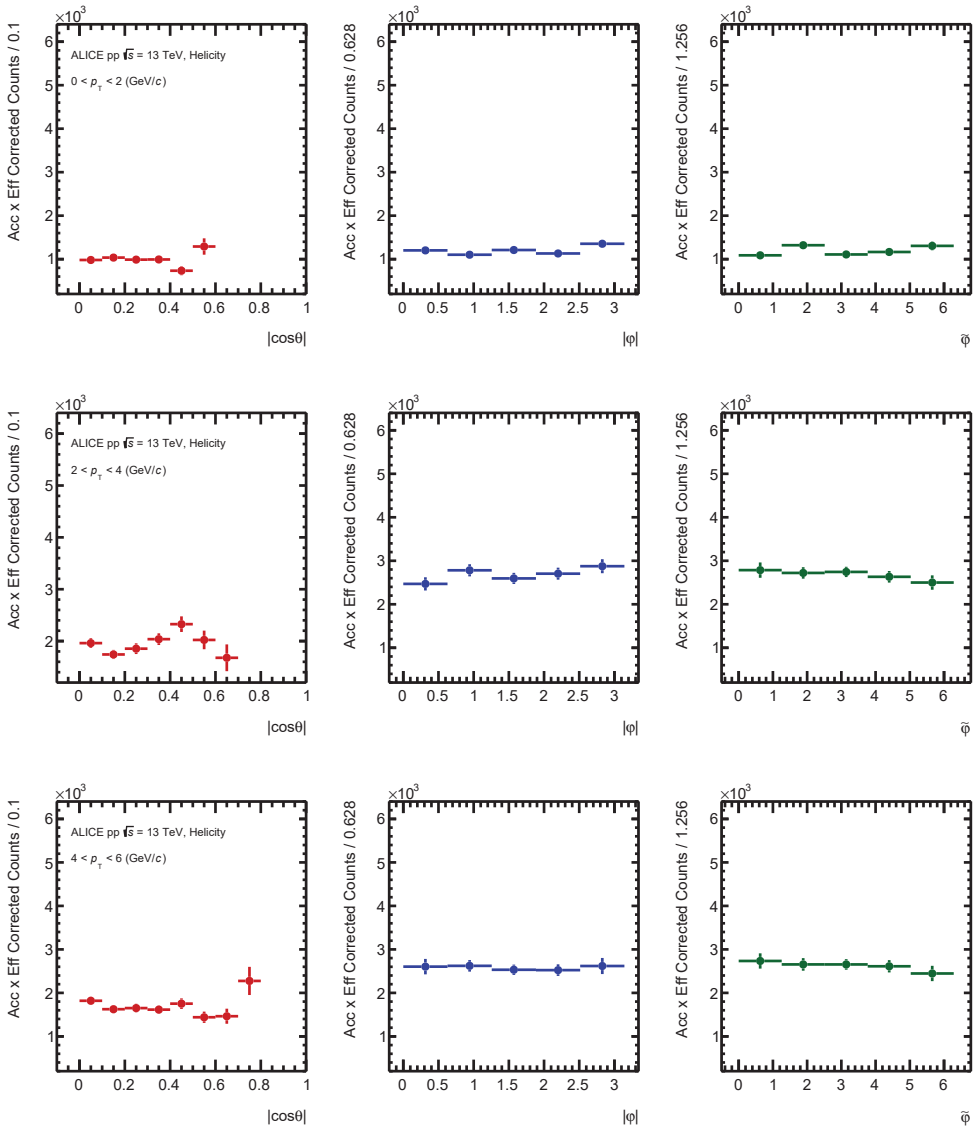

Figure B.11: Corrected number of Υ(1S) as a function of $|\cos\theta|$, $|\varphi|$ and $\tilde{\varphi}$ in p_{T} ranges (from 0 to 6 GeV/c) in the Helicity reference frame.

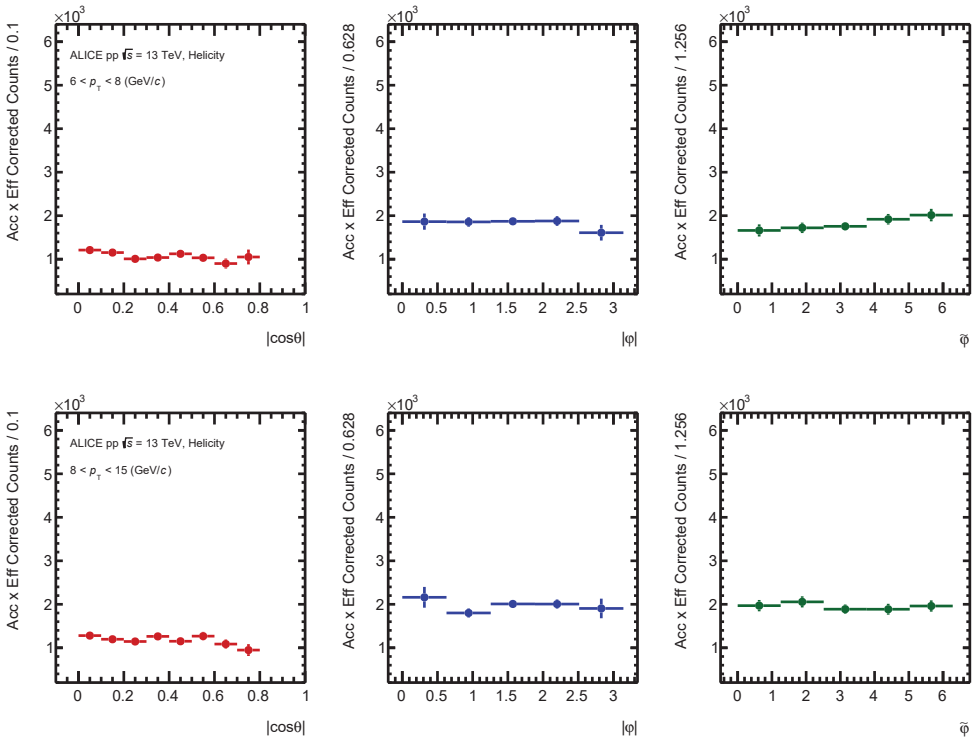

Figure B.12: Corrected number of Υ(1S) as a function of $|\cos\theta|$, $|\varphi|$ and $\tilde{\varphi}$ in p_{T} ranges (from 6 to 15 GeV/c) in the Helicity reference frame.

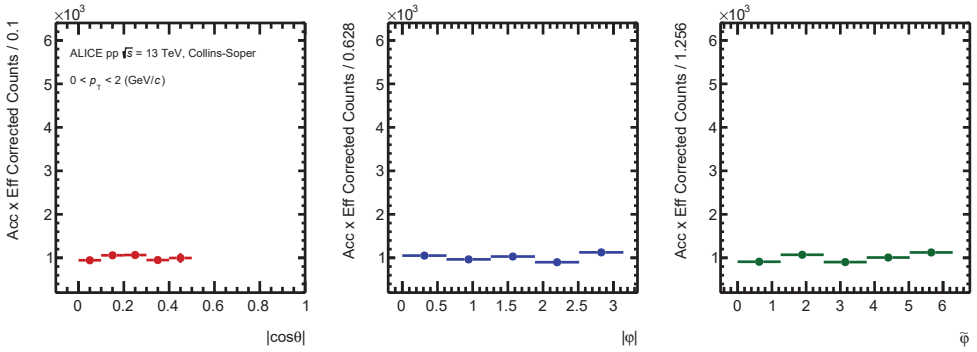

Figure B.13: Corrected number of Υ(1S) as a function of $|\cos\theta|$, $|\varphi|$ and $\tilde{\varphi}$ in p_{T} ranges (from 0 to 2 GeV/c) in the Collins-Soper reference frame.

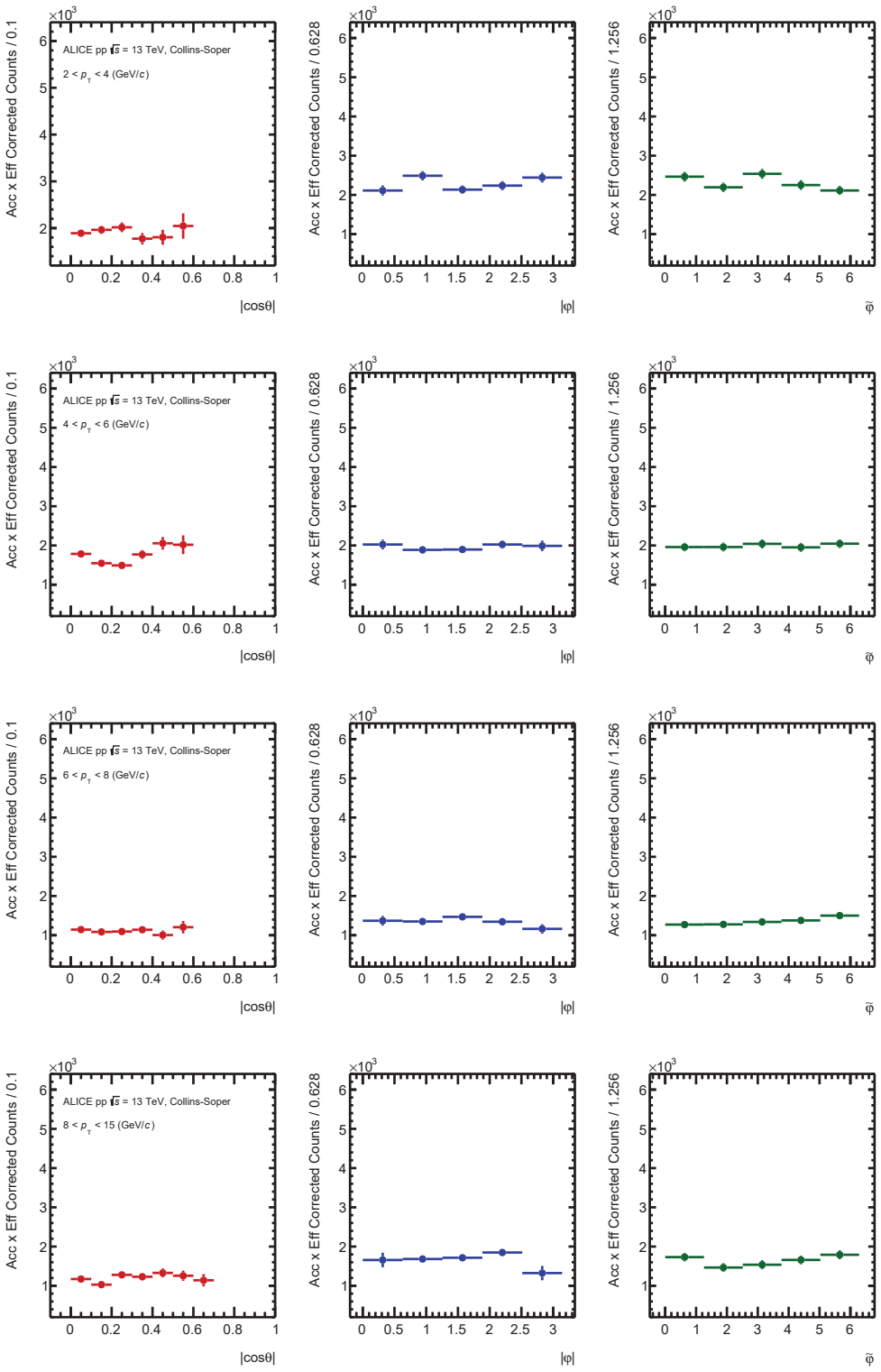

Figure B.14: Corrected number of Υ(1S) as a function of $|\cos\theta|$, $|\varphi|$ and $\tilde{\varphi}$ in p_{T} ranges (from 2 to 15 GeV/c) in the Collins-Soper reference frame.

B.7 Simultaneous fit to the corrected spectra

B.7.1 Simultaneous fit to the corrected spectra in both the Helicity and Collins-Soper reference frames

The results of the fit to the A$\times\varepsilon$ corrected spectra are here shown for the chosen p_{T} range. The fits were performed in a simultaneous way in the two reference frames (Helicity and Collins-Soper), imposing a $\tilde{\lambda}$ constraint Eq. B.1. In this case, one of the parameters can be eliminated. It is confirmed that no matter what parameter is chosen to be eliminated, the results are comparable within uncertainties (see Fig. B.18). As for the default approach (used in this analysis), $\lambda_{\varphi}^{\mathrm{CS}}$ is eliminated, and it is expressed as Eq. B.2.

$$\tilde{\lambda} = \frac{\lambda_{\theta}^{\mathrm{HE}} + 3\lambda_{\varphi}^{\mathrm{HE}}}{1 - \lambda_{\varphi}^{\mathrm{HE}}} = \frac{\lambda_{\theta}^{\mathrm{CS}} + 3\lambda_{\varphi}^{\mathrm{CS}}}{1 - \lambda_{\varphi}^{\mathrm{CS}}} \tag{B.1}$$

$$\lambda_{\varphi}^{\mathrm{CS}} = 1 - \frac{\lambda_{\theta}^{\mathrm{CS}} + 3}{\lambda_{\theta}^{\mathrm{HE}} + 3}(1 - \lambda_{\varphi}^{\mathrm{HE}}) \tag{B.2}$$

$$\lambda_{\theta}^{\mathrm{CS}} = \frac{1 - \lambda_{\varphi}^{\mathrm{CS}}}{1 - \lambda_{\varphi}^{\mathrm{HE}}}(\lambda_{\theta}^{\mathrm{HE}} + 3) - 3 \tag{B.3}$$

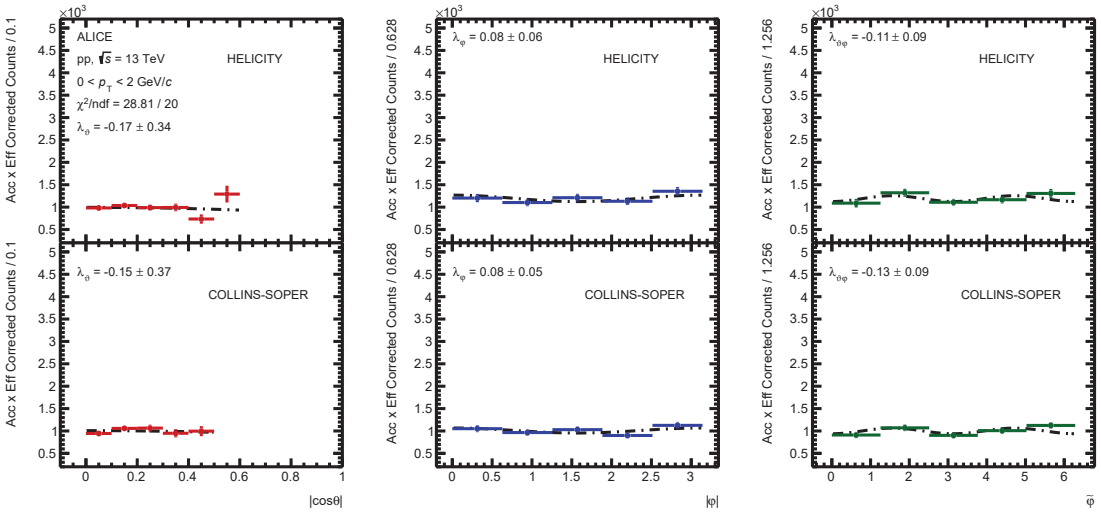

Figure B.15: Polarization parameters determination with a simultaneous fit in $0 < p_{\mathrm{T}} < 2$ GeV/c interval in both Helicity and Collins-Soper frames, imposing $\tilde{\lambda}$ constraint. The error bars are the statistical uncertainties, the dash lines are the fits.

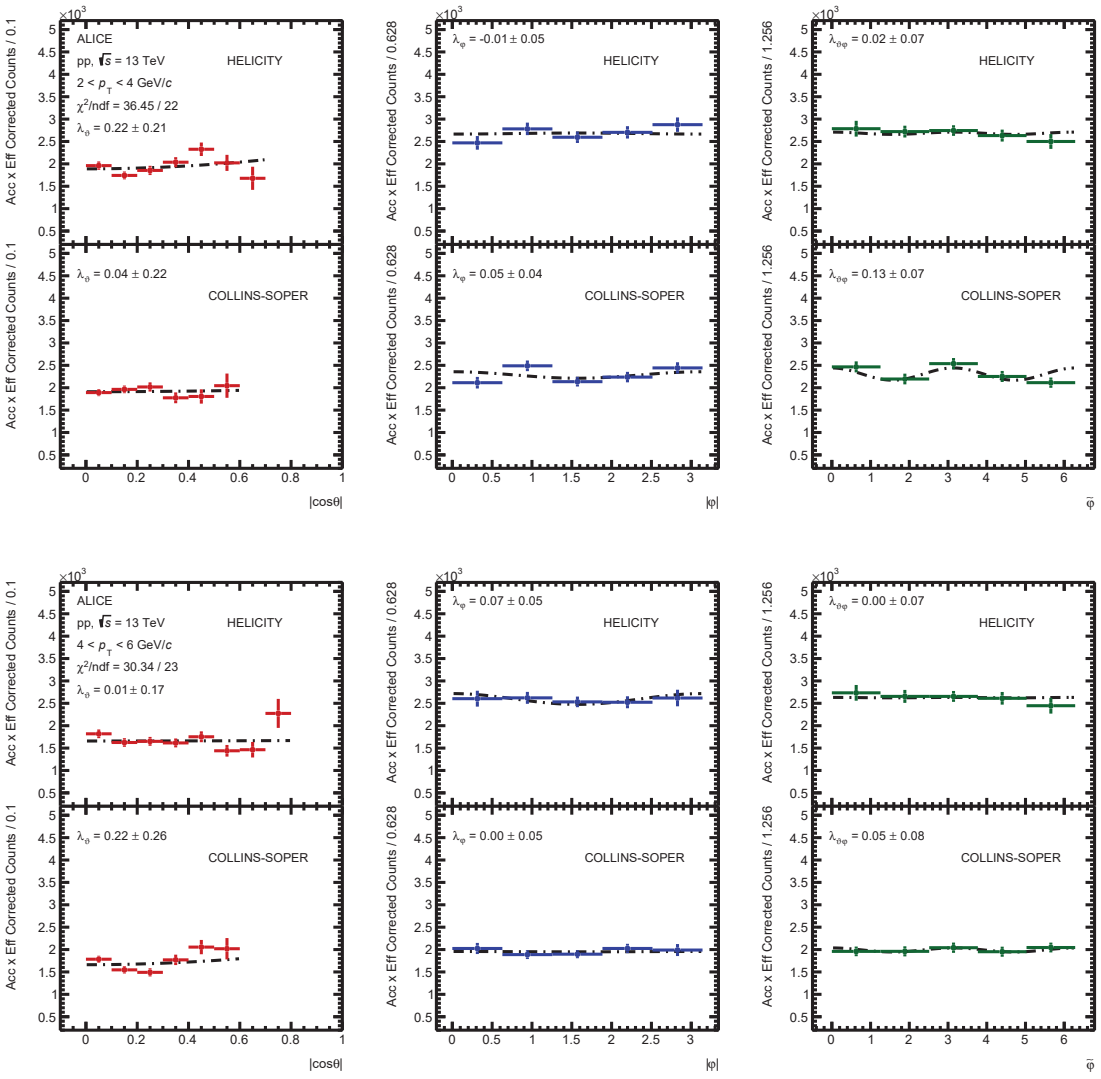

Figure B.16: Polarization parameters determination with a simultaneous fit in $2 < p_{\mathrm{T}} < 4$ and $4 < p_{\mathrm{T}} < 6$ GeV/c intervals in both Helicity and Collins-Soper frames, imposing $\tilde{\lambda}$ constraint. The error bars are the statistical uncertainties, the dash lines are the fits.

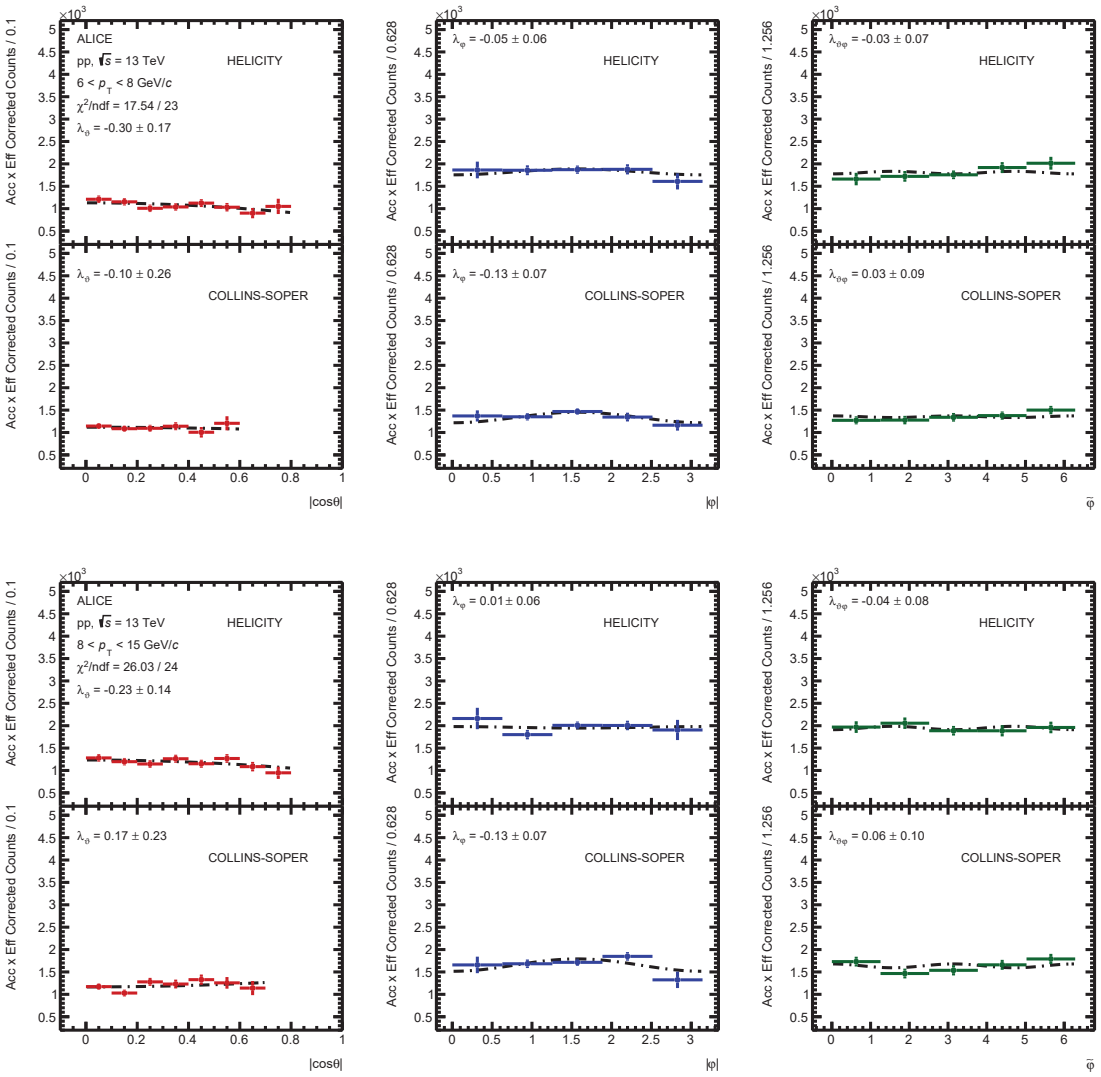

Figure B.17: Polarization parameters determination with a simultaneous fit in $6 < p_{\mathrm{T}} < 8$ and $8 < p_{\mathrm{T}} < 15$ GeV/c intervals in both Helicity and Collins-Soper frames, imposing $\tilde{\lambda}$ constraint. The error bars are the statistical uncertainties, the dash lines are the fits.

B.7.2 Separated fit to the corrected spectra in both the Helicity and Collins-Soper reference frames

As mentioned before, the fit to the corrected spectra was performed in a simultaneous way for the two reference frames, imposing an invariant quantity $\tilde{\lambda}$ in order to further constrain the fit and to reduce the statistical errors in the results. It is nevertheless interesting to try to perform the fit separately for the two frames without the invariant quantity constraint to understand whether the condition alters the final results or not. For this reason, the whole fit procedure was re-performed separately in the two frames. The results can be found in Fig. B.18. Good agreement between the two techniques is observed, i.e. with or without imposing the constraint in the fit, assessing the

goodness of the default approach.

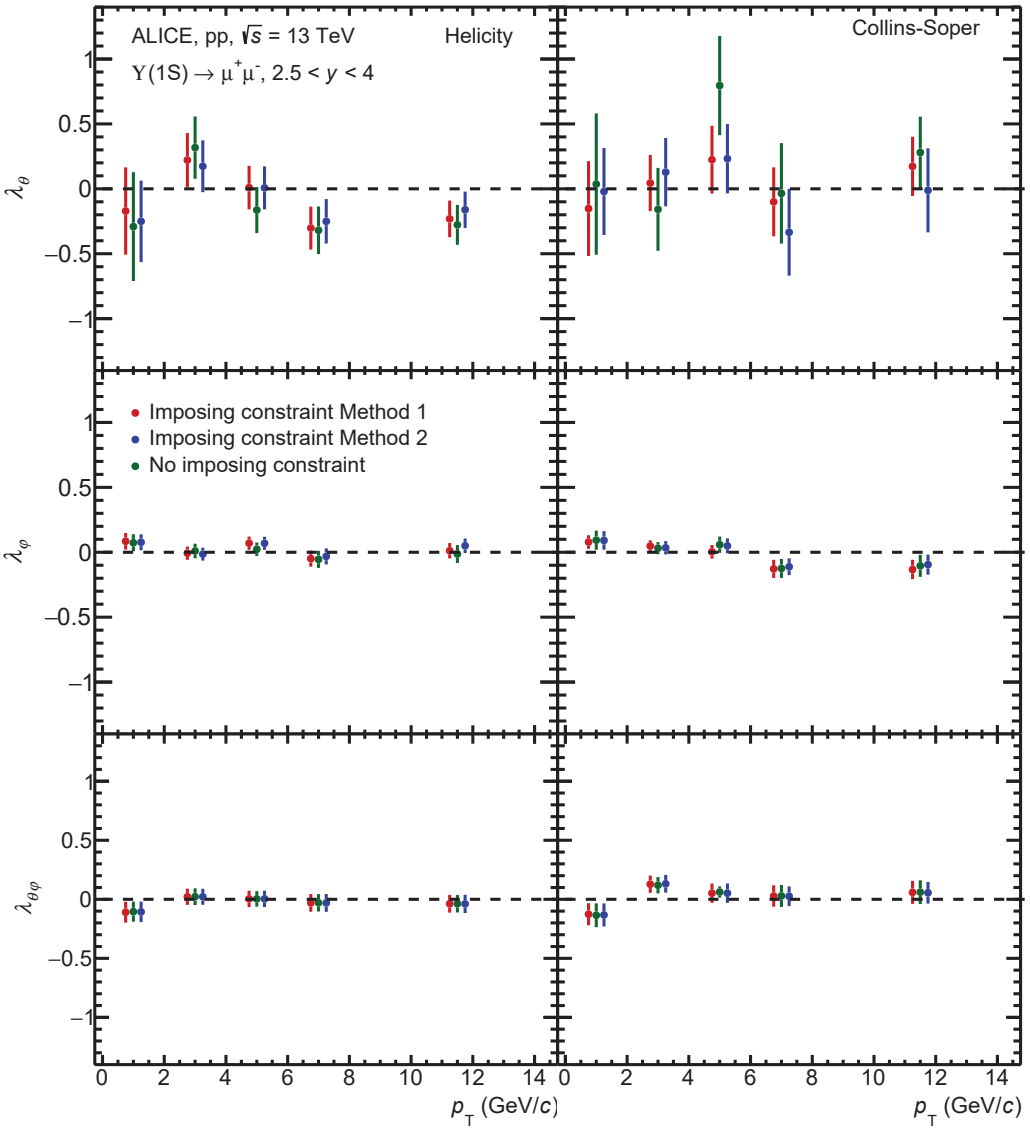

Figure B.18: Polarization parameters as a function of transverse momentum in the Helicity and Collins-Soper frames. The red points and blue points are estimated with imposing the $\tilde{\lambda}$ constraint, the green points are estimated without requiring the constraint. The red point results (default approach) were used in this analysis, which eliminated $\lambda_{\varphi}^{\mathrm{CS}}$, the blue point results were for the cross check, which eliminated $\lambda_{\theta}^{\mathrm{CS}}$.

B.8 Systematic uncertainty estimation from signal extraction

The systematic uncertainty from the signal extraction contribution comes from the background shapes and the fitting ranges. The backgound shapes are: variable-width Gaussian(VWG), the product of two exponentials (DExp), or the product of an exponential and a power low function (Pol2Exp), and three fitting ranges are 5–14 (L), 6–13 (M), and 7–12 (H) GeV/c^2.

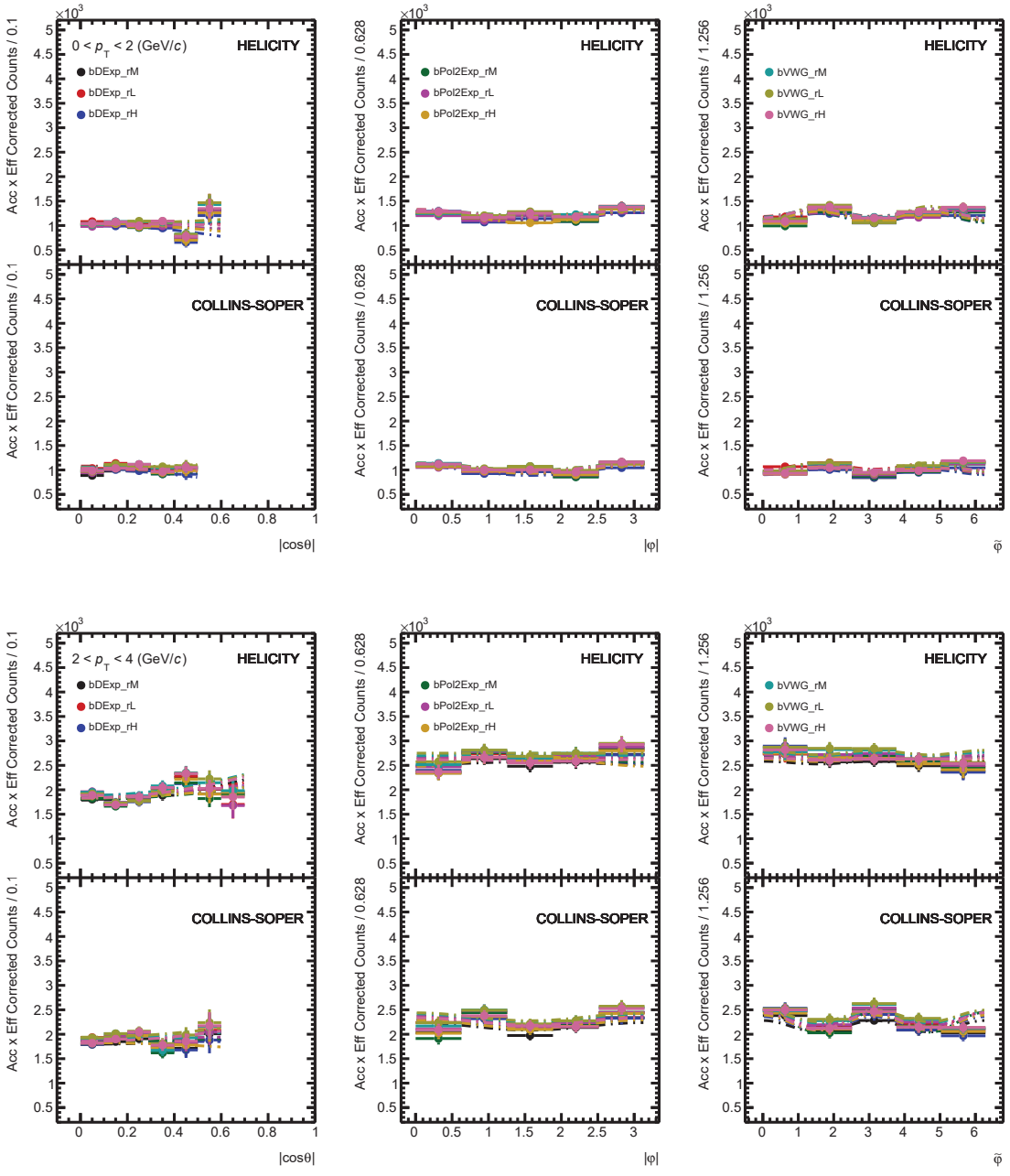

Figure B.19: Fit to the corrected spectra in $0 < p_{\mathrm{T}} < 2$ and $2 < p_{\mathrm{T}} < 4$ GeV/c intervals in both Helicity and Collins-Soper frames.

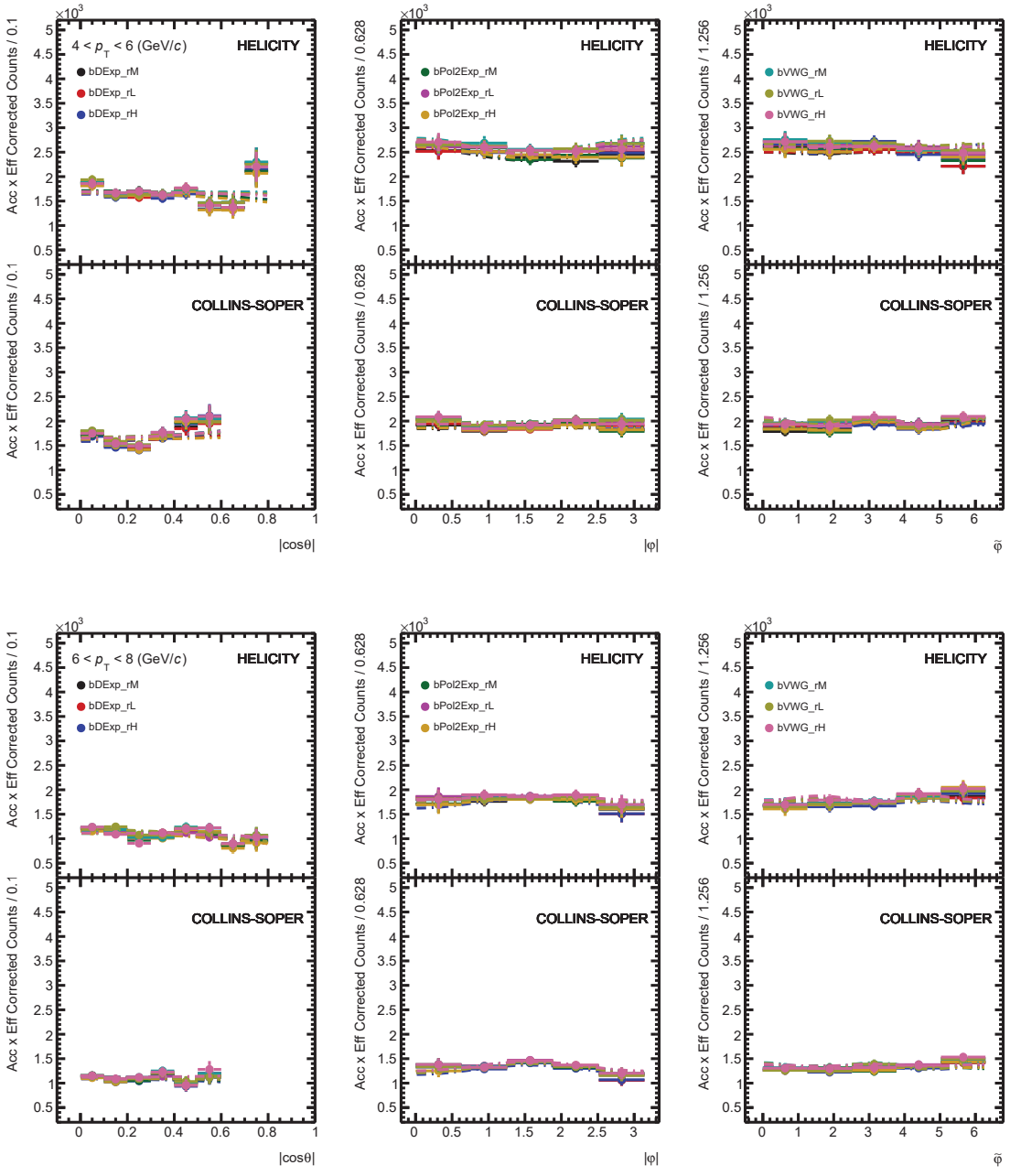

Figure B.20: Fit to the corrected spectra in $4 < p_{\mathrm{T}} < 6$ and $6 < p_{\mathrm{T}} < 8$ GeV/c intervals in both the Helicity and Collins-Soper reference frames.

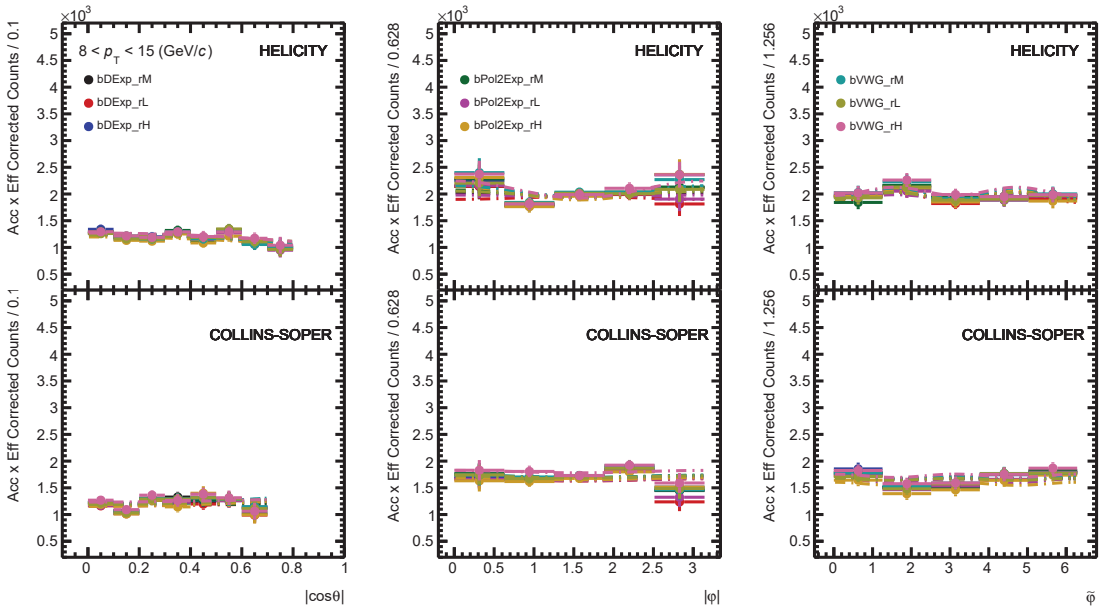

Figure B.21: Fit to the corrected spectra in $8 < p_{\mathrm{T}} < 15$ GeV/c interval in both the Helicity and Collins-Soper reference frames.

Appendix C

Rivetization: charmonia production as a function of charged-particle multiplicity in pp collisions at $\sqrt{s} = 7$ and 13 TeV

C.1 An introduction to RIVET

The Robust Independent Validation of Experiment and Theory (RIVET) is a software tool used for event generation and analysis in particle physics. It is a modular software package written in C++ and designed to interface with Monte Carlo (MC) event generators, such as PYTHIA [91] and Herwig [163, 164], to analyze their output. RIVET provides a standardized framework for comparing theoretical simulations with experimental data, as shown in Fig. C.1, which depicts how the RIVET framework connects experiment to theory. The diagram demonstrates how the comparison between the outcomes of event generators and experimental findings creates a feedback loop for the development of phenomenological models and the concrete event generator. The utilization of this feedback loop is extensive in the development of MC event generators [91, 165, 166], as well as their validation, and tuning [167–169].

RIVET allows users to define their own analysis methods, which can be used to extract physics information from simulated particle collisions. This information can then be compared with experimental data to test theoretical models of particle physics. One of the key features of RIVET is its flexibility. Users can easily modify existing analyses or create new ones by writing simple code. RIVET also provides a large library of predefined analyses, which cover a wide range of physics topics.

Nowadays, RIVET boasts a collection of over 1000 analyses from various high-energy physics collaborations, and it is able to directly access data from HepData [171] whenever it is available. Additionally, RIVET has the

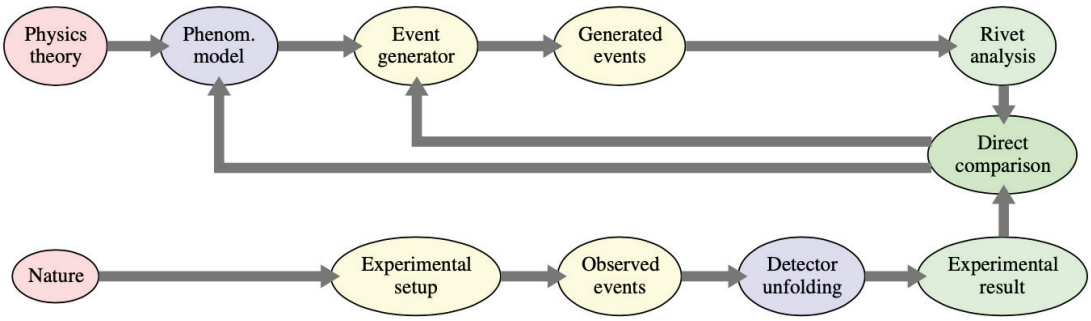

Figure C.1: Outline of how RIVET facilitates the connection between experimental analyses and theory validation by following a typical workflow in a physics program. Figure taken from [170].

capability to utilize any model that is integrated into an event generator capable of generating output that adheres to the HepMC framework [172]. This allows for effective comparison of the generated data with experimental data. A RIVET analysis typically includes the following main components, illustrated in Fig. C.2:

— Initialization: In this step, the analysis class initializes any necessary variables, reads in any configuration files or input data, and sets up any required histograms or analysis objects. This is typically implemented as a member function of the analysis class called ”init()”.

— Event loop: In this step, the analysis class loops over the input events and performs any required calculations or analysis on each event. This is typically implemented as a member function of the analysis class called ”analyze(const Event event)”.

— Finalization: In this step, the analysis class finalizes any necessary calculations or processing and writes out any results or histograms. This is typically implemented as a member function of the analysis class called ”finalize()”.

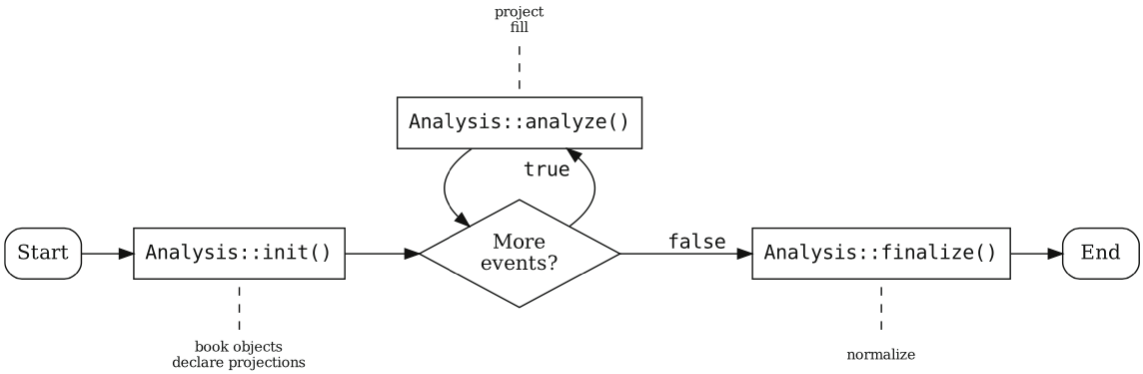

Figure C.2: The execution flow of an analysis class. Figure taken from [170].

C.2 Rivetization: J/ψ production as a function of multiplicity in pp collisions

The rivetization of J/ψ production as a function of multiplicity in pp collisions at $\sqrt{s}$ = 7 TeV has been studied. The J/ψ is measured at the forward rapidity ($2.5 < |\eta| < 4.0$) or midrapidity ($|\eta| < 0.8$). The multiplicity is measured at the midrapidity ($|\eta| < 1$). This RIVET analysis utilized input from 60 million events that were generated using the PYTHIA 8 event generator (Monash 2013) [167]. The main code "analyze(const Event event)" is shown in Fig. C.3.

```
    /// Perform the per-event analysis
    void analyze(const Event &event) {

      int mult = 0;
//      const double weight = event.weight();
      const double weight = 1.;

      const ALICE::PrimaryParticles& aprim = apply<ALICE::PrimaryParticles>(event, "APRIM");
      for( const Particle &p : aprim.particles() ){
        if(!p.charge()) continue;
         ++ mult;
      }

      _histMult->fill(mult);
      totalMult += mult;

      string ufsString[nRap] = {"UFSMID", "UFSFWD"};

      for(int iRap=0; iRap < nRap; ++iRap){

        const UnstableParticles &ufs = apply<UnstableParticles>(event, ufsString[iRap] );
        for (const Particle &p : ufs.particles()) {
          if (p.abspid() == 443 ) {
            _histJpsiVsMultTmp[iRap]->fill(mult);
            totalJpsi[iRap] += weight;
          }
        }
      }
    }
```

Figure C.3: Main part of the code of the RIVET analysis.

The comparison between data and the RIVET results is presented in Fig. C.4. It can be seen that self-normalized yield of J/ψ as a function of self-normalized multiplicity obtained in PYTHIA 8 with the RIVET framework has same trend as observed in data. The same code was applied for the J/ψ observed at midrapidity at a higher colliding energy – 13 TeV. Except the Monash 2013 tune, the 4C tune was considered, as depicted in Fig. C.5. And 60 million events were generated by the PYTHIA 8 in this case.

Further effort is still required to study the multiplicity dependence of charmonia production using RIVET. If a unified research framework can be established, one can attempt to extend this approach to the study of multiplicity dependence for other particles (e.g. Υ). This would help to standardize research methods, making research results more reliable and comparable.

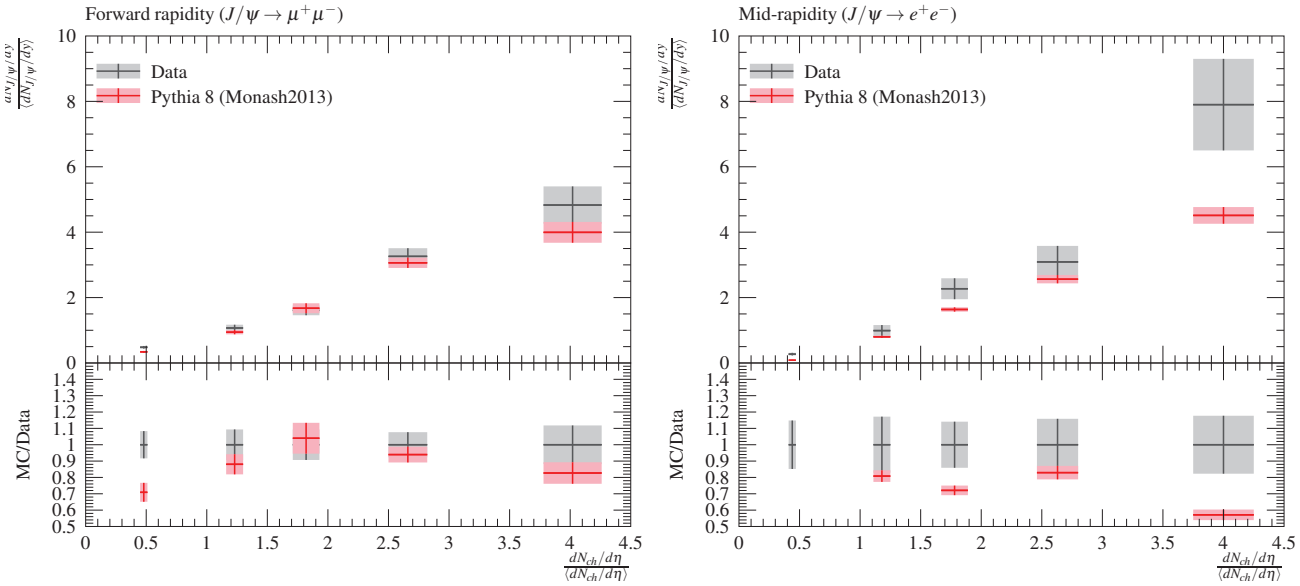

Figure C.4: J/ψ production as a function of multiplicity in pp collisions at $\sqrt{s}$ = 7 TeV. Left: J/$\psi \to \mu^+\mu^-$ (forward rapidity); right: J/$\psi \to e^+e^-$ (midrapidity).

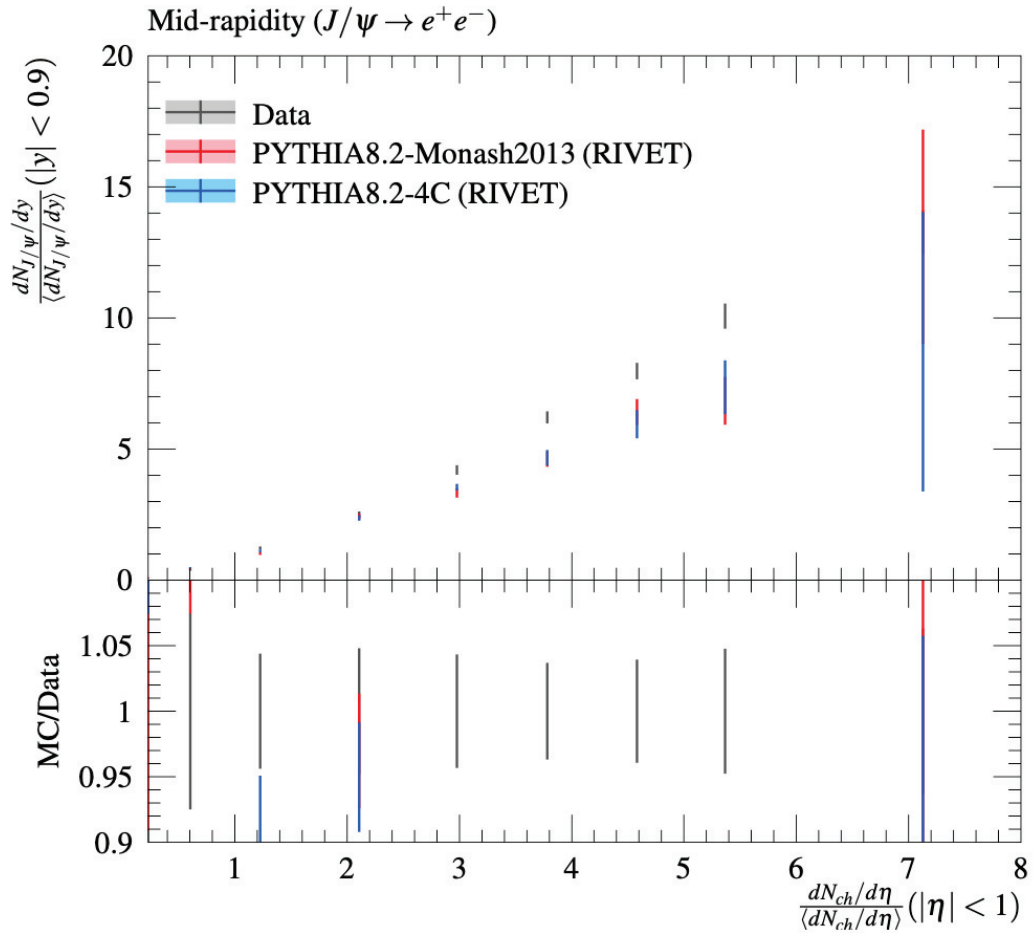

Figure C.5: J/ψ production as a function of multiplicity in pp collisions at $\sqrt{s}$ = 13 TeV (midrapidity).

List of Figures

List of Tables

Acknowledgements

The completion of my doctoral thesis marks the end of my student journey. At this moment, I find myself with mixed emotions - nostalgia for the past and expectations for the future. However, above all, I am overwhelmed with gratitude.

First of all, I would like to express my sincere gratitude to my supervisors Brigitte Cheynis, Antonio Uras, Daicui Zhou and Xiaoming Zhang for their valuable guidance, unwavering support and endless patience during my doctoral studies. It was their careful guidance that allowed me to successfully complete the writing of my graduation thesis. In life, they all gave me meticulous care and concern. I remember that when the COVID-19 first broke out, they all kept greeting me, caring about me, and helping me solve the difficulties I encountered in life. This made my life in Lyon full of warmth and made me no longer afraid and lonely. I am very grateful to have such great mentors in my life.

I am also deeply indebted to the members of my dissertation committee, Prof. Nicole Bastid, Prof. Jinhui Chen, Prof. Mei Huang, Prof. Imad Laktineh and Dr. Laure Massacrier for their insightful comments and valuable suggestions. Their feedback and suggestions helped me refine my research, clarify my arguments, and present my results in a coherent and convincing manner.

I would like to thank the IP2I and CCNU for providing me with the resources, facilities and opportunities for research. Special thanks to Prof. Cvetan, Prof. Mao, Prof. Yin and Prof. Pei for their guidance and discussion on my research topic. In addition, I would like to thank all members of the ALICE PWG-DQ for the discussions and the constructive comments, which greatly enhanced my expertise in quarkonium studies.

I would also like to thank my colleagues Lucrezia Migliorin, Sarah Herrmann, Lang Xu, Mingyu Zhang, Biao Zhang, Yongzhen Hou, Ran Xu, and Feng Fan for their encouragement and help. Their diverse perspectives and rich experiences have been instrumental in my research and personal growth.

Finally, I would like to thank my family and friends for their love, support, and encouragement during my doctoral studies. Their belief and encouragement in me sustained me during difficult times and inspired me to strive for excellence.

Thank you all for your invaluable contributions to my doctoral journey.